Radial Turbine ExpanderDesign, Modelling and Testing for Automotive Organic Rankine Cycle Waste Heat Recovery

A thesis submitted for the degree of

Doctor of Philosophy

Fuhaid Alshammari

College of Engineering, Design and Physical Sciences

Brunel University London

Uxbridge, UB8 3PH

United Kingdom

2018

I. Abstract

Since the late 19th century, the average temperature on Earth has risen by approximately 1.1 °Cbecause of the increased carbon dioxide (CO_2) and other man-made emissions to the atmosphere. The transportation sector is responsible for approximately 33% of the global CO_2 emissions and 14% of the overall greenhouse gas emissions. Therefore, increasingly stringent regulations in the European Union require CO_2 emissions to be lower than 95 gCO_2/km by 2020. In this regard, improvements in internal combustion engines (ICEs)must be achieved in terms of fuel consumption and CO_2 emissions. Given that only up to 35% of fuel energy is converted into mechanical power, the wasted energy can be reused through waste heat recovery (WHR) technologies. Consequently, organic Rankine cycle (ORC) has received significant attention as a WHR technology because of its ability to recover wasted heat in low- to medium-heat sources.

The Expansion machine is the key component in ORC systems, and its performance has a direct and significant impact on overall cycle efficiency. However, the thermal efficiencies of ORC systems are typically low due to low working temperatures. Moreover, supersonic conditions at the high pressure ratios are usually encountered in the expander due to the thermal properties of the working fluids selected which are different to water.Therefore, this thesis aims to design an efficient radial-inflow turbine to avoid further efficiency reductions in the overall system. To fulfil this aim, a novel design and optimisation methodology was developed. A design of experiments technique was incorporated in the methodology toexplorethe effects of input parameters on turbine performance and overall size. Importantly, performance prediction modelling by means of 1D mean-line modelling was employed in the proposed methodology to examine the performance of ORC turbines at constant geometries. The proposed methodology was validated by three methods: computational fluid dynamics analysis, experimental work available in the literature, and experimental work in the current project.Owing to the lack of actual experimental works in ORC-ICE applications, a test rig was built around a heavy-duty diesel engine at Brunel University London and tested at partial load conditions

due to the requirement for a realistic off-high representation of the performance of the system rather than its best (design) point, while taking into account the limitation of the engine dynamometer employed.

Results of the design methodology developed for this projectpresented an efficient single-stage high-pressure ratio radial-inflow turbine with a total to static efficiency of 74.4% and an output power of 13.6 kW.Experimental results showed that the ORC system had a thermal efficiency of 4.3%, and the brake-specific fuel consumption of the engine was reduced by 3%. The novel meanlineoff-designcode (MOC) was validated with the experimental works from three turbines. In comparison with the experimental results conducted at Brunel University London, the predicted and measured results were in good agreement with a maximum deviation of 2.8%.

II. Acknowledgments

First, I would like to express my sincere gratitude to my supervisor, Dr. Apostolos Pesyridis, for hiscontinuous support of my Ph.D. study, and for sharing his related research, patience and immense knowledgewith me. His guidance and motivation helped me conducting my research, writing this thesis and overcoming the difficulties I encountered during my study. I couldnotask for a better supervisor and mentor for my Ph.D. study.

I would also like to thank aresearch fellow, Dr. Apostolos Karvountzis, for his support, feedback, cooperation and friendship. My sincere thanks go to Dr. Nicholas Baines from Concepts NREC for his support and valuable comments during the design process.

I would like to acknowledge the financial support provided by Innovate UK through grant TS/M012220/1 in support of this project.In addition, I would like to express my thanks to theindustrial partner (Entropea Labs) for itssupport during the laboratory testing.

I am likewisegrateful to my office mates and best friends, Mr. Khalifa Bureshaid, Mr. Mamdouh Alshammari and Mr. Jabbar Al-Dulaimi,who stood beside me through the toughesttimes during my research. They are the perfect examples oftrue friends.

I would like to thank my family with all my heart for supporting me spiritually throughout my research and my life in general. I dedicate this thesis to my parents,Mr. Aziz and Mrs. Joziah, for their everlasting faith. I am very grateful to my sons,Anas and Aziz,forinspiring me with their love and care.

To my wife, Mrs. Dalal, words are inadequate to express my gratitude toand feelings foryou. Thank you for your enduring love, for believing in me long after Ilost faithin myself and for your patience. Praise be to God for your presence in my life.

III. Author's Declaration

I hereby declare that the work contained in this thesis has not been submitted for any other award and is my own work. Ialso confirm that this work fully acknowledges the opinions, ideas and contributions of other individuals/works.

Signature:

Fuhaid Alshammari

IV. Journal Publications from this Work

- **Fuhaid Alshammari**, Apostolos Karvountzis-Kontakiotis and Apostolos Pesyridis. "*Effect of Radial Turbo-Expander Design on Off-Highway Vehicle Organic Rankine Cycle System Efficiency.*" International Journal of Powertrains- ACCEPTED, **[Chapter 3 and Chapter 5]**

- **Fuhaid Alshammari**, A. Karvountzis-Kontakiotis, A. Pesiridis, Timothy Minton, "*Radial Expander Design for an Engine Organic Rankine Cycle Waste Heat Recovery System.*" Elsevier, Energy Procedia, Volume 129, 2017, Pages 285-292, ISSN 1876-6102, https://doi.org/10.1016/j.egypro.2017.09.155, **[Chapter 5].**

- **Fuhaid Alshammari**, Apostolos Pesyridis, Apostolos Karvountzis-Kontakiotis, Ben Franchetti and Yagos Pesmazoglou "Experimental Study of a Small Scale Organic Rankine Cycle Waste Heat Recovery System for a Heavy Duty Diesel Engine with Focus on the Radial Inflow Turbine Expander Performance." Elsevier, Applied Energy- ACCEPTED, **[Chapter 7].**

- **Fuhaid Alshammari**, Apostolos Karvountzis,Apostolos Pesyridis and Mamdouh Alshammari. "*Expander Technologies for Engine Organic Rankine Cycle Applications.*" Elsevier, Applied Thermal Engineering- UNDER REVIEW, **[Chapter 2].**

- **Fuhaid Alshammari**, Apostolos Karvountzis-Kontakiotis and Apostolos Pesyridis. "*Towards Predicting Radial Inflow Turbine Performance operating with Ideal and Real Working Fluids..*" Elsevier, Energy Conversion and Management-UNDER REVIEW, **[Chapter 5].**

- **Fuhaid Alshammari**, Apostolos Karvountzis-Kontakiotis and Apostolos Pesyridis. "*CFD and FE Analyses of High Pressure Ratio ORC Radial Turbine*" Elsevier, Energy- UNDER PREPARATION**[Chapter 6].**

V. Conferences Presentations and Resulting Publications fromthis Work

- A. Karvountzis-Kontakiotis, **Fuhaid Alshammari** and A. Pesiridis ''*Adapting a Variable Geometry Turbine in Organic Rankine Cycle for Waste Heat Recovery in Off-Highway Vehicles*" THIESEL, Conference on Thermo- and Fluid Dynamic Processes in Direct Injection Engines, Valencia, Spain, 2016.

- **Fuhaid Alshammari**, A.Karvountzis-Kontakiotis, A.Pesiridis "Radial Turbine Expander Design for Organic Rankine Cycle Waste Heat Recovery in High Efficiency, Off-Highway Vehicles." Powertrain Modelling and Control,Loughborough, UK, 2016

- Karvountzis-Kontakiotis, A., Pesiridis, A., Zhao, H., **Alshammari, F**. et al., "*Effect of an ORC Waste Heat Recovery System on Diesel Engine Fuel Economy for Off-Highway Vehicles.*" SAE Technical Paper 2017-01-0136, 2017.

- **Fuhaid Alshammari**, Apostolos Karvountzis-Kontakiotis, Apostolos Pesiridis " *Design of an Efficient Back-Swept Turbo-Expander for an Engine Organic Rankine Cycle Waste Heat Recovery System*" EBER , 2nd International Symposium on Engine Boosting and Energy Recovery , Johor Bahru, Malaysia, 2017.

- **Fuhaid Alshammari**, A. Karvountzis-Kontakiotis, A. Pesiridis, Timothy Minton, ''*Radial Expander Design for an Engine Organic Rankine Cycle Waste Heat Recovery System."* 4th International Seminar on ORC Power Systems, Milan, Italy, 2017.

VI. Table of Contents

VII. List of Figures

VIII. List of Tables

IX. Nomenclature

1-5	Stations through turbine
a	Speed of sound [m/s]
A	area
b	blade height [m]
BK	Blockage factor [-]
C	Absolute velocity [m/s]
Cf	Friction factor [-]
Cm	Meridional velocity [m/s]
Cθ	Tangential velocity [m/s]
Ca	Axial coefficient [-]
Cr	Radial coefficient [-]
d	diameter [m]
h	Enthalpy [kJ/kg]
Ka	Discharge coefficient of the axial component [-]
Kr	Discharge coefficient of the radial component [-]
Ka,r	Cross coupling coefficient of the axial and radial components [-]
l	length [m]
M	Mach number [-]
m'	Mass flow rate [kg/s]
N	Rotational speed [RPM]
o	Throat opening [m]
P	Pressure [kPa]
Q	Volume flow rate (m^3/s)
r	radius [m]
Re	Reynold number [-]
rr	Wall relative roughness [m]
s	Entropy [kJ/kg.k]
T	Temperature [K]
U	Tip speed [m/s]
w	Relative velocity [m/s]
W	work [kW]
z	Axial length [m]

Subscript

b	back face
h	hub
hyd	hydraulic
opt	optimum
r	radial, rotor
rms	root mean square
s	insentropic, stator
t	tip, total
x	axial

Greek Symbols

μ	Viscosity [Pa.s]
η	Efficiency [-]
ß	Relative angle [deg]
δ	Deviation angle [deg]
ε	Clearance [m]
ρ	Density [kg/m3]
α	Absolute flow angle [deg]
γ_3	Setting angle
ψ	Azimuth angle

Abbreviations

BSFC	Break specific fuel consumption
CAC	charge air cooler
CFD	Computational fluid dynamics
DoE	Design of experiment
DoEC	Design of experiment code
DP	Design point
DPC	Design point code
EoS	Equation of state
FGT	Fixed geometry turbine
GWP	Global warming potential
HDD	Heavy duty diesel engine
ICE	Internal combustion engine
MFP	Mass flow parameter
NIST	National Institute of Standards and Technology
NOx	Nitrogen Oxide
OC	Optimisation code
ORC	Organic Ranke cycle
PDE	Positive displacement expander
PM	Particulate matter
STHE	Single flow heat exchanger
TC	Turbo-compounding
TEG	Thermo-electric generation
VGT	Variable geometry turbine
WHR	Waste heat recovery

Chapter 1 : Introduction

1.1 Background

Carbon dioxide (CO_2) emissions of the transportation sector have a significant global impact on air quality and the environment. Amongfuel-based applications, transportation burns most of the world's fuel,accounting for more than 67%of the total fuel consumption in the United States [1] and 73% in the United Kingdom in 2013 [2]. Transportation contributes to air pollution through mono-nitrogen oxides(NOx) and particulate matter (PM) emissions and to global warming through CO_2 emissions. In addition, fuel prices have continually increased, from 60 pence/litre in 1997 to 120 pence/litre in 2013 in the United Kingdom [3]. Theseconcerns necessitate the development of more efficient combustion engines.

Recently, organic Rankine cycle (ORC) systems as waste heat recovery (WHR) systems in internal combustion engines (ICEs) have received increasing interest. This technology is most widely used in low- to medium-temperature heat sources, typically between 80°C and 350°C, due to the low boiling point of organic fluids compared to steam,which is widely used in large-scale applications. However, further development is still required to implement such technology in modern passenger cars because of the need for compact integration and controllability in the engine [4].

1.1.1 Potential of Energy Recovery in Internal Combustion Engines

This section presents a general outlook on the state of the art of energy and environmental concerns in ICEs. A detailed explanation is presented in Chapter 2.

ICEs are devices in which chemical energy is transformedinto mechanical energy through fossil fuel combustion. Fossil fuel remains the main global energy source. Owing to the limited amount of such fuels, prices fluctuate significantly, with consistent general rising trends, resulting in economic issues in non-oil-producing countries. Figure 1-1presents the fuel prices in the UK, depicting an increase of 68% in diesel prices from 2003 to 2013. Moreover, the majority of fuel energy (approximately 60%–70%) is released to the environment as heat[5]. This wasted heat, which is burned fossil fuel,

is associated with dangerous chemical compounds, such as carbon monoxide, NOx, hydrocarbons, and PMs. These chemical compounds, which are proportional to fuel consumption, contribute to severe environmental issues such as pollution.Figure 1-2 and Figure 1-3 present the stringent fleet emission requirements in heavy-duty and light-duty vehicles, respectively. Both figures show the currently required improvement in CO_2 emissions. The figures also present the proposed reduction in CO_2 emissions until 2025. Phase 2 in Figure 1-2indicates that heavy-duty vehicles should deliver 20%–45% reduction in CO_2 emissions, and the dotted lines in Figure 1-3indicate that light-duty vehicles should deliver 7.5%–47% reduction in CO_2 emissions. Therefore, automobile manufacturers mustextend their efforts to introduce new carbon-reducing technologies.

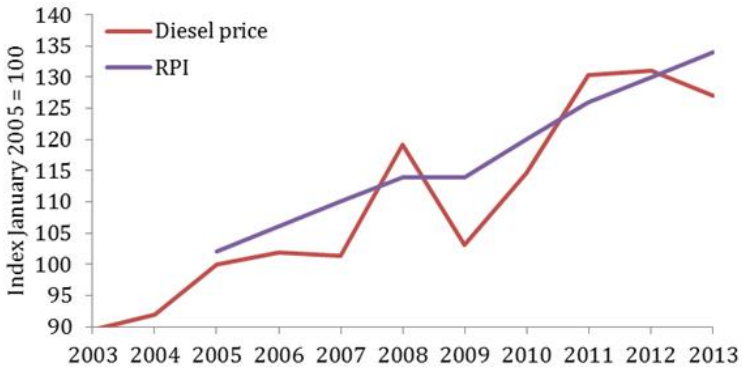

Figure 1-1: Road fuel prices in the UK [6].

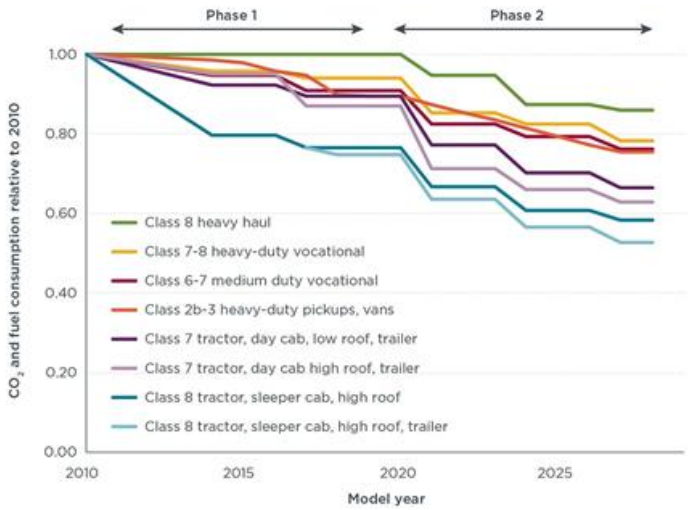

Figure 1-2: Summary of CO_2 and fuel consumption reduction from adopted Phase 1 and proposed Phase 2 heavy-duty vehicle standards for selected vehicle categories [7].

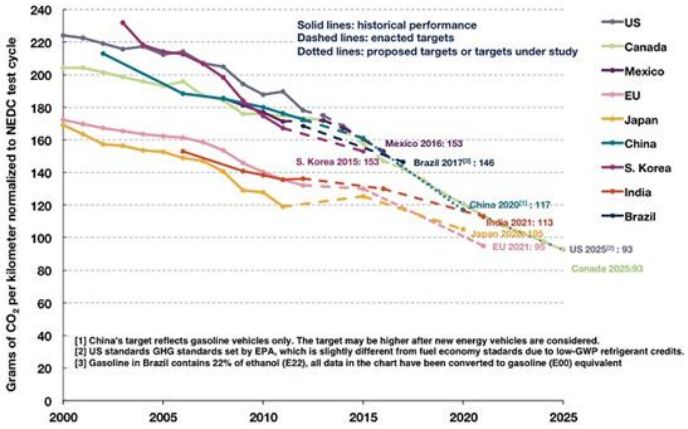

Figure 1-3: Global comparison of passenger vehicle GHG emission standardsnormalised to NEDC gCO_2/km[7].

Fuel energy is lost as heat through exhaust gases, exhaust gas recirculation (EGR) and charge air cooler (CAC) systems. The exhaust gases of ICEs contain the largest portion of wasted heat, which is approximately20%–42% of the total wasted heat [8]. Most modern diesel engines recirculate exhaust gases. Recirculating exhaust gases back to the combustion chamber is beneficial as it helpsat reducing NOx emissions. EGR contributes to 15%–20% of wasted fuel energy [9]. Finally, most modern diesel engines are equipped with turbochargers to increase the efficiency of the ICE. However, the implementation of turbochargers results in high air temperature at the intake manifold. Therefore, CAC is implemented to reduce the air temperature and maintain the high air density. CAC contributes to 10% of the wasted fuel energy [10]. Among heat loss sources, exhaust gases are considered the most beneficialdue to their high temperature levels.

Vazquez et al.[11] stated that converting just 10% of the wasted heat could result in a 20% increase in fuel efficiency. Therefore, efficient technologies should be developed to save fuel and reduce exhaust emissions, which eventually lead to high engine efficiency. Three main technologies are currently investigated as Waste Heat Recovery (WHR) technologies, namely,ORC, turbo-compounding (TC) and thermo-electric generation (TEG). Although ORC is briefly discussedin the next section, Chapter 2 presents such technology in detail.

1.1.2 Organic Rankine Cycle

ORC is basically a thermodynamic cycle that converts heat into work by using organic fluids as working fluids. Figure 1-4presents theschematic of a typical Rankine cycle that consists of four main components: evaporator, turbine, pump and condenser. As stated, ORC is a Rankine cycle, and hence the same operating principle applies. The working fluid is compressed isentropically in the pump (Process 1-2). Then, the fluid is heated and vapourised in the boiler (evaporator),whichcauses the fluid to change instate from liquid to vapour (Process 2-3). Next, the vapour is expanded in anexpander that extracts energy from the superheated working fluid to produce power (Process 3-4). Finally, the vapour is condensed in acondenser that changes the state from vapour to liquid again (Process 4-1), and the cycle is repeated.

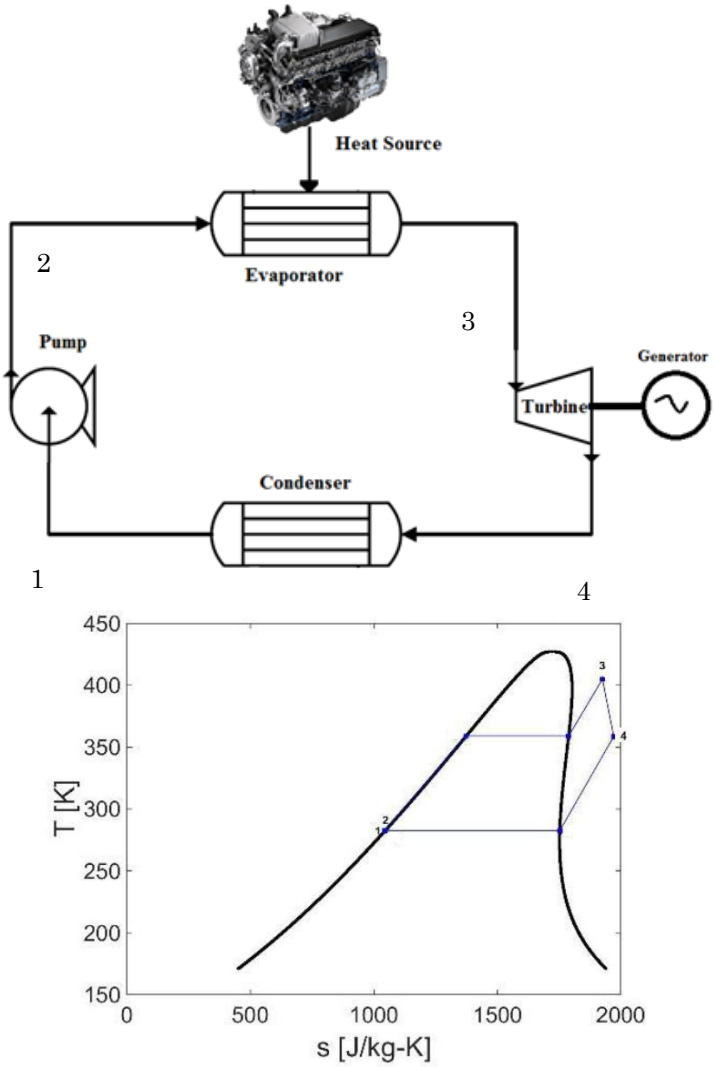

Figure 1-4: Schematic representation of atypical Rankine cycle(top) and the T–sdiagram(bottom).

The performance of ORC systems can be increased throughseveral ways. The extracted work is represented in the enclosed area in the T–sdiagram, as shown in Figure 1-4. Lowering the condenser pressure (bottom line) could increase the cycle efficiency. The low condenser pressure is constrained by the saturation pressure of the cooling system. However, lowering the condenser pressure might increase the moisture content at the turbine blades. To overcome this obstacle, superheating, which is defined as increasing the average temperature at which heat is transferred to the working fluid, can be used. Superheating also increases the enclosed area in the T–s diagram and,consequently, increases thecycle performance. However, the metallurgical considerations of working fluids control the superheat limit. Cycle performance can also be improved by increasing the evaporator pressure. This change increases the average temperature at which heat is transferred to the working fluid. Overall, ORC performance can be improved by the following activities:

- Lowering the condenser pressure
- Superheating the working fluid
- Increasing the evaporating pressure

1.1.3 Radial-Inflow Turbines in Organic Rankine Cycle

Radial-inflow turbine is one of most common types of rotordynamic machines. It is a work-producing device thathas two essential parts (Figure 1-5). The first part is a fixed part thatconsists of volute and stator vanes. The volute introducessome swirl to the fluid, and the nozzle vanes guide the flow, accelerate it and remove any circumferential non-uniformity. The second part is the rotating part, which is called the rotor. In the rotor, the flow is further expanded to rotate the blades and producemechanical work.

The working fluid enters the volute in a superheated stateto gain some swirl and then radially enters the nozzle vanes. The fluid then expands and accelerates through the nozzle vanes where the pressure energy transforms to kinetic energy, resulting in a temperature drop. A vaneless space is required between the stator vane exit and the rotor inlet. This space is a

radial gap that contributes to the flow acceleration process in a nearly loss-free fashion[12]. It also helps the non-uniformities in the flow to integrate with the main stream flow before entering the rotor. The accelerated fluid leaves the nozzle vanes with the required flow angle and a high tangential velocity component and impinges on the rotor's leading edge to rotatethe rotor blades. The flow then leaves the rotor blades near the rotationaxis. Generally, for small- or medium-sized plants, the rotor is oriented vertically. This orientation helps eliminating radial loads on the bearings and facilitates installation and maintenance,as shown in Figure 1-5. In some applications, a diffuser is mounted downstream of the rotor when the installation space is not a constraint. It is employed to recover the kinetic energy at the rotor exit and convert it into static pressure, whichreducesrotor losses.

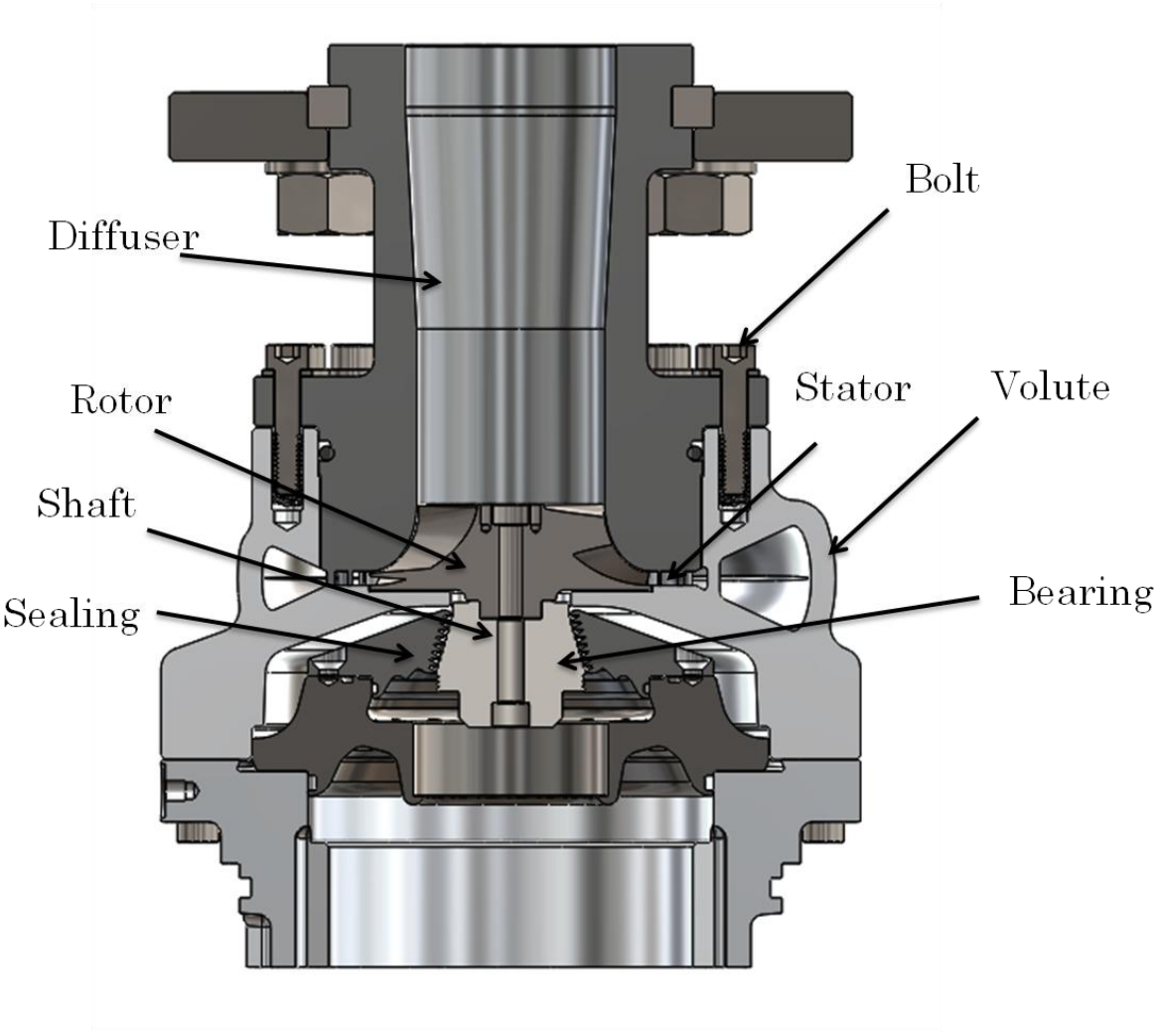

Figure 1-5: Schematic of the turbine assembly.

As previously stated, the ORC system is a promising technology forconverting low- to medium-heat sources into electricity. However, unlike conventional turbines, the real thermodynamic properties of the working fluid should be considered when designing the turbine. Such considerationmakes the design procedure more difficult than the available conventional methodologies. Moreover, the turbine is a component within a larger system (i.e., ORC). Therefore, cycle analysis should be considered during the turbinedesign stage. A performance map of the turbine should also be generated to investigate itseffect on the whole cycle performance at off-design conditions. For this investigation, a novel design methodology forradial-inflow turbine was developed and is presented in detail in Chapter 5.

1.1.4 Design Considerations for Radial Turbines

In designing radial-inflow turbines, the design point is first defined by a specific set of inlet conditions. In ORC applications, these input conditions are defined by the exit conditions of the evaporator. New turbine geometry is created for each set of input conditions. In real-life applications, the turbine geometry is fixed. Therefore, the turbine geometryshould be optimised and its performance at different operating points investigated before manufacturing.

In heat sources such as ICEs, the thermodynamic parameters of the exhaust gas, such as mass flow rate and temperature,can vary widely with time. This variance causes heat sources to become unstable and uncontrollable. Therefore, the performance behaviour of aturbine when the machine runs at off-design rotational speeds, mass flow rates, and pressure ratios should be accurately predicted. However, there is a scarcity of information in open literature regarding the mean-line modelling to obtain the off-design performance of ORC turbines, a point confirmed in [13] and [14].This work had the primary aim of developing a novel design methodology for radial turbine expanders for ORC applications that could be validated through a range of computational and experimental tools described in later chapters.

1.2 Thesis Objectives and Scope

This research aims to design and optimise a highly efficient radial-inflow turbine as an expansion machine in small-scale ORC systems. In addition, and as stated in the previous section, this work aims todevelop a performance prediction mean-line model forevaluatingthe performance of ORC radial-inflow turbines in ICEs. This is a crucial model owingto the variable conditions of the heat source in this work,namely, exhaust gas. This work is part of a project funded by Innovate UK to build a small-scale ORC system as a heat recovery system in heavy-duty diesel (HDD) engines. The main objectives of this research are listed below:

- To develop a novel mean-line model that aims to improvethe design, optimisation and performance prediction of ORC radial-inflow turbines using real gas formulation. Thisnovel model can be employed as a primary tool in the performance prediction of radial-inflow turbines at the early stage of a project. Furthermore, this work aims to analyse the flow field using computational fluid dynamics (CFD) using ANSYS;and to validate the proposed model using real experimental tests.
- To explore the pros and cons of different expansion machines on ORC system performance by conducting anin-depthreview of the open literature.
- To theoretically explore the pros and cons of ORC systems as WHR systems in HDD engines in terms of fuel consumption and exhaust backpressure using realistic engine maps. This includes aninvestigation intothe effects of radial-inflow turbines on the ORC and powertrain performances. This objective is accomplished by constructing two simulation models: one for the ORC system and the other for the radial turbine as a part.
- To obtain and quantify the potential of ORC systems in the use of wasted heat in automotive engines. This is accomplished by building a small-scale ORC system at Brunel University London laboratory

and coupling the system to a real 7.3L HDD engine. Then, the coupled engine-ORC system is tested under steady-state conditions to helpvalidatingthe proposed off-design model mentioned in the first bullet.

1.3 Thesis Structure

This thesis isorganised in eight chapters. Each chapter presents a major aspect of the work and consistsof sections and subsections.

Chapter 1is theintroductory chapter that presents an overview of the worldwide concerns onfossil fuel, particularly its increasing prices and environmental impact. This chapter also briefly presents the working principle of ORC systems and the demand for a mean-line model topredict turbine performance at the early stage of a project, which leads to reduced consumptionof time and resources.

Chapter 2presents a comprehensive literature review of WHR technologies that focus on ORC systems. This chapter also presents state-of-the-art studies onORC systems as WHR systems in automotive applications. The main aim of Chapter 2 is to intensivelyreview the different types of expansion machines, both turbo and volumetric expanders, and discuss the pros and cons of each type in automotive applications.It also aims toconstruct a selection guide that depends on the performance and cost of each expander.

Chapter 3is mainly a feasibility study to investigate ORC systems as bottoming cycles in HDD engines. This chapter consists of two main parts. For each part, a separate ORC model is built using MATLAB software. The first part is a typical ORC model for exploringthe effects of theradial-inflow turbine as an expansion on the ORC and powertrain performances. This part includes a study of the assumption of the constant expander's efficiency that is widely used in ORC studies. To this end, it integrates a mean-line model of the turbine,whichis explained in Chapter 5. This part also explores the differences between the fixed geometry turbine (FGT) and the variable geometry turbine (VGT) and their effects on ORC and powertrain performances. The second part is a two-loop ORC system consisting of an oil

loop that extracts the wasted heat from exhaust gas and the ORC system. This part considers the effect of exhaust backpressure on engine fuel consumption and the potential changes in thepower-to-weight ratio due to the additional weight of the ORC.

Chapter 4is an introductory presentation of the radial-inflow turbineand providesa deep insight into the turbine before the discussion of the design process in Chapter 5. This chapter explains the reasons behindthe selectionof radial inflow turbine as the expansion machine for the current project. It also presents the architecture of the radial turbine with individual pictures of the different turbine parts.

Chapter 5presents the design methodology of ORC radial-inflow turbines, from the design procedure and optimisation algorithmtothe performance prediction methodology. This chapter presents a novel mean-line model that can predict turbine performance by utilising organic fluids (where ideal gas equations are not applicable) at the early stage of a project. It also presents the design of experiment (DoE) technique, which can be employed to explorethe effects of single or multiple input parameters on other turbine parameters, such as overall size, Mach numbers and performance.

Chapter 6presents the generation of solid modelling of the turbine parts to apply complex 3D CFD analysis. This is a crucial step to validatethe off-design modelling (Chapter 5) before sending the turbine for manufacturing. In contrast to the experimental measurements in whichonly global variables are checked, CFD can analyse the complete flow field through the turbine stage.

Chapter 7presents the test rig built at Brunel University London and the experimental results. This chapter also discusses the feasibility of the ORC system as a WHR system in ICEs and presents the turbine performance results,which can be used as final validation ofthe design methodology presented in Chapter 5.

Chapter 8summarises the thesis withthe conclusion of the current work and the author's recommendations for future work.

Chapter 2 : Literature Review

2.1 Introduction

The transportation sector accounts for ~33% of the global CO_2 emissions and approximately 14% of the overall greenhouse gas (GHG) emissions [15]. Light commercial and heavy-duty vehicle emissions are responsible for one-third of the total CO_2 emission by the transportation sector, although these vehicles account for only 5% of the vehicles in the EU [16]. The EU legislation sets mandatory emission reduction targets as the fleet average to be achieved by all new passenger cars; specifically, 95 g CO_2/km by 2021 from 130 g CO_2/km in 2015 [17]. Regarding HDD engines, a 9% reduction in CO_2 is required by 2017 compared to 2010 [18]. Fuel consumption is not only limited by emission standards but is also related to high operating cost for heavy-duty vehicles, which can reach up to 40% [19] as fossil fuel prices fluctuate. For these reasons, the early pivotal demand to employ WHR systems such as ORCs to decrease pollutant GHG emissions and fuel consumption will become more intensive in the near future.

WHR in ICEs lies in the range of low- to high-grade heat rates, depending on the engine operating conditions and the heat sources. The main heat sources where fuel energy is wasted are exhaust gases, cooling systems [20] and the relatively smaller amounts of heat available from the EGR system [21]. Exhaust gases account for most of the wasted heat burnt at a range of 33%–40% [22], [23]. Up to 33% of this wasted heat can be recovered and converted into useful work [24]. Meanwhile, wasted heat from engine coolants accounts for up to 30% [25]. Owing to the low coolant temperature, the recovery potential of coolant energy is much lower than that ofexhaust gas energy[26]. The remaining wasted heat dissipates through other engine components, such as the EGR and CAC systems. The efficiency of the heat source is a trade-off between its quantity (energy contained in the heat source) and quality (temperature range of the heat source)[20]. In some applications, wasted heat has high temperature but low exhaust gas mass, which leads to less waste heat loss as a percentage of fuel input [27]. Nonetheless, Dolz et al. [28] stated that the Rankine cycle efficiency depends on the temperature of the heat source. According to Nadaf and Gangavati [29], exhaust gas presents high-quality and high-

quantityexergetic content. Engine coolant, on the other hand, presents high-quality but low-quantityexergetic content, while the EGR system presents low-quality but high-quantity exergetic content. Therefore, engine exhaust gases are the most useful heat source owing to their high exergetic content [22][30]. EGR can also be used to recover waste heat because the level of useful exergy in the EGR is higher than that in the after-turbine exhaustand its temperature range is high[31]. Teng et al. [32] showed that EGR and exhaust gases are the most interesting recoverable heat sources because of their high exergy values. Their results showed that 20% of wasted heat can be recovered, resulting in 18% ORC efficiency. However, Espinosa et al. [33] mentioned that using both exhaust and EGR gases adds complexity and increases cost. Boretti [34] used exhaust gas and engine coolant as the heat sources in his study. He reported thatfuel conversion efficiency increasesby a maximum of 6.4% when only exhaust gas is used and by a maximum value of 2.8% when only engine coolant is used. When the two heat sources are combined, the efficiency increases up to 8.2%,but so does the system complexity and weight.

The effect of implementing an ORC WHR system in the powertrain of a diesel or gasoline power-assisted vehicle in terms of ORC efficiency, engine efficiency and powertrain performance has been presented by many studies. On a theoretical basis, the ORC efficiency of anHDD engine and a light-duty gasoline engine can reach up to 20% and 14%, respectively, by using ORC as a bottoming cycle [35]. Dolz et al. [28] proved that ORC efficiency can reach up to 6% when a 12L two-stage turbocharged HDD engine is used. The experimental results of Cipollone et al. [36] showed that the efficiency of the regenerative ORC system rangesfrom 3.8%to 4.8% when the exhaust gas of an IVECO F1C diesel engine is used. In another experimental study, Yang et al. [37]utilised a six-cylinder, four-stroke diesel engine in which the ORC efficiency reached a maximum value of 9.9%. Katsanos et al. [38] showed in a theoretical study that cycle efficiency could significantly increase when using exhaust gas and the EGR system and a maximum ORC efficiency of approximately 26% could be achieved. Meanwhile, the experimental results of Wang et al. [39] showed a maximum Rankine efficiency of 7% when both

exhaust gas and coolant of a gasoline engine are used. ORC has also been investigated in gasoline applications. Galindo et al.[40]utilised the exhaust of a 2L turbocharged gasoline engine to present a 6% ORC efficiency. Although the exhaust quality of diesel engines is lower than that of gasoline engines [41], the ORC shows better performance with diesel engines than with gasoline engines due to the higher mass flow rate values of higher displacement HDD engines.

The appropriate expander and working fluid are the most crucial among ORC componentsbecause of their significant effects on the performance, size and cost of the overall cycle [42]–[44]. While no single expander is predominant, the choice of expander strongly depends on the type of working fluid and its working conditions, space and weight restrictions, size of the system [23] and power output [45]. The selection of expander type is discussed in detail in a later section. However, volumetric expanders are generally likely to be suitable for low-power outputs [45]. On the contrary, turbo-expanders can be used for high power outputs and present high isentropic efficiencies [46]. However, they are expensive due to their high rotational speeds, which necessitate the use of a gearbox, good shaft sealing and strong rotating parts [47]. Nonetheless, volumetric expanders possess high weight, which results in high backpressure.

2.2 Organic Rankine Cycles

Recently, technologies forrecovering wasted heat in ICEs have been studied intensively. According to the open literature [48]–[51], the common technologies in WHRinclude ORC, TEG and TC. However, the deep investigation of TEG and TC is beyond the scope of this thesis.

The ORC system is regarded as the candidate with the most potential in terms of generating electricity from low- to medium-heat sources for its simplicity and the availability of its components [52]. It is also the most implemented system [53]. ORC is a Clausius–Rankine cycle but with an organic fluid instead of steam. It has higher thermal efficiency and net power than the steam Rankine cycle. It can follow the heat source to be cooled better than water at the same boiling

temperature,therebydownsizing the system volume and weight, and has high turbine efficiency [54].

2.2.1 Configurations of Rankine Cycles

Traditional Rankine cycles havetwo main configurations,namely,reheat and regenerate(Figure 2-1). In the reheat configuration, the working fluid is expanded in a high-pressure turbine (Process 1-2) and sent back to the evaporator, where it is reheated at constant pressure to the inlet temperature of the high-pressure turbine. Then, the steam is sent to a low-pressure turbine and expanded to the condenser pressure (Process 2-3). Utilisation of the reheat Rankine cycle increases the average temperature at which heat is transferred to the working fluid, thereby improving the cycle efficiency by 4%–5% [55]. This configuration also increases the quality at the expander exit [56], which in turn reduces the moisture content that damages turbine blades.

The regenerative Rankine cycle is utilised when the working fluid temperature after expansion remains relatively high. A portion of the high temperature working fluid preheats the liquid at the condenser exit before it enters the evaporator (Process 5-6). When theregenerative Rankine cycle is used, the thermal efficiency increases as a result of the elevated average temperature [56].

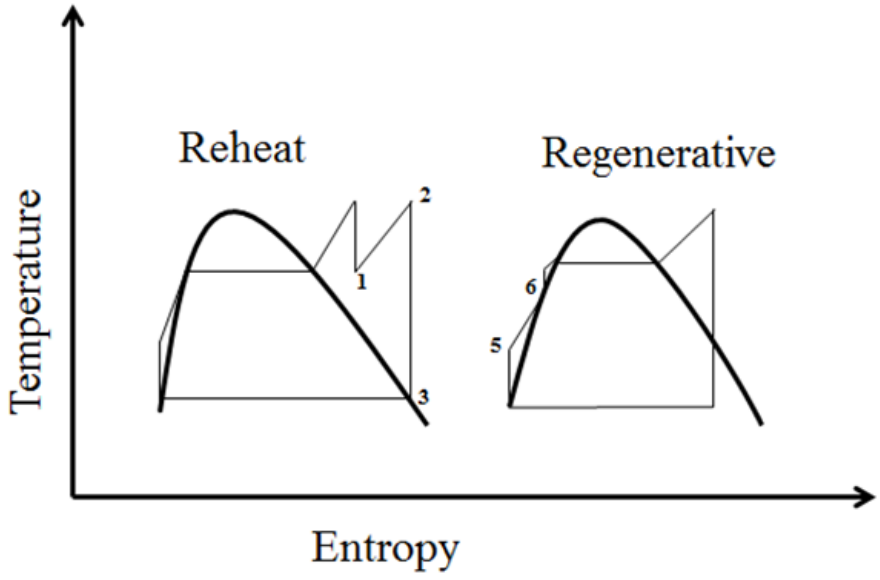

Figure 2-1: Representation of the reheat cycle (left) and the regenerative cycle(right).

2.2.2 Organic Rankine Cyclein Internal Combustion Engines

The utilisation of ORC systems in mobile applications is not a new idea. The first concept on a train wascommercialised in the 1920s, taking advantage of the price difference between diesel and coal [57]. Unfortunately, this system quickly became uncompetitive because the difference was unprofitable [58]. Interest in WHR can be traced back to the 1973 energy crisis when oil prices rose significantly [59]. However, several systems were developed, mostly for trucks or marine applications, and then interest dissipated until the 2000s when automotive manufacturers again became interested in the technology [58]. In 1976, Patel and Doyle [60] built an ORC system prototype that was used as a bottoming cycle in a Mack 676 diesel engine. They stated that at the peak power condition, 36 additional horsepower was produced, resulting in a gain of 13% in power without additional fuel. However, only few commercial ORC power plants have been established since the 1980s [61]. Studieson ORC technology in ICEs have increased since the last decade. In 2007, Endo et al. [62] installed a Rankine cycle in a 2.0 L Honda Stream SI engine using exhaust gas and engine coolant as heat sources. The results of their vehicle testing showed that thermal efficiency increased from 28.9% to 32.7% (13.2%) at constant speed (100 km/h). A project by the DOE Super Truck Program [63] demonstrated a brake thermal efficiency of over 50%. Quoilin [64] conducted an experimental test of a small-scale ORC system using hot air at a temperature ranging from 150 °C to 200°C as the heat source. His results showed a maximum cycle efficiency of 7.4%. Ringler et al. [65] analysed the potential of Rankine cycle as an additional power generation process that uses the waste heat of a car engine. Their experimental test showed that WHR can produce an additional power output of approximately 10% at typical highway cruising speeds. Hence, on the basis of the above selective references, ORCs are very promising technologies in WHR systems. Moreover, different heat sources can be utilised, namely, engine exhaust gas, EGR and engine coolant.

Nonetheless, the weight of the ORC system and the engine power are two of the most critical parameters that affect fuel consumption and harmful exhaust emissions [66]. Inertia and rolling resistance increase with the

vehicle weight, resulting in increased fuel consumption because the engine is required to propel the vehicle to the required speed. Frictional forces that act on the vehicle operating at constant speeds increase as well because of the added weight [67]. In the open literature, only few works considered the ORCweight when implementing the systemas a bottoming cycle in automobiles. In their modelling study, Oh et al. [68] stated that a 10% increase in vehicle weight could result in a 4%–6% increase in fuel consumption. Imran et al. [67] presented a method for estimating the weight of different ORC components as a function of their capacities. To obtain the weight of the expander, Imran et al. [67] used the data of scroll compressors with similar power rating to plot the expander weight against the power. Their results showed that the added weight of the ORC system (140.52 Kg) caused a power loss in the range of 0.82–2.28 KW. The weight of the expander was in the range of 4.2%–12.8% of the total weight. Battista et al. [69] considered the weight of the ORC system to study its effects on the fuel consumption of a light-duty diesel engine. An extra weight of 50 Kg was added to the original vehicle weight (3350 Kg), and the results showed an increase of 1.25% in fuel consumption at 1000 rpm and 0.7% at 3500 rpm. Assuming a 20 Kg ORC system, Horst et al. [70] stated that the fuel consumption increased by 1.5%. In addition to the weight issue, Boretti [71], [72] stated that the ORC technology has several disadvantages that prevent the uptake of the technology, such as increased backpressures, increased packaging complexity, increased control complexity, troublesome transient operation and cold start issues.

2.2.3 Working Fluids in Organic Ranking Cycle

The choice of working fluid for an ORC system is of key importance for the cycle efficiency and net work. ORC systems should only utilise working fluids with low global warming potential (GWP) and ozone depletion potential (ODP) [73]. According to Lee et al. [74], the system efficiency of ORC correlates with the fluid's normal boiling point, critical pressure and molecular weight. The main difference between conventional Rankine cycles and ORCsis that the latter uses organic fluids (hydrocarbons or

refrigerants) instead of water. Organic fluids exhibit unique advantages over water or steam [75]because they are better adapted to low heat source temperatures than water, enabling ORC systems to efficiently produce shaftwork from medium temperature heat sources of up to 370 °C [76]. Compared to conventional Rankine cycles, a smaller plant size will be produced when organic fluids are used because of their high density. The higher the density is, the lower the volumetric flow rateis and, subsequently, the smaller the component size becomes. Steam can be applied in applications where heat source temperatures are very high without the fear of thermal decomposition due to its thermal stability [48]. By contrast, organic fluids can be used in low temperature heat sources because of their low normal boiling point, which enables them to evaporate and recover thermal energy from low-grade heat sources better than steam. Statistical investigations indicate that low-grade waste heat accounts for 50% or more of the total heat generated inindustry [76]. Additionally, more advantages can be exhibited by the ORC over conventional Rankine cycles, such as a simple control system and a cheap and simple turbine [77]. Low sound speed is another characteristic of organic fluids. Thus, this speed is reached faster in an ORC than in a steam cycle and constitutes an important limitation because high Mach numbers are related to the high irreversibility properties thatresult in low turbine efficiencies [77].

The selection of working fluid is determined by the application and the waste heat level [78]. Based on the slope of the saturation vapour line,as shown inFigure 2-2, working fluids can be classified into three groups: wet, dry and isentropic. Dry and isentropic fluids have enormous advantages for turbo-machinery expanders becausethey leave the expander as superheated vapour and eliminate the corrosion that results from liquid droplets that impinge onthe turbine blades during the expansion [79]. Another advantage is that overheating the vapour before entering the expander is not required, which meansa small and cheap heat exchanger can be used [80]. Moreover, asuperheated apparatus is not requiredwhen using dry and isentropic fluids [81]. However, if the fluid is too dry, the expanded vapour will leave the turbine with substantial superheat, which is a waste and adds to the cooling

load in the condenser [82], [83]. The hydrogen bond in certain molecules, such as water, ammonia and ethanol, may result in wet fluid conditions due to the large vapourising enthalpy. Hence, wet fluids are regarded as inappropriate options for ORC systems [81]. Isentropic fluids are free fromthe issue of moisture content (fluid droplets);the only issues of concern are their cost, chemical stability and safety [84]. A summary of studiesrelated to working fluids in the open literatureis presented in the following paragraph.

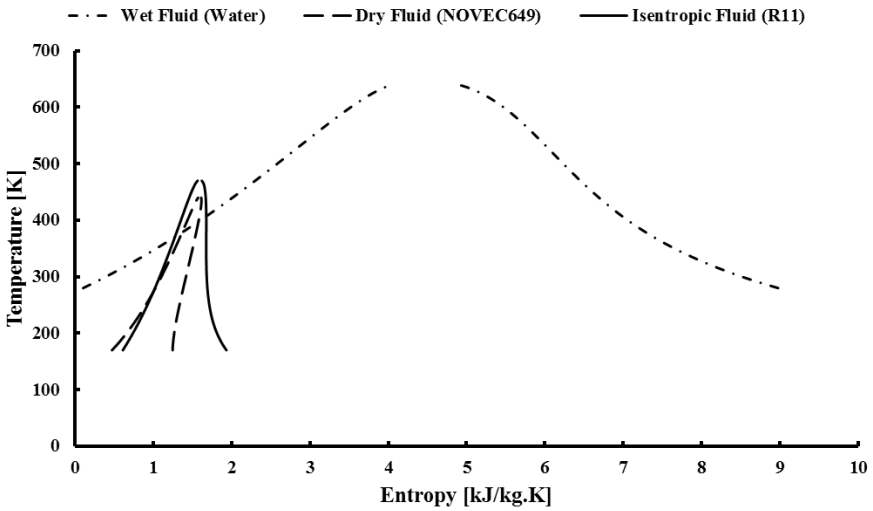

Figure 2-2: Categories of working fluids.

Hung [85] analysed and compared the efficiency and irreversibility of ORCs using various dry fluids, namely,benzene, toluene, p-xylene, R113and R123. In the study, p-xylene presented the highest efficiency, while benzenepresented the lowest efficiency. R113 and R123 presented better performances than the other two in terms of recovering low-temperature waste heat. Saleh et al. [86] presented a study of 31 pure component working fluids for ORCs in geothermal power plants. Among the studied fluids, n-hexane showed the highest thermal efficiency (14.14%), while R32 showed the lowest thermal efficiency (0.53%). Hung et al. [84] conducted a study to identify suitable working fluids that may yield high system efficiencies in an ORC system. Their results showed that R11 and C7H8 have the highest system efficiencyatapproximately8.5%, while R152 has the lowest system efficiency at6.7%. The authors stated that wet fluids with

very steep saturated vapour curves in the T–s diagram have better overall performance in energy conversion efficiencies than dry fluids. The authors also stated that dry fluids generally generate superheated vapour at the turbine exit, which reduces the area of network in the T–s diagram, and a generator may be needed to relieve the cooling load of the condenser. Wang et al. [87] constructed a MATLAB code to investigate the performance of nineworking fluids. Their results showed that R11, R141b, R113 and R123 have slightly higher thermal efficiencies than the others. In terms of safety levels and environmental impacts, the results showed that R245fa and R245ca are the most suitable working fluids for an engine WHR application. Shu et al. [88] investigated the influences of alkanes as working fluids by using the high-temperature exhaust heat recovery of a diesel engine. Cyclohexane showed the best performance, with an improvement of 10% in brake-specific fuel consumption (BSFC). However, the authors stated that high flammability and toxicity must be considered when alkane-based working fluids are used, which necessitates good sealing and excellent ventilation. Ringler et al. [65] conducted an experimental test to investigate the results of using a high-temperature source (exhaust gas) and a low-temperature source (engine coolant). The authors concluded that water is a preferable working fluid for a system that uses exhaust gas with a high temperature level heat source (T>300°C), whereas an alcohol (e.g. ethanol) would be the right choice for a low-temperature system. Javanshir et al. [89] studied the performance of a regenerative ORC system using 14 dry fluids. Their results showed that butane,followed by iso-butane and R113, offer the highest specific net work output. In addition, working fluids with high specific heat (C_p) produce high specific net work output, while working fluids with high critical temperature produce high thermal efficiency. Dai et al. [90] conducted an experimental test to investigate the thermal stability of hydrofluorocarbons using fluoride ion as an indicator of fluid decomposition. Their results showed that most common hydrofluorocarbons have thermal stability temperatures that are suitable for supercritical ORCs. However, they must be used below the decomposition temperatures to ensure system safety. Similarly, Invernizzi et al. [91] investigated the

thermal stability of three representative hydrocarbons used as working fluids in ORCs, namely, n-pentane, cyclo-pentane and toluene,by using vapour pressure as an indicator. Their results showed that cyclo-pentane is stable at 350 °C after eight hours, with a decomposition rate that is 20times lower than the corresponding value for n-putane. The results also confirmed that the toluene sample remained remarkably stable at high temperatures, which makes it a preferable fluid in high-temperate applications. Saloux et al.[92] proposed a methodology for selecting the most appropriate organic fluid for WHR applications based on primitive variables, such as working pressure, temperature and mass flow rate. The analytical results of He et al. [93] showed that the R236FA fluid has the highest thermal efficiency at21.6%, and the fuel economy of a 12-cylinder four-stroke stationary natural gas engine can be improved by 14.7% compared to that without ORC. Recently, Seyedkavoosi et al. [94] compared three working fluids in terms of exergy efficiency using the exhaust gas of a 12-cylinder gas-fired ICE. The investigated fluids were R123 (dry), R134a (isentropic) and water (wet). Their results showed that R123 presented the best performance. They concluded that using dry fluids such as R123 for ICE applications could potentiallyrealise maximum useful power and exergy efficiencies.

2.2.4 Comparison between Organic Rankine Cycle System and Other Technologies (Thermo-electric Generation and Turbo-compounding)

The selection of appropriate WHR technology depends on the application, system size and heat source. However, ORC systems provide an attractive combination of efficiency and affordability forengine exhaust WHR [21]. It also exhibits great flexibility, high safety and low maintenance requirements [95]. Although anin-depth comparison of the technologies is beyond the scope of the chapter, a brief comparison is discussed in the followingparagraphs.

ORC exhibits higher BSFC reduction potential thanTC[96]. The main disadvantage of TCis the interaction with the engine. This interaction increases the exhaust backpressure of the engine, which affects the exhaust

gas after treatment system and the engine performance [97]. In a well-designed ORC, the net backpressure can be loweredbecause ofexcessive cooling of the exhaust gas in the evaporator [98]. The combination of the ORC system and the automotive engine also increases the thermal efficiencies of the engine without increasing the exhaust backpressure [99]. Another main drawback of TC technology is the increase in pumping losses due the existence of the extra turbine. Mechanical TC has only beentraditionally applied to large diesel engines because of the complexity of mechanically coupling a high-speed turbine to the engine crankshaft [100]. However, the ORC system is a heat energy recovery method, which means it is a heavier and more expensive system,whereas theTC system is a mechanical energy recovery method, and thus cheaper and lighter. In addition, the implementation of the ORC system requires a complex technological architecture, which makes it an unfavourable solution for a small-scale mobile application [101]. Overall, Rankine cycle can offer substantial gains in fuel economy, potentially in the order of 20%, compared to the established TC[50].

The other WHR technology is TEG,which has three main challenges. First, it exhibits poor efficiency, typically less than 4% [102];second, the radiator is big and the piping is extended to the exhaust manifold [48]; and third, thermoelectric generators are not mature yet, and some efficient materials still need to be manufactured [97]. However, new nano-crystalline or nano-wire thermoelectric materials are currently in the development stage to improve the conversion efficiency of thermoelectric generators [103]. TEG technology is used at high temperatures and only when small amounts of power are needed,whereas ORC is used when a low- to medium-temperature heat source is utilised [104]. Although TEG has a small effect on engine performance and can improve engine power by up to17.9% [105], energy from the gases is lost and causes an increase in pumping losses, which reduces the engine performance [106]. Beside the challenges mentioned above, TEG technology is expensive and exerts an extra load on the cooling system owing to the large temperature difference between the hot and cold surfaces [107]. It is also very time-consuming because the evaluation of

system stability requires prolonged aging and thermal cycling tests [108]. However, TEG technology is lightweight, while ORC has high volume and weight. In addition, thermoelectric technology is environmentally friendly [109],whereasORC could be harmful when toxic working fluids are used.

2.3 Expander Technologies for Organic Ranking Cycle in Internal Combustion Engines

The selection of an appropriate expander type is crucial because the expander is a critical component in an efficient and cost-effective ORC system. The choice of expander type strongly depends on the working conditions, type of working fluid, space and weight restrictions and size of the system [23]. Other important factors should be considered when selecting expanders, such as high isentropic efficiency, pressure ratio, power output, lubrication requirements, complexity, rotational speed, dynamic balance, reliability cost, working temperatures and pressures, leaking, noise and safety [45][47]. Expanders can be classified into two groups: displacement expanders (volume expanders) and turbo-machine expanders (velocity expanders). Most ORC systems have been developed with scroll and vane typesbecause of their efficiency and low cost [110]. However, these devices are not suitable for placement in small and restricted places,such as the interior of a conventional car [110]. Meanwhile, turbo-machine expanders are preferred in a high-temperature WHR application with an expected regenerated power in the order of 15 kW [111].

2.3.1 Positive Displacement Expanders

As the name implies, positive displacement expanders (PDEs) are machines whose principal feature is a fixed volumetric ratio. In PDEs, fluid is forced into a closed volume and then pushed out with low pressure, resulting in mechanical work caused bythe expansion process. PDEs have several types with different working principles. These types are scroll expanders, screw expanders, reciprocating piston expanders and rotary vane expanders, all of which are schematically presented in*Figure 2-3*.

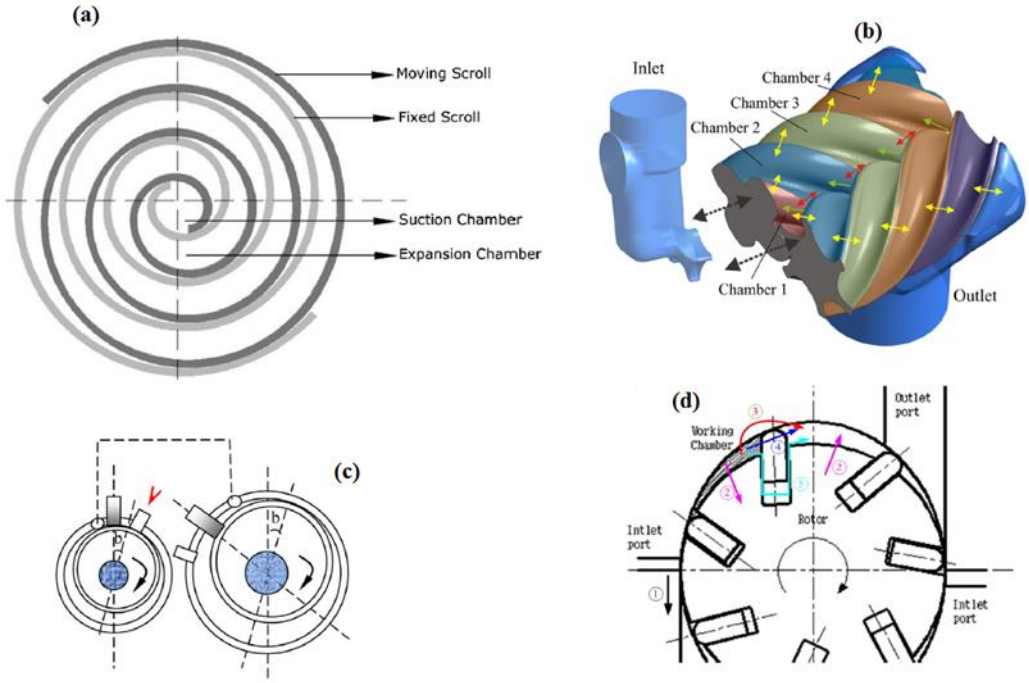

Figure 2-3: (a)Scroll expander [112]*, (b) Screw expander* [113]*, (c) Piston expander* [114] *and Rotary Vane expander* [115].

Among PDEs, the scroll expander has the most complicated geometry [47]. It can be categorised into two main groups: compliant scroll expanders and cinematically constrained scroll expanders. In the former type, lubrication is compulsory to operate efficiently without causing wear due to the contact of the wrap sidewalls. In the latter category, lubrication is not required due to the existence of the linking mechanism between the orbiting and fixed scrolls. An advantage of the cinematically constrained scroll expanders is that they do not require inlet and exhaust valves; therefore, noise is reduced and the durability of the device is increased [77]. However, sealing is required to prevent internal leakage.

In screw expanders, lubrication is required due to the direct contact between the two lobes. Given the high rotational speed of screw expanders, reduction gear boxes and speed control equipment might be required [47]. When a dry fluid is used as the working fluid in ORC systems, seals are required, which increases the machine cost significantly[116]. Unlike piston expanders, both scroll and screw expanders can work with wet fluids without damaging the devices because they can generally accept large liquid mass fractions[117].

Reciprocating pistons are complex devices that require the precise timing of the intake and exhaust valves [47]. They also have a large friction loss of approximately80% oftotal losses [118]because of their large interacting surfaces. However, piston expanders usually show lower internal leakage than scroll and screw expanders [117]. This outcome also results in easier design and construction [119]. Like some PDEs, lubrication is required in piston expanders but entails difficulties because the oil should be mixed with the working fluid, which reduces the efficiency of the cycle [120].

Rotary vane expanders, which are often based on the Wankel concept [121], [122], do not require the use of valves [123]. These expandershavea simpler structure and can bemanufactured more easily than other expander concepts [115]. They have low noise vibration and high volumetric expansion ratios [124]. However, their performance is poor at low speed because ofthesignificantinfluence of internal leakage at low speed [125], and they show implementation difficulties [126]. Furthermore, the machine must be lubricated to minimise wear and enhance sealing [47].

2.3.1.1 Brief History of PDEs in ORC-ICEs

a) Scroll Expanders

In 1993, Oomori and Ogino [127] conducted an experimental test for a scroll expander with HCFC123 as the working fluid. The engine water jacket of a four-cylinder passenger car was employed as the heat source. With increasing pressure ratio, the results showed that the energy recovery began to drop as the revolution became lower than 800 rpm due to the drop inexpander efficiency. The results also showed that the expander efficiency increased up to approximately 50% at 1000 rpmof expander speed, and then began to drop due to the deterioration of the sealing performance between the rotor and the housing in line with the lowered revolution speed, which resulted in working fluidleakage. In terms of overall performance, the test results showed that approximately 3% of the engine output energy was

recovered at the ambient temperature of 25 °C, with a maximum energy recovery of 400 W.

In 2003, Kane[128] tested an ORC system to recover thermal energy from a bio-gas diesel engine. The cycle was a bottoming cycle with R134a as the working fluid, and the scroll expander was modified from standard hermetic scroll compressor units. The laboratory tests showed that the total power range was from 3 kWe to 10 kWe, and the maximum overall superposed cycle efficiency was (14.1 ± 0.2)%. The authors stated that this performance is satisfactory due to the relatively low supply temperature (up to 165 °C) and low power range (up to 10 kWe).

In 2007, Kane et al.[129] conducted an experimental test to recover the wasted heat in a 200kWe biogas engine coolant using a scroll expander ORC. Their results showed that the ORC system can be operated even at a very low power output, below 20% of its nominal design value, and a cycle net efficiency of 7% can be achieved for a low-temperature application (< 90 °C).

Two years later, Mathias et al. [130] presented an experimental test of two types of expanders, namely,scroll and rotary vane expanders. R123 was selected as the working fluid and the exhaust gas of a stationary ICEas the heat source. The scroll expander used in the test was a scroll compressor thatwas modified and operated as an ORC expander in the experiment. The experimental results showed that the maximum isentropic efficiency and output power achieved by the modified expander were 83% and 2.96 kW, respectively. In addition, the reduction in diesel fuel was 4,012 L, and the overall energy efficiency of the cycle was 7.7%.

In 2012, Clemente et al. [131] studied the performance of a scroll expander with R245fa and isopentane as working fluids. The scroll efficiency andpower output were higher when R245fa was used as theworking fluid at 40 °C condensing temperature. Using the exhaust gas of the ICE, the authors stated that the designed cycle could recover 10 kW. A net mechanical power of approximately1 kW was also delivered by the scroll expander, achieving 10.8% thermal efficiency.

A year later, Yu et al. [132] conducted a simulation study on an ORC system with exhaust gas and jacket water as heat sources and R245fa as the working fluid. Their results showed that the maximum expansion power and recovery efficiency were approximately14.5 kW and 9.2%, respectively. The results also showed that the maximum expander pressure ratio and isentropic efficiency were 11.7 and 60%, respectively. The authors concluded that the ORC system can effectively recover heat in exhaust gas but behaves badly in recovering heat in jacket water.

In 2014, Kim et al. [133] studied the performance of a scroll expander at off-design conditions using a dual-loop ORC with R134a as the cycle working fluid. The scroll expander was applied in a low-temperature cycle using the engine coolant and the condensation heat from the high temperature as heat sources. The authors claimed that the scroll expander is not suitable for high-temperature cycles because of the uneven thermal deformation of the scrolls, which is difficult to handle. Their results showed that a gradual decrease in expansion efficiency was observed during the under-expansion operation (i.e. the design pressure ratio was lower than the operating pressure ratio), whereas a rapid decrease in expansion efficiency was apparent during the over-expansion operation (i.e. the design pressure ratio was higher than the operating pressure ratio).

Recently, Petr et al. [134] conducted a simulation study to investigate the performance of an ORC system by using ethanol as the working fluid and a scroll expander as the expansion machine. Their results showed an increase in the net power output of 7% compared to the conventional controller with operation points optimised at steady-state conditions.

b) Screw Expanders

In 2006, Leibowitz et al. [135] studied the possibilities of recovering power from low-temperature heat sources. They utilised a twin-screw expander due to its availability and low cost and itscapability tooperate at high rotational speeds. According to the authors, these expanders can provide adiabatic shaft efficiencies of approximately70% when working at low speed.

The screw expander would then develop a gross shaft output of 24 kW. The results also showed that the total increase in power output was 8.5%.

In 2014, Yang et al. [37] conducted an experimental study to investigate the performance of ORC and the screw expander under various diesel engine operating conditions. They used R245fa as the working fluid and the exhaust gas of a six-cylinder diesel engine as the heat source. The performance of the expander was investigated at different values of expander inlet pressure and rotational speed. Their results showed that the power output and isentropic efficiency of the screw expander increase with the inlet pressure and rotational speed. The expansion ratio of the expander was shown to decrease with the increasing inlet pressure and rotational speed of the expander.

Recently, Wu et al. [136] conducted an experimental test to study the influence of different engine loads and expander torques on the performance of ORC systems. They used the exhaust gas of a diesel engine and R123 as the heat source and cycle working fluid, respectively. Their results showed that the power output of the single-screw expander increased in the form of a parabola with the rising expander torque. In terms of ORC efficiency, the results showed that efficiency increases with the expander torque, with a maximum value of 6.48% at approximately64 N.m. For the single-screw expander, themaximum power output of 10.38kW and a shaft efficiency of 57.88% were achieved at 1538rpm.The maximum improvement of the diesel engine with ORC over that of the diesel engine without ORC was 1.53% at 250kW.

c) Piston Expanders

In 1984, Poulin et al. [137] simulated an ORC system using several adiabatic diesel configurations. The results of their study showed that the maximum recoverable power was achieved by the turbocharged non-after-cooled diesel engine with a maximum BSFC improvement of 16.2%. They also stated that the expander efficiency improved with the fluid temperature

and decreased slightly with the increasing pressure. Moreover, the expander efficiency decreased with the condensing pressure.

Four years later, Kubo [138] conducted a study to evaluate the concept of bottoming cycle inheavy-duty transport diesel engine applications using three cycles, namely,steam cycle, ORC and Stirling cycle. In the study, most of the components were similar, except for the expansion machine. In the ORC, a turbine was used with a rated speed of approximately 20,000 rpm, while the steam system used a two-cylinder reciprocating piston expander with a rated speed of 2,000 rpm. In terms of fuel consumption, ORC showed the best improvement at 13.7%, followed by steam cycle at13.3% andStirling cycle at 9.1%.

In 2012, Seher et al. [139] conducted a simulation and an experimental study using a12L heavy duty engine with ORC as the WHR technology. The results ofthe simulation study showed that the effective power output of the piston machine was 12 kW. The experimental results of the prototype showed that a mechanical output power up to 14 kW was realised, with a mechanical efficiencybetter than 85% at 1500 rpm. The authors concluded that water and ethanol are favourable when using a piston expander.

In 2013, Wenzhi et al. [126] conducted a study to investigate the combined effects of heat exchangers and a single-stage piston expander on the performance of the Rankine cycle system. The authors used the exhaust gas of a high-speed turbocharged diesel engine as the heat source. They concluded that the expander efficiency increased withthe intake pressure until 2 MPa and then startedto decrease. The expander efficiency, power output and global efficiency increased withthe intake temperaturebecause of the enthalpy increase. In the experimental test, a maximum of 12% power output increasewas obtained when the diesel engine operatedat 80 kW/2590 rpm and the expander workedat 4 MPa of intake pressure.

The following year, Daccord et al. [140] studied the influences of utilising axial piston expanders on the performance of an ORC used in WHR. The authors employed the exhaust gas of a 1.6L gasoline engine as the heat source. They concluded that a piston expander with a capacity of 183 cm^3 and an expansion ratio of 8 is the best compromise between low and high

loads. Overall, the authors stated that an axial piston expander with non-lubricated hot parts would fit perfectly with a mobile application becauseofits ability to deal with droplets in transient conditions.

Recently, Chiong et al. [141] presented a new nozzle steam piston expanderto recover the exhaust energy of a Cummins 6BT turbocharged direct injection diesel engine. Their results demonstrated that the power output of the nozzle piston expander was 3.53 KW higher than the conventional one when operating at 1500 rpm. Moreover, the improvement of the BSFC was 3% higher in the nozzle piston expander.

Galindo et al. [142] conducted a simulation and an experimental test to study the performance of an ORC system when used as a WHR in ICEs. Swash-plate piston expander was used as the expansion machine and ethanol as the working fluid in the ORC system. The performance of the expander was studied at different speeds with a maximum efficiency of 58.8% and a power output of 2kW at 2500 rpm.

d) Rotary Vane Expanders

In 2009, Teng and Regner [31]analysed the fuel-saving benefit for a class-8 truck diesel engine equipped with an ORC system using the EGR as the heat source. The authors stated that becausethe expansion ratio in a supercritical cycle is extremelylarge for a single-stage turbine, the turbine is replaced with a positive displacement rotary expander with an expansion ratio of 6.4 for the subcritical cycle and 33 for the supercritical one. The results of their analysis showed that a fuel saving of up to 5% could be realisedand further improvementcould be achieved if charge air cooling is integrated in the Rankine cycle loop.

The following year, Tahir et al. [143]conducted an experimental study to investigate the performance of ORC systems when used as a WHR system to recover wasted heat from low-temperature heat sources. The authors selected a rotaryvanetype as the expansion machine and R245fa as the working fluid. Their results showed that the highest measured efficiency

and maximum power of the expander were 48% and 32W, respectively, and the measured thermal efficiency was 3.82%.

In 2011, Xinxinet al. [46]conducted a steady-state experiment to investigate the performance of an ORC system using the exhaust gas of a Toyota 8A-FE gasoline engine as the heat source and R113 as the ORC working fluid. The achieved expander isentropic efficiency was 79.42%, and the practical thermal efficiency of the system was approximately14.44%.

Battista et al. [69]recentlyconducted an experimental study to investigate the influence of implementing an ORC system when using the exhaust gas of a turbocharged IVECO F1C diesel engine as the heat source and R236fa as the cycle working fluid. In their study, a sliding vane rotary machine was selected as the ORC expander because, according to the authors, it is noiseless, compact, flexible from a geometrical perspective (diameter/length ratio), very reliable and does not require important maintenance actions. The results of their test showed that a gross benefit of the ORC-based unit power was 4%–5%

2.3.1.2 Performance of PDEs

In general, the performance of volumetric expanders is expressed in terms of overall isentropic effectiveness,as shown in equation (2-1).

$$\varepsilon = \frac{P}{m\cdot(h_s - h_{ex})} \tag{2-1}$$

where P and $m\cdot$ are the power and mass flow rate displayed by the expander, respectively. $h_s and h_{ex}$ are the supply and exhaust enthalpies, respectively. v and x are the supply specific volume and expander displacement, respectively. The performance of various types of expanders is investigated based on rotational speeds and mass flow rates (Table 2-1) and the off-design performance (isentropic efficiency vs. pressure ratio), as shown inFigure 2-4,Figure 2-5, Figure 2-6, Figure 2-7, Figure 2-9 and Figure 2-10.

Figure 2-4presents the isentropic effectiveness of scroll expanders as a function of their pressure ratios based on the investigations achieved by numerous researchers [52], [144]–[147]. Figure 2-4shows that scroll expanders can operate under high pressure ratios with isentropic efficiencies ranging from 40% to 75%. Isentropic efficiency increases with pressure ratio until a certain value and then starts decreasing. Moreover, scroll expanders are suitable choices for applications with low mass flow rates and power outputs. Table 2-1 shows that the mass flow rates inthe selected literature are in the range of 0.02–0.17 Kg/s, while the power outputs are in the range of 0.2–2.5 KW. The rotational speed values that result in acceptable performance are between 700 and4000 rpm.

Table 2-1: Summary of ORC Studies with Different Expansion Machines

Ref.	Type	Pout [KW]	Speed [rpm]	MFR [Kg/s]	W.F
[148]	Radial	25–250	7500–16500	3–7.4	R245fa
[149]	Radial	640–780	8000	41.1	R134a
[14]	Radial	16–27	67660	1.18–1.82	R134a
[150]	Radial	5–12	22000	0.1–1	R134a
[151]	Radial	3–8	20000–60000	0.1–0.5	R245fa
[152]	Radial	0.54–0.55	35000	0.058– 0.065	R123
[153]	Radial	6.8–8	30000–207300	0.274	R245fa
[147]	Scroll	0.58–0.64	2000–3700	0.022–0.0245	R134a
[146]	Scroll	2.8	N/A	0.139	R245fa
[52]	Scroll	0.2–2	700–4000	0.05–0.095	R123
[144]	Scroll	0.2–2.5	3010–3090	0.07–0.17	Water
[154]	Screw	0–8	400–8000	0.07–0.28	R245fa
[155]	Screw	10–35	1600–3200	N/A	compressed air
[156]	Screw	200–560	1250–6000	18–66	R123
[157]	Screw	4.4–5	2200–3000	0.14	compressed air
[158]	Screw	1–8	2000–3300	0.51	R245fa
[28]	Screw	2–11	1000–2600	N/A	R123
[159]	Piston	0.25–2	1000–4000	0.03–0.11	R245fa
[40]	Piston	0.2–1.6	1000–5000	0.01–0.75	Ethanol
[160]	Piston	0.16–0.32	400–700	N/A	R245fa
[161]	Piston	N/A	N/A	0.1	Water
[162]	Piston	N/A	1500	0–1.5	R123
[163]	Vane	0.55–1.075	2550–4012	0.056–0.07	HMDSO
[164]	Vane	0.1–0.4	N/A	N/A	R123
[164]	Vane	3.9–31	500–1500	0.012–0.032	R245fa
[165]	Vane	0.8–0.955	800–1800	N/A	N/A

[143]	Vane	0.012–0.031	2600–3000	N/A	R245fa
[151]	Axial	2.8–7.8	10000–60000	0.1–0.5	R245fa
[166]	Axial	N/A	2500–20000	10–150	N/A
[167]	Axial	N/A	5000–65000	0.909	R245fa
[168]	Axial	260–350	4101–14561	10–100	R245fa

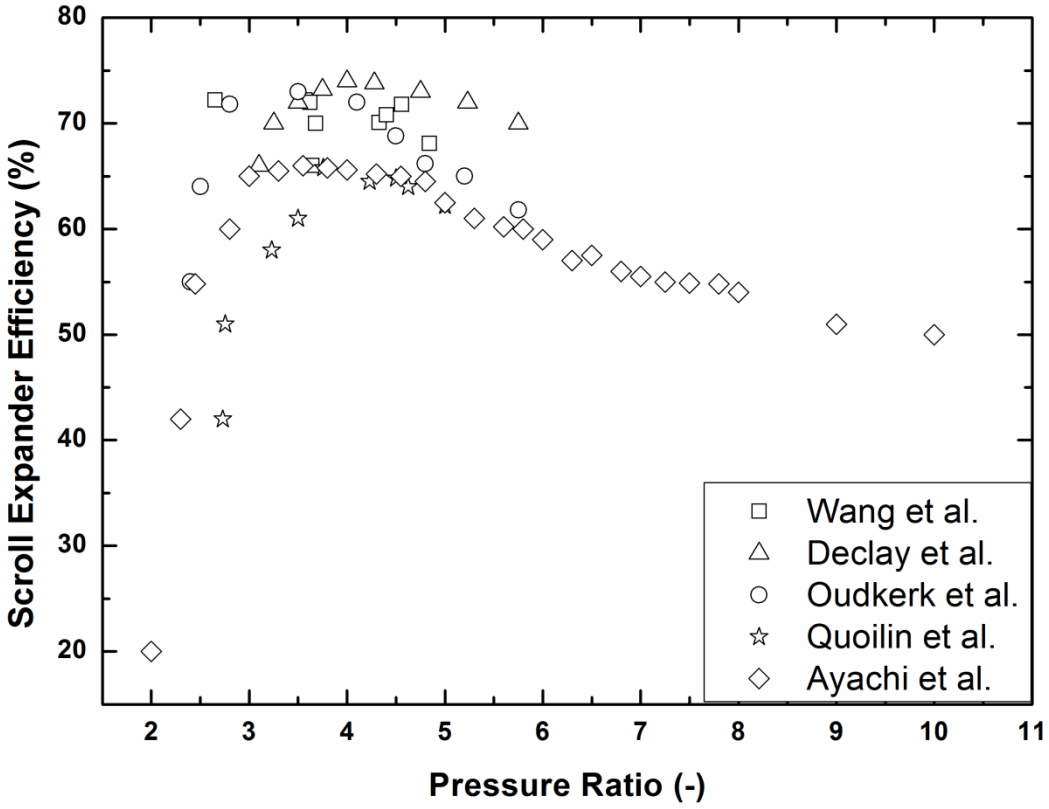

Figure 2-4: Performance of scroll expanders.

The effectiveness of the screw expanders is investigated in Figure 2-5on the basis of the results of several studies [154], [158], [169]. The efficiencies of screw expanders are relatively lower than thoseof scroll expanders. Figure 2-5 shows that the efficiencies are below 65% and can be as low as 25%. Meanwhile, screw expanders can handle higher mass flow rates and rotational speeds than scroll expanders,therebyresulting in higher power outputs (Table 2-1). They can even produce significantlyhigher power, as shown inTang et al. [156], due to the high mass flow rates (18–66 Kg/s), which make them preferableover other volumetric expanders for theirwide range of capacities. However, because their rotational speed (400–8000 rpm) is higher than those of other volumetric expanders, a reduction gearbox

might be required. Similar to scroll expanders, screw expanders can work under high pressure ratios (2–16).

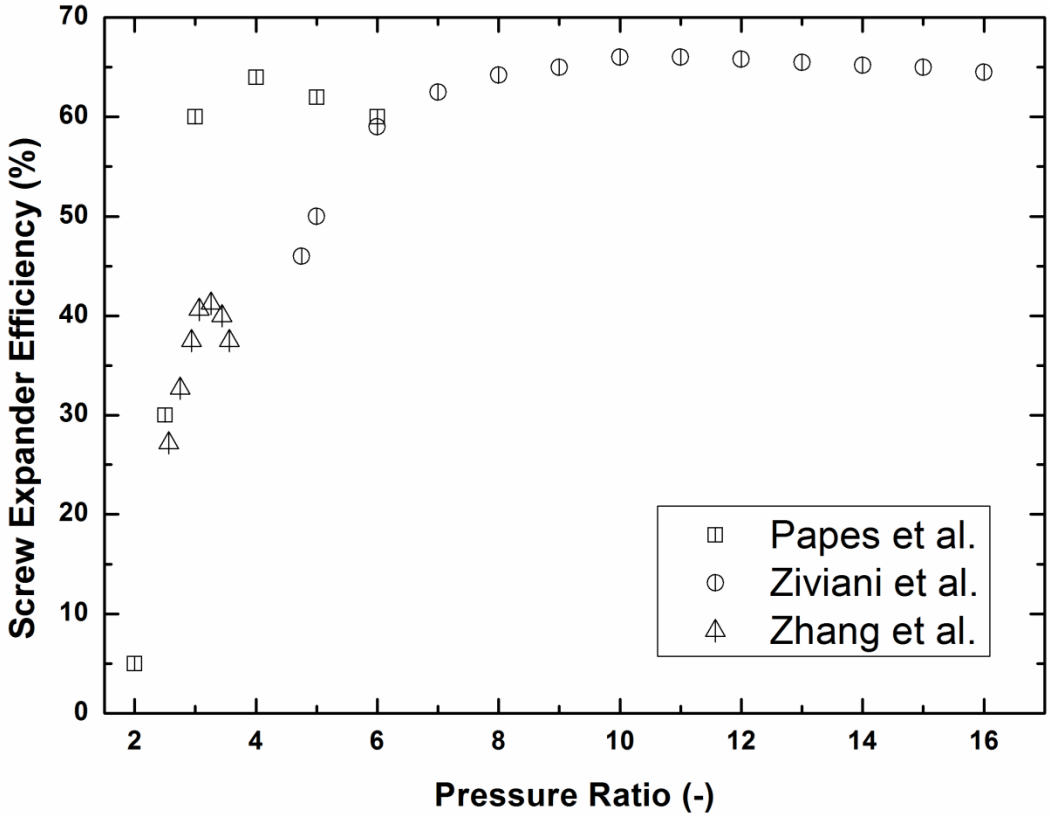

Figure 2-5: Performance of screw expanders.

Figure 2-6presents the performance of the piston expander on the basis of the results of previous studies [159], [161], [162]. Piston expanders can operate under very large pressure ratios (up to 30) with acceptable isentropic efficiencies (related to the high-pressure ratios) due to their large internal volume ratios. Among volumetric expanders, piston expanders present lower power outputs (0.16–2 KW) with mass flow rates in the range of 0.03–1.5 Kg/s. Table 2-1 shows that piston expanders operate with low rotational speeds, which enablethem to be attached directly to the generator without the need for a gearbox.

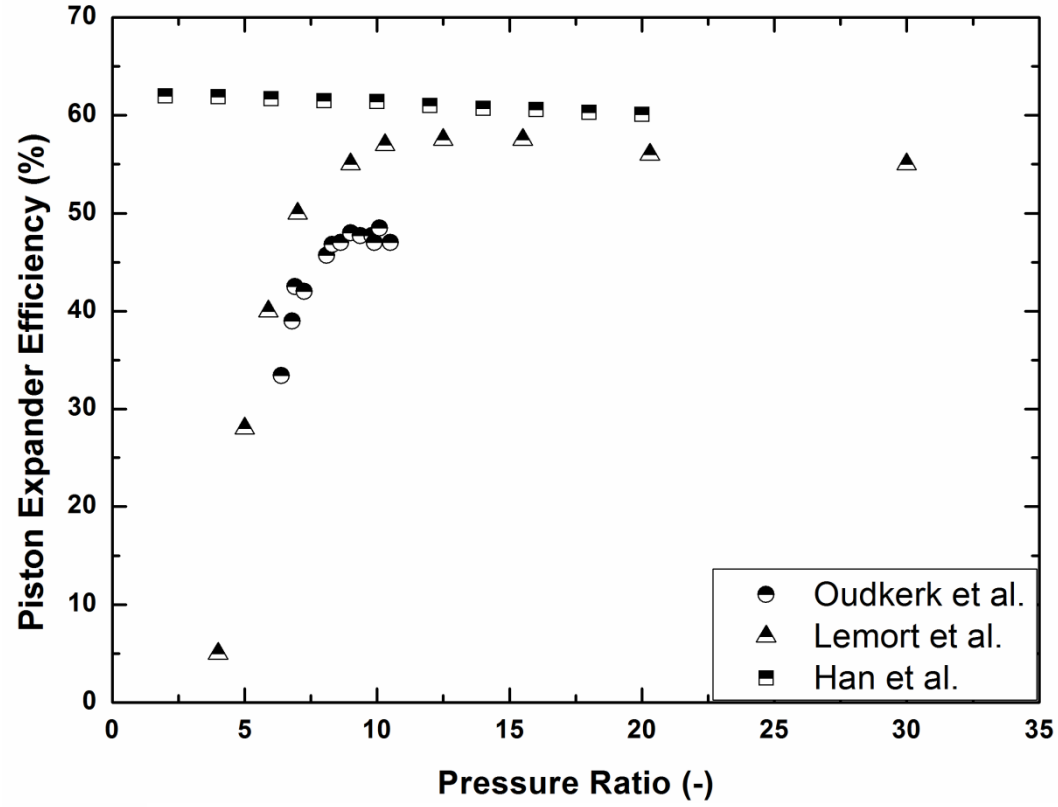

Figure 2-6: Performance of piston expanders.

Rotary vane expanders are also capable of operatingat relatively high pressure ratios of up to 10, as shown in Figure 2-7,which presents the results of previousstudies [123], [163], [164]. The reported power outputs in Table 2-1are relatively low due to the low mass flow rates (0.012–0.07). However, Antonelli et al. [123] increased the mass flow rates to high levels, which resulted in power outputs of up to 31 KW. The isentropic efficiencies of such expanders are in the range of 45%–80%. The low values of efficiencies and power outputs are due to operational losses, such as leakage friction loss and leakage [170]. Kolasinski et al. [164] indicated that isentropic efficiency is a flat curve over a wide range of operating conditions(Figure 2-7). Moreover, rotary vane expanders have low rotational speeds (up to 4000 rpm), as shown in Table 2-1,which enable them to be coupled directly to the generator.

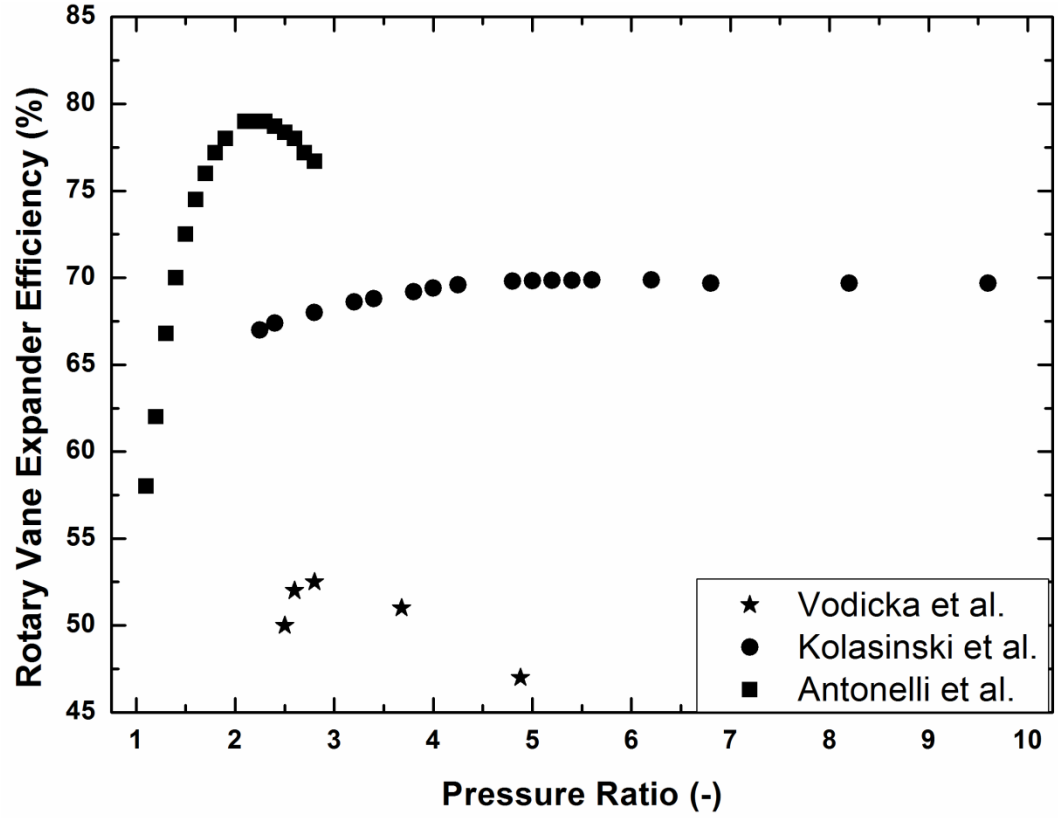

Figure 2-7: Performance of rotary vane expanders.

Overall, the rotational speeds of volumetric expanders are relatively low, which enable them to be coupled directly to the generator without the need for a reduction gearbox. Moreover, operating with two-phase fluids is a main advantage of PDEs, as itincreases the cycle efficiency and decreases the heat exchangercost. This outcome makes such expanders suitable choices for WHR systems that integrateORC systems with wet fluids. In terms of reported power, screw expander is superior, which makes such expanders suitable candidates for small- and medium-scale applications. Scroll, piston and vane expanders can be applied in small- or micro-scale applications owingto their low power outputs. In terms of efficiency, scroll and rotary vane expanders are superior,whereaspiston presents the lowest values. However, piston expanders can operate at significantlyhigher pressure ratios than the other expanders. In PDEs, lubrication is compulsory for sealing purposes or the contact between their parts. Hence, an oil separator should be installed with reciprocating expanders, which increase system complexity [23]. Although oil-free expanders exist, they suffer from high leakages. In addition, reciprocating expanders, particularly reciprocating

piston expanders, are usually bulkier and heavier than other expanders [171].

2.3.2 Turbo-Expanders

The operation of turbo-expanders or turbines is dependent on the high-pressure working fluid directed through the turbine blades,causing them to rotate as the fluid expands. As stated, the main difference between ORC and steam cycle is the working fluid used in the cycle. In steam cycles, the enthalpy drop is much higher than that in ORCs. Thus, fewer turbine stages are required in ORCs [117]. Turbo-expanders have two main types, axial and radial turbines. No standard approach to selecting and designing ORC turbines exists. Moreover, the choice of turbines depends on the application, though the superiority of any one type is not always clear [172]. Figure 2-8presents the 3D geometries of axial and radial machines.

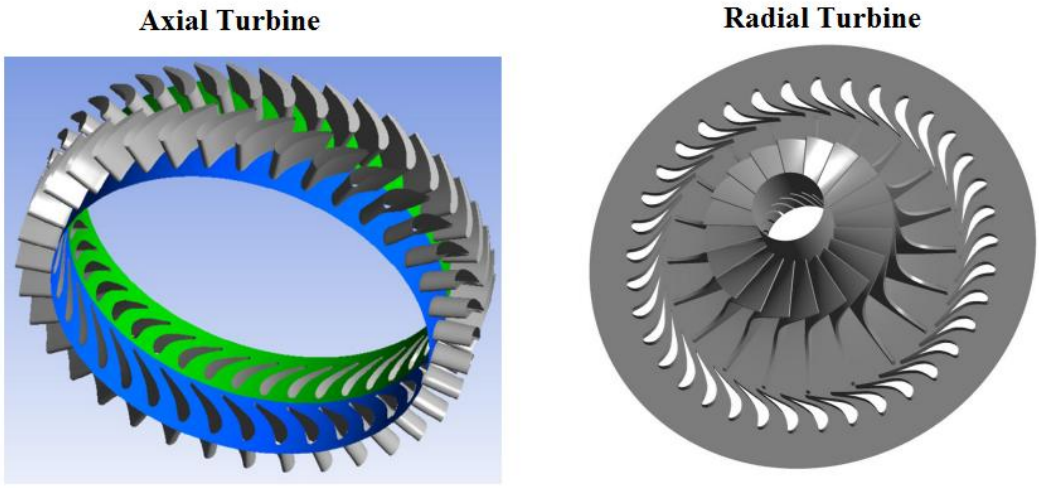

Figure 2-8: 3D geometries of axial turbine (left) [173] *and radial turbine(right)* [174].

The main difference between axial and radial turbines is the way the working fluid flows in relation to the shaft. In axial turbines, the flow of the working fluid is parallel to the shaft, whereas in radial turbines, it is radial to the shaft. In general, axial flow turbines are used in almost all gas turbine power plant applications, while radial turbines are used in turbochargers for commercial (diesel) engines and fire pumps [172]. Large-

size axial flow turbines are typically more efficient than radial flow turbines because the flow turn in the meridional plane is eliminated [175]. Axial turbines are commonly used with high flow rates and low-pressure ratios. This is because at low mass flow, the blades of an axial turbine become very small, which makes maintaining a small tip clearance difficult andresults in a significant drop in efficiency [176]. Meanwhile, radial turbines are used with high pressure ratios and low mass flow rates, which make them practical for use in ORCs. In terms of expansion, radial turbines can accommodate an expansion ratio of approximately 9 to 1 in a single stage, while axial turbines would commonly require two or three stages to handle such an expansion [177]. However, axial turbines have a distinct advantage, which is the possibility of being air cooled when operating under high temperatures [177]. Nevertheless, cooling is not an issue in ORCs because they are always preferred when low- to medium-heat sources are used. In terms of manufacturing cost, radial turbines are less expensive as they could be derived from standard production and are not sensitive to the blade profile [120]. In addition, radial turbines are preferred over axial ones because their geometries allow higher peripheral speeds than those of axial turbines and, therefore, a higher enthalpy drop per stage [117]. The author [178]proved that the isentropic efficiencies of radial-inflow turbines can be maintained high, which is beneficial for ORC performance, by controlling the generator rotational speeds.In addition, Sauret and Rowlands[179] stated that radial turbines are preferred over axial ones because forthe following reasons:

- Radial turbines are less sensitive to blade profile inaccuracies than axial machines,thereby enabling need to maintain high efficiencies as size decreases.
- Radial turbines are more robust under increased blade load from using high-density fluids at either subcritical or supercritical conditions.
- Radial-inflow turbines are easier to manufacture relative to axial machines as the blades are attached to the hub. The rotor dynamic stability of the system is also improved due to the high stiffness.

2.3.2.1 Brief History of Turbo-Expanders in ORC-ICEs

a) Axial Turbines

Patel and Doyle [60] used ORC in ICEs in 1976. They used the exhaust gas of a Mack 676 diesel engine as the heat source. For the ORC system, they used a three-stage axial turbine as the expansion machine and Fluorinol-50 (mixture) as the cycle working fluid. The authors stated that the most attractive use of ORC is in large, HDD trucks for distance hauling, where the engine load and speed requirements are nearly constant over a large portion of operating hours and high mileages. The authors concluded that the addition of an ORC system to a long-haul diesel truck can improve fuel economy by 15% over a typical duty cycle.

Three years later, Doyle et al.[180] conducted a one-year program on a Model 676 diesel engine equipped with a bottoming ORC system using the same turbine and working fluid as ina previous study[60]. Their lab results showed that a BSFC improvement of 10%–12% was achieved,which was verified by highway tests. The authors also stated that 3120 gallons of fuel could be saved for every 100,000 miles travelled by the truck.

In 1982, Hnat et al. [181] conducted a study to recover wasted heat in the exhaust gas of a diesel engine using ORC with toluene as working fluid and Rankine cycle with steam as working fluid. The authors recommended that a six-stage axial steam turbine could be used for the steam Rankine cycle and one- or two-stage turbine could be used for the ORC. In terms of cycle efficiency, the Rankine cycle efficiencies for the toluene and steam heat recovery systems are 24% and 19%, respectively, indicating that organic fluid can convert a greater portion of the heat absorbed to mechanical or electrical power.

The results of the simulation study of Seher et al.[139] showed that at the design point, a power of approximately 10 kW can be generated at a turbine efficiency of 66%. Their results also showed that at full engine load, the turbine delivered a power of up to 16 kW. When they tested the prototype, the turbine showed low thermal power (a maximum of approximately 9 kW).

According to the authors, the major reasons for the outcomewere the different gaps and surface roughness of the prototype compared to the model assumptions.

In 2013, Kunte and Seume [182] conducted a study on utilising wasted heat in the exhaust gases of a truckapplication using ORC. For the expander selection, the authors considered four turbines, namely, Pelton, Heron, radial inflow and axial impulse turbines as a pre-selection. They compared the above turbines based on their performance characteristics, such as efficiency, power output and rotational speed. Based on the investigations, they selected the single-stage axial impulse turbine because of its high efficiency at high pressure ratio and the possible compact design due to a single-stage design. According to the high expansion ratio, the turbine required a supersonic blade design becausea high expansion ratio leads to a big drop in enthalpy and a strong increase in outlet velocity. At the design point, using CFD Solver ANSYS CFX, the turbine provided a power of 8.39 kW with an efficiency of 58%. The ORC efficiency and the estimated fuel consumption were 13% and 3.4%, respectively.

In 2015, Serrano et al. [183] conducted a simulation and experimental tests on recovering wasted heat in the exhaust gas of several diesel engines of a diesel-electric train. R245fa and fluid B (kept confidential) were selected as the working fluids. The expansion machine was an axial turbine coupled with a generator on the same axle. The simulation results showed that the expected ORC efficiency was approximately 6%–7%. The electrical power generated by the turbine was expected to range from 14 kW to 16 kW.

Recently, Cipollone et al. [184] tested an ORC-based power unit on an IVECO NEF 67 turbocharged diesel engine with R245fa as the cycle working fluid and a single-stage axial turbine as the expansion machine. The results showed that as the expansion ratio increased, the turbine power and isentropic efficiency increased with maximum values of approximately 83% and 6.9 kW, respectively.

b) Radial Turbines

In 2010, Briggs et al. [185] used an ORC system equipped with a light-duty diesel engine with R245fa as the working fluid and radial-inflow turbine as the expansion machine. The experimental results demonstrated a peak thermal efficiency of 42.6% for a light-duty diesel engine system. The turbine-generator was designed for a peak operating speed of 80,000 rpm, and the achieved power output was 4.6 KW. The authors stated that the expansion wouldnot bring the fluid (R245fa) to a saturated vapour state, and hence a two-phase flow was not encountered in the turbine. The achieved cycle efficiency was 12.7%.

The following year, Cogswell et al. [186] designed an ORC power generation system to recover the heat from the exhaust gas of a 60kW diesel engine (John Deere 6059T). Novec649 was selected as the working fluid because it is non-flammable and has a near-zero GWP. The expander was a single-inflow radial turbine with a 4.6cm rotor diameter and a pressure ratio of 12. The achieved isentropic efficiency and power output were 83% and 7.8 kW, respectively. The results also showed that the ORC system generated 5.7kW net power.

In the same year, Teng et al.[111], [187] developed and tested an ORC with ethanol as the working fluid to investigate the fuel economy benefit of recovering waste heat from a 10.8 LHD truck diesel engine. The authors used a radial-inflow turbine with an impeller diameter of 53 mm available in a Garret GT25 turbocharger. However, the authors removed the original turbine housing and replaced it with a special design for the working fluid application where a nozzle ring with conical-shaped nozzles was added. The turbine presented an isentropic efficiency of 78%. The first study [111] demonstrated that 5% fuel savings could be achieved using the WHR Rankine cycle. However, the experimental results in the second study [187] showed that an improvement of up to 3% engine fuel consumption could be recovered using EGR and exhaust gas heat sources.

In 2013, Wolfgang Lang et al. [188] conducted a study on utilising ORC to recover waste heat in the exhaust gas and EGR system of a high-duty diesel

engine. The working fluid and the expansion machine were siloxane and radial-inflow turbine, respectively. The turbine efficiency was calculated as 78%,which would run at 25,990 rpm. The results of the ORC system showed that the turbo-generator can provide approximately 9.6kW of additional power to the diesel engine operating in cruising conditions of 150kW power output at 1500 rpm, without significantly altering its operation.

In the same year, Takatoshi et al. [189] conducted an experimental test on the ORC used to recover the heat of the engine coolant with hydro-fluoro-ether as the working fluid. The study focused on optimising each component of the cycle. To optimise the turbine, a small nozzle angle was set to increase the saturation temperature in the evaporator. In addition, ball bearings were applied to a shaft, and a permanent magnet type generator was adopted. System efficiency was improved by expanding the difference of the saturation temperature, improving the heat exchanger performance and using a high-pressure turbine. The results showed that a 7.5% improvement in fuel economy was accomplished by using the developed Rankine cycle generating system.

In 2015, Costall et al. [190] designed a radial-inflow turbinefor use in an ORC system that recovers wasted heat of off-high way diesel engine. The authors designed three radial turbines and selected toluene as the working fluid due to its high critical temperature, which aligns with the 300°C heat source. However, the small turbine (~20 mm dia.) led toimpractical blade geometry (1.6mm blade height). The medium turbine (62.9 mm) produced 34.1 kW with 51.5% efficiency,whereasthe large turbine (83.0 mm) produced 45.6 kW for maximum isentropic efficiency (56.1%).

Rudenko et al. [191] designed two nozzleless radial-inflow turbines for use as expansion machines in a dual-loop ORC system using R245fa as the working fluid. The achieved total-to-static efficiency and the power output of the high-pressure turbine were 85.18% and 211.4 KW, respectively, while they were 91.33% and 394.6 KW for the low-pressure turbine. The results also showed that up to 19.73% of power boost for the ICE can be achieved without burning additional fuel.

Guillaume et al. [192]conducted an experimental study that intensively investigated the performance of a radial turbine with two working fluids (R245fa and R1233zd)using the exhaust of a truck engine as the heat source. However, the heat wasted by the truck through the exhaust gases was simulated using an electric oil boiler coupled to the ORC loop. R245fa showed high electrical power from the turbine-generator with a maximum value of 2.5kW, whereas R1233zd showed improvedturbine efficiency with a maximum value of 32%.

Recently, IFPEN and ENOGIA [193] investigated the possibility of recovering the wasted heat in the coolant of a heavy-duty engine. They used NOVEC649 as the working fluids and a radial-inflow turbine as the expansion machine. The maximum measured cycle efficiency was 10%, and the fuel economy improvement achieved wasapproximately 2%–3%.

The author[194] proposed a design methodology for a radial-inflow turbine in ORC-ICEs. The study focused on optimising the objective function, namely, isentropic efficiency, by optimising two variables: exit tip radius and inlet blade angle. As the exit tipradius increases, the tip clearance loss, mainly the radial tip clearance, decreases.Therefore,a high turbine performance is achieved. Moreover, the tangential component of the velocity decreases with the increasing exit tip radius, which results in high specific work. Increasing the inlet blade angle likewise results in high tangential velocity and,therefore,high specific work.

2.3.2.2 Performance of Turbo-Expanders

The performance of turbo-expanders is expressed in terms of isentropic efficiency as shown in equation (2-2):

$$\eta_{is} = \frac{actual\ work}{Ideal\ work} \tag{2-2}$$

The performance of axial and radial turbines is investigated based on the rotational speeds and mass flow rates as shown inTable 2-1. The off-design performance is presented in Figure 2-9 and Figure 2-10.

Axial turbines are used in systems with low pressure ratios and high mass flow rates. Figure 2-9shows the results of several studies [151], [166], [167]where the pressure ratios are in the range of 0–5. For higher pressure ratios, a multi-stage axial turbine is required to achieve the required expansion. However, Seta et al.[166] used a single-stage axial turbine for high-pressure ratios, but the isentropic efficiency of the turbine dropped dramatically (Figure 2-9). Axial turbines usually present high isentropic efficiencies, as shown in Figure 2-9, which fall in the range of 75%–82.5%. Table 2-1 shows that axial turbines have lower rotational speeds compared to radial turbines, but they operate efficiently with high mass flow rates and power conditions.

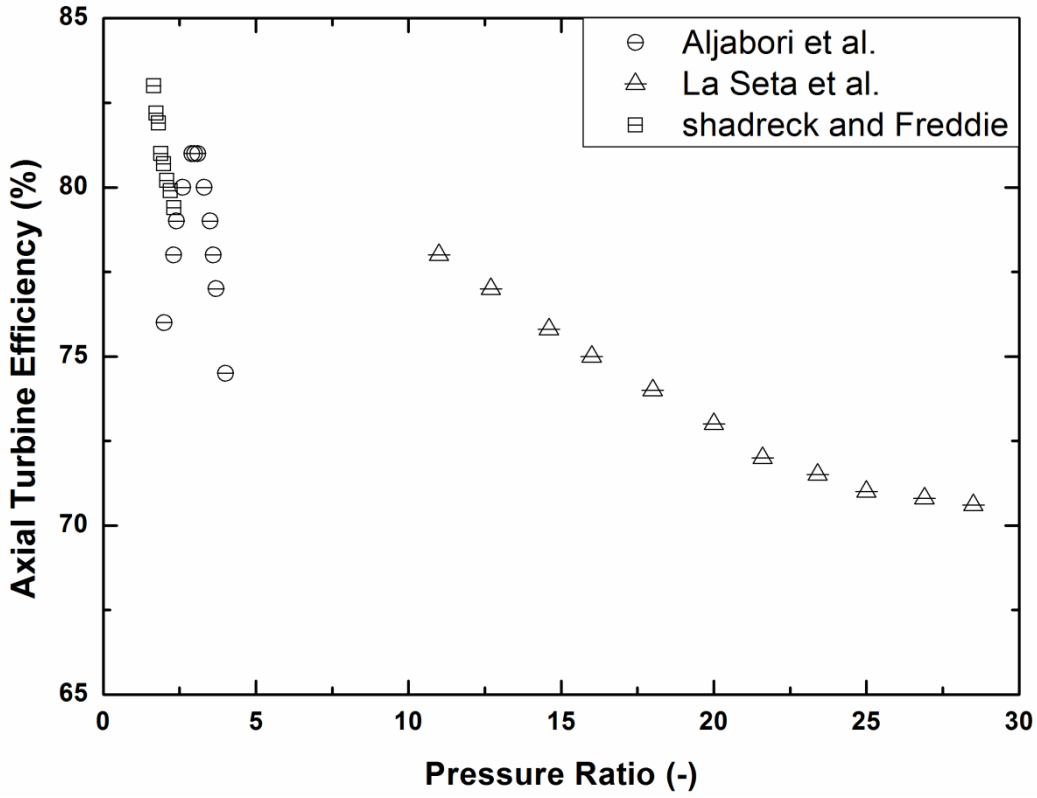

Figure 2-9: Performance of axial turbines.

Radial-inflow turbines are good candidates for systems with high pressure ratios and low mass flow rates. Figure 2-10shows the results ofseveral

studies[14], [148], [149], [153], where the radial turbines generally show higher expansions ratios than the axial turbines without getting supersonic, while their mass flow rates, as shown in Table 2-1, are significantly lower. Moreover, the radial turbines present high efficiency levels at off-design conditions, as shown inFigure 2-10. The isentropic efficiency can be even higher when using two-stage radial turbines, as shown in Han et al. [148],whose isentropic efficiencies reached 89%. The efficiency curve was also nearly flat at pressure ratios of 5 to 9. The power outputs of radial turbines are in the range of 0.54–750 kW, depending on the application, as shown inTable 2-1. However, radial turbines work with high rotational speeds, where a reduction gearbox might be required. Nonetheless, for micro turbines, the wheel can be directly coupled to the generator shaft.

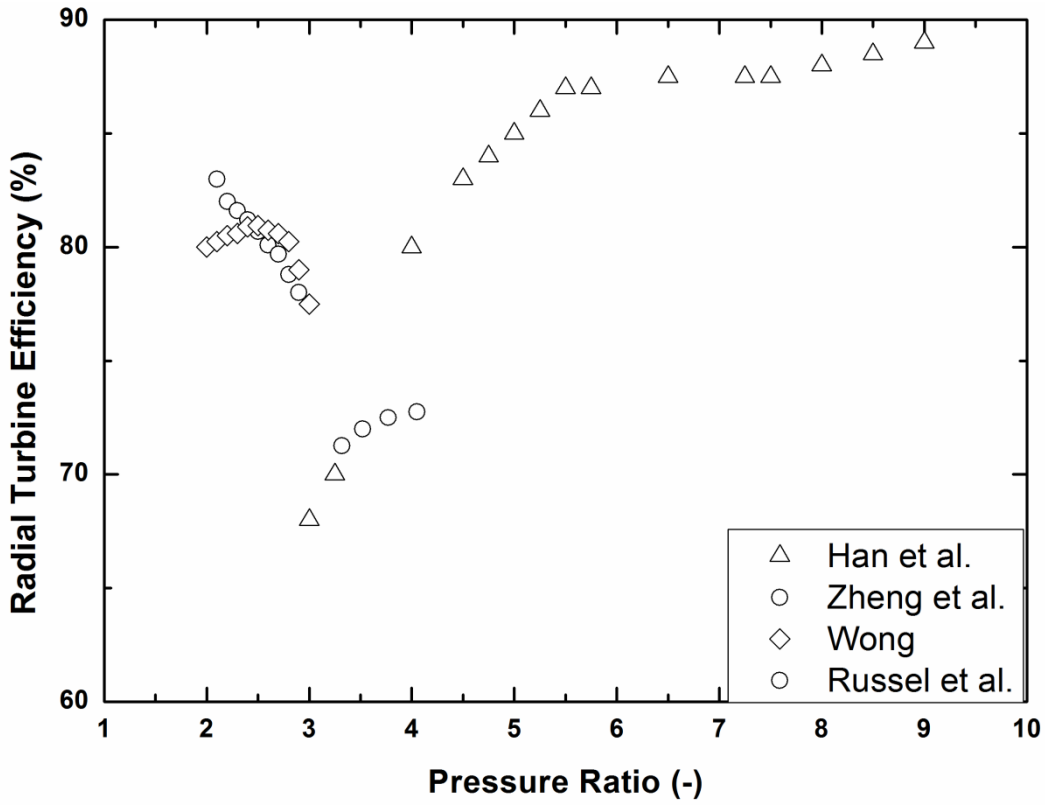

Figure 2-10: Performance of radial turbines.

Overall, the rotational speeds of turbo-expanders are generally high, which means that reduction gearboxes are required. However, micro turbines can be mounted directly to the generator shaft to eliminate gearboxes. The power outputs of turbo-expanders are higher than those of

PDEs, which make them suitable candidates for large-scale systems. A main disadvantage of turbo-expanders is that they cannot withstand two-phase fluids due to the possibility of corrosion at the turbine blades. Axial turbine presents very high efficiencies for a wide range of pressure ratios. However, a multi-stage configuration is required for high pressure ratios, which increase the weight of the turbine. Meanwhile, radial-inflow turbines present reasonably high efficiencies and higher power outputs. In general, the efficiency curve of the radial turbine is flatter than the axial turbinein terms of the off-design performance. Compared to PDEs, the design of turbo-machines is simpler. They can also be adjusted and optimised for different operating conditions and resources without changing the overall size. Moreover, no lubrication is required in turbo-expanders, which could spoil the working fluid, due the absence of contact seals [195].

2.3.3 Selection of an Optimum Expansion Machine

Expansion machines are the mechanical power conversion devices used in the ORC heat recovery process converting heat to electricity. As stated, no single expansion machine is superior over other applications. However, the thermodynamic operating conditions in the ORC system can be derived and expressed as dimensionless parameters that can be utilised to select the preferable expansion machine. In addition to the thermodynamic conditions, the operating speed of the expander has a major impact on the expander type. Moreover, size and weight should be considered in some applications, such as the interior of vehicles where space is limited.

In this study, the potential efficiencies and power outputs of ORC expanders based on the literature for different expansion machines are presented. Well-known studies in the literature, such as those of Balje [196], Dixon and Hall [197], Badr et al. [198] and Watson and Janota [199]discussed the correlated turbine efficiency against the specific speed for air turbines. Specific speed, as shown in equation(2-3), is a function of operating conditions. Therefore, it can be utilised at the early stage of the project to specify the optimum expander type for a certain application without considering the geometrical parameters.

$$N_s = \frac{\omega\sqrt{Q}}{\Delta h_{act}^{0.75}} \tag{2-3}$$

Figure 2-11 and Figure 2-12 present the results of the papers studied in Figure 2-4, Figure 2-5, Figure 2-6, Figure 2-7, Figure 2-9 and Figure 2-10. The performance of expanders as a function of specific speed $N_s$is presented, where $N_s$is calculated by equation (2-3). Given the power, speed and flow rate in the selected studies, the calculation is straightforward. Although roughly, Figure 2-11 and Figure 2-12 together can be a useful guide forselecting the most appropriate type of expansion machine in ORC applications.

Generally, the positive displacement of expanders ispreferred for low values of specific speed ($0.003 \leq N_s \leq 0.1$). Meanwhile, turbo-machines are optimum candidates for higher values of N_s($0.4 \leq N_s \leq 1$). In steam Rankine cycles, the enthalpy drop is relatively higher than that in ORCs. In addition, the volume flow rate at the expander exit is lower. Therefore, the specific speed values for ORC expanders are higher than those in steam Rankine cycles based on equation(2-3).

Clearly, scroll expanders present good machine performance for all ranges of power outputs when the specific speed N_s is in the range 0.006 to 0.008. Figure 2-12also shows that rotary vane expanders present similar N_s values for various power outputs with optimum performance when the specific speed (N_s) values fall in the range 0.012 to 0.037. Similarly, piston expanders are studied for applications with power outputs in the range 0.3–2 kW. The values of specific speed N_s fall in the range 0.0048–0.006. Screw expanders are investigated at low- to medium-power applications. The power outputs fall in the range of 1–17 kW. Specific speed N_s values are limited within 0.01–0.09. Overall, PDEs are preferred for low values of specific speed N_s . For very low N_s values, scroll and piston expanders are nominated. For slightly higher values, rotary vane and screw expanders are preferable.

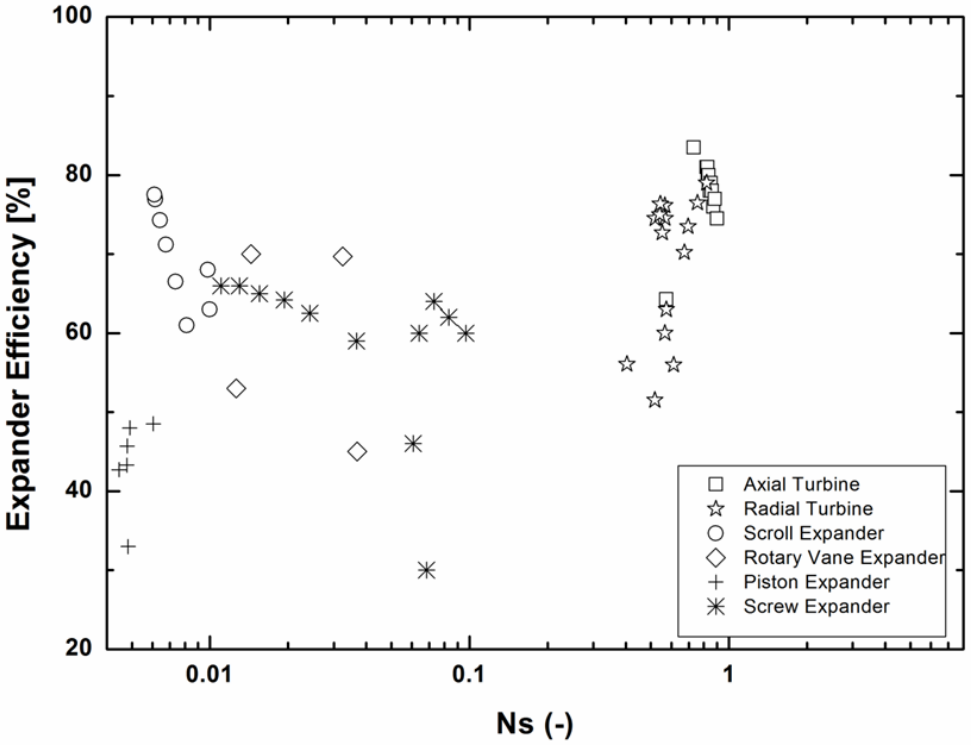

Figure 2-11: Expander efficiency versusspecific speed for different expanders.

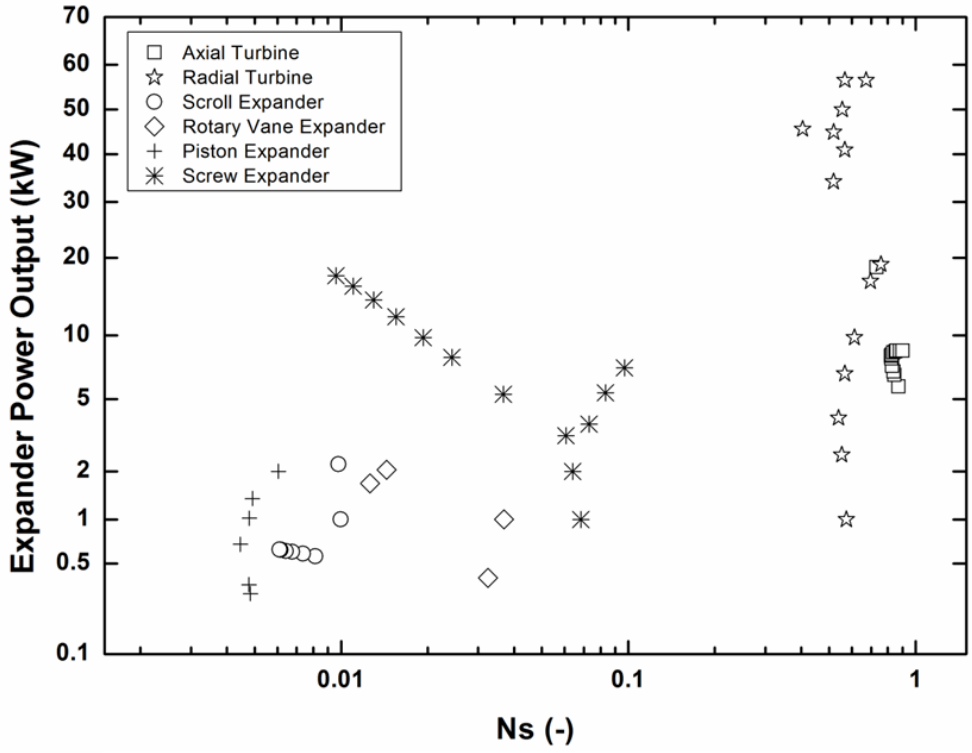

Figure 2-12: Expander power outputs versusspecific speed for different expanders

Meanwhile,turbo-machines present much higher values of specific speed N_s . Axial turbines are investigated for different power outputs that range from 5 kW to 20 kW. The values of specific speed N_s fall in the range of 0.7–0.9.

The radial turbines are investigated for higher powers. The investigated applications produce power outputs in the range of 1–60 kW. For the whole range of power outputs, the values of specific speed N_s fall in the range 0.4–1.

Overall, the combination of Figure 2-11 and Figure 2-12can be applied as an expander's selection guide at the early stage of a project. Based on the application (required power output), the appropriate expansion machine can be nominated and its efficiency can be roughly known. Then, other constraints, such as size and weight, can be evaluated. For instance, PDEs are generally larger in size and heavier in weight than their turbine counterparts, which make them unfavourable in passenger vehicles.

2.3.4 Cost Estimation of Expansion Machines

Expansion machines are typically the most costly component [200]–[204]becausethey need to be precision-engineered [205]. Open literature is lacking a direct cost comparison between the various types of expanders. Cost estimation, along with the plots in Figure 2-11 and Figure 2-12, can help designers decide which expander to select at the early stage of a project.

Gutiérrez-Arriaga et al. [206] presented a correlation, as expressed in equation(2-4), to estimate the cost of ORC expanders in terms of their power outputs. The correlation is based on an exponential scaling law and was updated in 2014. However, using this correlation, the prices vary considerably as the power output changes, which cause each type of expansion machine to have a wide range of prices. Therefore, for each type, the power output is averaged and the price is estimated as depicted in Figure 2-13.

$$CAP_{turb} = 2237\, W_T^{0.41} \qquad 2\text{-}4)$$

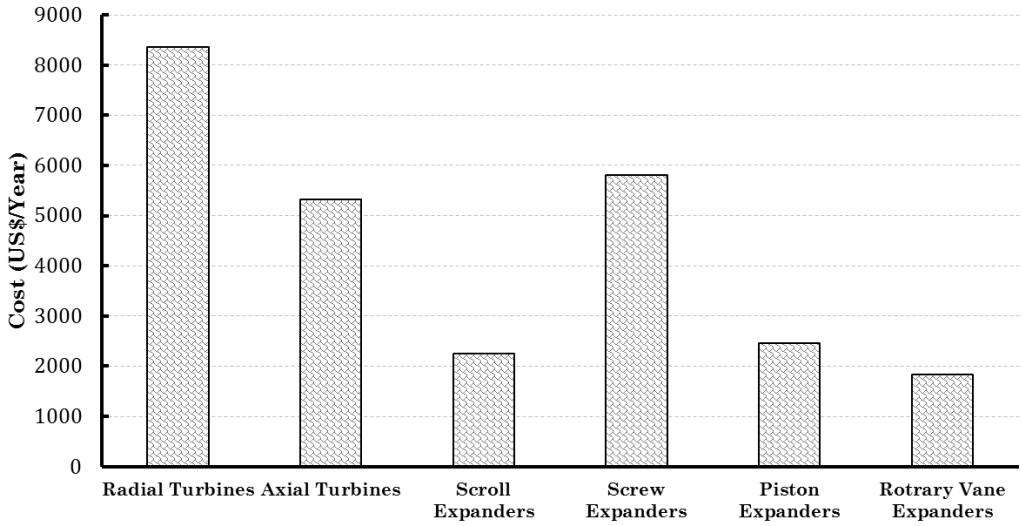

Figure 2-13: Cost estimation of expanders based on power output only.

Clearly, radial turbines present a higher cost, which corresponds to 33% of the total cost, followed by screw expanders at22%. Rotary vane expanders are the cheapest, with an estimated contribution of 7% compared to the total cost of the expanders. Axial turbines, piston expanders and scroll expanders contribute 20%, 9.4% and 8.6%, respectively. However, the larger the system is, the more expensive the componentwill be. The above estimations are purely based on the power outputs regardless of the system or application.

To perform a more feasible comparison between the different expander technologies, each type should be compared with the rest of the system's components. For each system, an expansion machine is designed in accordance withthe system requirements. Therefore, the cost of each expander is compared with its own system. The module costing technique is applied in this study. This technique is presented by Turton et al. [207], as shown in equation 2-5), based on the data from a survey of manufacturers during the period of May 2001 to September 2001. This correlation is widely used in the literature [208]–[211]. Toffolo et al. [212]appliedthe aforementioned correlation to estimate the costs of a real ORC plant built in 2009 for utilising low/medium enthalpy resources in the USA. The results of their study were in good agreement with the actual cost of the ORC equipment.

$$log_{10}C_p^0 = K_1 + K_2 log_{10}(X) + K_3[log_{10}(X)]^2 \quad (2\text{-}5)$$

C_p^0 is the purchased equipment cost at ambient pressure using carbon steel. X is the equipment variable. For the pump and expander, it corresponds respectively to the power input and output in kW. For the evaporator and condenser, it corresponds to the heat exchanger area in (m^2). The coefficients for each component are summarised in Table 2-2.

Table 2-2: Coefficients for Different Cycle Components [207].

Component	**Purchased Cost C_p^0**	**Coefficients**		
		K_1	K_2	K_3
Expander	$log_{10}C_p^0 = K_1 + K_2 log_{10}(X) + K_3[log_{10}(X)]^2$	2.2476	1.4965	-0.1618
Evaporator		4.6656	-0.1557	0.1547
Condenser		4.6656	-0.1557	0.1547
Pump		3.3892	0.0536	0.1538

The investigated works in this study include those of[213]on axial turbines;[214]on radial turbines;[215]on scroll expanders;[169] on screw expanders;[216]on piston expanders; and [143]on rotary vane expandersowingto the availability of the required information. Figure 2-14 and Figure 2-15 present the distribution of the costs for each component and the contribution of each component's cost with respect to the system. Clearly, heat exchangers (evaporators and condensers) bear the brunt of the total cost, whereas the pumps' cost is insignificant compared to the system cost. The heat exchangers costapproximately $43,203–$80,740, while the pumps cost approximately $450–$510. The marginal cost between evaporators and condensers is due to the different heat exchanger areas between the two components.

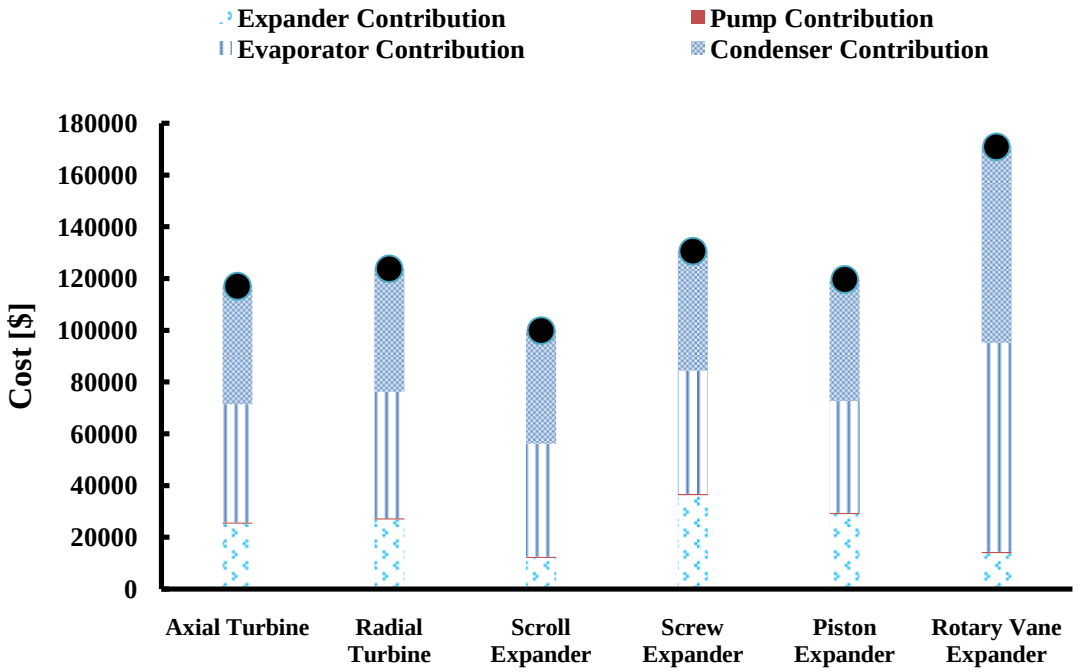

Figure 2-14: Cost contribution of different expansion machines in relation to ORC component and total costs.

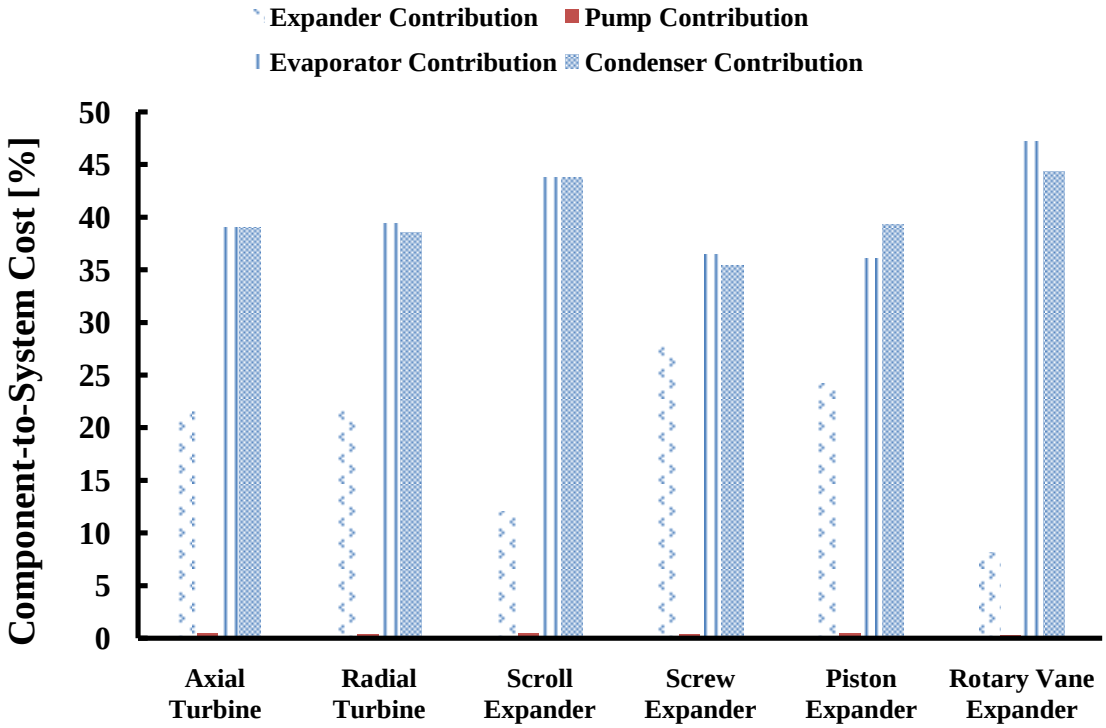

Figure 2-15: Contributions of component costs to total system cost.

Finally, an estimation of the accurate capital cost should consider the direct and indirect costs,including theexpander's parts, installation,

material, insurance, taxes, utilities and shipping. Generally, scroll expanders are popular for their relatively low cost [45] as they can operate without inlet and exhaust valves, with low parts count and high-volume production. They could be even cheaper if they were modified from scroll compressors. Meanwhile, piston expanders have not become common practice due to their need for bearings and outlet valves that increase the production cost [217]. Screw expanders are not cheap because they might require a reduction gearbox [218]. Vane expanders are the cheapest as they can be designed with less weight [219], fewer mechanical parts and without suction valves. Lubrication requirements, technical complexities and frictional and leakage losses are the main technical barriers in the commercialisation of volumetric expanders [67]. Compared to PDEs, turbo-expanders are in the middle in terms of cost. However, turbo-expanders with high rotational speeds place strict requirements on the bearing, shaft seal and strength of rotating parts [47]. Given thatcosts increase proportionally with size, multi-stage turbo-expanders are even more expensive and are thus not included inFigure 2-14 and Figure 2-15.

2.4 Conclusion

The literature review can be summarised as following:

- Most of the applied waste heat recovery technologies in vehicular engines are either theoretical studies or experimental results using prototypes. These technologies should be investigated using actual exhaust gases of vehicular engines.
- Compared to other waste heat recovery technologies, ORCs provide an attractive combination of efficiency and affordability for engine exhaust. It also exhibits great flexibility, high safety and low maintenance requirements. In comparison with steam cycles, ORCs show better efficiency but their costs are higher.
- Exhaust gases, jacket water, EGR and engine coolant are the most common heat sources when applied in WHR systems, with priority for

exhaust gases. However, some studies showed that ORCs behave badly in recovering heat in jacket water.

- No working fluid is superior for an ORC system. The selection of an optimum working fluid depends on the application, working conditions, environmental concerns and waste heat level. However, R245fa is the most common fluid used for ORCs engine waste heat recovery applications since it is the most environment-friendly working fluid.
- Under transient conditions, performance and power output of ORC systems increase as energy of the heat source and mass flow rate increase. The exhaust energy increases gradually when the engine is running at higher speed and torque. However, the BSFC has higher values at high engine speed and low torque.
- For applications with high temperature and high power output, turbo-machines are dominant. On the other hand, reciprocating expanders are superior in applications with low temperature and low power output.
- Efficiencies of turbo-machines are higher than the reciprocating ones. However, turbo-machines are more expensive and suffer from the droplets at the expansion stage when using wet fluids, whereas reciprocating expanders can cope with two-phase expansion.
- Expander efficiency is usually assumed constant at different operating conditions and different working fluids in most of the ORCs studies. In reality, this efficiency is highly sensitive to the operating conditions and selected working fluid.
- Radial inflow turbine is preferred over the axial one when applied in applications with low mass flow rates and high expansion ratios such as mobile engines. Axial flow turbines are commonly used in gas turbine power plants.
- Especially in vehicular applications, heat source temperatures are not constant and uncontrollable. Therefore, it is very crucial to predict the performance of expansion machine at wide range of operating conditions. From the literature review, it was clear that there is a

need for a mean-line off-design model to achieve the task. Accordingto the author's knowledge, the literature still lacks of such models for ORC expansion machines.

- This chapter presented a sufficient guide that can be used at the early stage of a project in order to select the most appropriate expander type for the corresponding application. This guide consists of three plots: performance vs. specific speed, performance vs. operating characteristics, and cost estimation. Overall, the selection of the expansion machine is a trade-off between better performance and higher cost. However, once the required power of a certain application is known, the guide can be used in order to select the optimum expander where efficiency and price can be roughly estimated.

The next chapter presents theoretically the effects of ORCs as WHR technologies on internal combustion engines (ICEs) in terms of back pressure, performance and BSFC. In addition, the effects of radial inflow turbines in both forms, FGT and VGT, on ORC-ICE powertrains are also investigated in details.

Chapter 3 : Modelling of Organic Rankine Cycle

3.1 Introduction

Compared to TC and TEG technologies, ORC is an alternative and more efficient WHR solution that has been used in recent years to gain ground in the automotive industry because of the stricter CO_2 emission standards. Many theoretical studies regarding integrated ORC systems in vehicle powertrain present thermal efficiencies between 6% and 15% [117], [220]–[222]. This variation in ORC thermal efficiency mainly depends on the heat sources used in engine operating conditions. Exhaust gases are a source of high-grade heat for extracting energy through a heat exchanger for an ORC system.

However, importing any additional device (i.e. the ORC system) in the exhaust system increases the engine backpressure and has an additional cost on fuel consumption. Fitting a heat exchanger in the exhaust manifold results in an increase in backpressure, but compared to the TC technology, this increase is approximately one order of magnitude lower. The amount of both the extracted heat and the exhaust backpressure depends on the ORC configuration and the heat exchanger type [222]–[224]. Engine waste heat can be transferred directly through the evaporator to the ORC loop, but in some studies, an intermediate thermal oil loop between the exhaust gases and the ORC is used [225]. Direct heat transfer from the exhaust gases to the organic fluid is often preferred in transport applications as it increases the heat transfer efficiency and reduces the weight of the WHR system, while the thermal oil loop requires an extra heat exchanger and pump. However, cycles with an intermediate oil loop guarantees steady-state conditions for the ORC operation, while any potential decomposition of the working fluid at high exhaust enthalpy conditions can be avoided [225].

Another drawback of the integration of an ORC system with a vehicle platform is the weight increase. The effect of weight increase on fuel consumption has been investigated in the past, mainly by using vehicle simulation tools [226]–[228]. In the case of a regional delivery truck, a 20% reduction of its weight can lead to a 12% reduction in fuel consumption [228]. A high vehicle weight is a negative performance factor because this results in high vehicle inertial mass. Consequently, both engine load and

fuel consumption during acceleration increase, while the frictional forces are enhanced under all operating conditions. To this end, the installation of an ORC system is expected to constrict the vehicle performance, especially under partial engine load conditions. A recent study showed that the weight of an ORC system that utilises a 200kW$_{th}$ exhausts waste heat of a tractor and presents a theoretical 10%thermal efficiency that can reach approximately 300 Kg [229]. The latter means that an additional 20 kWe is accompanied by a significant increase in vehicle weight mass. This drawback, however, is less important in the case of an off-highway vehicle, as most of the operating time the vehicle may work as a stationary machine (e.g. excavators and cranes).

This chapter explores the effects of implementing an ORC WHR system on an off-highway vehicle in terms of ORC efficiency, engine efficiency and powertrain performance. The analysis considers the effect of exhaust backpressure on engine fuel consumption and the potential changes of power-to-weight ratio due to the ORC additional weight. Furthermore, the impact of radial-inflow turbines in both forms, FGT and VGT, on the cycle and engine performance is investigated. The study includes the experimental data of anHDD engine, and a simplified thermodynamic ORC model that operates with various working fluids. A mean-line model (explained in detail in Chapter 5) is employed to model the radial turbine at the optimum operating point. Then, a VGT map is scaled to match the optimum efficiency of the designed expander with the one provided from the map.

3.2 Working Fluid Selection

The types of working fluids and the selection criteria of the working fluids have been discussed in Chapter 2. Among the best mentioned fluids, four working fluids are chosen for further screening because they have zero toxicity, low GWP, maximum power output compared to others, and both are inflammable. In addition, they are popular and widely usedin ORC applications. Table 3-1 presents the thermo-physical properties of the selected fluids adopted from [230], and Figure 3-2 presents the T–s diagram.

The negative slopes indicate that the selected fluids are dry fluids, which are beneficial in avoiding fluid droplets at the turbine blades.

Table 3-1: Properties of the selected fluids.

Fluid	T_{cr} (K)	P_{cr} (bar)	P_{cr} Kg/m^3	Boiling Point (K)	Molecular Mass (g/kmol)	GWP	ODP
R1233zde	438.75	35.709	476.3	291.47	130.5	20	0
Novec649	441.81	18.69	606.8	322.2	316.04	1	0
R245fa	427.16	36.51	516	288.29	134.05	950	0
R123	456.83	36.618	550	300.97	152.93	77	0.02

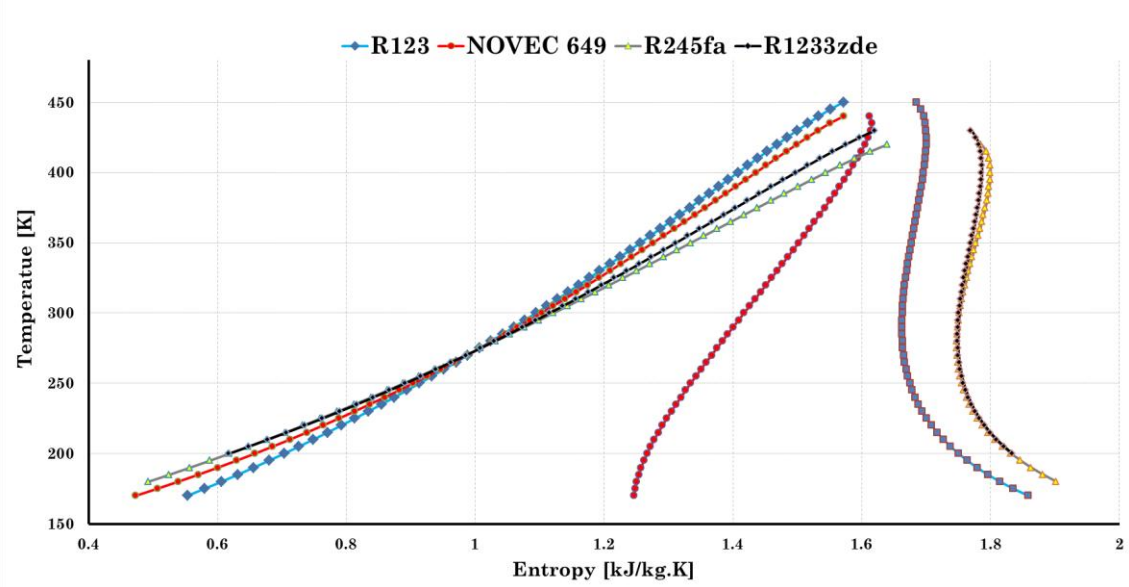

Figure 3-1: T–S diagram of different working fluids.

3.3 ORC Modelling

Two ORC models were developed for the simulation study. The two proposed integrated powertrain models are schematically presented in Figure 3-2 andFigure 3-4. Figure 3-3 presents the T–s diagram of the first model. The thermodynamic model of each cycle was developed using an in-house MATLAB code. The cycle simulator defines the cycle properties at each of

the points of the ORC. To this end, the mass and energy balance equations are used for each point.

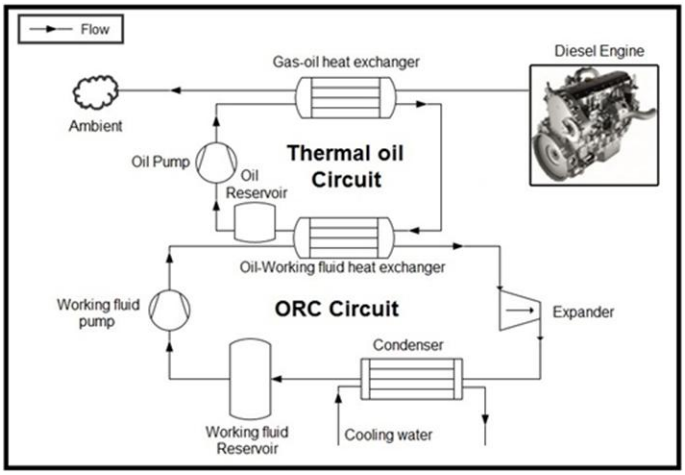

Figure 3-2: Schematic presentation of the engine–ORC system for the first model.

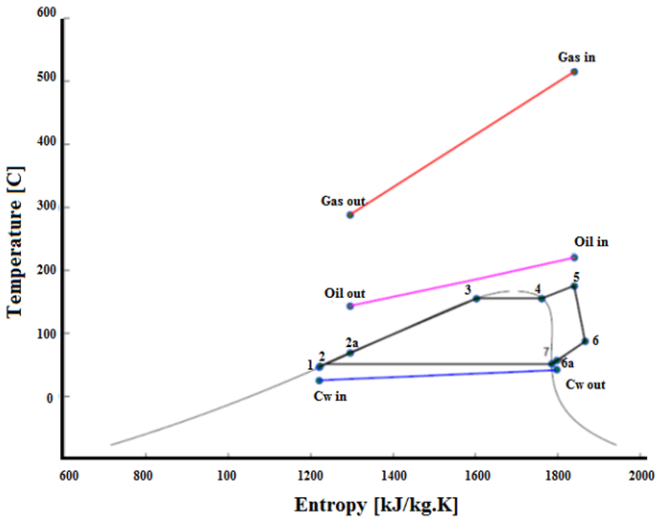

Figure 3-3: T–s Diagram of the engine–ORC system for the first model.

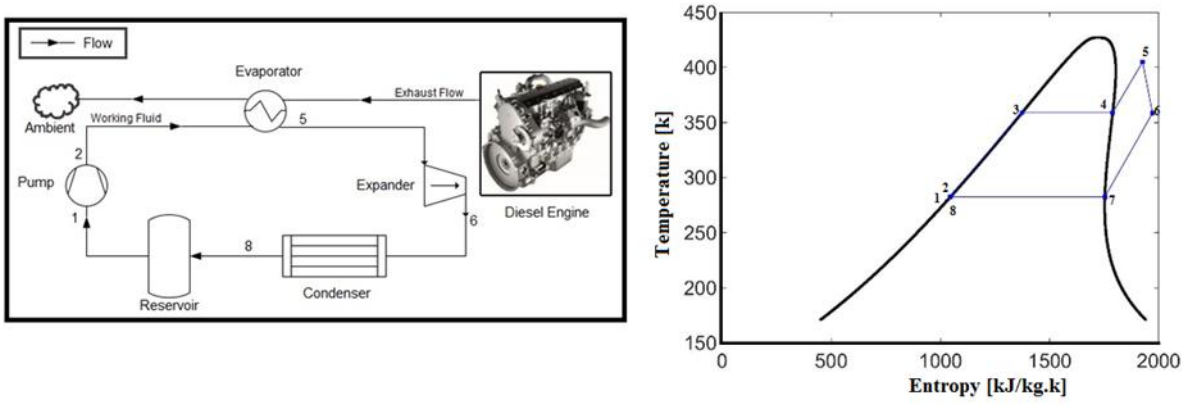

Figure 3-4: Schematic presentation of the engine–ORC system for the second model.

The first model (Figure 3-2) is utilised to explore the pros and cons of the ORC system on engine performance and fuel consumption. The thermal oil in the thermal oil loop absorbs the heat from the exhaust gas in the gas-oil heat exchanger. Then, the designed ORC system exchangesheat in the oil-working fluid heat exchanger with the thermal-oil loop that guarantees the smooth power output of the ORC system and avoids any potential decomposition of the working fluid. The working fluid then enters the turbine to generate power. Next, it enters the condenser to be condensed back to the liquid phace and pumped again with high pressure to the evaporator. The condenser is assumed to exchange heat with an ultimate heat sink (cooling air). The T–s diagram of the current model is depicted in Figure 3-3.

The second model aims to investigate the effects of the radial-inflow turbine on the powertrain system. Therefore, the thermal oil loop is eliminated as shown in Figure 3-4. The working principle of the second model is similar to that of the first model, and the T–s diagram is shown in Figure 3-4. Figure 3-5 presents the flowchart of the second model.

3.3.1 Thermal-Oil Heat Exchanger Modelling

The thermal-oil heat exchanger model describes a shell-and-tube heat exchanger (STHE), where the exhaust gas exchanges heat with the thermal oil. The model calculates the heat transfer coefficients and the pressure drop at both sides of the heat exchanger. The simulation of the heat exchanger and the cycle modelling are performed in cooperation with Entropea Labs (the industrial partner).

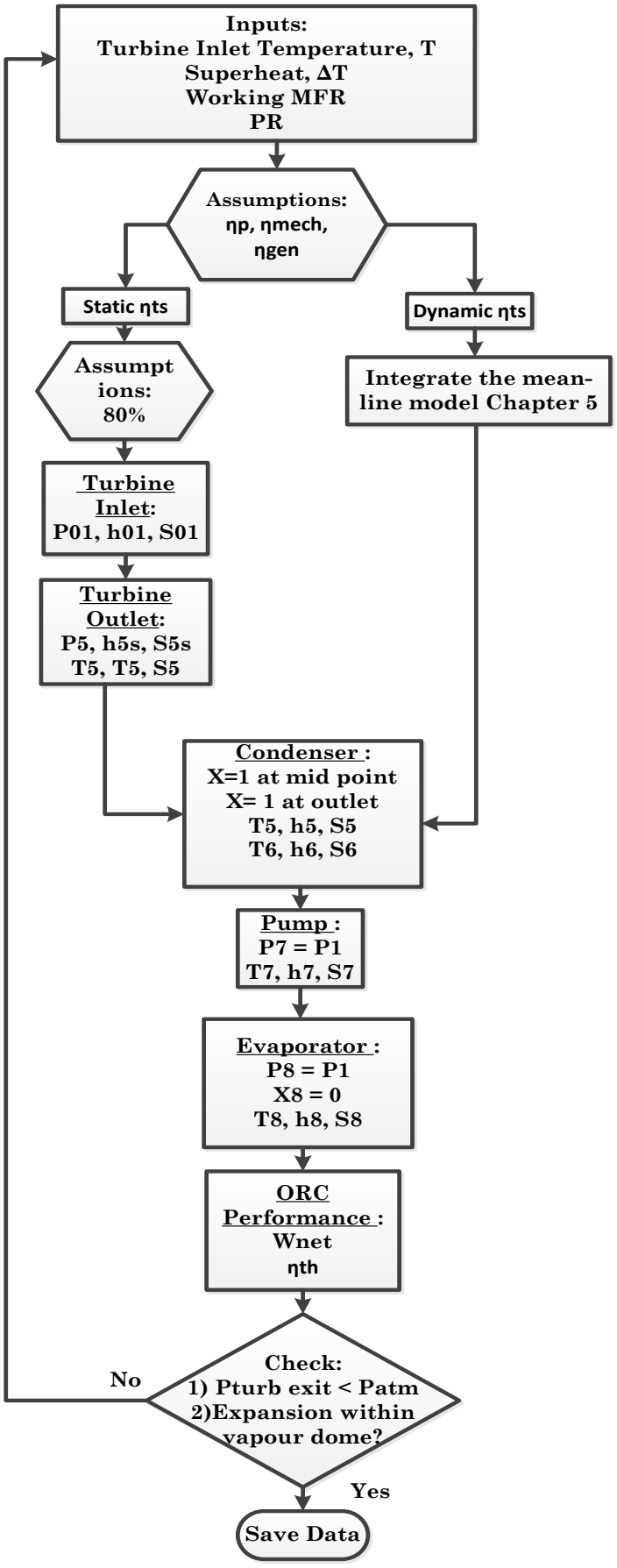

Figure 3-5: ORC model with constant and dynamic expander efficiency.

3.3.2 Evaporator Modelling

The evaporator is the heat exchanger where the heat transfers from the thermal oil (exhaust gas in the second model) to the organic fluid. The organic fluid leaves the pump, enters the evaporator as compressed liquid and then leaves as superheated vapour after exchanging heat with the thermal oil. The total energy that balances through the evaporator is expressed in equation(3-1).

$$Q_{Evap} = \dot{m}_{oil}\left(h_{oil,in} - h_{oil,out}\right) = \dot{m}_{wf}\left(h_{wf,out} - h_{wf,in}\right) \tag{3-1}$$

3.3.3 Condenser Modelling

The condenser is the heat exchanger where the heat transfers from the working fluid in a gaseous state to the cooling medium, which is air in this study. Therefore, the aim of the condenser is to reject the still heat in the working fluid to the cold sink with an isobaric process. The thermodynamic analysis of the condenser is similar to that of the evaporator. The energy balance through the condenser is expressed in equation(3-2).

$$Q_{cond} = \dot{m}_{wf}\left(h_{wf,in} - h_{wf,out}\right) = \dot{m}_{exh}\left(h_{exh,out} - h_{exh,in}\right) \tag{3-2}$$

Saturated liquid is assumed at the exit of the condenser with a sub-cooling of 2° to ensure a liquid phase at the pump inlet. Hence, the quality x at the condenser exit is known. The condenser exit quality is likewise already known. Therefore, the thermodynamic properties can be calculated at the condenser exit using equation(3-3).

$$\left\{x_{cond,out}, T_{cond,out}\right\} = EoS\left(\rho_{cond,out}, P_{cond,out}, fluid\right) \tag{3-3}$$

3.3.4 Pump Modelling

The pump is assumed to be electrically powered with the absence of leakages and for adiabatic operation. Its efficiency η_{pump} , as shown in

equation(3-4), is assumed to be 65% and is considered a realistic value for reducing the impact on the total ORC performance. As η_{pump} decreases, the amount of power consumed by the pump increases, which results in low cycle efficiency. The pump inlet conditions are the same as the condenser outlet conditions. The pump outlet conditions can be obtained through the known isentropic efficiency and the pump power. Assuming an isentropic compression through the pump, the required pump power can be calculated using equation (3-5).

$$\eta_{pump} = \frac{h_{s,wf,out} - h_{wf,in}}{h_{wf,out} - h_{wf,in}} \tag{3-4}$$

$$P_{pump} = \frac{\dot{m}_{wf}\left(h_{s,wf,out} - h_{wf,in}\right)}{\eta_{pump}\,\eta_{motor}} \tag{3-5}$$

3.3.5 Turbine Modelling

Expander modelling considers the turbine volute, stator and rotor. Given that volute is responsible for the turning of the fluid, the stator vanes aim to accelerate the flow and deliver it to the rotor inlet uniformly and at the correct angle.

An isentropic efficiency is assumed at the beginning. Then, the actual enthalpy drop on the rotor, stator and volute are calculated. Once the losses are calculated, the new isentropic efficiency is calculated. The loop ends when the estimated and calculated isentropic efficiencies converge. The turbine power output of the turbine expander is calculated using equation (3-6). The turbine model is detailed in Chapter 5.

$$P_{turbine} = \eta_{ts}\dot{m}_{wf}\left(h_5 - h_{6,is}\right) \tag{3-6}$$

3.3.6 Integrated Heavy-Duty Diesel Engine

The design of the ORC system is based on the exhaust heat flow of a 7.25 L Yuchai engine. This HDD engine is turbocharged, direct injection and fulfils EURO III regulatory constraints. Theengine is tested at Brunel University

London and does not present any EGR or VGT system, while potential after-treatment systemsare removed. The characteristics of the HDD engine are presented in Table 3-2.

Table 3-2: Yuchai YC6A280-30 diesel engine characteristics

Displaced volume	7255 cc
Stroke	132 mm
Bore	108 mm
Compression ratio	17.5:1
Number of Cylinders	6
Number of Valves	4
Maximum Torque	1100Nm @ 1400–1600rpm
Maximum Power	206kW @ 2300rpm
Optimum bsfc point	≤205 g/kWh

The entire engine operating map is measured on the engine dynamometer, and a schematic presentation of the exhaust heat is presented in Figure 3-6. The maximum power point at 2300rpm presents the highest enthalpy flow; therefore, this engine operating point is selected for the design of the WHR system. Then, a throttle valve is installed in the exhaust pipe at an appropriate distance downstream of the turbocharger to avoid affecting its operation. The throttle experimentally simulates the effect of exhaust backpressure on fuel consumption for the selected ORC engine operating point. The tests are conducted using two pressure sensors upstream and downstream of the throttle valve.

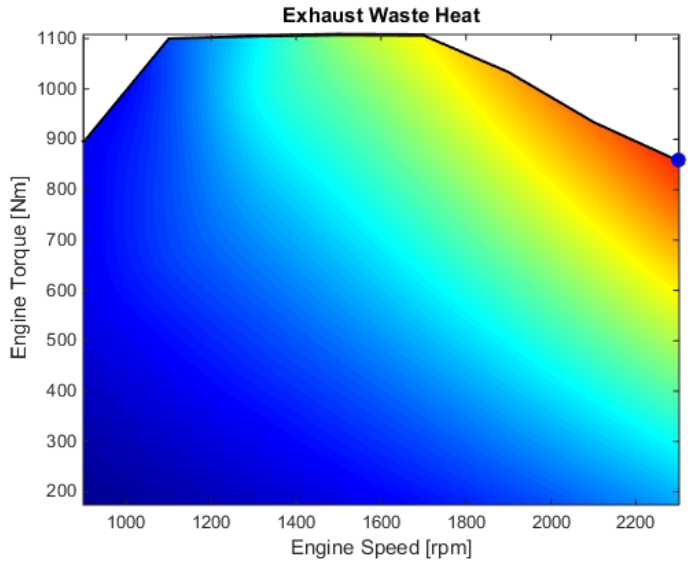

Figure 3-6: Diesel engine map with the design point highlighted through a blue dot.

3.3.7 Effects of Turbine Efficiency on ORC Performance

According to Rahbar et al. [75], turbine isentropic efficiency is considered constant for various types of working fluids. Therefore, the second cycle modelling presented in Figure 3-4 is applied to investigate this consideration. In the second cycle modelling,pressure and heat losses in the components and the connecting pipes are ignored. Arbitrary input conditions are selected as shown in Table 3-3. The input conditions are kept the same for the four screened working fluidsbecause this section emphasises evaluating the assumption of constant turbine efficiency.

Table 3-3: Input Conditions for the Second Modelling.

Input Parameter	Range
P_{01}	Saturated Vapour Pressure at T_{01} [kPa]
T_{01}	370 [K]
MFR	0.05–0.3 [Kg/s]
N	20,000 [rpm]
Ψ	0.9
φ	0.2
ΔT	2 [K]

The energy balance equations expressed in Section 3.3 are applied to investigate the effects of different working fluids on ORC system performance. In addition, the effects of static (80%) and dynamic turbine efficiencies on cycle performance are explored. As depicted in Figure 3-7, a significant deviation in the cycle efficiency from one fluid to anotheroccurs. In both cases (constant and dynamic turbine efficiencies), R1233zde showed the best cycle performance at 11.09%, whereas R123 showed the lowest efficiency at 6.77%.

Figure 3-7 also shows a substantial variation between the cycle thermal efficiencies of the models of constant and dynamic turbine efficiencies. A maximum deviation of 5.8% is produced for R1233zde, while a minimum deviation of4% is produced for NOVEC649. These significant differences are due to the high-pressure ratio and low mass flow rates through the turbine, which drastically reduces its efficiency.

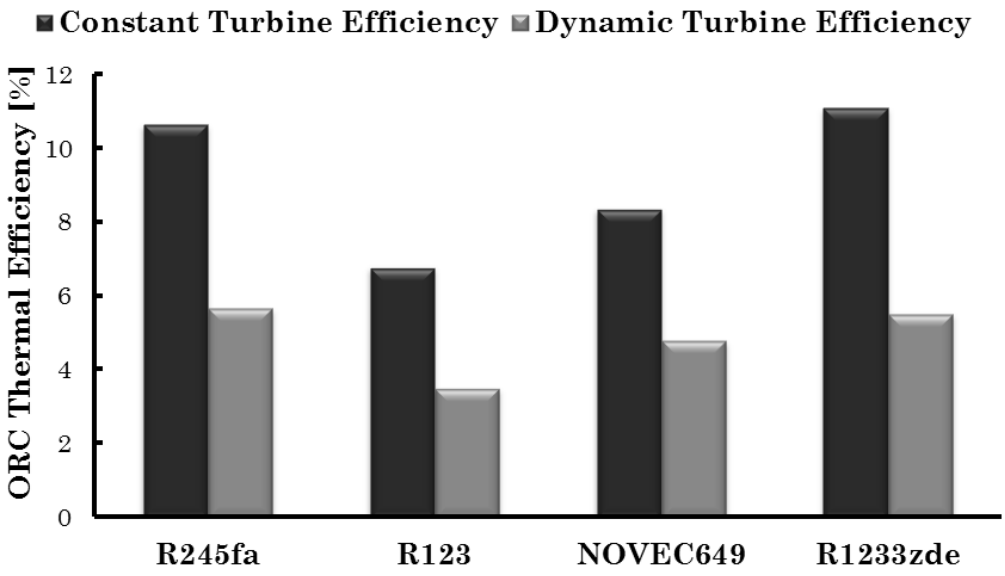

Figure 3-7: Thermal efficiency at constant and dynamic turbine performance for different working fluids.

The novel off-design (explained in Chapter 5) is also integrated to investigate the effect of different turbine input conditions on cycle efficiency. For each working fluid, the geometry is kept fixed and exported to the off-design code linked to the simple ORC model presented in Figure 3-5. The results are presented in Figure 3-8. At constant turbine efficiencies (dotted lines in the figure), the cycle efficiencies are constant as the mass flow rate increases. The inlet conditions of the ORC system are subject to changes because the heat source (exhaust gas) conditions are unstable. Consequently, the assumption of constant turbine efficiency is deceptive. As can be seen in Figure 3-8, the cycle thermal efficiency increases with the working fluid mass flow rates. For R245fa, the cycle thermal efficiency increases from 5.65% to 7.3% (1.65% variation) as the mass flow rate increases from 0.05 Kg/s to 0.3 Kg/s. The maximum variation of R123, NOVEC 649 and R1233zde are 1.52%, 1.43% and 1.5%, respectively.

Therefore, the assumption of constant turbine efficiency for different working fluids and various operating condition is highly inaccurate as proved in Figure 3-7andFigure 3-8.

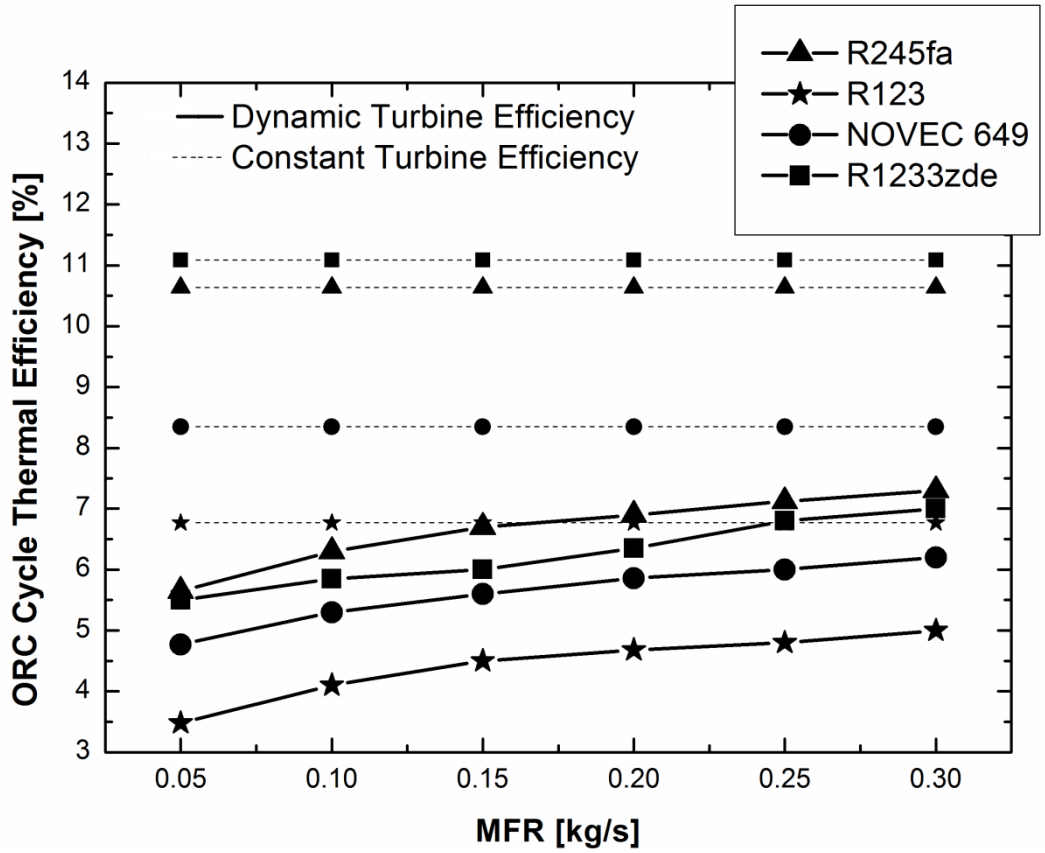

Figure 3-8: Thermal efficiency at constant and dynamic turbine performance for different working fluids at various mass flow rates.

3.3.8 ORC–Engine Powertrain with Fixed and Variable Geometry Turbines

In this project both FGT and VGT configurations were investigated early on for potential implementation with FGT being implemented not because of higher relative merit but because of its relative simplicity of implementation, despite the VGT turbines superior performance as will become apparent in the following pages.

The proposed integrated powertrain model is schematically presented in Figure 3-4. To explore the effects of the turbine on engine performance, the engine model is calibrated at three load/speed operating points as follows: optimum BSFC engine operating point (P1), maximum engine torque (P2) and maximum engine power (P3). Table 3-4 briefly presents the engine simulation values regarding fuel consumption and exhaust gas conditions.

The exhaust gas conditions at the three selected operating points are fed into the simple ORC model.

Table 3-4: Presentation of the Engine Simulation Values

Parameters	P1	P2	P3
Engine Speed [rpm]	1400	1500	2301
Torque [N.m]	440	1108.2	858.2
Power [kW]	69.4	173.98	186.7
Exhaust Temperature, C	338.6	474.8	512
Exhaust Mass Flow Rate [Kg/s]	0.1533	0.2224	0.5194

The optimisation algorithm explained in Chapter 5 is applied to design and optimise the turbine at engine operating point P3. P3 is selected as the design point due to itshigh exhaust waste heat content, which can potentially lead to high inlet pressure and temperature for the turbine. After this process, the optimised geometry is then exported to the off-design code (Chapter 5) to generate turbine maps. R245fa is selected as the working fluid for the FGT and VGT becauseit presents a high thermal efficiency (Figure 3-8) and is also considered a dry fluid, which is favourable for avoiding fluid droplets at the turbine blades. The optimised turbine geometry is presented inTable 3-5. Figure 3-9 shows the nozzle vanes positions for closed, medium and fully open arrangements. The nozzle position is expressed by the turbine throat area, where 0.3 corresponds to 30% opening and 1 corresponds to 100% opening.

Table 3-5: Turbine optimised geometry

Parameter	Value
Diameter d2 (mm)	105
Diameter d3 (mm)	81
Diameter d4 (mm)	77
Diameter d5 (mm)	38
Diameter d_{5,tip} (mm)	6.6
Diameter d_{5,hub} (mm)	15.4
Blade height b4 (mm)	3.8
Blade height b5 (mm)	22.6
Number of rotor blades	16
Reaction (–)	0.41
Specific speed, Ns (–)	0.486
Total to static efficiency	75.8
Turbine power output, KW	18.15

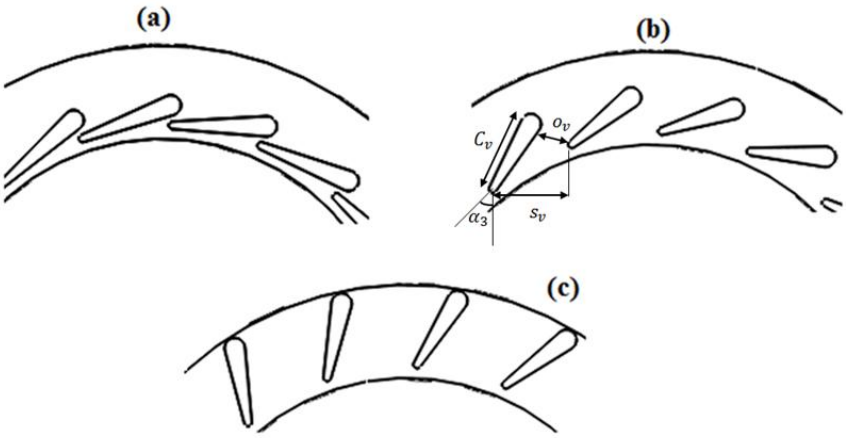

Figure 3-9: Radial-inflow turbine with different stator positions (VGT)

Figure 3-10 and Figure 3-11show the impact of the nozzle positions on ORC efficiency and turbine efficiency, respectively, under various engine conditions. As the nozzles are closed (moving towards 0.3 from an initial value of 1.0), the expander's total to static isentropic efficiency initially increases until it reaches its peak and then decreases. This trend holds for the three engine operating pointstested. Similarly, the ORC thermal efficiency follows the trend of the turbine efficiency qualitatively but not quantitatively. In fact, the VGT position affects the organic fluid mass flow, which seems to affect the efficiency of the heat exchanger (evaporator). Finally, the maximum ORC thermal efficiency is a trade-off between the efficiencies of the evaporator and the expander, while the same trend can be observed for the net power of the ORC system (Figure 3-12).Another observation is the superior advantages of P3 compared to P1 and P2. This is due to the higher exhaust mass flow rate which is 133% greater than that in P2. As a result, the cycle efficiency and net power (Figure 3-10 and Figure 3-12) are significantly better with P3. Similarly, the expander efficiency (Figure 3-11) is higher at P3 due to the higher mass flow rate and temperature at the inlet.

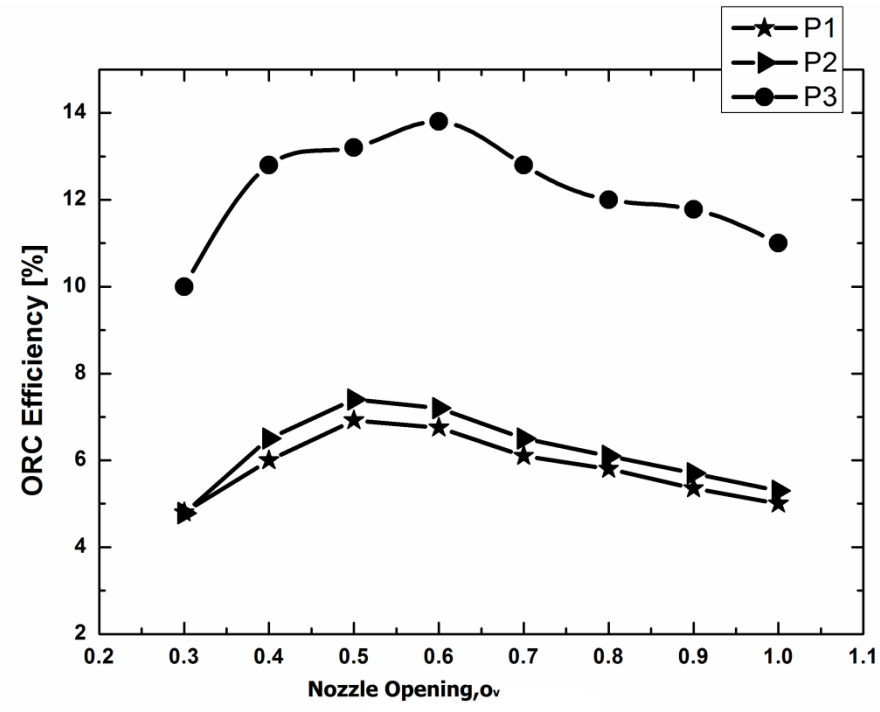

Figure 3-10: ORC thermal efficiency at different nozzle positions for the three engine's operating points.

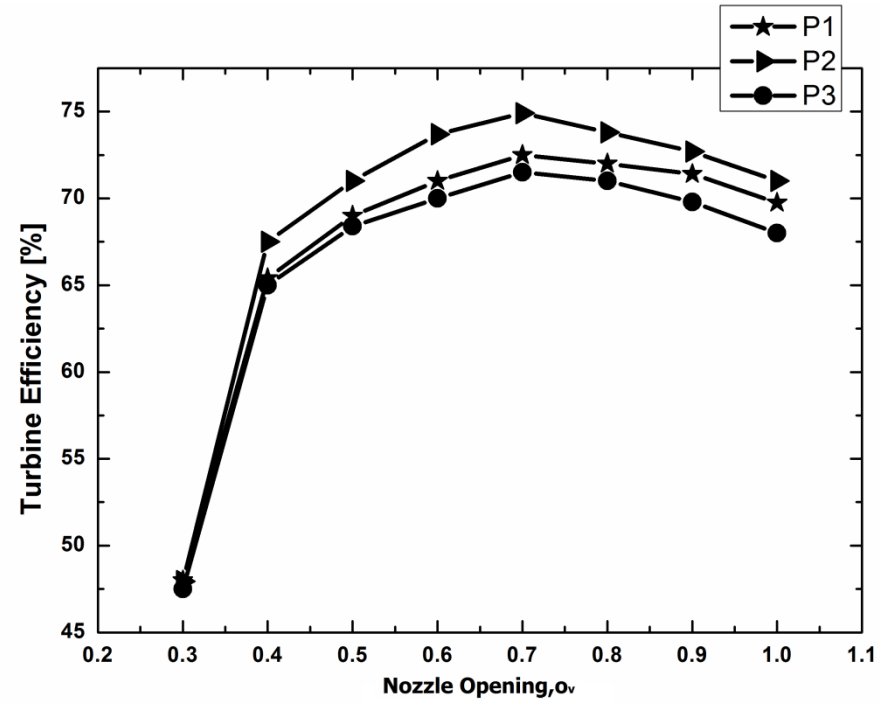

Figure 3-11: Expander efficiency at different nozzle positions for the three engine's operating points.

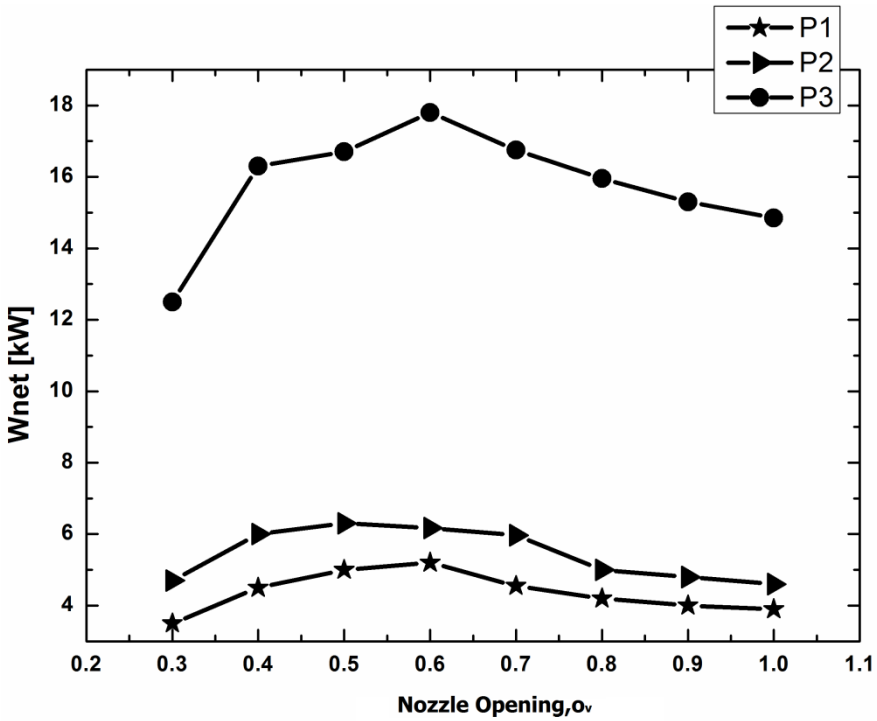

Figure 3-12: Cycle at different nozzle positions for the three engine's operating points.

Figure 3-13 illustrates the T–S diagrams for the three (P3 is similar to P2) operating points at the optimum nozzle position for ORC efficiency. As the engine load and the speed are increased, more exhaust heat energy is available due to the almost constant organic fluid mass flow and, therefore, superheating is increased. Although superheating is important in ensuring the full evaporation of the organic fluid, excessive superheating, as that obtained at operating point P2 (or P3 as it presents similar thermodynamic points), is detrimental to ORC efficiency becauseit contributes to condenser load. Superheating can be decreased by increasing the organic fluid mass flow rate. Additionally, the turbine power is proportionally related to the increase in mass flow rate, which means that increasing the organic fluid flow rate can only be beneficial in the final ORC efficiency. The latter indicates that in the hypothetical case of a variable flow rate ORC system, a variable geometry expander can potentially provide even better results under all operating points than the fixed flow rate ORC system.

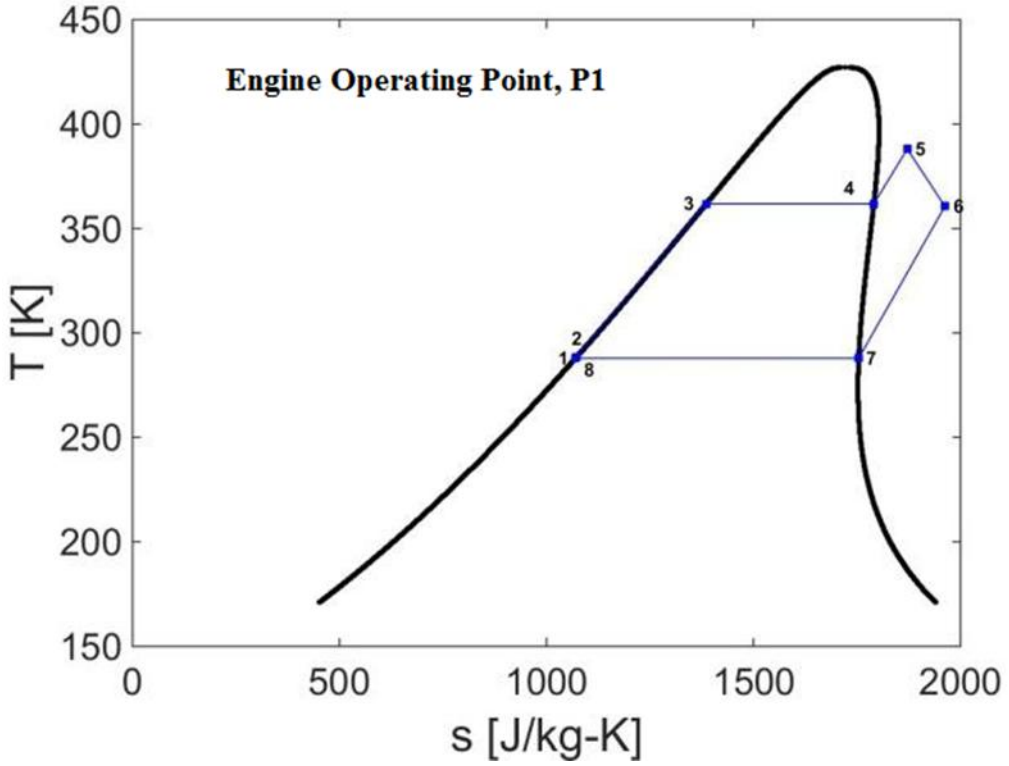

Figure 3-13: T–sdiagram of the ORC at engine point P1.

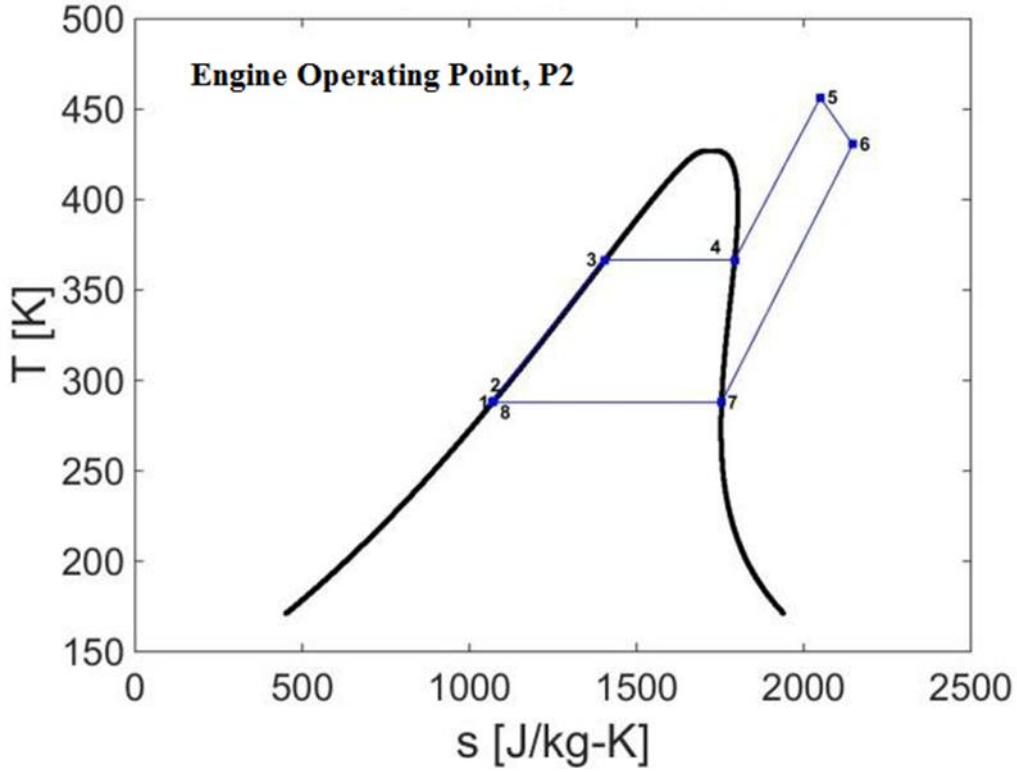

Figure 3-14: T–sdiagram of the ORC at engine points P3.

The VGT achieves ORC efficiency benefits compared to the fixed geometry expander even under a fixed organic fluid mass flow. Figure 3-15 and Figure 3-16 present the impact of the VGT on ORC efficiency and ORC net power, respectively, compared to a FGT at optimum conditions. The VGT achieves high ORC efficiency and net power at all engine points, with a minimum improvement of 1.3% at P1, and a maximum improvement of 2.7% at P3. In addition, at high loads, the extra power of the VGT technology compared to the FGT is nearly 3 kW, while the ORC efficiency exceeds 12%, which appears in most studies to be the upper limit performance of an ORC system.

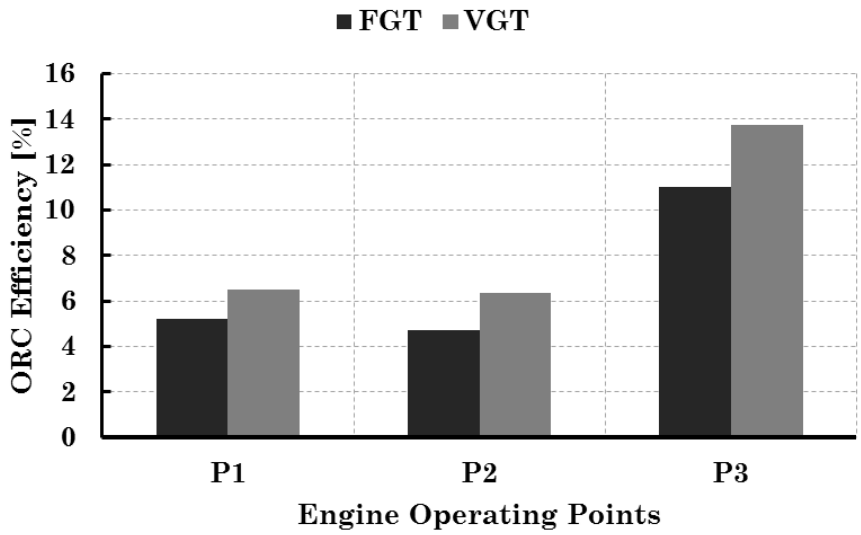

Figure 3-15:Comparison between fixed and variable geometry turbines on ORC efficiency.

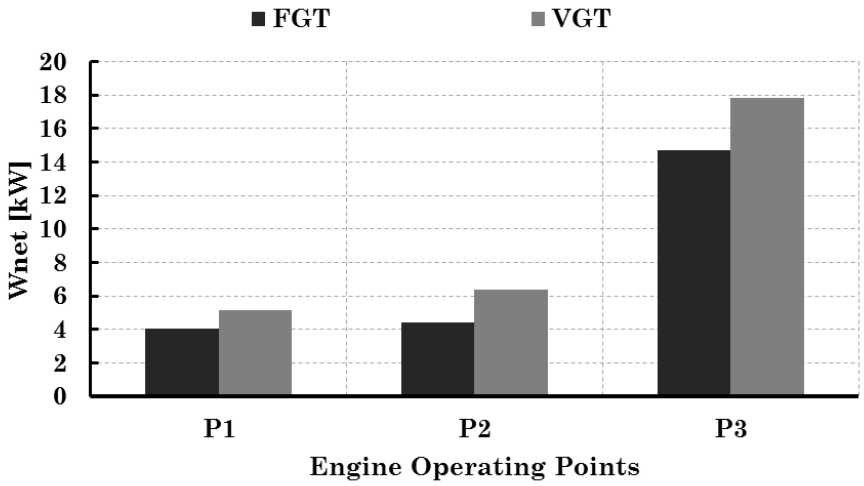

Figure 3-16: Comparison between fixed and variable geometry turbines on ORC power.

The implementation of an ORC system in the ICE's powertrain can improve powertrain power, fuel consumption and emissions. One of the targets of this section is to explore the potential for improvement of the ORC powertrain when a VGT is implemented. Figure 3-17 presents the improvement in powertrain power due to the ORC system with and without the VGT technology. At maximum engine power, the powertrain power is increased by 15 kW (4.5% increase), while the implementation of a VGT technology provides an additional 1% increase in powertrain power (transmission losses are ignored as this is a feasibility investigation). At the other operating points, the VGT shows an improvement in ORC powertrain power from 0.9% to 1.2% compared to the FGT.

The main purpose of WHR is to improve engine fuel consumption. Figure 3-18 shows the percentage of powertrain BSFC improvement due to the ORC system. In general, the BSFC can be improved by up to 4.2% with a FGT and over 5% when a VGT is implemented.

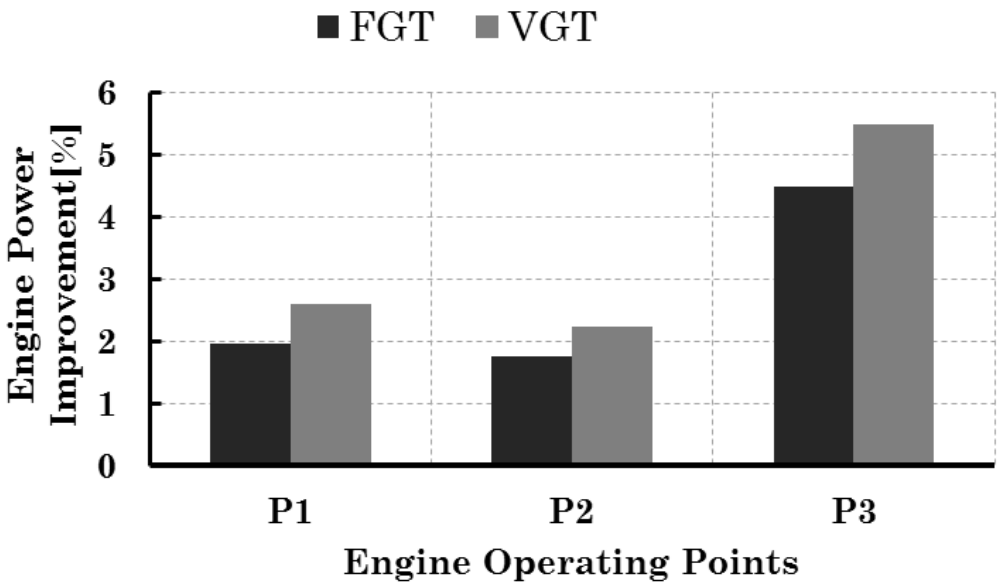

Figure 3-17: Comparison between fixed and variable geometry turbines on engine power.

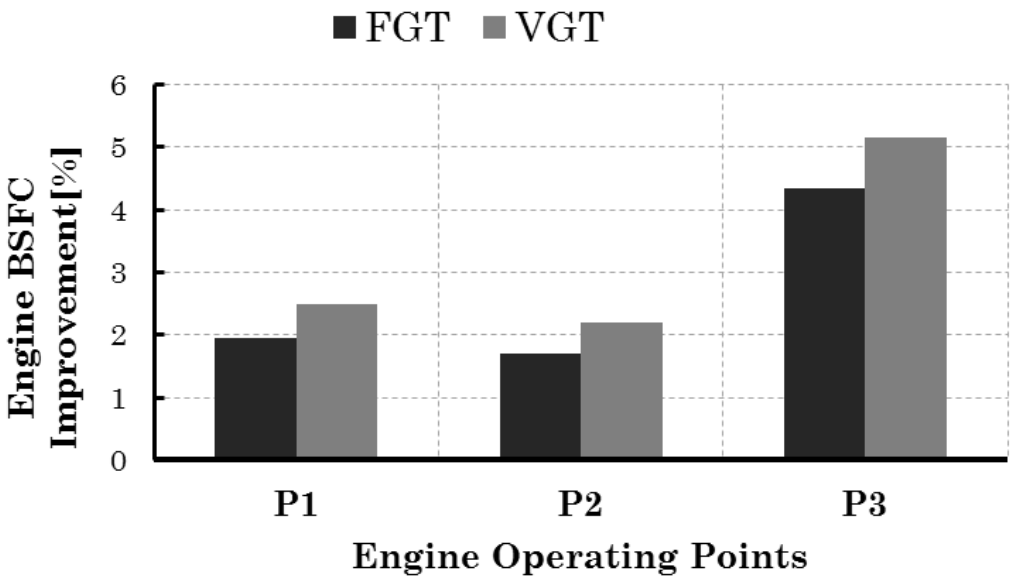

Figure 3-18: Comparison between fixed and variable geometry turbines on engine BSFC.

3.3.9 Effect of an ORC-WHR System on Diesel Engine Fuel Economy

Given that the gas–oil heat exchanger is the link between the ICE and the ORC system, the model presented in Figure 3-2 is applied. This section presents the relationship between the various parameters of the heat exchanger in terms of engine performance, backpressure and fuel consumption. The effect of the WHR system's weight is also explored. In this section, the other screened working fluids are selected, namely, NOVEC649 and R1233zde.

The relationship between the exhaust backpressure at the heat exchanger exit and the heat exchanger length are provided by the industrial partner (Entropea Labs) on the basis of their CFD results.Figure 3-19clearly shows that increasing the heat exchanger surface area leads to increased recovered heat. However, this increase is achieved at the expense of high exhaust backpressure and WHR system weight. A high backpressure results in high fuel consumption, as shown in Figure 3-20. As the exhaust backpressure is increased, the engine must consume more fuel to maintain the same engine power output, which leads to high exhaust temperature and slightly low exhaust mass flow. A high WHR system weight indicates a high available

exhaust enthalpy, which can potentially increase the ORC system efficiency. Meanwhile, a high backpressure corresponds to a long and heavy heat exchanger, which can significantly affect the power-to-weight ratio of the vehicle. Figure 3-19 compares the two fluids considered in terms of the change in exhaust gas backpressure and extracted thermal energy from the exhaust gases or varying heat exchanger surface area. The extracted heat from increasing the heat exchanger length is increasingly diminished at the expense of the backpressure as the ΔT between the exhaust gases and the thermal oil approaches zero. This behaviour is observed for both fluids. However, the ORC that employs R1233zde can extract more energy before reaching its plateau. This outcome can be explained by Figure 3-21 and Figure 3-22. The temperature profile of the thermal oil for the R1233zde configuration follows the exhaust gases more closely (a large ΔT between the inlet and the outlet and a small mass flow rate). Thermodynamically, the ORC cycle that employs R1233zde is more efficient, meaning that it generates more power for the same heat input. Consequently, for the same ORC power output, R1233zde would require a smaller heat exchanger. Alternatively, for the same heat exchanger length, its temperature profile allows the extraction of more heat.

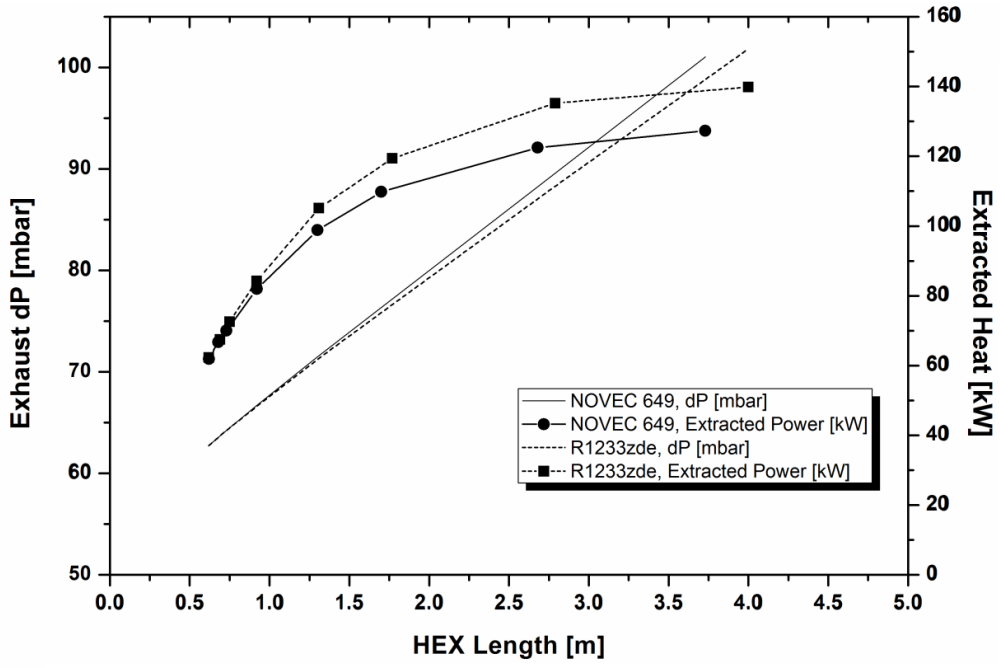

Figure 3-19: Effect of thermal oil heat exchanger length on exhaust pressure drop and absorbed heat for both tested fluids.

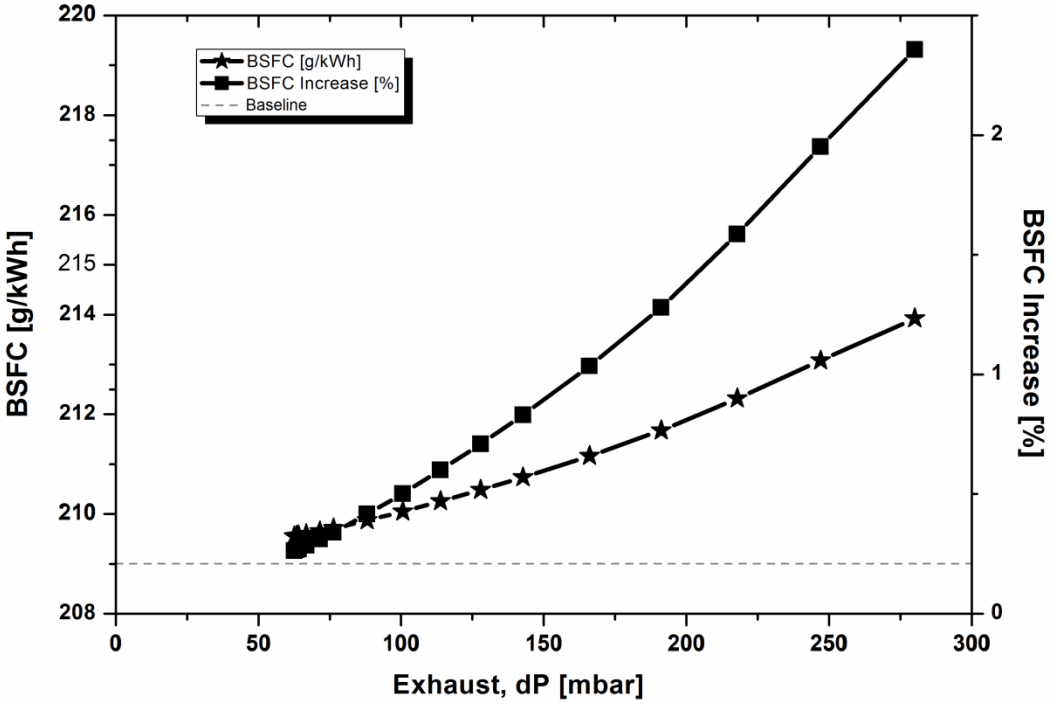

Figure 3-20: Effect of exhaust backpressure on engine BSFC at the maximum engine load and speed conditions.

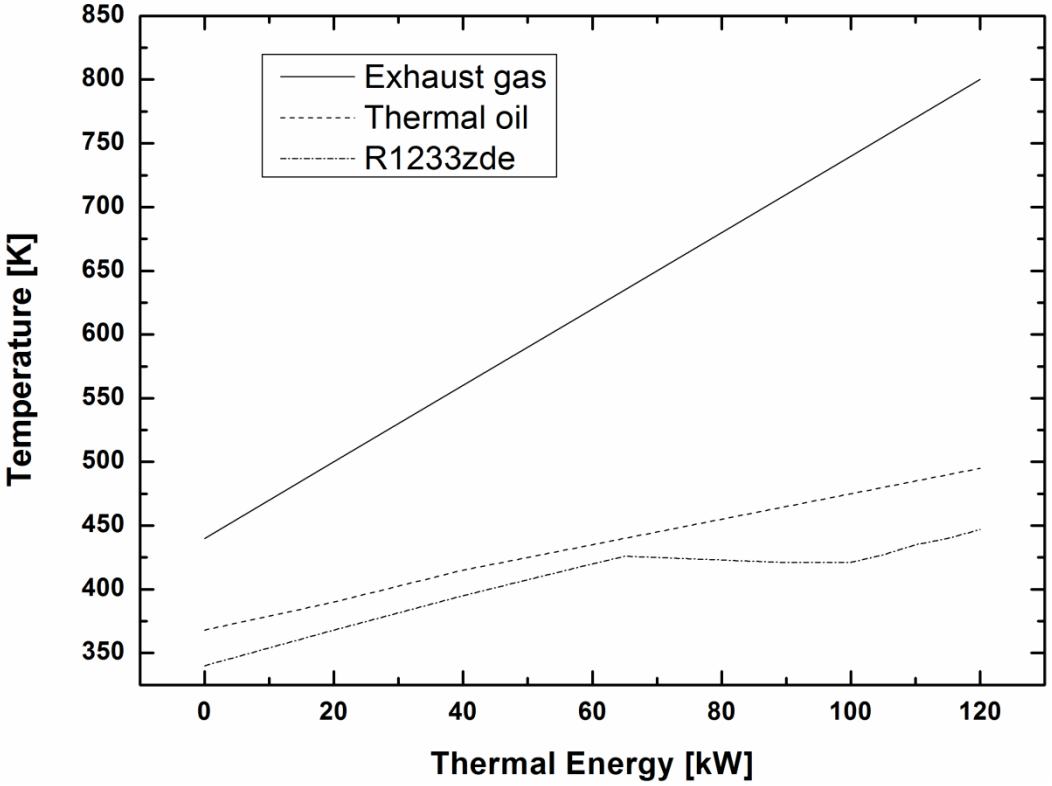

Figure 3-21: Temperature profile of R1233zde.

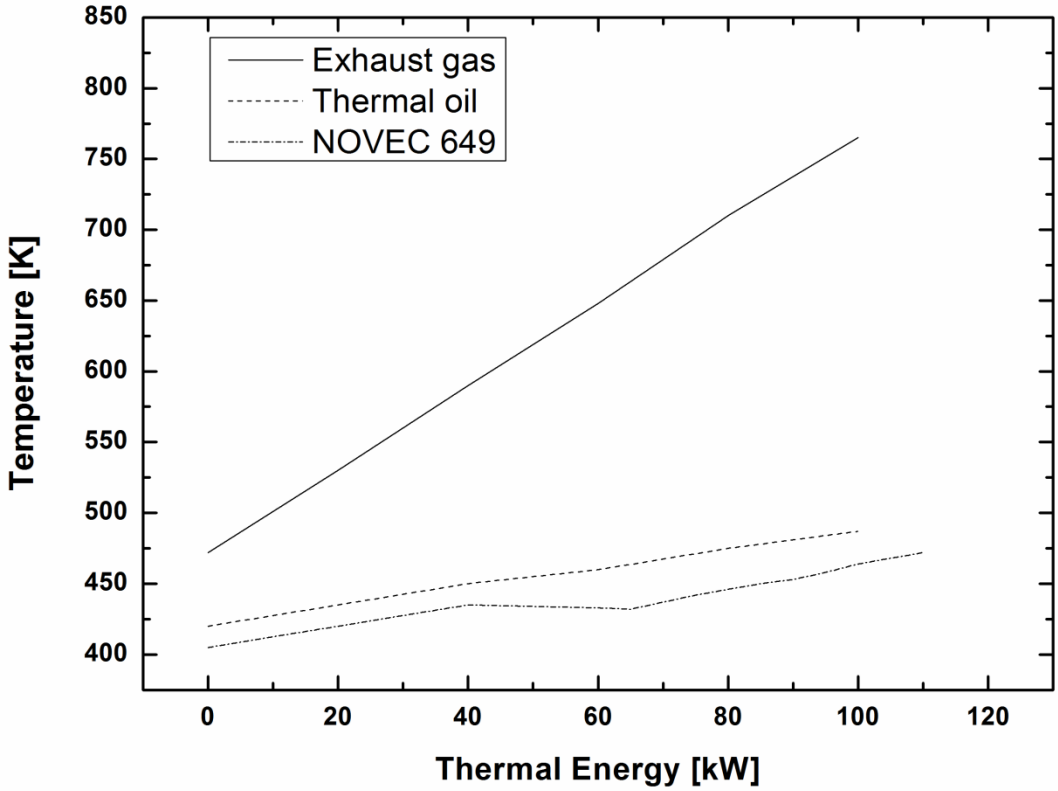

Figure 3-22: Temperature profile of NOVEC649.

Figure 3-23 presents the effect of ORC net power as a function of exhaust backpressure on powertrain power. The relationships between the ORC and the powertrain powers against exhaust backpressure are expressed in equations (3-7)and (*3-8*).

$$W_{net} = W_{turb} - P_{oil\ pump} - P_{working\ \ fluid\ \ pump} \quad (3\text{-}7)$$

$$P_{powertrain} = W_{net} + P_{engine} \quad (3\text{-}8)$$

At low exhaust backpressure values, a 10mbar increase in exhaust backpressure results in a significant increase in ORC power output of the order of 5kWe. However, at higher exhaust backpressure values a 10mbar increase in exhaust backpressure results in a 1kWe increase in the ORC net power output. Figure 3-23 depicts the powertrain power output as a function of exhaust backpressure. Similar to the ORC net power case, powertrain power increases at low backpressure conditions, while a plateau is reached at high backpressure values.Atextremely high backpressure values, the powertrain power is expected to drop as the engine power drops.

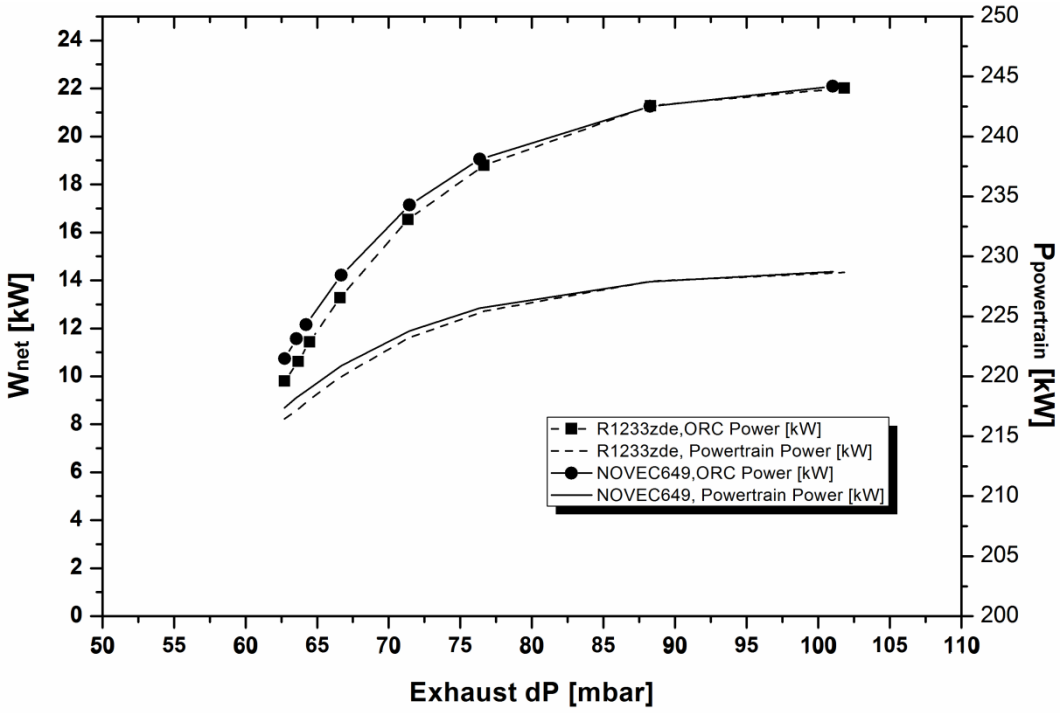

Figure 3-23: Effect of thermal oil heat exchanger eexhaust pressure drop on ORC net power and cumulative powertrain power.

An ORC system is not only an additional power-assisted device but can also assist the powertrain fuel consumption. The implementation of an ORC system in powertrain has both negative and positive aspects in terms of fuel consumption. Figure 3-24 illustrates the negative effect of exhaust backpressure due to the thermal-oil heat exchanger length and the positive impact of the ORC system on engine BSFC using equation (3-9).

$$BSFC = \frac{engine\ fuel\ consumption}{3600\ P_{powertrain}} \tag{3-9}$$

As exhaust backpressure increases, the rate of the extracted heat from the thermal-oil heat exchanger decreases, which is depicted by the rate of fuel consumption of the integrated system. Furthermore, different fluids have a small but not negligible effect on fuel consumption, especially under low exhaust backpressure conditions. Finally, further increase of the thermal-oil heat exchanger size is not expected to be beneficial tothe fuel consumption of the integrated system, as the effect of the exhaust backpressure on fuel

economy is more important to the small amount of additional extracted heat.

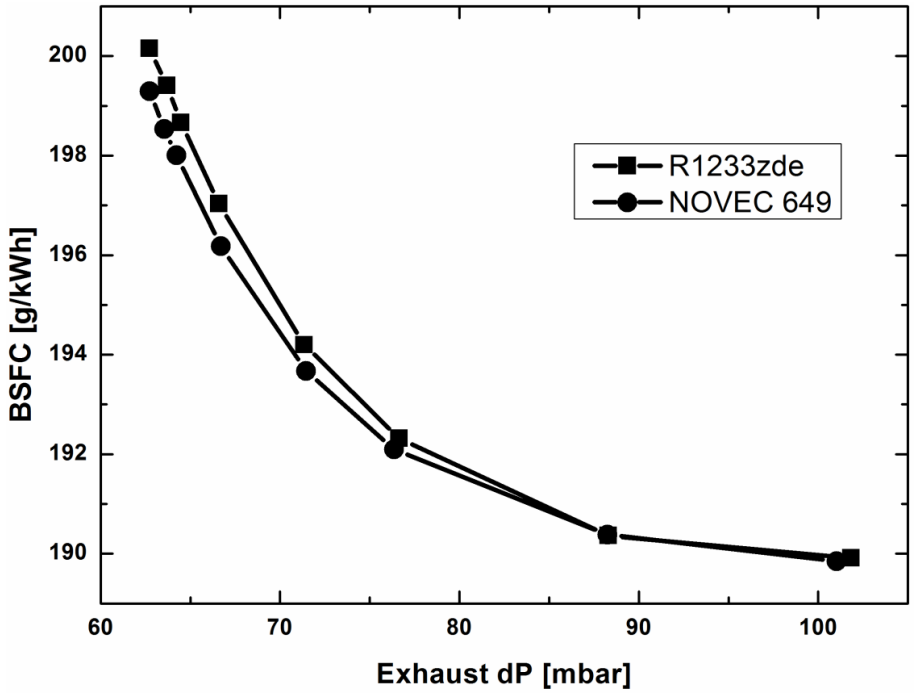

Figure 3-24: Relationship between thermal oil heat exchanger exhaust pressure drop and powertrain fuel consumption.

Weight is another important parameter in selectinga suitable WHR system. A high-power WHR system is expected to weigh more compared to a less powerful one. However, most studies deal only with the thermodynamic characteristics of the WHR system,ignoring the additional weight. In this study, the weight of the WHR system can be calculatedand is assumed to consist of the thermal-oil heat exchanger and the ORC system weight. The weight of the thermal-oil heat exchanger (i.e. STHE) can be calculated for varying surface areas using equation (3-10). The ORC system weight is determined by adopting the empirical equation, equation (3-11), reported in a previous study of Usman et al.[229].

$$Y_{\text{thermal}\ -\text{oil STHE}} = \rho_{oil} V_{metal} \tag{3-10}$$

$$\mathrm{Y_{ORC}} = 14.641\,\mathrm{X_{ORC}} + 40.087 \tag{3-11}$$

X_{ORC} is the ORC system power in kW, and Y_{ORC} is the ORC system weight in Kg. Figure 3-25 illustrates the relationship between the weight and the power of a WHR system considering the thermal-oil cycle. As the weight of the WHR system is increased, the power output is almost linearly increased until 18 kWe, at which the weight is increased more compared to the additional power benefit. The latter is expected becausethe heat exchanger should be longer and heavier as the temperature difference between the hot and cold flows is decreased. The same figure shows that the selection of working fluids has anacceptably low impact on the total WHR system.

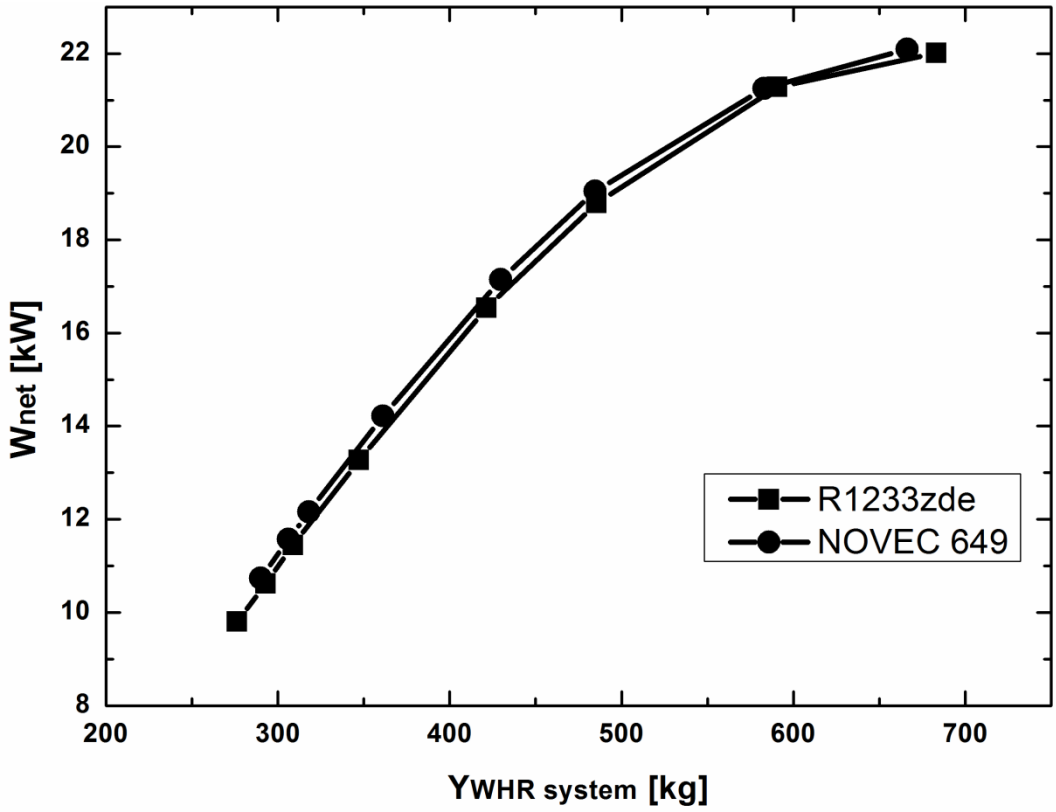

Figure 3-25: Relationship between WHR system weight and power output.

Although Figure 3-25 depicts the relationship between the weight and power of the WHR system, it does not present the optimum weight-to-power ratio for the proposed WHR system. This ratio is illustrated by Figure 3-26, which presents the power-to-weight ratio as a function of the thermal-oil heat exchanger length based on equation (3-12).

$$W_{net}/Y_{WHR} = \frac{W_{net} + Y_{ORC}}{Y_{\text{thermal }-\text{oil STHE}}} \quad (3\text{-}12)$$

The maximum power-to-weight ratio is given for a short thermal-oil heat exchanger, and the further increase of the heat exchanger length results in a power-to-weight ratiodrop. However, the optimum heat exchanger length in terms of the power-to-weight ratio can result only in an average benefit of 4.6% on fuel consumption and 5% on additional power output for both fluids. Meanwhile, for a slightly heavier WHR system that achieves a ratio of 2 kWe/kg, the averaged benefit on fuel consumption for both fluids is 8% and the powertrain power is increased by 9%.

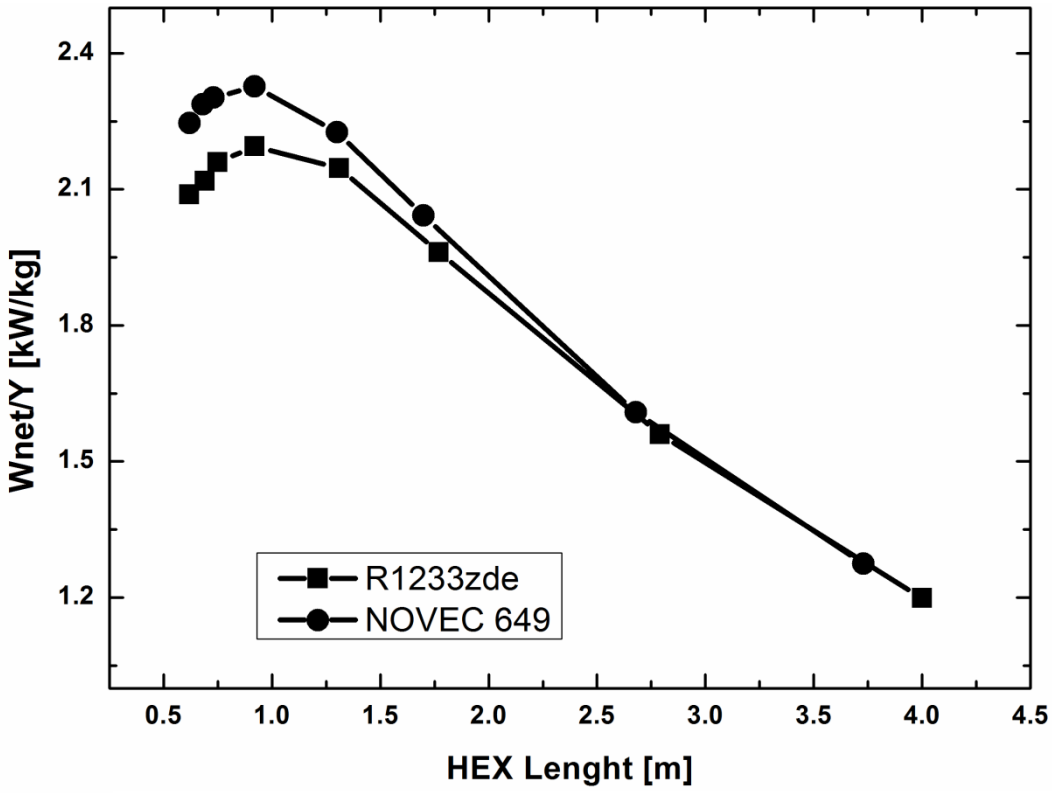

Figure 3-26: Effect of thermal oil heat exchanger length on power-to-weight ratio of the WHR system.

The above results indicate that the design of the ORC system is a trade-off between the effect of additional power, fuel consumption benefit and device weight. The optimum ORC characteristics also depend on the application.In the case of on-highway vehicles, the weight increase may be a more

important parameter under real driving engine conditions in the design of the WHR system than under off-highway or stationary applications.

3.4 Conclusion

Two ORC-radial inflow turbine models were built to evaluate the integration between the ORC-ICE powertrains. The results showed that VGT presented better ORC efficiency and net power compared to FGT. In addition, the results also proved the invalidity of the common assumption of the constant expander efficiency. The results showed that the ORC efficiency changed by a minimum of 1.43% between the constant and dynamic turbine efficiency models.

The results also showed that increasing the heat exchanger surface area leads to higher heat recovered at the expense of higher exhaust backpressure and higher WHR system weight. Moreover, the maximum power to weight ratio of a WHR system is not always the optimum in terms of fuel consumption improvement and additional power, as 10% worst power-to-weight ratio can give up to 42.5% additional benefit on fuel consumption and power increase of the ORC system.

The next chapter is an opening for the detailed turbine design, optimization and performance prediction presented in the following chapter. The next chapter explains the reasons beyond selecting the radial inflow turbine as the expansion machine for the current project. In addition, the turbine architecture and the overview of the novel design and performance methodology are presented.

Chapter 4 : Radial-Inflow Turbine

4.1 Introduction

A radial-inflow turbine is a work-producing machine that is used in a large range of applications. Radial turbines are differentiated from axial turbines by adapting a significant radius change from the rotor inlet to the rotor outlet [231]. Although axial turbines are more common due to their high efficiencies in large-size applications such as gas turbines, interest on radial turbines as expansion machines in ORC systems is increasingbecause of their ability to operate with low mass flow rates and high-pressure ratios. An extensive comparison between radial and axial turbines is presented in Chapter 2.

In conventional radial turbines, air is used as the working medium. Thus, it is assumed to bean ideal gas, either perfect or semi-perfect. This means that the specific heat capacity at constant pressure C_p is either constant or a function of temperature only. Organic fluids, which are much denser than air, are utilised in ORC turbines. Therefore, real gas equations of state (EoS) should be applied to evaluate the thermodynamic properties of the fluid at each station (fromvolute inlet to rotor exit). This makes the conventional design procedures, where the Mach relationships for ideal gas are applied, inapplicable. Consequently, a novel design procedure is required and this was implemented in this project and described in the present work. An optimisation technique is also integrated to reach the optimum performance of the machine. Importantly, a novel mean-line performance prediction methodology (MOC) is proposed to predict the turbine performance at various cycle operating points at the early stage of the project. The methodology's overview is briefly presented in Section 4.3.7 and more intensively in Chapter 5.

This chapter presents key and basic information onradial-inflow turbines. The method of selecting anappropriate expansion machine and the dimensional analysis are also discussed. In addition, the architecture of a radial-inflow turbine is discussed in detail to be used as reference for the succeeding chapters. The developed design methodology of radial-inflow turbines depends mainly on two groups: flow and loading coefficients and specific speed. These groups are discussed in the next sections.

4.2 Turbine Architecture

Figure 4-1 presents the full turbine stage. Radial-inflow turbines consist of three main components: volute, stator vanes and rotor blades. In some applications, a fourth component called diffuser (Figure 1-5) is added to recover the otherwise wasted kinetic energy at the rotor exit and convert it into static pressure. The flow firstly enters the volute and is accelerated due to the reduced cross-section area in the stream-wise direction from 360° at the inlet to nearly 0° at the exit. Moreover, the tangential component of velocity increases before entering the nozzle vanes due to the reduced cross-section area, and flow is distributed evenly around the periphery of the stator inlet. After leaving the volute, the flow enters the stator vane where the fluid is further expanded and turned to enter the rotor blades in the optimum direction with the necessary tangential velocity. Finally, the fluid enters the most critical component of the turbine, which is the rotor, where the fluid is further expanded, converting the kinetic energy of the fluid into shaft power. In the design process, the required outlet conditions should be specified. Therefore, the rotor is responsible for sizing the inlet and outlet of the component to efficiently expand the flow from certain inlet conditions to the required outlet conditions. Figure 4-2 presents a schematic meridional view of the turbine stage, and Figure 4-3 presents the h–s diagram through the turbine stage.

Turbine casings can take different forms depending on the application. The cross-sectional area can be either constant, in which the casing is called a collector, or reduced, in which case the casing is called a volute(Figure 4-4). In the former, the flow velocity is very low, and the main aim of the collector is to collect the flow and deliver it to the downstream component without increasing the velocity. Such form is usually used in gas turbine applications. The latter has a spiral shape and is used in turbochargers to introduce some swirl to the flow.

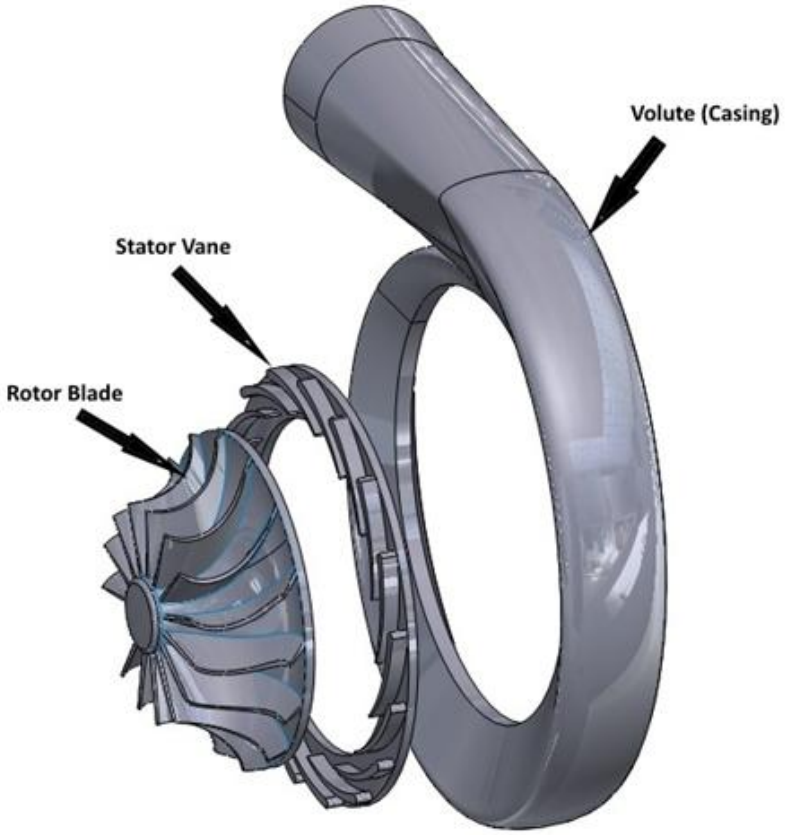

Figure 4-1: Architecture of the radial turbine stage.

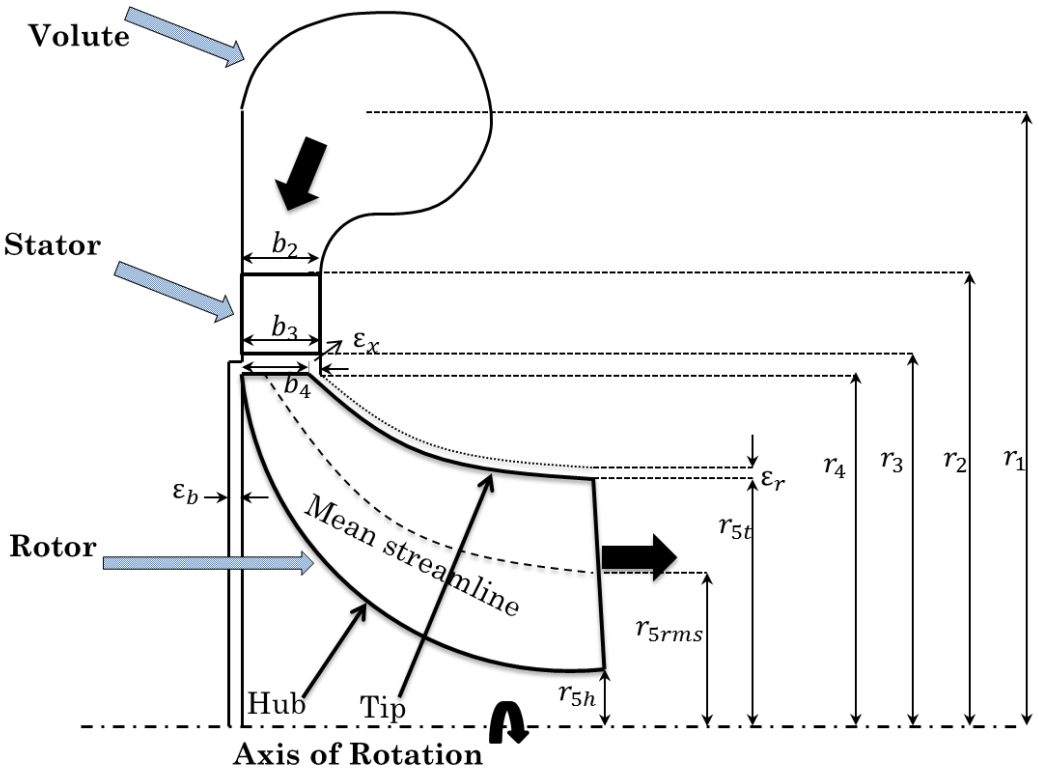

Figure 4-2: Meridional view of the turbine stage.

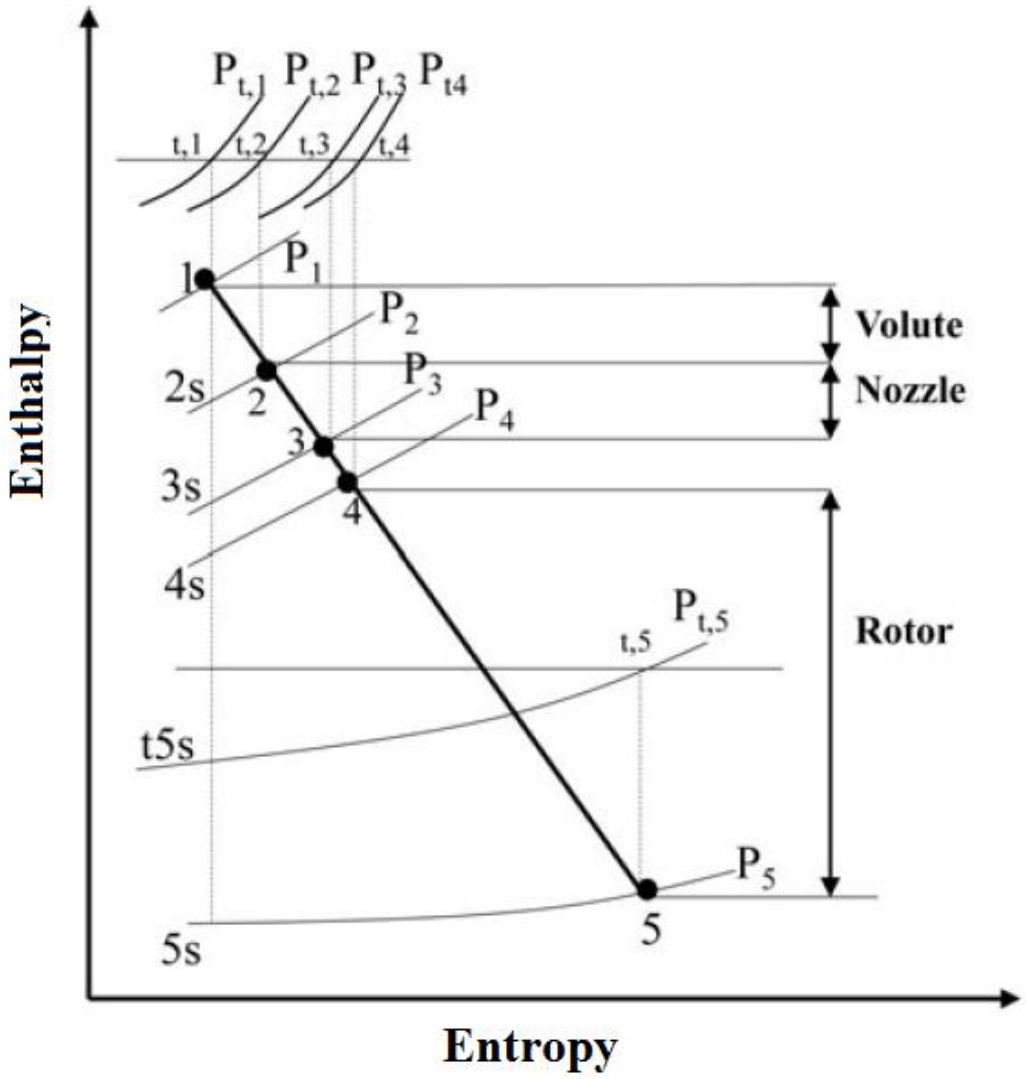

Figure 4-3:Entalpy–Entropy diagram of the turbine stage.

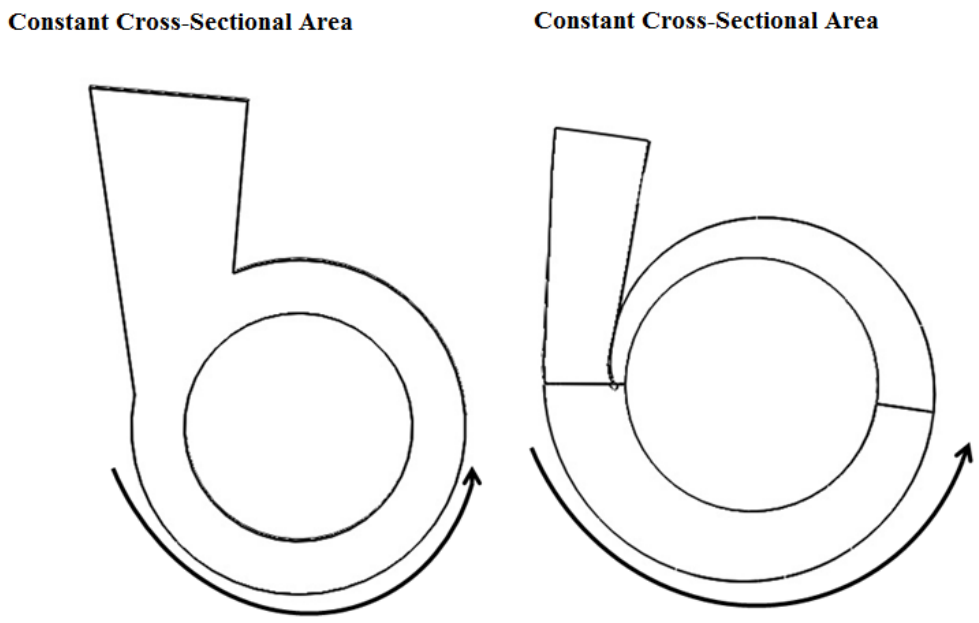

Figure 4-4:Configurations of the turbine casing.

A stator or nozzle consists of an annular ring of vanes, which set the angle of approach of the working fluid to the rotor [231]. The main function of the nozzle vanes is to guide the flow, accelerate it, and remove any circumferential non-uniformity. The presence of stator vanes depends on whether a collector or volute is used in the upstream component. In the case of a collector, stator vanes are mandatory to turn, accelerate and deliver the flow to the rotor at the correct angle. In some applications, such as turbochargers, stator vanes are omitted because of cost and size constraints,in which case, the volute is spiralled. In addition to the presence of stator vanes, the shape of the turbine casing dictates the shape of the vane nozzles. They can be either cambered or un-cambered, as shown in Figure 4-5. Cambered vanes are usually applied when the nozzle ring is preceded by a collector; therefore, cambered vanes are required to provide the required swirl in the rotor inlet. Un-cambered vanes are utilised when they are preceded by a volute that introduces some swirl to the flow. In many current radial turbines, the stator vanes are un-cambered due to their design simplicity and low manufacturing cost. The expansion ratios of ORC turbines are usually high due to the low speed of sound of the organic fluids; therefore, a large swirl at the rotor inlet is required, which necessitates the utilisation of cambered vanes in the current work.

Figure 4-5: Configurations of stator vanes: cambered (left) and un-cambered (right).

Rotor is the most significant component in the turbine stage because work transfer occurs in this region. Two main concerns about the rotor of a radial turbine exist in turbo-machinery books. Firstly, the flow in the rotor is highly unsteady, 3Dand viscous. Secondly, bending stresses are usually high at the rotor's leading edge. The former can only be checked using advanced CFD analysis. The latter can be avoided by adopting invariably radial blades at the rotor inlet [232][233]. However, ORC turbines usually operate at low temperatures, which mean that bending stresses are less sensitive than those in conventional turbines. This enables the adoption of non-radial blades, as shown in Figure 4-6. Figure 4-7 shows that in non-radial blades, the tangential velocity at rotor inlet $C_{\theta 4}$ is higher, and hence a higher power output is achieved according to the Euler equation as presented in Chapter 5. A preliminary checking of stresses using mean-line modelling is possible, as discussed in the next chapter.

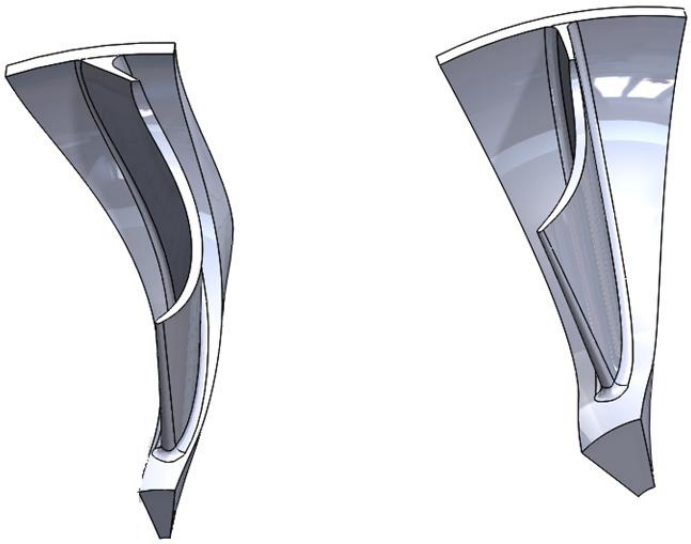

Figure 4-6: Non-radial (left) andradial turbine blades (right).

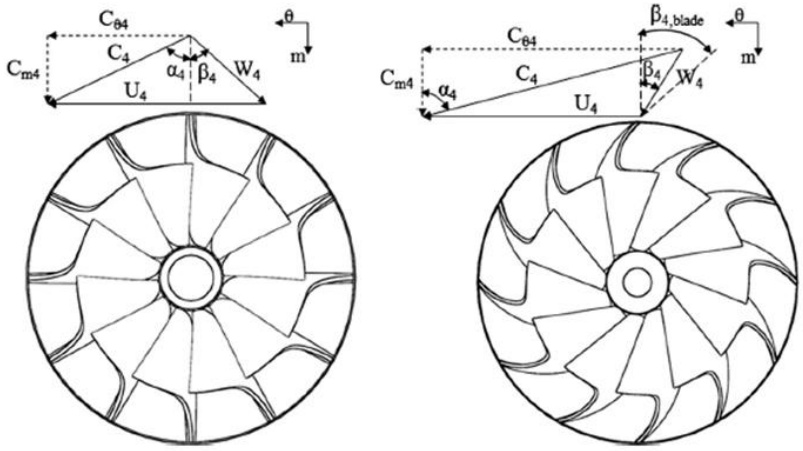

Figure 4-7:Velocity triangles of radial (left) and non-radial (right) blades [75].

4.3 Overall Performance of Radial-Inflow Turbines

Expansion machines can be evaluated, selected and compared based on a set of non-dimensional parameters. Several of these parameters can also be used to scale existing designs to different sizes. The non-dimensional parameters are isentropic efficiency η, specific speed (N_s), specific diameter (D_s), velocity ratio (v_s), degree of reaction (R) and flow (φ) and loading (Ψ) coefficients.

4.3.1 Total to Static Efficiency, η_{ts}

Total to static efficiency η_{ts} is a very important performance indicator. It is defined as the ratio between the actual and ideal works of the turbine stage, as expressed byequation (4-1)where the ideal work is limited by the static enthalpy at the exit. In some applications, part of the kinetic energy is lost at the turbine exit. Therefore, a diffuser is used to recover the kinetic energy. This condition is captured by the total to total efficiency η_{tt} equation as expressed byequation (4-2).

$$\eta_{ts} = \frac{h_{01} - h_{05}}{h_{01} - h_{5s}} \tag{4-1}$$

$$\eta_{tt} = \frac{h_{01} - h_{05}}{h_{01} - h_{05s}} \tag{4-2}$$

4.3.2 Specific Speed N_s and Specific Diameter D_s

The selection of anappropriate expansion machine depends mainly on the operating conditions of the application. However, these two non-dimensional parameters are functions of operating conditions only and can be applied to determine the optimum turbine for a specific application. They also indicate the required rotational speed and diameter of the rotor. The two parameters are related to the volumetric flow rate and the enthalpy drop across the turbine [231]. Their equations are presented in Section 2.3.3.

Balje [196]developed a performance chart for different expansion machines (Figure 4-8). For a radial-inflow turbine, N_s should lie between 30 and 300 (imperial units). Dixon and Hall [197]developed another correlation for turbo machinery devices only. As can be seen in Figure 4-9, N_s should lie between 0.5 and 0.9 (SI units) to fall within the radial turbine operating range. Watson and Janota [199] correlated turbine efficiency against specific speed and specific diameter, as can be seen in Figure 4-10. Peak efficiencies can be achieved when the specific speed lies in the range of 0.4–0.8 and the specific diameter lies in the range of 2.5–4.

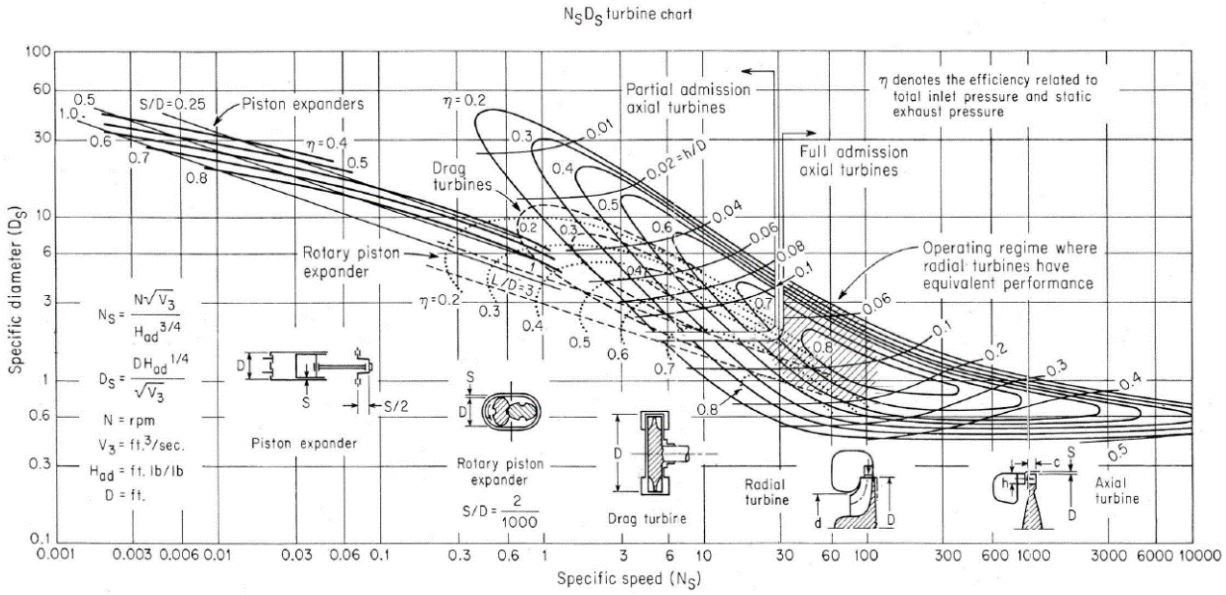

Figure 4-8: Expansion machines as functions of $N_s$and D_s[196].

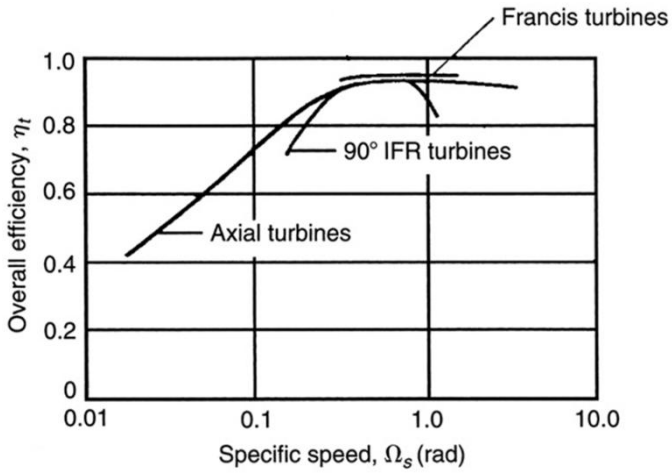

Figure 4-9:Turbomachines as functions of N_s[197].

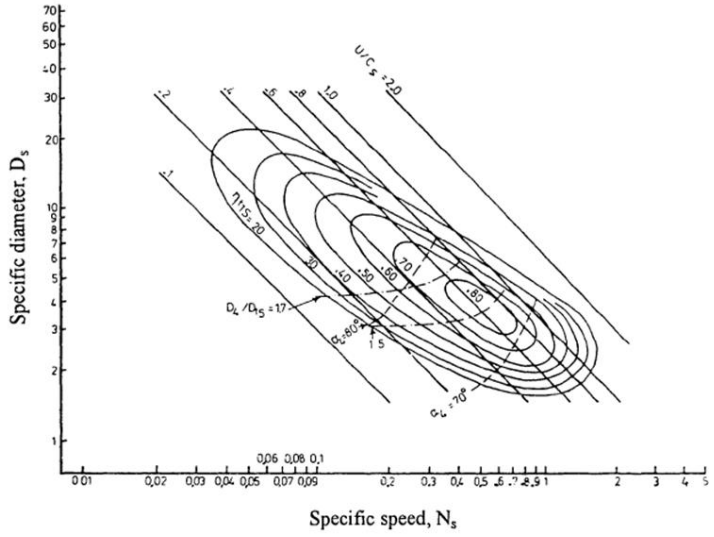

Figure 4-10: Radial turbine performance versus N_s[199].

4.3.3 Velocity Ratio, v_s

Velocity ratio is the ratio between the rotor blade speed and the spouting velocity, as expressed by equation (4-3). Spouting velocity $C_0$is the velocity obtained if the entire isentropic enthalpy drop is converted into speed, as expressed by equation (4-4).

$$v_s = \frac{U_4}{C_0} \tag{4-3}$$

$$C_0 = \sqrt{2\Delta h_{is}} \tag{4-4}$$

Dixon and Hall [197] recommended that for the best turbine efficiency, the velocity ratio should fall in the range $0.68 \leq v \leq 0.71$.

4.3.4 Degree of Reaction, R

Stage reaction is the ratio of static enthalpy drop at the rotor to the total enthalpy change across the stage, as expressed by equation(4-5). Aungier [234] suggested that the stage reaction shouldfall in the range of $0.45 \leq R \leq 0.65$ for enhancedturbine performance.

$$R = \frac{h_4 - h_5}{h_{01} - h_{05}} \tag{4-5}$$

4.3.5 Flow φ and Loading Ψ Coefficients

Flow and loading coefficients are extensively used in axial turbines [232]. Flow coefficient φ is a characteristic of the mass flow behaviour through the stage and defined as the ratio of the exit meridional velocity to the inlet blade speed. Loading coefficient Ψ is a measure of the work and loading of the stage. Equations(4-6)and (4-7) present the flow and loading coefficients, respectively.

$$\varphi = \frac{C_{m5}}{U_4} \tag{4-6}$$

$$\Psi = \frac{\Delta h_{act}}{U_4^2} \tag{4-7}$$

Rodgers[235] developed a performance chart that relates the efficiency of radial-inflow turbines to the flow coefficients (φ) based on the performance of 30 radial turbines, as depicted in Figure 4-11. Clearly, the optimum turbine performance lies in the range of 0.2–0.3. Chen et al. [232] suggested a chart that can be used as a guide in the selection of the optimum flow and loading coefficients (Figure 4-12). According to the figure, the peak efficiencies of radial-inflow turbines lie in the range of 0.2–0.3 for φ and 0.8–1 for Ψ.

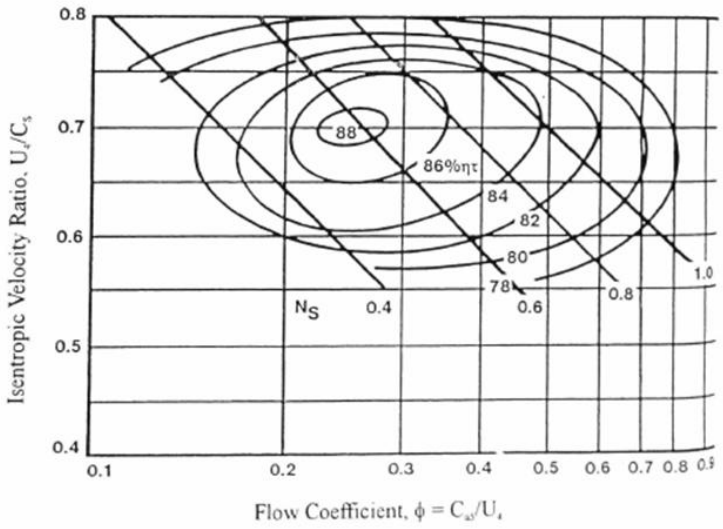

Figure 4-11: Performance of radial turbine versusflow coefficient [235].

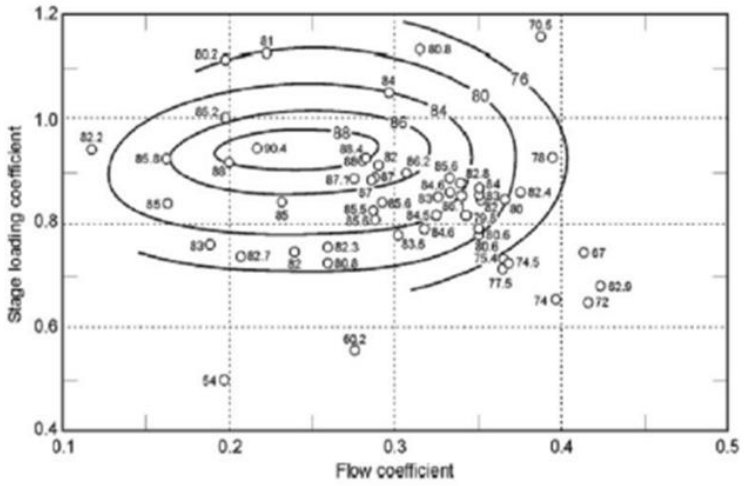

Figure 4-12: Performance of radial turbine versus φ and Ψ[232].

4.3.6 Selection of the Appropriate Expansion Machine

The advantages and disadvantages of both types of expansion machines and the speed and power ranges are explained in Chapter 2. This section is a case study for evaluating the data shown in Table 4-1,which are provided by Entropea Labs (the industrial partner), and eventually selecting the optimum expansion machine. The decision-making is based on two types of parameters: N_s and D_s,φ and Ψ. Astypes are dimensionless, the units of the variables must be consistent.

Table 4-1: Input Conditions of the Current Turbine

Variable	Value	Unit
$\boldsymbol{P_0}$	900	KPa
$\boldsymbol{T_0}$	471.5	K
$\boldsymbol{P_5}$	130	KPa
N	40,000	rpm
$\boldsymbol{d_{max}}$	52	mm
$\boldsymbol{\dot{m}}$	0.8	Kg/s
Fluid	NOVEC 649	-

Balje [196] stated that the volume flow rate Q, Equation (4-8), should be used in the rotor exit. However, only the exit pressure is provided in Table 4-1. To obtain the density at the turbine exit ρ_5, another variable should be known to apply the EoS. Given that the static pressure P_5 is equals to the isentropic static pressure P_{5s}, the isentropic conditions are applied rather than static ones. This is acceptable because the difference is insignificant, although this depends mainly on the boundary conditions and the type of working fluid. For the current conditions (Table 4-1), the difference between h_5 *and* h_{5s} is approximately 2.65% which is acceptably low.

$$\dot{Q_5} = \frac{\dot{m}}{\rho_5} \tag{4-8}$$

The required diameter should by identified to obtain the specific diameter, D_s, as expressed by equation (4-9). However, the exact value of the rotor diameter is not given by the industrial partner. Rather, the maximum allowable diameter is specified as shown in Table 4-1. Therefore, D_s is calculated for the minimum and maximum values of rotor diameter.

$$D_s = \frac{d_4 \Delta h_{act}^{0.25}}{\sqrt{Q}} \tag{4-9}$$

The second type of parameters, $\varphi \ and \ \Psi$, requires velocity values at the inlet and exit of the turbine, which are not available at the early stage of the project. However, Dixon and Hall [197] presented useful relationships between the two types of parameters, as shown in equations (4-10)and (4-11).

$$\varphi = \frac{1}{(N_s D_s^3)} \tag{4-10}$$

$$\Psi = \frac{1}{(N_s^2 D_s^2)} \tag{4-11}$$

The results of both pairs of parameters are depicted in Figure 4-13. The N_s values are 0.52 (SI system) and 68 (US system). D_s is plotted at two diameter and its values are 1.96 and 2.68. The second pair of parameters is calculated using equations (4-10) and (4-11). The results show that $\varphi = 0.254 \ and \ \Psi = 0.957$, which indicate that the intersection of the two parameters lies in the optimum turbine performance area.

However, the utilised charts are presented for air turbines only. Therefore, the developed guide, presented in Section 2.3.3,is also applied to confirm the final decision on the expander's type using organic expansion machines as depicted in Figure 4-14. Along with the advantages mentioned in Chapter 2, Figure 4-13andFigure 4-14(red dotted lines) nominate the radial-inflow turbine as the optimum expansion machine for the current application.

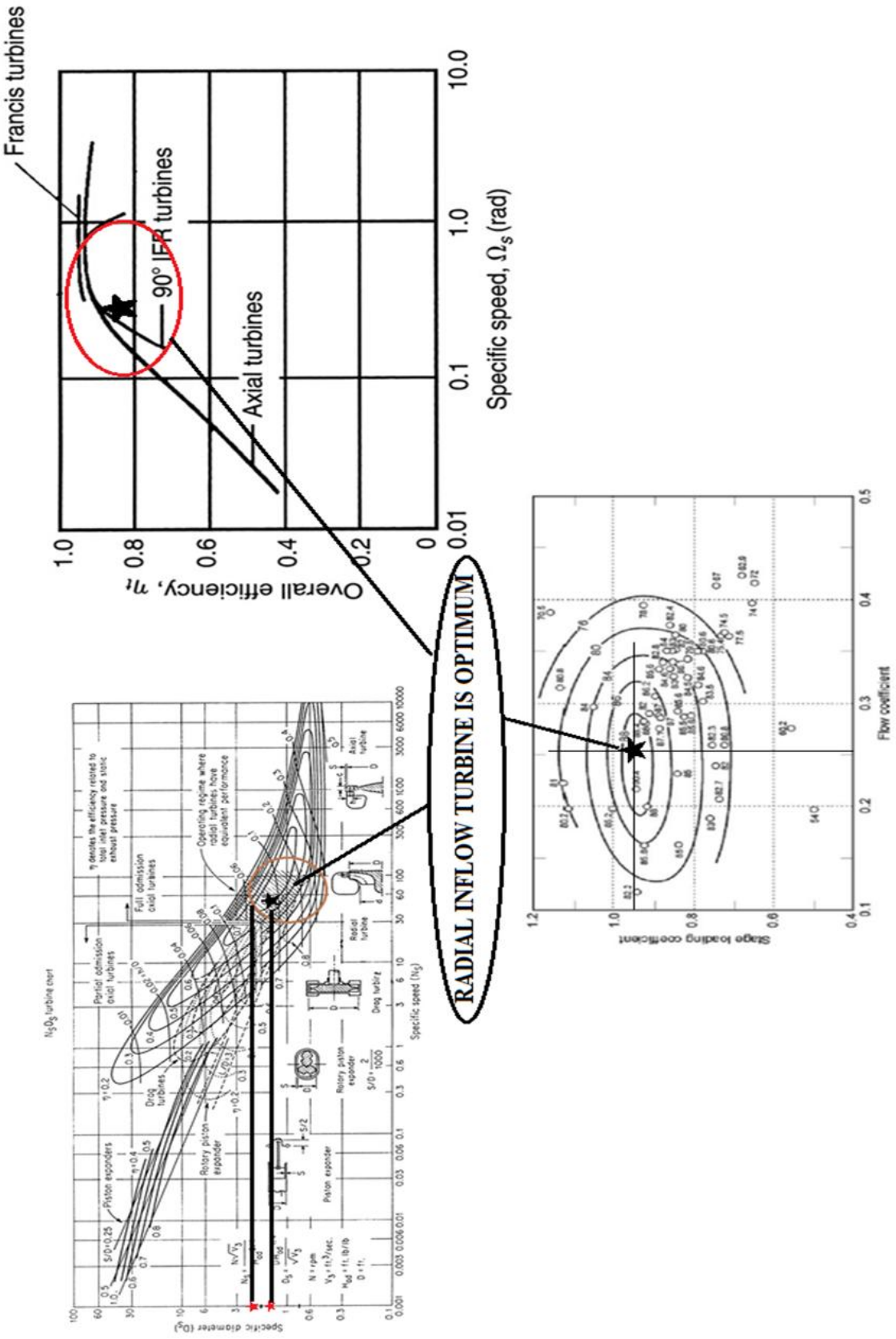

Figure 4-13:Location of the current expansion machine based on air turbine correlations [197][232][196].

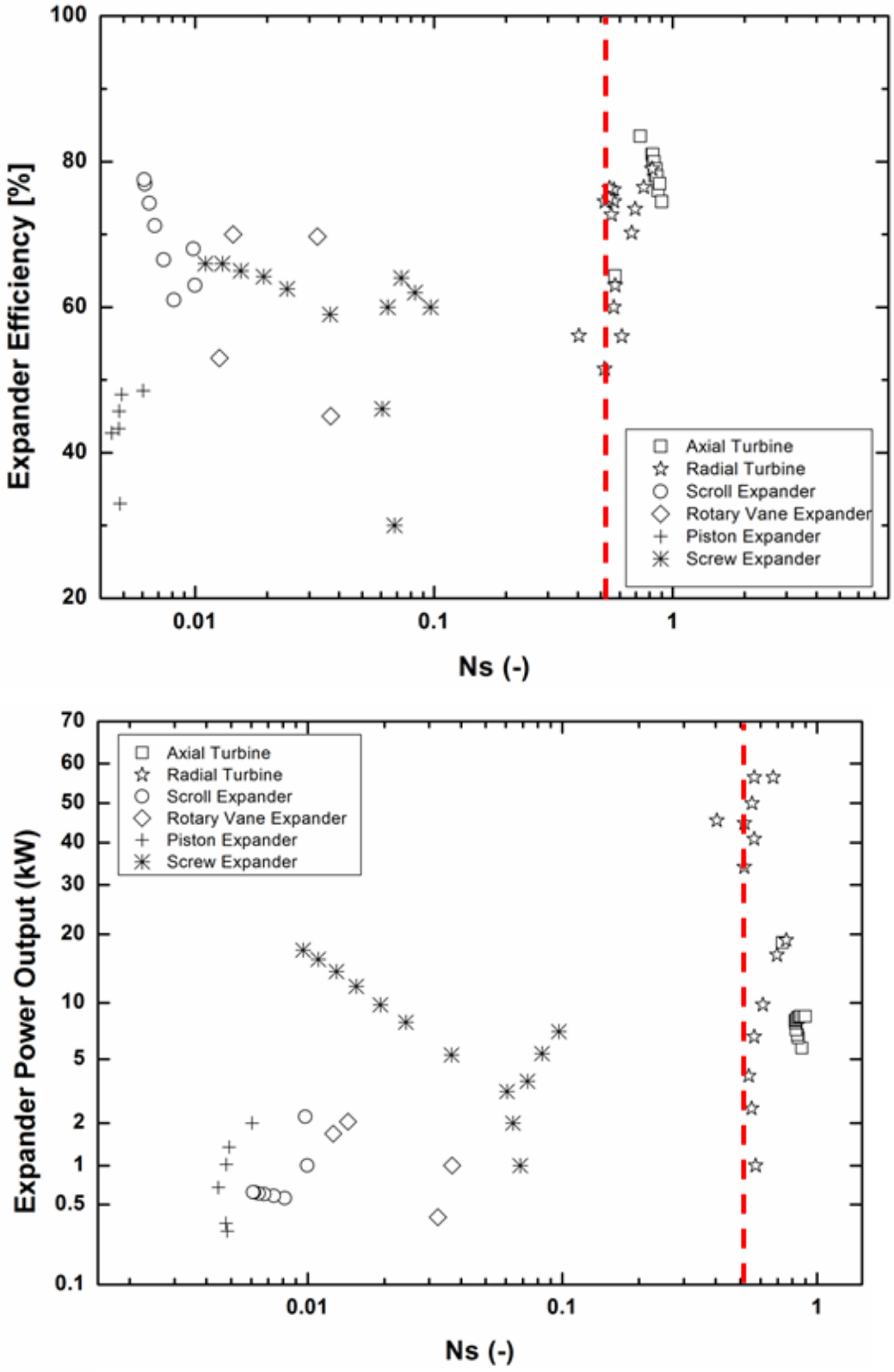

Figure 4-14: Location of the current expansion machine based on organic expansion machines by the author (see Section 2.3.3).

4.3.7 Overview of the Development Methodology

In most ORC studies, constant expander efficiency is considered for a wide range of cycle operating conditions and for various working fluids. However, according to the results in Chapter 3, this assumption is not valid because efficiency changes substantially with the changing operating conditions and/or working fluid. One of the contributions of this study is the design of a radial-inflow turbine with a dynamic efficiency that is unique for each set of working fluid properties and at different operating conditions. In addition, an optimisation code (OC) is developed to select optimum values of input parameters.Consequently, the optimum objective function is obtained. ADoE code is also developed to investigate the influence of each input parameter on turbine performance and geometry. Importantly, a meanline off-design code (MOC) was developed. The MOC can assist in investigating the turbine performance at off-design points. This code is crucial due to the unstable operating conditions of heat sources. The open literature still lacks mean-line off-design methodologies to evaluate the off-design conditions of ORC turbines [13], [14]. To achieve the aforementioned aims, an in-house code is constructed at Brunel University London. The in-house code consists of several sub-codes, including DPC, OC, DoE code (DoEC) and MOC. Each sub-code is briefly discussed in the next paragraphs. The code is constructed using MATLAB [236] and explained in detailin Chapter 5. Figure 4-15 presents the flowchart of the proposed methodology from design to testing.

DPC aims to produce the main geometrical parameters and solve velocity triangles of radial-inflow turbines based on a set of given input values. However, this code does not consider constraints, such as excessive blade angle, blade heights and flow angles. Therefore, a second code called OC is constructed to optimise the turbine based on a set of constraints. The MATLAB® optimisation Toolbox™[236]is used to optimise the turbine under design conditions.

The third code is DoEC, which is basically a mean-line code that aims at performing a parametric study to investigate the effects of one or more of the input parameters on the performance and geometry of the turbine while all other input parameters are maintained constant. In the next run, the

previous parameters are maintained constant and new parameters are varied. The process continues until all parameters are investigated and optimum values are identified. The geometry of the turbine changes simultaneously by changing these input parameters. Thus, the evaluation of the effects of changing these parameters on the performance of the turbine (with fixed geometry) is important. The next paragraph presents the code developed for this purpose.

The fourth code is called MOC or off-design code. This novel code aims to investigate the performance of the turbine at off-design points. Operating points are highly unstable in automotive engines. Therefore, checking the performance of the turbine under different conditions before sending the turbine out for manufacturing is extremely important so time and resources can be saved.

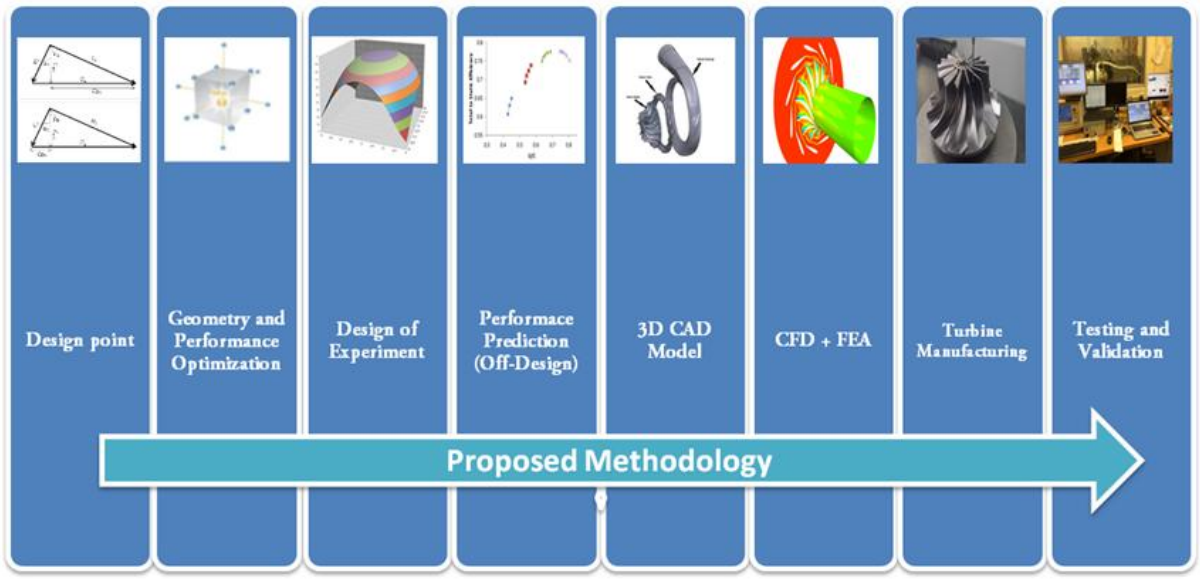

Figure 4-15: Flowchart of the proposed methodology.

4.4 Conclusion

This chapter presented basic information that readers require before going deeply in the proposed design methodology. The chapter also encompassed the required graphs of the turbine stage from volute to diffuser and the different configurations for each component. Importantly, the chapter

presented the advantage of selecting radial inflow turbine for the current project based on the developed guide presented in Chapter 2.

The next chapter presents the main contribution of the current thesis. The design methodology and MOC are presented in detail and validated with CFD results, and experimental works from three turbines.

Chapter 5 : Modelling of Radial-Inflow Turbines

5.1 Introduction

The designer has to run a mean-line analysis and a correlated optimisation technique to begin a convenient design process. An original model for the mean-line design of ORC radial-inflow turbine is developed. This model, which represents one of the main contributions of ORC turbines, can provide a complete preliminary design of the turbine volute, stator and rotor. The operating conditions at the volute inlet (Table 4-1) are specified by the steady-state model of the ORC to begin the mean-line methodology. Therefore, the designed turbine must match the operating conditions of the ORC model.

Several well-known preliminary design methodologies are included in the open literature such as[231], [233], [237]–[239]. However, these conventional methodologies use ideal gas as the working fluid, resulting in non-optimum turbine design when real gases, such as organic fluids, are used. These methodologies also require some known parameters, such as flow angles and radii, which have a non-negligible effect on the efficiency of the design. Lastly, such methodologies require a certain level of previous empirical knowledge [240].

The current work is concentrated on the development of a design process of a full radial-inflow turbine stage based on certain input parameters. These parameters are optimised using an optimisation technique integrated in the in-house code. In the optimisation algorithm (next section), the input parameters are considered and optimised as design variables to result in the optimum solution of the objective function. In a subsequent step, the optimised design variables are used as input parameters in the design code to estimate the performance and geometry of the turbine at the design point. Well-established models developed by the National Institute of Standards and Technology (NIST) (RefProP) [230]are integrated in the design procedure to account for the real gas properties. When the optimum design is achieved based on the optimisation algorithm, a further investigation of the design variables is achieved using the DoEC. The DoEC is used to investigate the impact of each single input parameter on the whole design process while the other input parameters are kept constant. However, the

designer also can investigate the influence of more than one parameter at the same time. Lastly, a novel MOC is integrated to explore the performance of the turbine at different operating conditions while the geometry is fixed.

5.2 Optimisation Algorithm

Although DoEC can be used to optimise the turbine, it is a time-consuming technique because the user is required to manually change the input parameters for each single run. However, DoEC is a helpful technique when applied as a parametric study to explore the effects of a single or a combination of variables on the geometry and performance of the turbine. An optimisation technique is developed and coupled to the design procedure. The OC is essential because it is used to optimise the turbine and eventually to achieve better ORC performance. This code is a genetic optimisation technique that eliminates the manual iterative procedure.

The MATLAB optimisation ToolboxTM® [236] is used to optimise the geometry and performance of the turbine under specified design conditions. This toolbox provides functions to maximise objectives and satisfy the user-defined constraints. It includes solvers for linear programming, mixed-integer linear programming, quadratic programming, nonlinear optimisation and nonlinear least squares. Fmincon, which is a constrained nonlinear minimisation or maximisation algorithm, is the solver used in this study. This algorithm finds the constrained minimum of a scalar function of several variables at an initial estimate. The objective function is shown in equation (5-1).

$$\gamma = a_0\eta_{ts} + a_0 W_{out} + a_2 \frac{W_{out}}{d_{max}}. \tag{5-1}$$

The multipliers a_0, a_1 and a_2 are used to define the objective function. Turbine total to static efficiency η_{ts}, expander power output W_{out} and the expander power over the turbine size $\frac{W_{out}}{d_{max}}$ are the important objective functions of the turbine. For example, if the turbine total to static efficiency η_{ts} is selected as the objective function, then the multipliers become as

follows: $a_0 = 1$, $a_1 = 0$ and $a_2 = 0$. Different design criteria can lead to various optimised expander geometries. The code solves for the selected objective function that considers the design constraints described in Section 5.4. These constraints are stated in several studies available in the open literature, such as [231], [233], [190] and [75]. The flowchart of the optimisation algorithm is presented in Figure 5-1. For brevity, the three terms in equation (5-1) are represented as F1, F2 and F3.

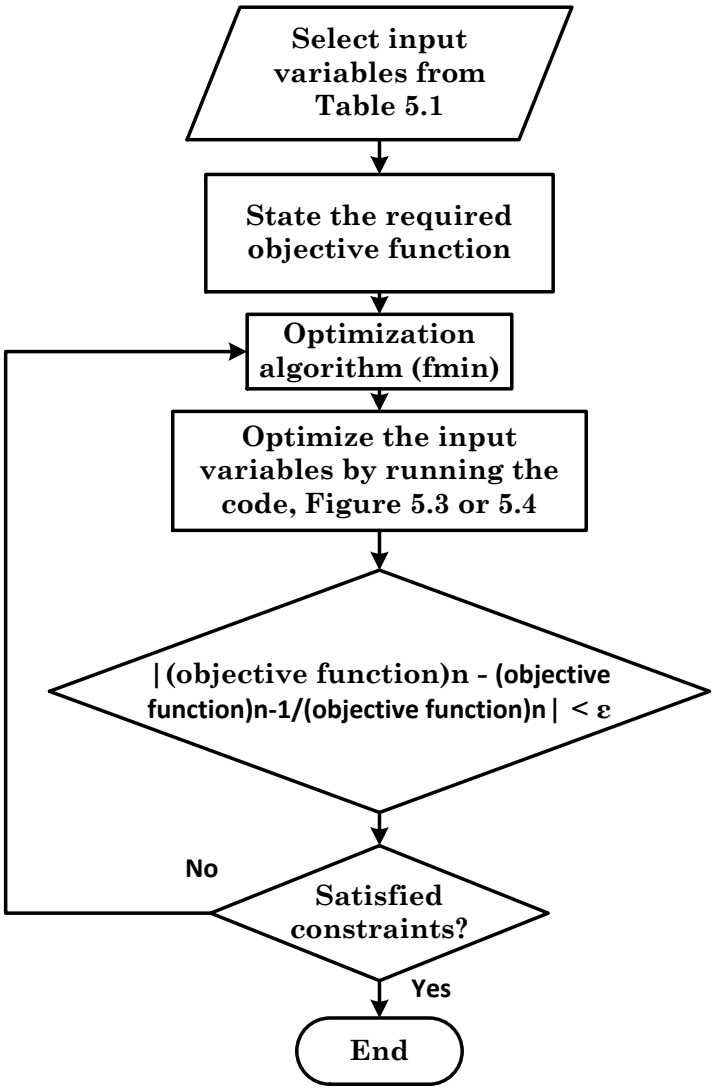

Figure 5-1: Flowchart of the optimisation algorithm

5.3 Design Point

This section presents the detailed procedure of the mean-line modelling at the design point. The DPC obtains the thermodynamic properties of the working fluid at each turbine stage (volute, stator and rotor) using the

integrated real gas EoS and determines the geometric and performance parameters using the genetic optimisation algorithm in Section 5.2.

5.3.1 General Stage Modelling

For simplicity, fluid properties are assumed to be constant on a plane normal to its direction of motion. Therefore, these properties vary only along the mean streamline of the blade [233]. Assuming the acceptable values of performance and geometric parameters is commonpractice to proceed with the design. Table 5-1 presents the input parameters specified by the designer. The exit radii r_{5h} and r_{5t} are not arbitrarily selected, as explained in Section 5.4.

Table 5-1: Design Input Parameters

Thermodynamic Inputs		Performance Input		Geometric Inputs	
Parameters	Unit	Parameter	Unit	Parameter	Unit
T_{01}	K	Specific speed,N_s	-	Radius ratio,r_3/r_4	-
P_{01}	kPa	**or**		Radius ratio,r_{5h}/r_4	-
P_5	kPa	Ψand φ			
$\dot{m}$	Kg/s				

The design procedure using $N_s$is an improved version of the methodology explained in [234]. Three non-dimensional parameters, namely, specific speed (N_s), velocity ratio (v_s) and total to static efficiency (η_{ts}), are used to begin with the design procedure. These correlations are widely applied with ideal gases.

$$v_s = 0.737 N_s^{0.2} \tag{5-2}$$

$$\eta_{ts} = 0.87 - 1.07(N_s - 0.55)^2 - 0.5(N_s - 0.55)^3 \tag{5-3}$$

Considering that the stagnation temperature and pressure are given, the other thermodynamic properties can be easily found using EoS, as shown in equation (5-4). Figure 4-3shows that $s_{5s} = s_{o1}$ based on the h–s diagram. In addition, the isentropic pressure at the rotor exit P_{5s} is calculated from the

given pressure ratio. Therefore, the isentropic enthalpy h_{5s} can be found using EoS, as shown in equation (5-5).

$$\{T_{01}, P_{01}\} = EoS(\rho_{01}, S_{01}, a_{01}, fluid) \tag{5-4}$$

$$\{P_{5s} = P_5, s_{5s} = s_{01}\} = EoS(h_{5s}, fluid) \tag{5-5}$$

Subsequently, the isentropic Δh_{is} and actual Δh_{act} enthalpies drops, and the turbine power output W_{out} can be obtained using the following equations:

$$\Delta h_{is} = h_{o1} - h_{5s} \tag{5-6}$$

$$\Delta h_{act} = \eta_{ts} \Delta h_{is} = h_{01} - h_{05} \tag{5-7}$$

$$W_{out} = \dot{m} \Delta h_{act} \tag{5-8}$$

5.3.2 Rotor Modelling

Rotor is the most significant component in the turbine stage because work transfer occurs in this region. Therefore, this component will be analysed first. In the DPC, the designer has the option to select either specific speed approach, or loading Ψand flow φ coefficients approach.

5.3.2.1 Mean-line Based on Specific Speed, N_s

In this approach, N_s is defined by the user, the rotational speed N is calculated using equation(2-3)and N is specified by the user in the second approach, which will be shown in the next section. Once v_s is calculated, rotor tip speed U_4, tangential speed $C_{\theta 4}$ and absolute flow angle α_4 are calculated using equations (5-9), (5-10)and(5-11), respectively [234]. It is worth mentioning that equation (5-11) is used in ideal gases. Therefore, the velocity triangle at the rotor inlet (Figure 5-2) is completed using trigonometry rules. Figure 5-3 presents the flowchart of the design point using N_s correlation.

$$U_4 = v_s \sqrt{2\Delta h_{is}} \tag{5-9}$$

$$C_{\theta 4} = \frac{U_4 \eta_{ts}}{2v_s^2} \tag{5-10}$$

$$\alpha_4 = 10.8 + 14.2n_s^2 \tag{5-11}$$

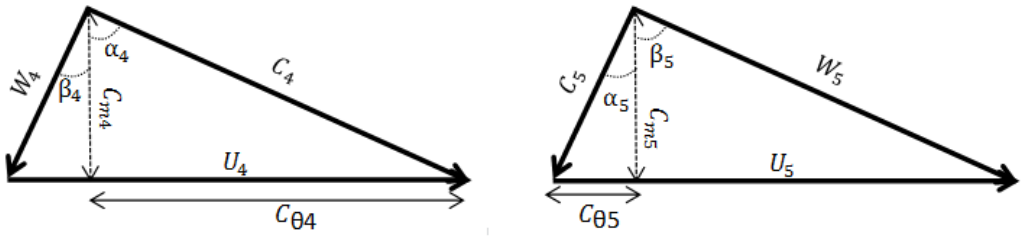

Figure 5-2: Velocity triangles of the rotor inlet(left) and rotor exit(right).

Given that U_4 is now calculated, the radius of the rotor inlet can be obtained using equation (5-12). The height of the rotor blade can be calculated using the mass continuity in equation (5-13). K_{B4} is the leading edge blockage factor calculated using equation (5-14)[234]. t_{b4} is the blade thickness at the leading edge of the rotor and obtained using the default value [234] using equation (5-15). Z_r is the number of blades of the rotor obtained by the Glassman correlation [238], which is widely used in ideal gas turbines, as shown in equation (5-16).

$$r_4 = \frac{U_4}{\omega} \tag{5-12}$$

$$\dot{m_{calc}} = 2(1 - K_{B4})\pi r_4 \rho_4 b_4 C_{m4} \tag{5-13}$$

$$K_{B4} = 1 - \frac{Z_r t_{b4}}{2\pi r_4 sin\beta_4} \tag{5-14}$$

$$t_{b4} = 0.04\, r_4 \tag{5-15}$$

$$Z_r = \frac{\pi}{30}(110 - \alpha_4)\tan\alpha_4 \tag{5-16}$$

The number of blades of the rotor Z_r can be obtained using different empirical correlations available in the open literature. An excessive number of blades will result in higher blade surface area and, hence, higher frictional loss [233]. Bycontrast, a flow reversal will take place when the

blade number is very low [241]. Jamieson [241] proposed a correlation to calculate the minimum number of blades, as shown in equation (5-17).

$$Z_r = 2\pi \tan \alpha_3 \tag{5-17}$$

However, Glassman [238] mentioned that the proposed correlation byJamieson[241] will result in a large number of blades at higher flow angles. Therefore, a reduction factor in Jamieson's equation is used and equation (5-16) is proposed by neglecting the difference in the flow angles between the stator exit and the rotor inlet. Whitfield and Baines [233] agreed with Glassman about Jamieson's correlation and stated that such large number of blades will result in an excessive blocking at the rotor exit. Therefore, an equation is proposed to calculate the number of blades at the minimum Mach number conditions, as shown in equation (5-18).

$$\cos^2 \alpha_3 = \frac{0.63\,\pi}{2Z_r} \tag{5-18}$$

The geometric parameters at the rotor inlet are now fully defined. The thermodynamic properties at this region have to be obtained to complete the design of the rotor inlet. The static enthalpy can be calculated using the First Law of Thermodynamics, as shown in equation (5-19). The h–s diagram in Figure 4-3 shows that the total and static entropies at the rotor inlet are identical. Total pressure P_{04} is calculated using equation (5-20)which applicable with ideal gases[234]. Now, the thermodynamic properties in stagnation and static states can be obtained using EoS, as shown in equations (5-21) and (5-22), respectively.

$$h_4 = h_{o4} + \frac{1}{2}C_4^2 \tag{5-19}$$

$$P_{04} = P_{01} - \frac{\rho_{01}\Delta h_{is}(1 - \eta_{ts})}{4} \tag{5-20}$$

$$\{h_{04}, P_{04}\} = EoS(\rho_{04}, T_{04}, a_{04}, s_{05}, fluid) \tag{5-21}$$

$$\{h_4, S_4\} = EoS(\rho_4, T_4, a_4, P_4, fluid) \tag{5-22}$$

According to the Euler equation, equation (5-23), the power output of the turbine increases with negative values of the exit swirl$C_{\theta 5}$. However, some reduction in efficiency will occur[233]. Therefore, $C_{\theta 5}$ is assumed to be zero to minimise the leaving loss of the rotor. The wheel speed at the rotor exit U_5 can be easily obtained because the radius ratios are given as inputs. One of the triangle parameters has to be obtainedto complete the velocity triangle at the rotor exit (Figure 5-2). Aungier [234]proposed an effective procedure to estimate meridional speed C_{m5}, equation (5-24). When this equation is applied, the velocity triangle at the rotor exit can be obtained using trigonometry rules.

$$W_{output} = m\cdot(U_4 C_{\theta 4} - U_5 C_{\theta 5}) \tag{5-23}$$

$$C_{m5} = C_{m4}\left(1 + 5\left(\frac{b_4}{r_4}\right)^2\right) \tag{5-24}$$

Subsequently, the static enthalpy h_5 is calculated using the First Law of Thermodynamics, as shown in equation (5-25), and the other thermodynamic properties are calculated using EoS, as shown in equation (5-26). Given that $s_{05} = s_5$, Figure 4-3, the stagnation thermodynamic properties can be found using equation (5-27).

$$h_5 = h_{o5} + \frac{1}{2}C_5^2 \tag{5-25}$$

$$\{h_5, P_5\} = EoS(\rho_5, T_5, a_5, s_5, fluid) \tag{5-26}$$

$$\{S_{05}, h_{05}\} = EoS(\rho_{05}, T_{05}, a_{05}, P_{05}, fluid) \tag{5-27}$$

To fully define the rotor geometry, the axial length and blade thickness of the rotor at its trailing edge are defined using equations(5-28) and (5-29), respectively [234]. The rotor mean throat o_5, which is the smallest distance between two adjacent blades, is calculated based on the value of the relative Mach number M_{5rel}, as shown in equation (5-30)[234].

$$\Delta z = 1.5\,(r_{5t} - r_{5h}) \tag{5-28}$$

$$t_{b5} = 0.02\,r_4 \tag{5-29}$$

$$\begin{cases} o_5 = \dfrac{s_5 C_{m5}}{W_5} & for \quad M_{5rel} < 1 \\ o_5 = \dfrac{s_5 C_{m5} \rho_5}{\rho_* W_*} & for \quad M_{5rel} \geq 1 \end{cases} \tag{5-30}$$

The blade angle of the rotor exit $\beta_{5,blade}$ can be obtained by the correlation shown in equation (5-31) as proposed bySuhrmann et al.[242], who stated that the correlation is based on the assumption that the relative flow angle β_5 is equal to $\beta_{5,blade}$ for zero mass flow, and the deviation $\delta_5$increases with mass flow.This equation is implicit in $\beta_{5,blade}$ and can be solved through the application of a bisection method. It is worth mentioning that this correlation is applied with ideal gases as the working fluid. Therefore, $\beta_{5,blade}$ can be specified by the designer in the proposed methodolofy.

$$\frac{90 - \beta_5}{90 - \beta_{5,blade}} = 1 + \left(m \cdot \frac{\sqrt{RT_{01}}}{P_5 D_4^2 (2 \tan(90 - \beta_{5,blade}) - 0.5} \right)^{0.02(90 - \beta_{5,blade}) - 0.255} \left(\frac{3\pi}{Z_r}\right) + 7.85 \frac{c_{rs}}{b_5} \tag{5-31}$$

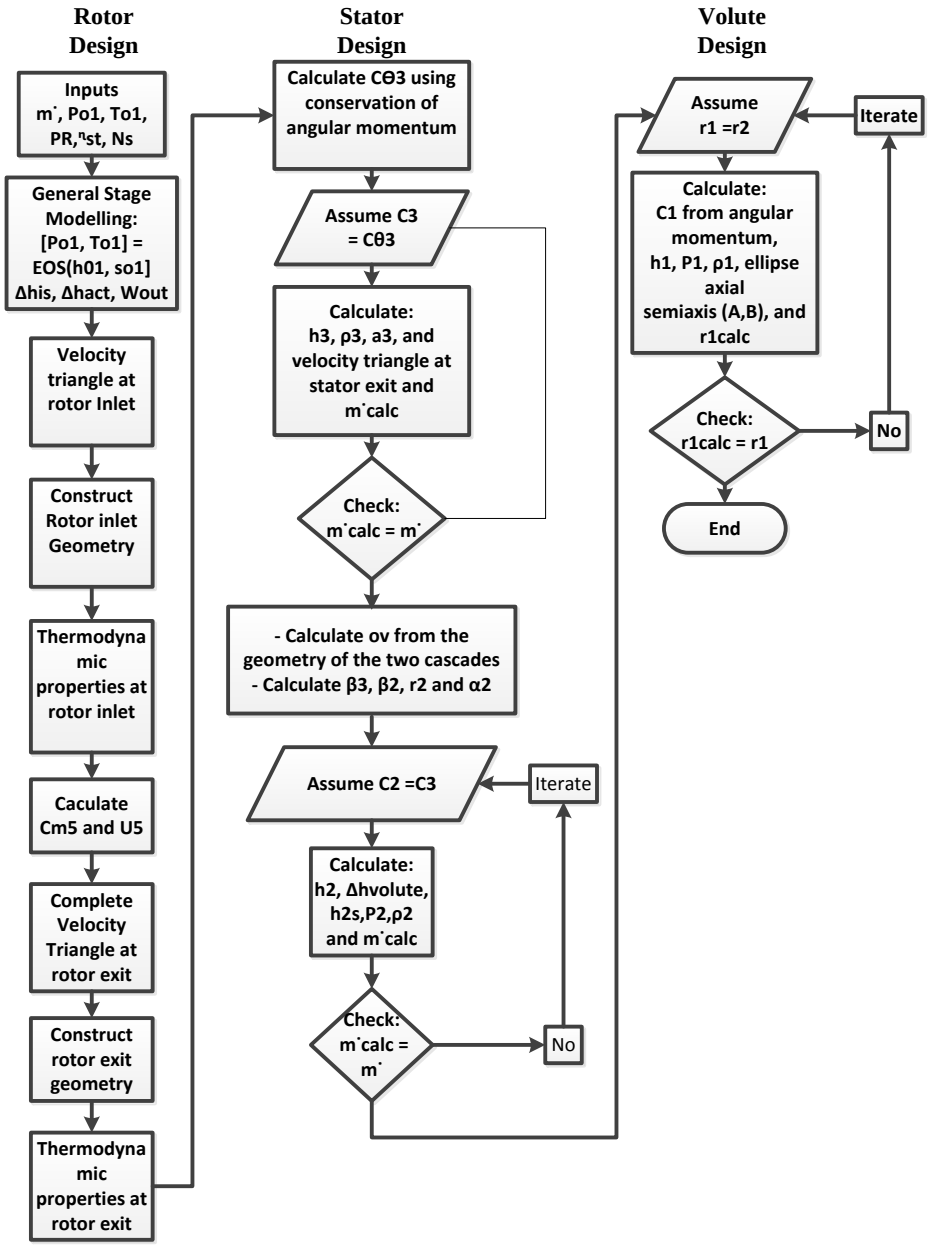

Figure 5-3: Flowchart of the design point using $N_s$correlation.

5.3.2.2 Mean-line Based on Flow and Loading Coefficients

The user has no control over the flow and loading coefficients when the proposed methodology in the previous section is used. Therefore, a new mean-line code that considers flow and loading coefficients as input parameters has been developed. This code is an improved version of the design procedure presented by Moustapha et al.[231]. The modelling of the stage, interspace and stator has similar methodologies. Figure 5-4 presents the flowchart using the methodology of flow and loading coefficients.

The rotor is modelled based on two non-dimensional parameters, namely, loading coefficient Ψ and flow coefficient φ, as outlined by [231]. These parameters are shown in equations(4-6)and(4-7)in the previous chapter. The rotational speed $U_4$and the meridional velocity C_{m5} at the rotor outlet can be calculated because the loading coefficient Ψ and flow coefficient φ are imported from the optimisation algorithm. Thus, the velocity triangle in Figure 5-2 and the flow angles at the rotor inlet can be calculated. Given the absolute velocity at rotor inlet C_4 is now known, the static enthalpy $h_4$can be calculated using the First Law of Thermodynamics. The $h-s$ diagram in Figure 4-3 shows that $s_4 = s_{o4}$. To obtain s_{o4}, the stagnation pressure P_{o4} is calculated using equation(5-32)[234]. Therefore, all other stagnation properties, including s_{o4}, at the rotor inlet can be obtained using EoS at $\{h_{04} = h_{01}, s_4 = s_{04}\}$.

$$P_{o4} = P_{01} - \left[\frac{\rho_{o1}\Delta h_{act}(1-\eta_{ts})}{4\eta_{ts}}\right] \tag{5-32}$$

Consequently, the static thermodynamic properties at the rotor inlet can be found using the EOS at $\{h_4, s_4\}$, as shown in equation (5-33).

$$\{h_4, s_4 = s_{04}\} = EoS(\rho_4, P_4, T_4, a_4, fluid) \tag{5-33}$$

The rotor exit geometry and thermodynamic properties are obtained in the same manner as in the specific speed approach (Section 5.3.2.1).

5.3.3 Interspace Modelling

A small space between the stator trailing edge and rotor leading edge is essential for the nozzle wakes to mix out before entering the rotor [231]. However, the value of the interspace is a trade-off among reduced mechanical coupling, large-size turbine and increased pressure losses. The increase in interspace distance results in higher fluid friction and boundary layer, whereas reducing the interspace distance will result in lower blade row interaction [231]. In his CFD analysis, White [13] stated that the

reduction of the total pressure from the stator trailing edge and rotor leading edge is 1.45%, which is sufficiently small to validate a constant total pressure in the interspace. Watanabe et al. [243]proposed a correlation to estimate a suitable clearance gap between the stator exit and the rotor inlet, as shown in equation (5-34). The maximum turbine efficiency can be achieved by placing a value of 2 for k.

$$r_3 - r_4 = k b_3 cos\left(\frac{\alpha_3 + \alpha_4}{2}\right), \tag{5-34}$$

where b_3 is the stator blade height calculated using equation (5-35). $\varepsilon_x$and $\varepsilon_r$are the axialand radial tip clearances, as shown in Figure 4-2, and they are calculated using equation (5-36)[234].

$$b_3 = b_4 + \varepsilon_x \tag{5-35}$$

$$\varepsilon_x = \varepsilon_r = 0.04\, b_5 \tag{5-36}$$

5.3.4 Stator Modelling

To reduce incidence loss, the nozzle vanes must be set at an appropriate blade angle to enable a smooth swirl flow at the rotor leading edge. The design procedure of the nozzle vanes are performed iteratively, as shown in the flowcharts inFigure 5-3 and Figure 5-4. Li et al. [244] stated that the conservation of angular momentum can be applied in the vaneless space because the swirl coefficient (SC) between the stator exit and the rotor inlet is close to unity. Therefore, the tangential component of the velocity at the stator exit $C_{\theta 3}$ can be calculated, as shown in equation(5-37).

$$C\theta 3 = \frac{C_{\theta 4} \cdot r_4}{r_3} \tag{5-37}$$

To construct the velocity triangle at the stator exit, the absolute velocity C_3 is calculated iteratively with a first assumption of $C_3 = C_{\theta 3}$. Subsequently, the static enthalpy h_3 is calculated from the total enthalpy and the kinetic energy, as shown in equation(5-38).

$$h_3 = h_{o3} + \frac{1}{2}C_3^2 \tag{5-38}$$

The other thermodynamic properties can now be obtained, as shown in Equation(5-39). The new value of mass flow rate $\dot{m}_{calc}$ is obtained using equation (5-40), and the process is repeated until convergence is achieved.

$$\{S_3 = S_4, h_3\} = EoS(\rho_3, T_3, a_3, P_3, fluid) \tag{5-39}$$

$$\dot{m}_{calc} = 2\pi r_3 \rho_3 b_3 C_{m3} \tag{5-40}$$

Similar to the rotor throat width, the stator throat width is calculated using equation (5-41)[234]. s_v is the vane pitch at the trailing edge, as shown in Figure 3-9. Moreover, it is related to the vane chord c_v , where $\frac{c_v}{s_v} = 1.2\ to 1.3$. This limit ratio is known as solidity σ, and it is implemented in the OC to reach the optimum value within the limit. If the flow at the stator exit is supersonic ($M_3 \geq 1$), then the nozzle throat width is calculated using the mass continuity equation between the throat passage and the exit station, as shown in Figure 3-9. ρ_* *and* a_* are the density and speed of sound at sonic conditions, respectively.

$$\begin{cases} o_3 = s_v sin\alpha_3 & for \quad M_3 < 1 \\ o_3 = \dfrac{C_{m3}\rho_3}{\rho_* a_*} & for \quad M_3 \geq 1 \end{cases} \tag{5-41}$$

The number of nozzle vanes $Z_s$can be either calculated using equation (5-42) or defined by the user.

$$Z_s = \frac{2\pi r_3}{s_v} \tag{5-42}$$

The stator setting angle γ_3 should be calculated iteratively to set the required throat width. The stator vane is positioned at the stator outlet radius r_3 and rotated around the trailing edge with an initial guess of $\gamma_3 \geq 5^{\circ}$. Subsequently, the second vane is constructed by rotating the first vane around the origin by $\frac{2\pi}{Z_s}$, and the throat width will be the minimum distance

between the two cascades. The iterative process is then repeated until convergence occurs at o_3. The radial chord length of the vane c_d is then calculated using equation(5-43).

$$c_d = c_v \cos \alpha_3 \tag{5-43}$$

Considering that the vane throat width o_3 is now known, cosine rule can be used to account for the change in angular momentum between vane throat and exit, as shown in equation (5-44). With the application of the conservation of momentum between stator throat and stator exit, static density can be calculated using equation (5-45).

$$\cos \alpha_{th} = \frac{o_3 Z_s}{2\pi r_3} \tag{5-44}$$

$$\rho_{th} = \rho_3 \frac{tan\alpha_{th}}{tan\alpha_3} \frac{r_{th}}{r_3} \tag{5-45}$$

Given that r_2 is calculated from the two cascades, the stator setting angle at the inlet γ_2 is obtained using equation (5-46). To calculate the velocity triangle at the stator inlet, an iterative process is essential to calculate the absolute velocity C_2 until convergence occurs at $\dot{m}$. The volute loss is calculated using equation (5-47)[231]. Consequently, the isentropic static enthalpy h_{2s} is calculated to obtain the rest of the thermodynamic properties at the stator inlet using equation (5-48). The static pressure P_2 and the rest of the thermodynamic properties are then obtained using EOS, as shown in equations(5-49)and(5-50), respectively. The new mass flow rate is then calculated using equation(5-51).

$$cos\gamma_2 = \frac{r_3 cos\gamma_3}{r_2} \tag{5-46}$$

$$\Delta h_{vol} = \frac{1}{2} k_{vol} C_2^2 \tag{5-47}$$

$$h_{2s} = h_2 - \Delta h_{vol} \tag{5-48}$$

$$\{h_{2s}, S_1\} = EoS(P_2, fluid) \tag{5-49}$$

$$\{h_2, P_2\} = EoS(\rho_2, T_2, a_2, s_2, fluid) \tag{5-50}$$

$$\dot{m}_{calc} = A_2 \rho_2 C_{m2} \tag{5-51}$$

The construction of the full stator vane, including the distribution of the vane thickness, is performed using the methodology described by Aungier[234] and detailed in Appendix A. Once the stator vane is fully defined, the flow angle at the stator leading edge α_2 can be obtained using equation(5-52)[234]. i^* is the empirical correlation developed by Emery et al.[245]for axial compressor cascades, as shown in equation(5-53).

$$\alpha_2 = \beta_2 - i^* sign(\beta_3 - \beta_2) \tag{5-52}$$

$$i^* = \left[3.6\sqrt{\frac{10t_2}{L}} + \frac{|\beta_3 - \beta_2|}{3.4}\right]\sqrt{\frac{L}{s_v}} - \frac{|\beta_3 - \beta_2|}{2} \tag{5-53}$$

$L, \beta_2 \; and \; \beta_3$ are the flow path length, stator bale angle at the inlet and stator bale angle at the exit,respectively, and they can be obtained numerically from the constructed vanes. To this end, the stator vane is now fully defined thermodynamically and geometrically.

5.3.5 Volute Modelling

Volute or the turbine inlet casing is used to distribute the fluid flow around the turbine periphery to provide a uniform mass distribution and uniform static pressure at the volute exit. The flow in the volute is highly complex and 3D, thereby implying the need for3D flow analysis[179], [231]. However, in the preliminary design process, a simple method presented in [199], [233], which considers the working fluid incompressible, is adopted. This process aims to estimate the volute passage area A_1 and mean radiusr_1. In such methods, the flow is assumed to be uniform with constant angular momentum (free vortex).

During the design stage, an elliptical cross-section area is assumed due to the mathematical simplicity of ellipse calculations. Aungier [234] recommended a relationship between the ellipse semi-axes and the aspect ratio (AR), as shown in equation (5-54). Therefore, the limit of AR is

implemented in the optimisation process to obtain the optimum value within the recommended limit.

$$0.75 \leq AR \leq 1.5 \tag{5-54}$$

Given that the volute radius is unknown, an iterative procedure is required with a first assumption of $r_1 = r_2$. Subsequently, equations (5-55) to (5-58) are solved iteratively until convergence is achieved.

$$C_1 = \frac{r_2 C\theta_2}{r_1 SC} \tag{5-55}$$

SC is the swirl coefficient that accounts for the effect of the wall friction in the volute. In some studies [233], [234], the value of SC is assumed to be equal to one. However, Moustapha et al.[231] stated that the analyses of radial turbine test data suggest a value in the limit of $0.85 < SC < 0.95$. In the current study, the value of SC is imported from the optimisation process, where the value lies in the limit of $0.85 < SC < 1$.

$$h_1 = h_{01} - \frac{C_1^2}{2} \tag{5-56}$$

$$\{h_1, s_1\} = EoS(\rho_1, T_1, a_1, P_1, fluid) \tag{5-57}$$

$$A_1 = \frac{\dot{m}}{\rho_1 C_1} \tag{5-58}$$

When the main geometrical parameters of the volute are obtained, the thermodynamic and other geometrical parameters can be calculated at each azimuth angle (ψ), beginning from 360° and ending at nearly 0°. The mass flow at any azimuth angle (ψ) can be calculated as follows:

$$\dot{m}_\psi = \dot{m}\left(1 - \frac{\psi}{2\pi}\right) \tag{5-59}$$

The area over radius at the volute inlet $\left(\frac{A_0}{r_0}\right)$ is calculated using the continuity equation and constant angular momentum as follows:

$$\frac{A_0}{r_0} = \frac{2\pi b_2}{\tan(\alpha_2)}, \tag{5-60}$$

where b_2 is the passage height at volute exit (stator inlet), and α_2 is the flow angle. The area over radius ratio $\frac{A_\psi}{r_\psi}$ at each azimuth angle can be obtained using equation (5-61):

$$\frac{A_\psi}{r_\psi} = \frac{A_0}{r_0}\left(1 - \frac{\psi}{360^\circ}\right) \tag{5-61}$$

With the area over the radius ratio now obtained at each azimuth angle, the calculation of the areas and radii of ellipses at different azimuth angles are straightforward, as shown in equations (5-62) to (5-65). t_t is the tongue thickness.

$$r_\psi = r_b + B \tag{5-62}$$

$$b = \sqrt{\frac{A_\psi / r_\psi}{\pi} \frac{r_\psi}{AR}} \tag{5-63}$$

$$A_\psi = \pi a b \tag{5-64}$$

$$t_t = r_1 - B - r_b \tag{5-65}$$

$\left(\frac{r_b}{r_2}\right)$ is the inlet-to-discharge radius ratio with given a value of 1.05, as reported in [234].

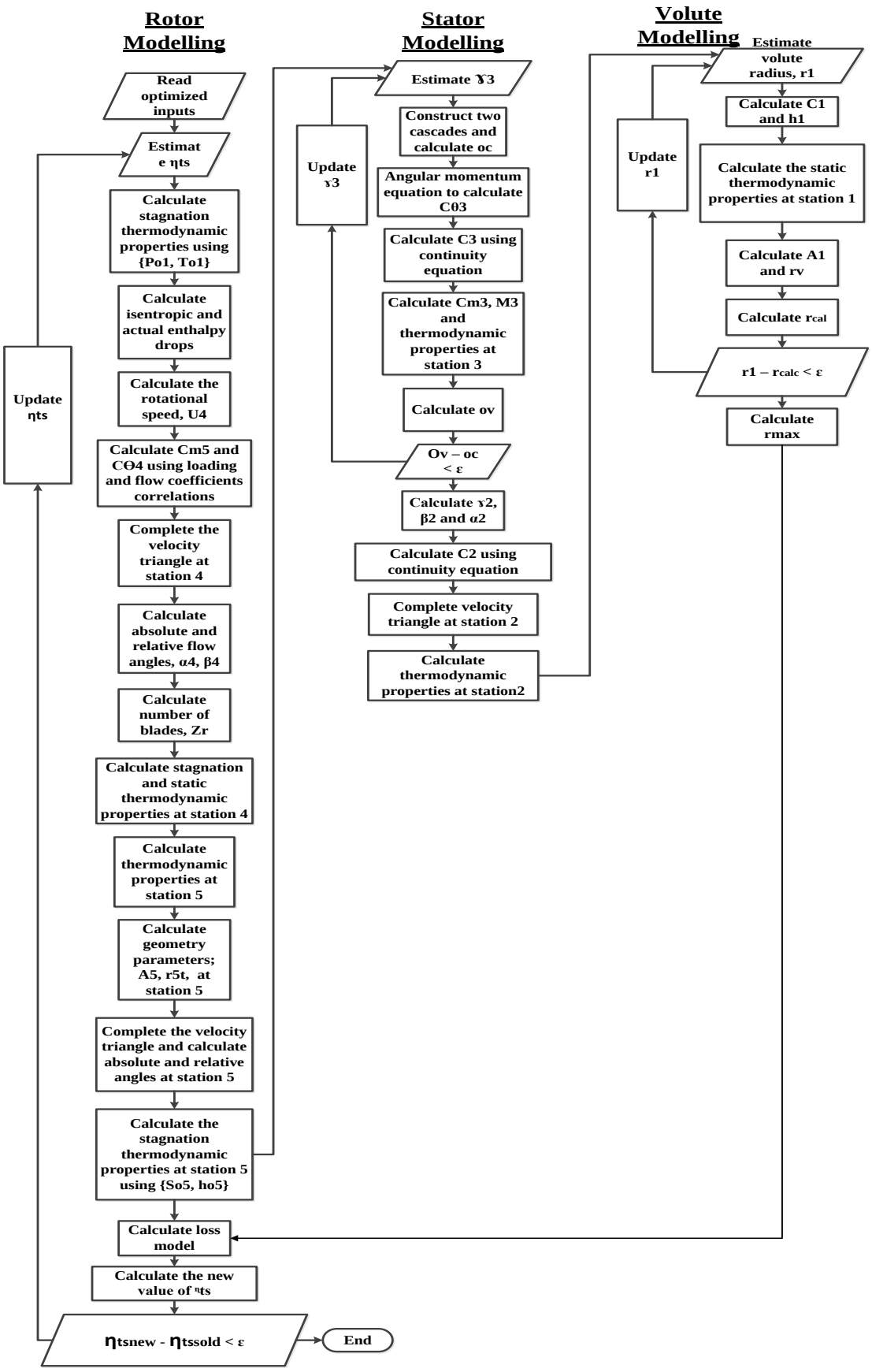

Figure 5-4: Flowchart of the design point using flow and loading coefficients correlation.

5.4 Design Feasibility

Generally, the feasibility of conventional radial-inflow turbines is checked by performing intensive CFD and FEA analyses after creating the 3D models. However, feasibility should be checked at the early stage of the design (i.e. at the preliminary design stage) to save time and resources. To do so, a wide research has been performed to collect the constraints reported in the open literature, including geometrical, flow, thermodynamic and structural constraints. These constraints are implemented in the design code to check the feasibility simultaneously.

5.4.1 Geometrical Constraints

This section mainly aims to ensure that the turbine can be manufactured. For easy manufacturing process, the rotor inlet radius r_4 and the inlet blade height b_4 must not fall below 10 mm and 2 mm, respectively [75]. To prevent excessive tip curvature, the radius ratio $\left(\frac{r_{5,tip}}{r_4}\right)$ should not exceed 0.78 [246]. However, Rohlik[237], andRodgers and Geiser[239] recommended that $\left(\frac{r_{5,tip}}{r_4}\right)$ should not exceed 0.7. Whitfield and Baines[233] stated that an excessively small radius ratio $\left(\frac{r_{5h}}{r_4}\right)$ will result in crowded blades at the exit hub, thereby limiting the available exit area. Therefore, a practical limit to the hub radius is proposed, as shown in equation (5-66).

$$r_{5h} > \frac{Z_r t_{5h}}{2\pi cos\beta_{5h}} \tag{5-66}$$

Lastly, the blade angle at the rotor leading edge $\beta_{4,b}$ should not exceed 70° to avoid manufacturing issues [75].

5.4.2 Flow Constraints

To achieve better flow guidance and easy manufacturability, some flow constraints are implemented in the model. To achieve a reasonable rotor blade number, the absolute flow angle at rotor inlet is set to less than 80°.

This method also helps minimise the friction and tip clearance losses. For better flow guidance, the incidence angle i_4 is selected to be in the range of$-20^{\circ} \leq i_4 \leq -40^{\circ}$. This range is widely suggested in the literature [231], [233].

5.4.3 Thermodynamic Constraints

The section is directly related to the condenser. The exit static pressure at the rotor exit is set to be above the atmospheric pressure $(P_5 > 1\ bar)$ to prevent air or water contamination that could cause fluid deterioration and the need for vacuum installation [179].

5.4.4 Structural Constraints

The structural analysis mainly aims to ensure that the turbine can stay in duty without failure. This analysis is usually performed after the aerodynamic evaluation because some of the aerodynamic parameters should be used as inputs to calculate the load forces, temperatures and stresses that result in differential thermal growths[231]. However, checking the stress levels in the mean-line stage is possible to avoid unacceptable solutions. When the material of the rotor blades is selected, calculating the elastic stress that resultsfrom centrifugal loading by using the following equation is possible [247].

$$\sigma_e = k\rho U_4^2 \tag{5-67}$$

ρ is the material density, and k is a geometric factor that has a value of 0.3 [231].

5.5 Design of Experiments with Different Turbine Configurations

The indicator of the turbine quality is the total to static efficiency and power output. In addition, the turbine is part of a complete system that is used as a WHR system in ICEs. Moreover, the space in the interior of the vehicles is

limited. Therefore, evaluating the size of the turbine is also important, and the maximum size of the turbine is r_1, as shown in Figure 4-2.

The DoE is a parametric study based on the simultaneous variation of one or more input parameters while the other input parameters are maintained constant. In each run, a single input parameter (or multiple) is varied while the other parameters are kept constant. Once the run is completed, the optimum value of the varied input parameter that leads to the optimum objective function is fixed. In the next run, another input parameter is varied and the process is repeated until the entire set of input parameters is examined.

5.6 Results of DPC and DoEC

The input conditions specified by the industrial partner are presented in Table 4-1. The aim at this point is to design, validate and perform a parametric of the radial-inflow turbine based on these input conditions.

5.6.1 Comparison with an Existing Model

The model is validated against a well-defined model [238]to evaluate its accuracy. In Glassman's case[238], some significant inputs, such as power, rotational speed, stator exit angle, angular momentum distribution, rotor exit flow, specific heat ratio of the gas and stator radius ratios, must be specified by the designer to solve the model. This method indicates that the designer has to have enough experience of empirical knowledge to specify the suitable input parameters. Therefore, the proposed methodology in this work requires substantially fewer input parameters, in which little or no experience of the empirical correlations is required. The results of both cases are compared in terms of geometry and performance of the turbine. Table 5-2 presents the design input parameters of the turbine presented in [238].

Table 5-2: Design Input Parameters [238].

Parameter	Value	Unit
Fluid	Argon	-
Inletstagnation temperature	1083.3	K
Inlet stagnation pressure	91	kPa
Exit static pressure	56.52	kPa
Rotational speed	38,500	rpm
Mass flow rate	0.277	Kg/s

The results of both cases are presented in Table 5-3, which clearly shows that the results of the current model are in good agreement with the test case (Glassman's model). In terms of turbine size, the current model overestimates the size, with 3.63% increase compared to the test case. The deviation in the turbine performance between the two models is 2.3%, indicating the overestimation of the current model. This result can be justified by the fact that the input parameters (φ, Ψ) in the current study are optimised for higher turbine performance. The next paragraphs show that the flow coefficient φ plays a vital role in the performance of the turbine. The maximum deviation between the two models in the prediction of the rotor exit tip radius $r_{5t}$is 5.38%. The results in Table 5-3 indicate that the results in the current model are in good agreement with the test case. Importantly, the model can optimise any existing turbine. It is worth mentioning that the test case is just a theoretical study and no experiment has been done to validate it.

Table 5-3: Comparsion between the Current Model and Glassman's Model.

Parameter	Unit	Glassman	Current Model	Deviation %
Stator inlet radius $\boldsymbol{r_2}$	mm	97.75	101.3	3.63
Stator exit radius $\boldsymbol{r_3}$	mm	79.38	82.6	4.06
Absolute flow angle $\boldsymbol{\alpha_3}$	deg	72	73.7	2.36
Number of nozzle vanes $\boldsymbol{N_v}$	-	16	16	0.00
Rotor inlet radius $\boldsymbol{r_4}$	mm	78.74	76	3.48
Rotor exit hub radius $\boldsymbol{r_{5h}}$	mm	19.36	18.7	3.41
Rotor exit tip radius $\boldsymbol{r_{5t}}$	mm	55.42	58.4	5.38
Absolute flow angle $\boldsymbol{\alpha_4}$	deg	71.92	72.5	0.81

Relative flow angle $\boldsymbol{\beta_4}$	deg	−31.5	−33	4.76
Relative flow angle $\boldsymbol{\beta_5}$	deg	−70.69	−72	1.85
Number of rotor blades $\boldsymbol{N_r}$	-	12	12	0.00
Stage total to static efficiency $\boldsymbol{\eta_{ts}}$	%	83	85.3	2.3

5.6.2 ORC Turbines

When the proposed methodology is validated, an efficient radial-inflow turbine can be designed based on the conditions provided in Table 4-1. Prior to running the OC, a parametric study that uses the DoEC is performed to explore the effects of input parameters on the performance and geometry of the turbine.

5.6.2.1 Parametric Study Using DOEC

Adopting a non-zero blade angle $\beta_{blade,4}$ at the rotor inlet without considering the bending stresses as in conventional turbines is possible because the operating temperature of the model is less than 200 °C. Figure 5-5 presents a schematic comparison between radial and non-radial blades. The increase in the inlet blade angle results in a hightangential velocity at the rotor leading edge $C_{\theta 4}$ and, hence, higher specific work. However, a further increase in $\beta_{blade,4}$ will result in excessive blade curvature and, hence, higher secondary losses. Therefore, efficiency deteriorates with any further increase in the blade angle.

Figure 5-5: (a) Shape of radial and non-radial blades and (b) effecct of non-zero blade angle $\beta_{blade,4}$ on the efficiency of the turbine.

Figure 5-6 presents the effect of flow coefficient φ on the performance of the turbine (power and efficiency), its maximum size, and Mach number at rotor inlet at different pressure ratios. Figure 5-6a and Figure 5-6c show that the flow coefficient φ has a significant impact on the turbine total to static efficiency η_{ts} and overall turbine sizer_1. The increase in flow coefficient φ is detrimental to the turbine total to static efficiency η_{ts} and beneficial to the turbine compact size. The definition of the flow coefficient in equation(4-6)implies that the increase of this parameter leads to higher meridional velocity at the rotor exit C_{m5} and, therefore, higher exit loss, as shown in equation(5-94) (next section). Figure 5-6bdepicts the effects of flow coefficient φ on the turbine power output W_{out}, which decreases slightly as φ increases. This phenomenon can be justified by the definition of φ and Euler equation in equation(5-23). As φ increases, the rotor blade speed U_4 decreases, thereby resulting in low power output. The effect of φ on the Mach number is insignificant because the two parameters have no direct relationship, as shown in Figure 5-6d. Figure 5-6also depicts the effect of turbine total to static pressure ratio PR_{ts} while increasing φ. The variation of PR_{ts} has remarkable effects on the investigated parameters. As PR_{ts} increases, the enthalpy drop through the turbine stage increases, leading to high turbine power output W_{out}. The increase in enthalpy drop leads to larger rotor diameter and, hence, larger turbine size r_1. The increase in the pressure ratio likewise leads to high Mach number M_4, where the flow becomes supersonic at $PR_{ts} \geq 5$.

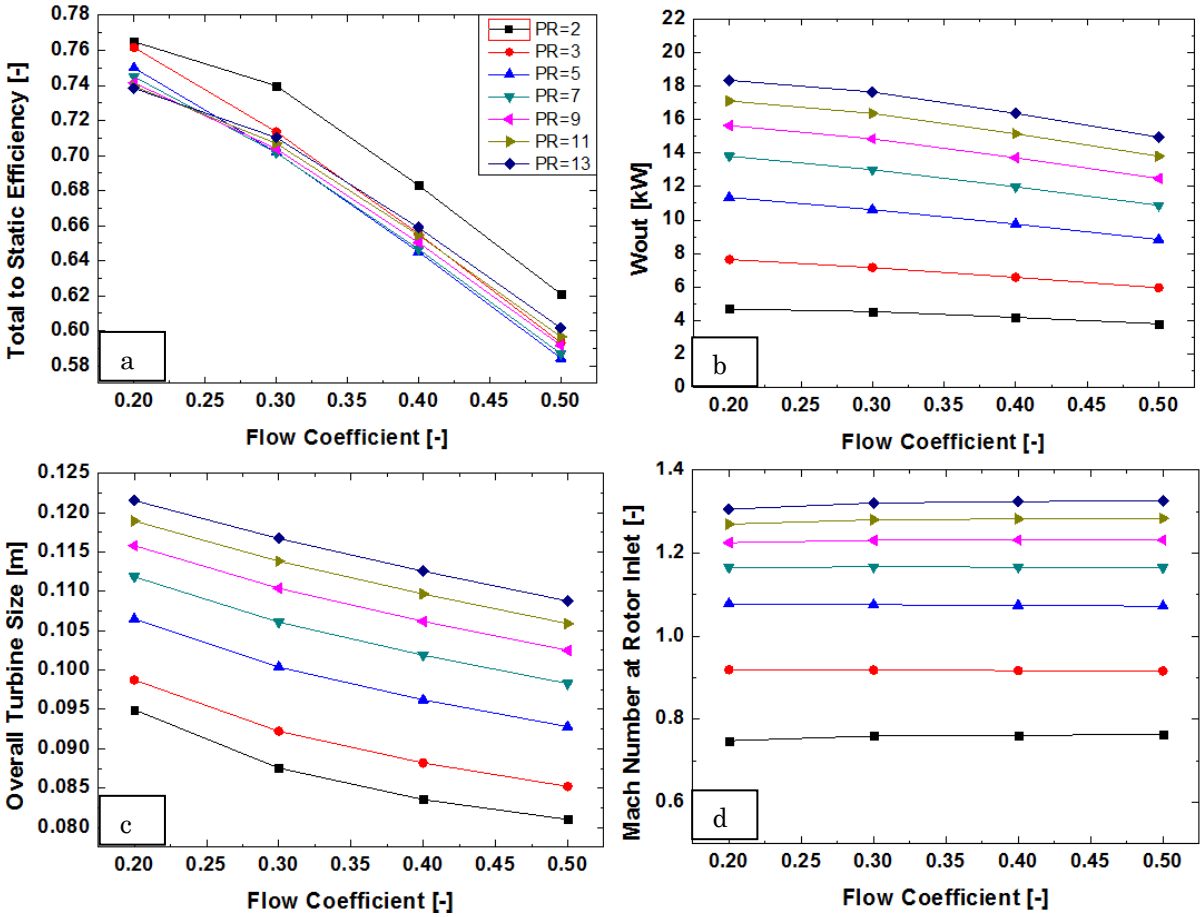

Figure 5-6: Effect of flow coefficient φ on the investigated parameters.

Figure 5-7 presents the effect of loading coefficient Ψ on the same parameters mentioned in the previous paragraph. Figure 5-7aand Figure 5-7b show that the effect of Ψ has a slight significanceon η_{ts} and is insignificant on W_{out}. However, the results in Figure 5-7agree well with [231], in which the turbine shows better performance with Ψ falling in the range of 0.8–1. Furthermore, loading coefficient Ψ has a significant effect on the turbine size and Mach number, as shown in Figure 5-7cand Figure 5-7d, respectively. This phenomenon is directly related to the definition of the loading coefficient Ψ in equation (4-7), where the increase of Ψ leads to higher enthalpy drop and,therefore, a smaller diameter. The decrease of U_4 results in higher absolute velocity at the rotor inlet C_4, thereby leading to the higher Mach number M_4(Figure 5-7d).

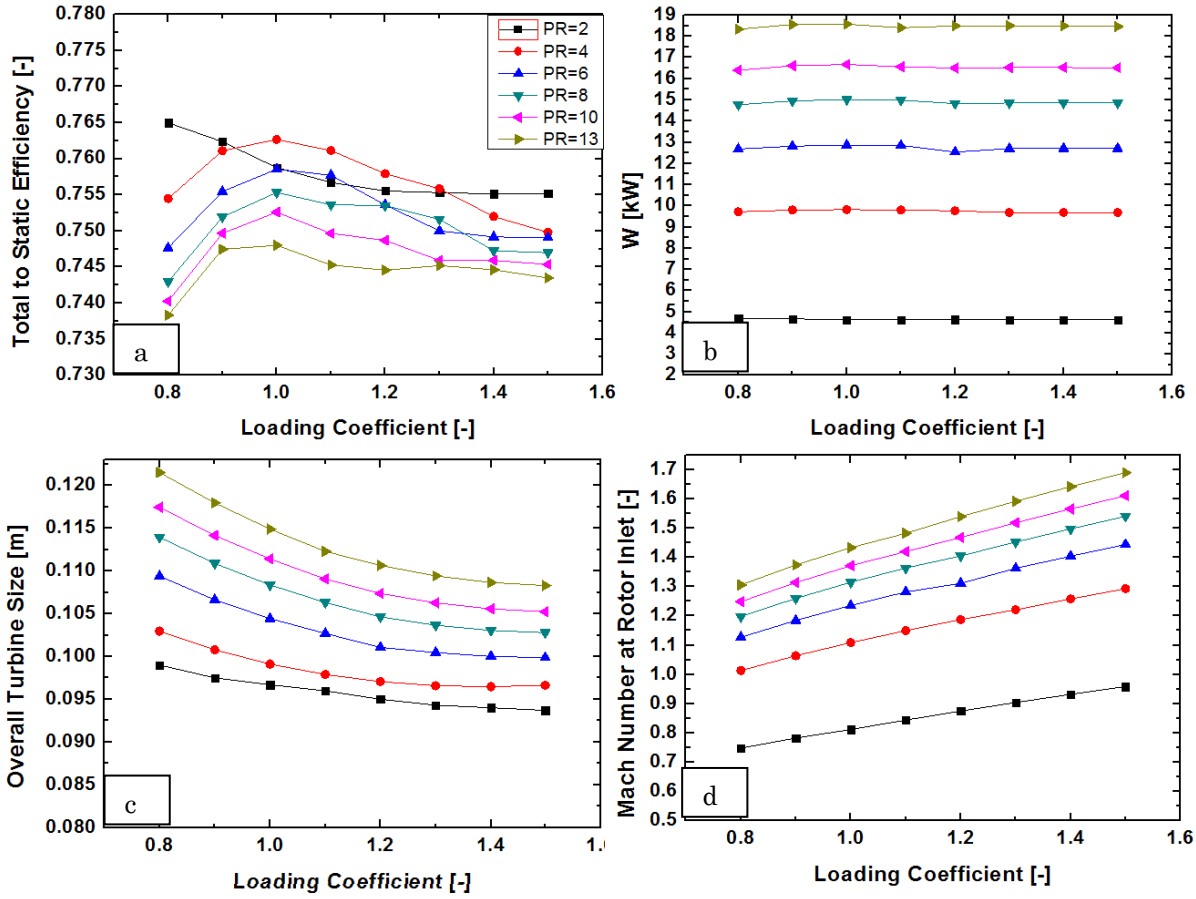

Figure 5-7: Effect of loading coefficient Ψ on the investigated parameters.

Figure 5-8 presents the effects of turbine rotational speed N on the four investigated parameters. Figure 5-8a shows that the static efficiency η_{ts} increases gradually with the turbine speed N with an increase of 11.7% from 20,000 rpm to 70,000 rpm. In agreement with the Euler equation in equation (5-23), the turbine power output W_{out} presents the same trend as the static efficiency η_{ts} with an increase of 12.5% from 20,000 rpm to 70,000 rpm. Figure 5-8bpresents the effect of N on the two remaining parameters. The increase in turbine speed N is significantly beneficial to the turbine size r_1. As N increases, r_1 substantially decreases with a decrease of 27.14% from 20,000 rpm to 70,000 rpm. This observation can be justified by the definition of loading coefficient Ψ in equation (4-7). For constant Ψ, the rotor radius r_4 is inversely proportional to the turbine speed N. This result also explains the increase in turbine efficiency η_{ts}, where the friction and exit loss decrease with turbine size. The losses model is presented in detail in Section 5.7.1. The effect of turbine speed on the

Mach number M_4 of the rotor inlet is insignificant with a maximum increase of 1% from 20,000 rpm to 70,000 rpm.

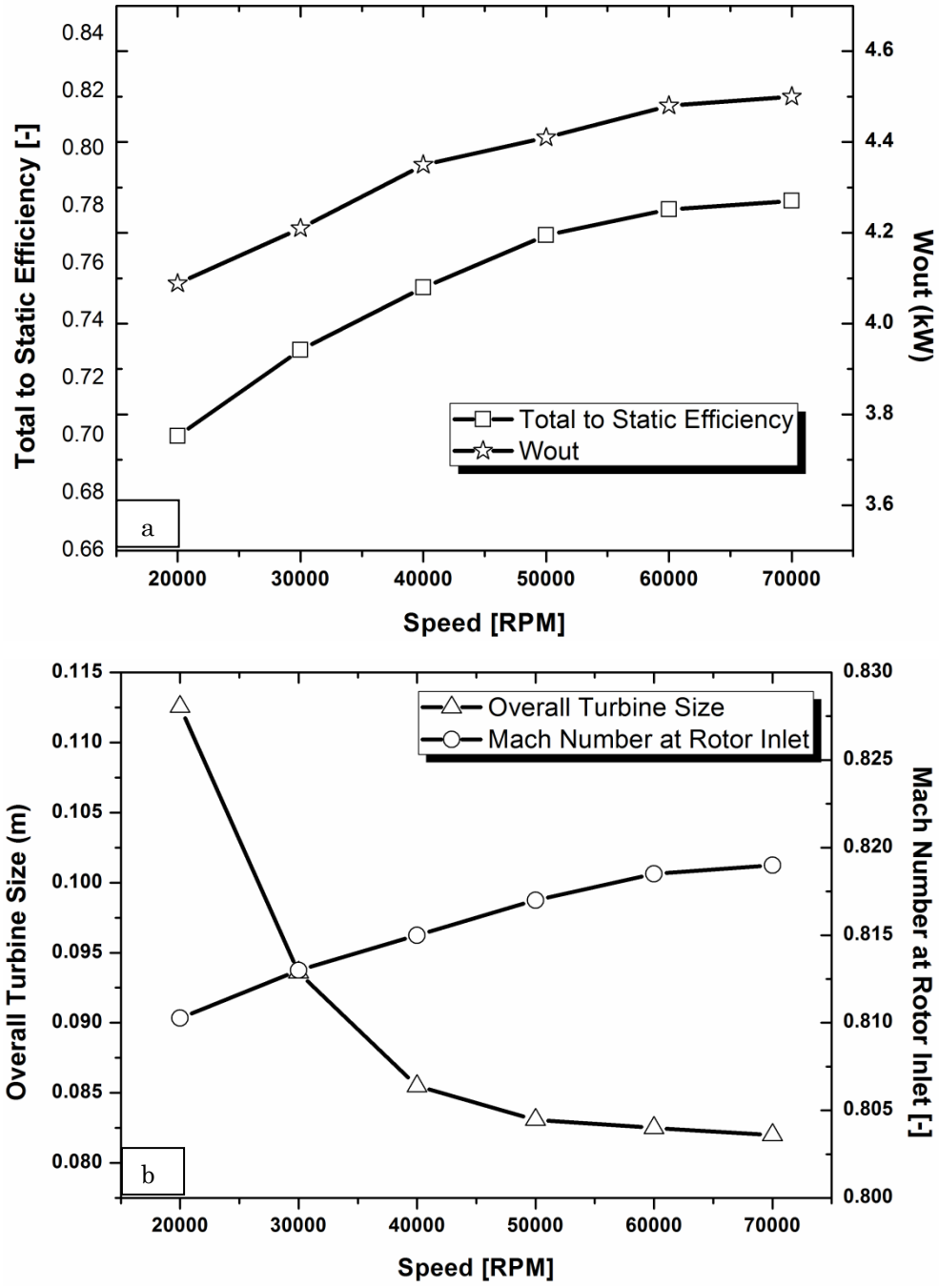

Figure 5-8: Effect of rotational speed N on the investigated parameters.

Figure 5-9 depicts the effect of working fluid MFR on the four investigated parameters. Figure 5-9ashows thatW_{out} and η_{ts} increase substantially with the MFR of the working fluid. This observation is directly related to the Euler equation, as shown in equation(5-23). Figure 5-9bdepicts the effect of the MFR on turbine size r_1 and Mach number M_4. Clearly, MFR has a

significant effect on the turbine size r_1 due to the increase in the enthalpy drop that leads to a larger turbine size. Similarly, M_4 increases substantially with MFR due to the increase in the enthalpy drop that leads to high rotor blade speed U_4. Therefore, a higher absolute velocity C_4 eventually results in higher M_4.

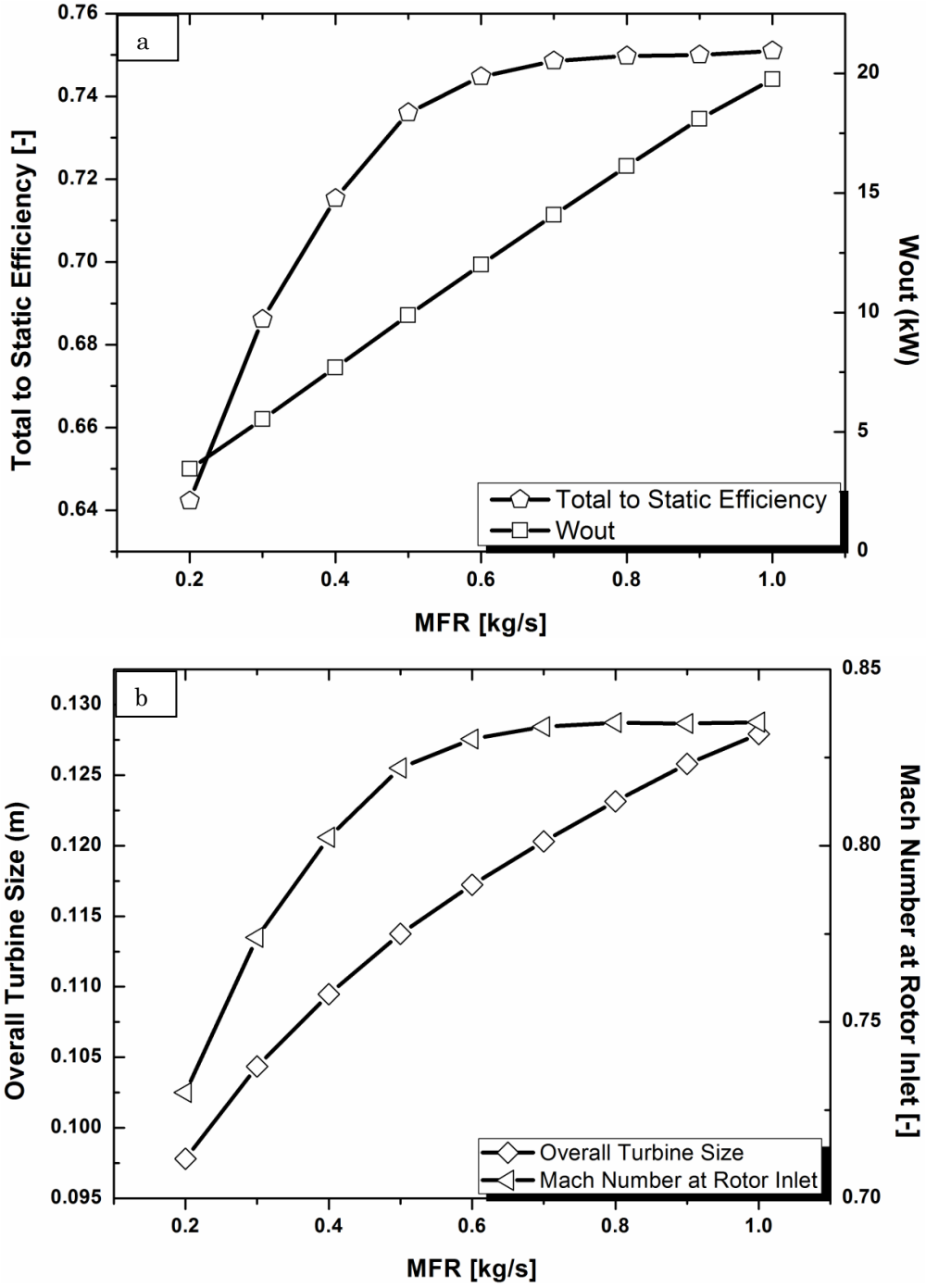

Figure 5-9: Effect of mass flow rate MFR on the investigated parameters.

Figure 5-10presents the effects when specific speed N_s is considered an input on the investigated parameters. According to the definition of the

specific speed N_s in equation(2-3),the rotational speed N and enthalpy drop Δh_{act} can be directly affected by changing the specific speed N_s, whereas the flow rate is constant (input parameter). Once the increase in the rotational speed N is prominent, the power and efficiency increase with N_s until a certain value is achieved. Subsequently, the performance decreases with the increase of N_s because the decrease in enthalpy drop Δh_{act} is more prominent than the increase in rotational speed N. This behaviour is depicted in Figure 5-10a. The increase ofN_s has a positive effect on turbine size $r_1$and Mach number M_4. The turbine size decreases due to the increase in the rotational speed N and the decrease in enthalpy drop, in which both parameters have a positive effect on the turbine size, as presented in Figure 5-8 and Figure 5-9. Figure 5-8bshows that the rotational speed N has an insignificant effect on M_4. However, the substantial decrease in M_4 is due to the low enthalpy drops. Therefore, this phenomenon leads to lower rotor blade speed U_4 and, hence, lower absolute velocity C_4 that eventually results in lower Mach numbers M_4.

Figure 5-11 summarises this section. The figure shows the positive or negative effect of each input parameter on the investigated parameters. The length of the bar indicates the strength of the effect of the input parameter, classified as strong, moderate or insignificant. The positive and negative signs indicate whether the input parameter has a positive or negative effect on the investigated parameters. Clearly, the four input parameters have a considerable positive effect on the turbine size r_1, and between an insignificant and considerable negative effect on Mach number M_4. These parameters also have a positive effect on the turbine power W_{out} and efficiency η_{ts}, except in the flow coefficient, in which the parameters have substantial negative effect on η_{ts} and a moderate negative effect on W_{out}. In addition, N_s has a positive effect on the performance of the turbine and becomes negative as $N_s$increases.

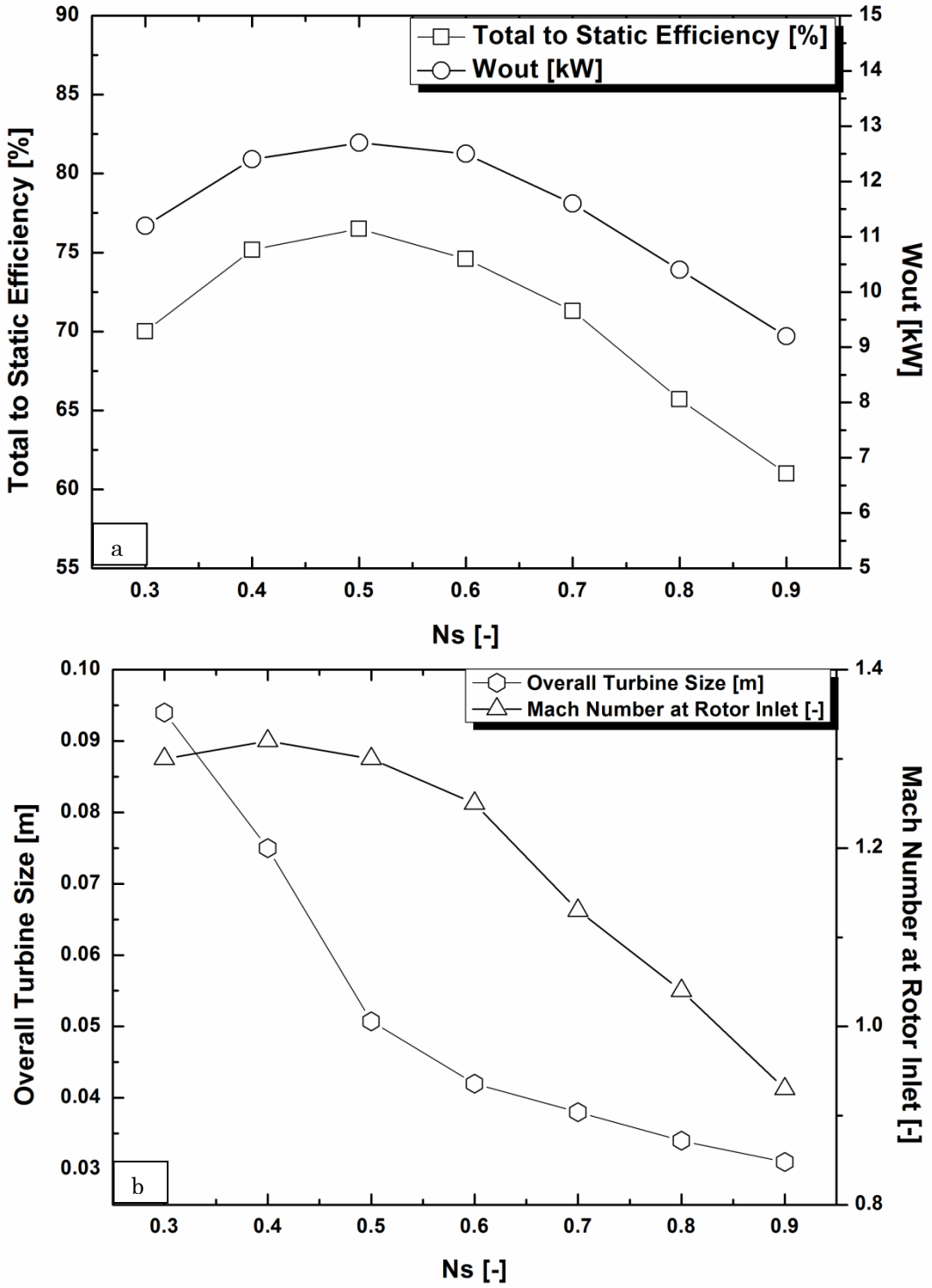

Figure 5-10: Effect of specific speed N_s on the investigated parameters.

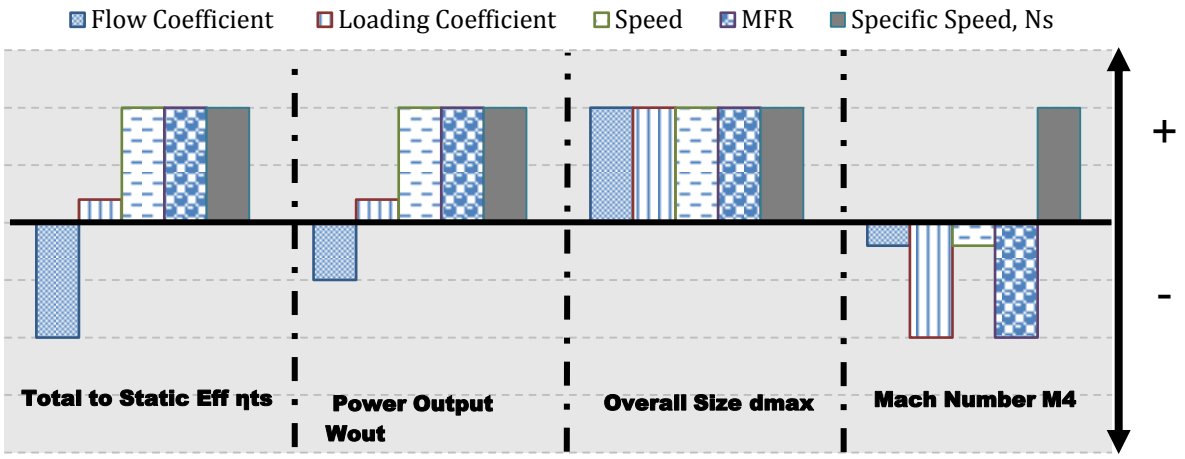

Figure 5-11: Summary of effects of the input conditions on the investigated parameters.

5.6.2.2 Design of Optimum Turbine

The initial estimates of the input parameters presented Table 4-1 are used to begin the optimisation process. This model has three objective functions:

- F_1: Total to static efficiency η_{ts}
- F_2: Turbine power output W_{out}
- F_3: Power density W_{out}/d_{max}

The results of the three objective functions are briefly presented in Figure 5-12. Figure 5-12ashows the results when F_1 is selected as the objective function. The optimum efficiency obtained is 74.4%, 71.8% and 70.1% whenF_1, F_2 and F_3 are selected, respectively. The high value of F_1 is due to the low enthalpy losses shown in Figure 5-13. The optimisation of F_1 results in low absolute velocity at turbine exit C_5 and, hence, low exit loss, as shown in equation (5-94). Moreover, the rotor speed U_4 and relative speed W_4 are the lowest, thereby resulting in lower tip clearance and incidence losses, as shown in equations (5-88) and(5-80), respectively.

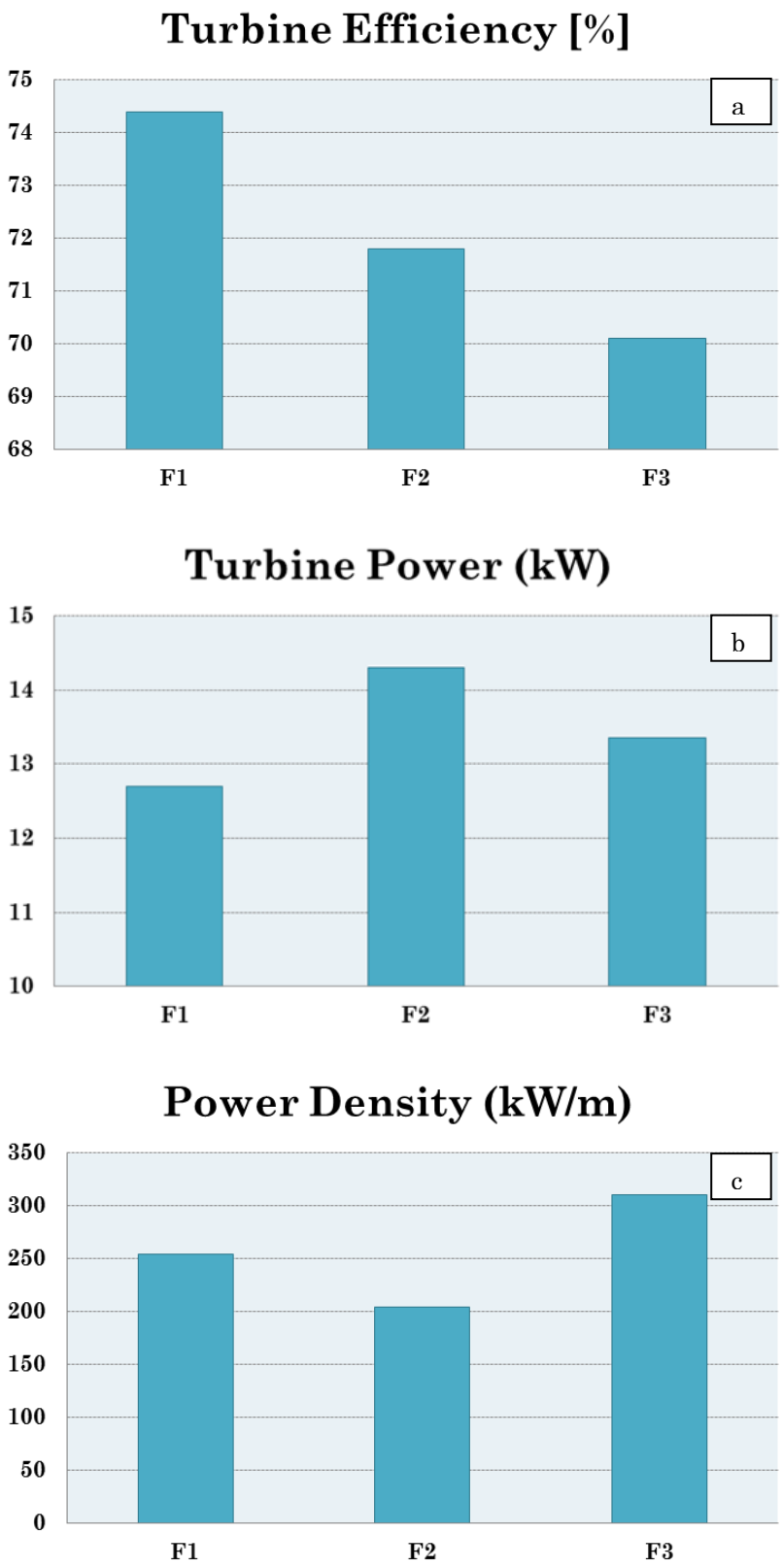

Figure 5-12: Results of the OC using different objective functions.

Figure 5-12b presents the result when F_2 is selected as the objective function. The maximum power output W_{out} is 14.3 kW, and 12.7 kW and 13.36 kW when F_1 andF_3 are selected, respectively. This result is directly

related to the Euler equation, where MFR and enthalpy drop Δh_{act} are the highest, as shown in equation(5-23).

Figure 5-12cshows the result when F_3 is selected as the objective function. In some applications in which the size of the component is limited, this objective function is very crucial because higher turbine power and compact size are combined. The optimum value of F_3 is 310.7 kW/m; with turbine power and size are 13.36 kW and 0.043 m, respectively. The turbine size is substantially improved; its values are 0.05m and 0.072m for F_1 and F_2, respectively.

Figure 5-13 presents the contribution of the rotor aerodynamic losses at the three objective functions. The losses model is explained in Section 5.7. For the three objective functions, the secondary losses are dominant. This phenomenon is due to the high turning at the blade exit that results in efficiency deterioration. Tip clearance is the second dominant loss, which is expected with organic fluids. Organic fluids have large densities and low operating mass flow rates, leading to smaller blade height at the rotor leading edge b_4 and,therefore, large tip clearance.

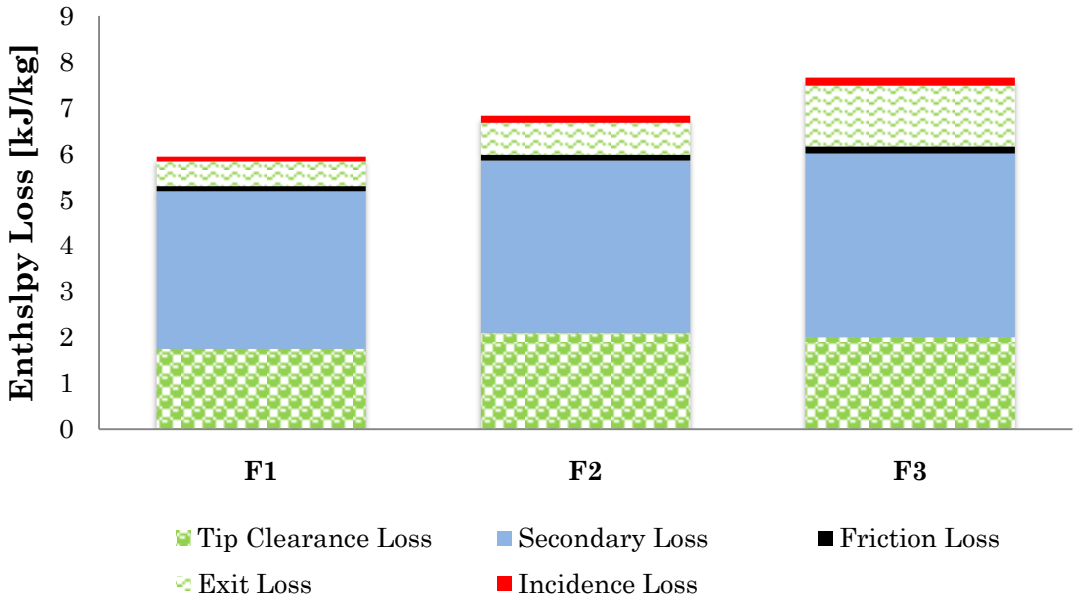

Figure 5-13: Contributions of the rotor enthalpy losses on the performance of the turbine.

Table 5-4 shows the details of the final optimised radial-inflow turbine. The relative flow angle β_4 is positive, which is in contrast with conventional turbines where a negative angle is always present. This phenomenon is beneficial to maintain optimum incidence at the rotor inlet.Table 5-4 shows also that the Mach number at the stator exit M_3 is greater than unity, thus indicating supersonic flows. However, this result is expected due to the high pressure ratio ($PR = 7$). Moreover, organic fluids usually have low values for the speed of sound, which leads to supersonic regimes. At the rotor exit, the values of Mach numbers ($M_{5,rel}$ *and* M_5) are way below unity, that is, the likelihood of the creation of shock waves at this region is low.

Table 5-4: Detailed Geometry and Performance of the Optimised Turbine

Parameter	Value	Unit
Volute: 1 Inlet 2: Exit		
r_1	0.0507	m
A_{th}	0.0004	m^2
Stator: 2 Inlet 3: Exit		
M_2	0.17	–
M_3	1.35	–
r_2	0.044	m
r_3	0.0356	m
b_2	0.004	m
b_3	0.004	m
α_2	68.9	deg
α_3	79.4	deg
s_v	0.013	m
$\beta_{blade\ ,2}$	76.3	deg
$\beta_{blade\ ,3}$	66.7	deg
Z_s	17	–
o_v	0.0016	m
c_v	0.01	m
Rotor: 4 Inlet 5: Exit		

M_5	0.45	
$M_{5,rel}$	0.58	
r_4	0.034	m
r_{5h}	0.008	m
r_{5t}	0.023	m
$r_{rms,5}$	0.017	m
b_4	0.003443	m
b_5	0.015	m
α_4	77	deg
α_5	10	deg
$\beta_{blade,4}$	54	deg
$\beta_{blade,5}$	-45	deg
N_r	15	$-$
z	0.0197	m
$\varepsilon_x = \varepsilon_r$	0.0005	m
	Performance	
N_s	0.5	$-$
R	0.46	$-$
v	0.642	$-$
η_{ts}	74.4	%
W_{out}	13.6	kW

5.7 Off-design Process (Performance Prediction)

Although the ORC system is a promising WHR technology, its cycle efficiency is low due to the low working temperatures. Therefore, designing an efficient turbine and predicting its performance are of great importance to avoid further efficiency reductions. In addition, the thermodynamic properties of heat sources are variable, thus making the prediction of turbine performance at different operating conditions even more important at the early stage of the design.

In recent studies, such as in [248]–[250], CFD has been used extensively to predict turbine performance. CFD is a reliable and powerful tool in analysing the flow within the turbine stage as it presents precise and detailed information about the flow nature at different turbine stagesin which the 1D mean-line is incapable to perform.ANSYS is one of the most powerful CFD tools available in the field. Beside the aforementioned benefits, ANSYS is capable of optimising the geometry of the turbine which results in higher performance, and creating full turbine maps that are beneficial to determine the performance of the turbine at off-design conditions.However, this method will consume time and computer resources. Therefore, predicting the off-design performance using a fast 1D model is a vital part during the design process.CFD, in turn, can be utilised to validate the 1D model and provide the required information about the flow nature through the turbine stage.

The output of off-design codes is basically the characteristic curves or performance maps. Subsequently, these maps are used to provide an estimate of turbine efficiency and power output at variable inlet conditions and rotational speeds. In the open literature, a number of off-design codes weredeveloped with air (ideal gas) as the working fluid.Jansen and Qvale[251] presented a performance prediction methodology of radial turbines. Although the results are in agreement with the experiments, the authors stated that this methodology was preferred with pressure ratios of up to 4. In 1969, Dadone and Pandolfi[252] conducted an off-design procedure for small- and large-size turbines. The results were in fairly good agreement with the experiments, except at high expansion ratios and low equivalent speeds where a slight discrepancy was noticed. NASA [253], [254] conducted off-design codes and the results were in good agreement with the experimental results. Other performance prediction procedures, such as those by [233], [255], [256], also exist. However, all the aforementioned methodologies are applicable when ideal gas is used as the working fluid. The thermodynamic properties of high-densityfluids, such as organic fluids, are different from those of ideal gas. For instance, organic fluids have high molecular weight, low boiling points and low speed of

sound. In addition, ORC radial turbines present high expansion ratio and Mach number at the stator exit due to the frequently changing specific volume, which results in supersonic flows. This outcome necessitates the use of a real EoS rather than the traditionally adopted Mach relationships for ideal gas. The thermodynamic properties at each station must likewise be checked simultaneously through the turbine stage. According to the authors' knowledge, no such methodologies are available in the open literature.

Once the basic geometric parameters of the turbine are calculated using the DPC, the geometry is subsequently exported to the off-design code to evaluate the turbine performance at different operating conditions. The outputs of the current code are the characteristic curves or performance maps. These maps can be integrated in any ORC model to investigate the effectiveness of the turbine in the overall cycle performance. A carefully selected nozzle model is used because supersonic expansion is an expected phenomenon in high-pressure ratio turbines. In addition, flow is expected to choke at the throat at high-pressure ratios. Therefore, a special treatment is also considered when choking occurs. The author implies that the proposed methodology is the first methodology that can be used to estimate the performance of radial-inflow turbines integrated in ORC applications.

5.7.1 Description of the Methodology

Compared with the DPC, the off-design procedure begins from the volute and ends at the rotor exit. In each station, the continuity equation is used as the control point where convergence must be achieved. A detailed loss model from the open literature is also applied to investigate the real performance of the turbine. Figure 5-14presents the flowchart of the full off-design modelling.

At the volute inlet, absolute velocity C_1 is considered an initial value. Static enthalpy is subsequently calculated using the First Law of Thermodynamics, as shown in equation(5-56). The other thermodynamic properties are subsequently calculated using the EoS at$\{h_1, S_1\}$. The process is repeated until convergence is achieved, as shown in equation(5-68).

$$C_1 = \frac{m_1}{\rho_1 A_1} \tag{5-68}$$

m_1 is assumed and must be verified at the end of the process, as shown in Figure 5-14. Similar to the design point, the volute loss model is applied to obtain the thermodynamic properties at the volute exit. Velocities are obtained iteratively using the continuity equation.

Special attention is paid in the investigation of the flow environment at the stator outlet because ORC turbines usually have high pressure ratios and, hence, supersonic flows at the stator trailing edge. The detailed procedure is shown in Figure 5-14. When the blade row is choked, sonic speed is assumed in the throat opening. Similar to the stator inlet, stator outlet is resolved iteratively until convergence at the mass flow rate is achieved. Baines[257] proposed a correlation to calculate the absolute flow angle at the stator exit α_3, as shown in equation (5-69). a_0, a_1 and a_2 are 6, 0.96 and -4, respectively.

$$\begin{cases} \alpha_3 = a_0 + a_1 cos^{-1}\left(\frac{o_3}{s_v}\right) + \delta_s \quad for \quad M_3 > 0.3 \\ \alpha_3 = a_0 + a_1 cos^{-1}\left(\frac{o_3}{s_v}\right) + a_2(Ma_3 - 0.3) + \delta_s \quad for \quad M_3 \leq 0.3 \end{cases} \tag{5-69}$$

The loss model at the stator outlet is appliedto resolve the thermodynamic properties at the stator outlet. Once the stator loss is calculated, the isentropic enthalpy is consequently calculated. Several stator loss models [235], [258]–[260] can be found in the open literature. However, all these available loss models are likely to be either assessed wholly empirically or approximated through flat plate and pipe flow fiction relations [233]. The stator loss model proposed by Balje[246] is applied because the loss model in this study are expressed in terms of enthalpy drop, as shown in equation (5-70)below.

$$\Delta h_{stator} = 4C_f \left(\frac{l_{hyd}}{d_{hyd}}\right)\left(\frac{C_2 + C_3}{2}\right)^2 \tag{5-70}$$

C_f is the friction coefficient in the nozzle row.Churchill[261], [262] developed a correlation of the coefficient of friction using the Moody diagram, as shown in equation (5-71). Re is the average of the Re between the inlet and exit of the nozzle and is expressed in Equation (5-72).

$$C_f = \left[\left(\frac{8}{\overline{Re}}\right)^2 + \left(\left[2.457\, ln\left(\frac{1}{\left[7\frac{1}{\overline{Re}}\right]^{0.9} + 0.27wr}\right)\right]^{16}\left(\frac{37530}{\overline{Re}}\right)^{16}\right)^{-\frac{3}{2}}\right]^{\frac{1}{12}} \quad (5\text{-}71)$$

$$\overline{Re}_{nozzle} = \frac{\frac{C_2 b_2 \rho_2}{\mu_2} + \frac{C_3 b_3 \rho_3}{\mu_3}}{2} \quad (5\text{-}72)$$

rr is the relative wall roughness, and a value of 0.0002 m is used as suggested by [234].

In ORC turbines, supersonic phenomenon ($M_3 > 1$)is expected at the stator exit due to the higher pressure ratio of the cycle and low speed of sound for organic fluids. For $M_3 > 1$, the flow is choked and the mass flow remains constant for any pressure ratio equal or greater than the choked value. In this case, the pressure ratio can have infinite number of values at the same mass flow rate. Therefore, the choked condition has been considered in the current model. When the blade raw is choked at the stator exit, the choked mass is kept fixed. Then, the velocity triangle is solved using the choking mass flow rate value without the need for iteration.

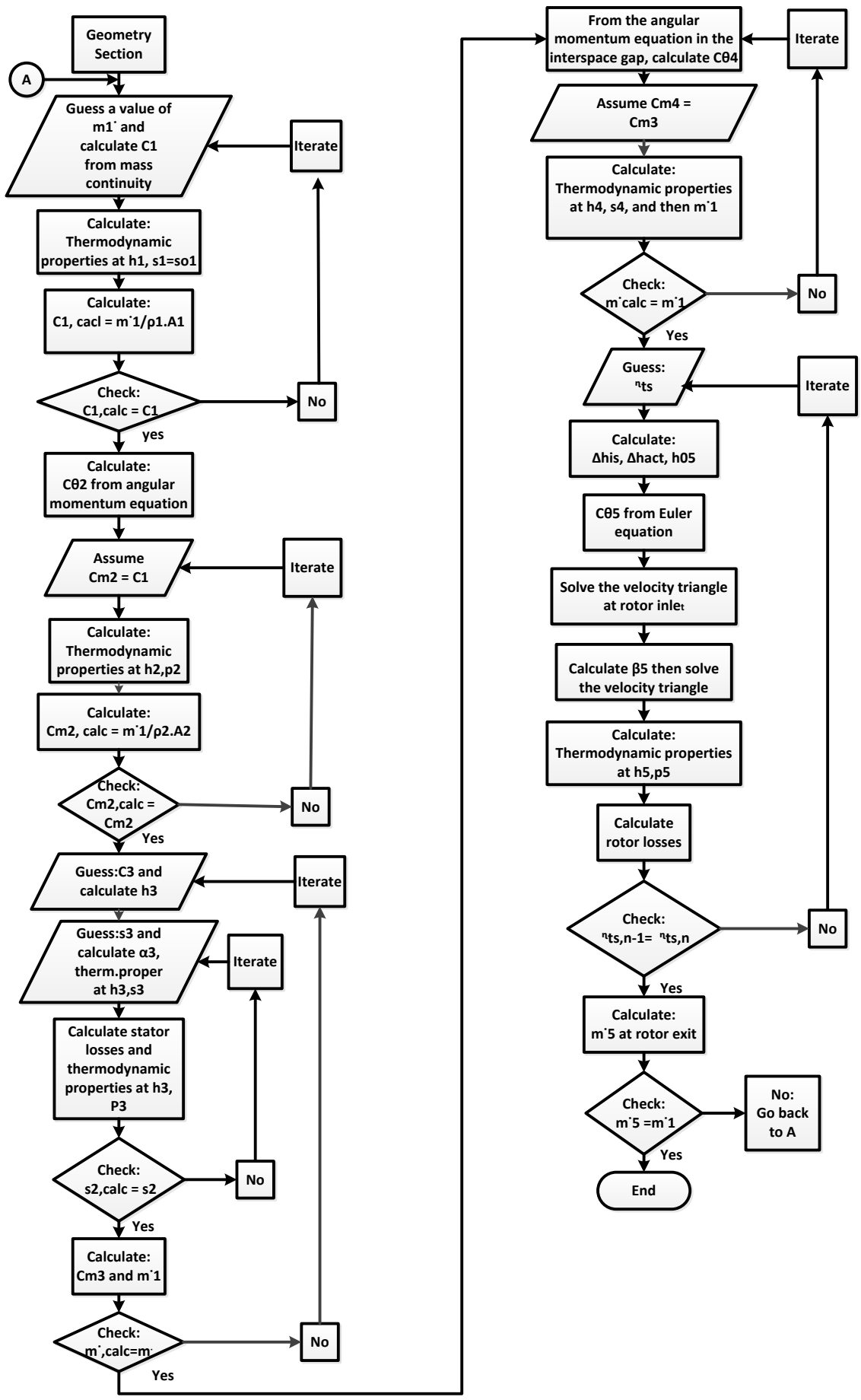

Figure 5-14: Flowchart of the off-design methodolgy.

As previously stated, the conservation of angular momentum can be applied in the interspace [244]. Therefore, the tangential component of the velocity at the rotor leading edge $C_{\theta 4}$ is calculated using equation (5-37). The rest of the velocity parameters and static thermodynamic properties are calculated iteratively with a first assumption of $C_{m4} = C_{m3}$ until convergence is achieved, as shown in equations (5-73) to (5-77).

$$C_4 = \sqrt{Cm_4^2 + C\theta_4^2} \tag{5-73}$$

$$W_4 = \sqrt{Cm_4^2 + (U_4 - C\theta_4)\text{^}2} \tag{5-74}$$

$$h_{04} = h_4 - \frac{1}{2}C_4^2 \tag{5-75}$$

$$\{h_4, S_4\} = EoS(\rho_4, T_4, a_4, P_4, fluid) \tag{5-76}$$

$$Cm_4 = \frac{\dot{m}}{\rho_4 A_4} \tag{5-77}$$

Predicting the velocity triangle and the thermodynamic properties at the rotor exit is a relatively long process. The isentropic and actual enthalpies are calculated using equations (5-6) and (5-7), respectively, after an initial value of the total to static efficiency η_{ts} is specified. The tangential velocity of the rotor exit $C_{\theta 5}$ is calculated at the off-design process using the Euler equation, as shown in equation (5-23). The relative flow angle of the rotor exit β_5 is calculated using the equation presented in [263].Benson[263] stated that β_5 should be calculated based on the cosine rule at the mean radius, and some deviation due to rotor speed may be present. Therefore, cosine rule is applied in the current study and flow deviation δ_r is considered, as shown in equation(5-78). The velocity triangle is now complete at the rotor exit, and the thermodynamic properties are subsequently obtained using the EoS.

$$\beta_5 = -\cos\left(\frac{o_{r,rms}}{s_{r,rms}}\right) + \delta_r \tag{5-78}$$

Therotor loss model is implementedto validate the initial assumption of the total to static efficiency η_{ts}. Different loss models in the radial inflow are proposed [231], [233], [235], [237], [238]. Most of these models are developed from the measurements and results in large-scale turbines and with ideal gas as the working fluid. The achieved turbine power output in turbo-machinery decreases with the overall size of the turbine [242]. Moreover, reducing the turbine size will result in high rotational speeds and low efficiency due to the increased aerodynamic losses.Suhrmann[242] stated that no size effect is usually implemented in known empirical loss models in the literature. Thus, they investigated the capability of the available losses in the literature to predict the flow in small-size turbines using full 3D CFD. The results of their study are mentioned in the relevant sections in the breakdown of losses.

The majority of losses in the turbine stage occurred in the rotor. The loss model of the rotor is based on a well-established model outlined in [242], [257]. Five main losses, namely, incidence, passage, tip clearance, windage and exit energy, are included in the present model. Subsequently, rotor loss is calculated as the sum of the total losses of the rotor, as shown inequation(5-79).

$$\Delta h_{loss,rotor} = \Delta h_{incidence} + \Delta h_{passage} + \Delta h_{tip} + \Delta h_{windage} + \Delta h_{exit} \quad (5\text{-}79)$$

- Incidence Loss

Incidence loss results from the loading of a blade, which causes the fluid to enter the rotor at an angle that differs from the optimum one. Equation(5-80) presents the incidence loss used in this work.

$$\Delta h_{incidence} = \frac{1}{2}[W_4 \sin(\beta_4 - \beta_{4,opt})]^n \quad (5\text{-}80)$$

The optimal relative flow angle $\beta_{4,opt}$ is determined by the empirical correlation by [233], as shown in equation (5-81). n is 2 for negative incidence and 3 for positive incidence [257].

$$\tan(\beta_{4,opt}) = \frac{-1.98\tan(\alpha_4)}{Z_r\left(1-\frac{1.98}{Z_r}\right)} \tag{5-81}$$

- Passage Loss

Passage loss includes any loss within the blade passage, such as secondary flow and mixing flow loss. Venture[240] used a loss model that combines the correlations by [242] and [235], as shown in equation (5-82).

$$\Delta h_{passage} = \frac{1}{2}\left(2f_t\frac{L_h}{D_h}\bar{W}^2 + \frac{r_4 C_4^2}{r_c Z_r}\right) \tag{5-82}$$

where

$$D_h = \frac{1}{2}\left[\frac{4\pi r_4 b_4}{2\pi r_4 + Z_r b_2} + \frac{\pi\left(r_{5,sh}^2 - r_{5,h}^2\right)}{\pi\left(r_{5,sh} - r_{5,h}\right) + Z_r\left(r_{5,sh} - r_{5,h}\right)}\right. \tag{5-83}$$

$$L_h = \frac{\pi}{2}\sqrt{\frac{1}{2}\left[\left(r_4 - r_{5,sh} + \frac{b_4}{2}\right)^2 + \left(\frac{r_{5,sh} - r_{5,h}}{2}\right)^2\right]} \tag{5-84}$$

$$f_c = f\left(1 + 0.075Re^{0.25}\sqrt{\frac{D_h}{2r_c}}\right) \tag{5-85}$$

$$f_t = f_c\left[Re\left(\frac{r_4}{r_c}\right)^2\right]^{0.05} \tag{5-86}$$

$$r_c = r_4 - r_5 \tag{5-87}$$

- Tip Clearance Loss

An inevitable leakage occurs in the rotor blades from the pressure surfaces to the suction surfaces owingto the existinggap between the turbine casing and the rotor. The minimum clearance is usually a compromise between manufacturing difficulty and aerodynamic requirements [197]. The axial and radial clearances shown inFigure 4-2 are defined as the distance between the rotor and the casing inlet and outlet, respectively. According to Baines [257], radial clearances are more important because of the complex development of secondary flow at the rotor exit. The clearance loss is calculated as follows:

$$\Delta h_{tip} = \frac{U_4^3 Z_r}{8\pi}\left(K_a \varepsilon_a C_a + K_r \varepsilon_r C_r + K_{a,r}\sqrt{(\varepsilon_a \varepsilon_r C_a C_r)}\right) \quad (5\text{-}88)$$

C_a and C_r are the axial and radial coefficients for the tip clearance model calculated using equations(5-89) and (5-90), respectively [233], [257]:

$$C_a = \frac{1 - \frac{r_{5,sh}}{r_4}}{C_{m4} b_4} \quad (5\text{-}89)$$

$$C_r = \left(\frac{r5, sh}{r_4}\right)\frac{Z_r - b_4}{C_{m5} r_5 b_5} \quad (5\text{-}90)$$

- Windage Loss

Another leakage occurs between the back-face and the housing of the rotor due to the existinggap, which results in another frictional loss. This gap also generates high centrifugal stresses at the gaps in the tip clearance [264]. The behaviour of fluid flow in the region was investigated by Daily and Nece[265],who considered a rotating disc in an enclosed casing, as shown in equation (5-91).

$$\Delta h_{windage} = k_f \frac{\bar{\rho} U_4^3 r_4^2}{2\dot{m}} \quad (5\text{-}91)$$

k_f denotes the empirical correlation for frictional torque bySuhrmann[265]with two equations based on the nature of the flow as follows:

$$k_f = \frac{3.7\left(\frac{\varepsilon}{r_4}\right)^{0.1}}{Re^{0.5}} \text{ for laminar flow } (Re < 10^5) \quad (5\text{-}92)$$

$$k_f = \frac{0.102\left(\frac{\varepsilon}{r_4}\right)^{0.1}}{Re^{0.2}} \text{for Turbulent flow } (Re > 10^5) \quad (5\text{-}93)$$

$\bar{\rho}$ is the mean fluid density evaluated by the static condition of rotor inlet and outlet. ε denotes the clearance gap between the back face and the housing of the rotor wheel.

- Exit Energy Loss

Lastly, the internal energy at the rotor exit is converted into kinetic energy, and it increases with high swirl angles. This kinetic energy is unusable, and therefore considered an additional loss. Some of the energy can be recovered by implementing a diffuser that convertsa portion of this kinetic energy into static pressure. The prediction of kinetic energy loss is based on equation (5-94), which is reported in [242].

$$\Delta h_{exit} = \frac{1}{2} C_5^2 \tag{5-94}$$

The new efficiency is subsequently calculated, as shown in equation (5-95). The process is repeated until convergence is achieved.

$$\eta_{ts} = \frac{\Delta h_{act}}{\Delta h_{act} + \Delta h_{loss,volute} + \Delta h_{loss,stator} + \Delta h_{loss,rotor}} \tag{5-95}$$

In addition, the mass flow rate at the rotor exit is calculated using equation (5-96) to validate the first assumption at the volute inlet. If the two values do not match, then a new value of the mass flow rate is assumed and the process is repeated, as shown in Figure 5-14.

$$\dot{m_5} = \rho_5 C_{m5} A_5 \tag{5-96}$$

Although choking is unlikely at the rotor throat, similar treatment to the stator model has been added when choking takes place at the rotor.

5.7.2 Validation of the Off-Design Code

The results are compared with three experimental works, namely, Turbine A, B and C,to evaluate the reliability of the proposed design methodology. Prior to the experimental validation, the work was firstly compared with

CFD results. The CFD results mentioned in this chapter are only for comparison. The full CFD results are detailed in Chapter 6.

Turbine Awas conducted by Spence et al. [266]using air as the working fluid. The tests were conducted at a range of turbine speeds between 30,000 rpm and 60,000 rpm and pressure ratios between 1.3 and 4. Seven stator configurations were used in the test. All configurations have the same basic blade shape but different vane angles and, consequently, different throat areas.

Evaluating the code using real fluids is crucial. Turbine B, that was conducted by Shao et al[267] using R123 (high dense organic fluid) as the working was used. Different heat source temperatures were investigated in the study. Isentropic total to total efficiency was also investigated at turbine speeds of 20,000–54,000 rpm and pressure ratios of 1.4–2.6. In the current study, a heat source of 120 °C was selected to validate the results of the proposed methodology. Detailed geometry parameters of Turbines A and B are presented in Table 5-5.

However, significant geometrical parameters (stator opening and blade height) were not provided in the aforementioned reference [267]. Therefore, the code was also validated with the current turbine (Turbine C), in which all the geometrical parameters are available. The experimental results of Turbine C are presented in Chapter 7. Table 5-6 presents the input thermodynamic parameters for three turbines.

Table 5-5: Geometric Parameters of Turbines A and B.

Parameter	Symbol	Turbine A	Turbine B
Nozzle vane number	-	16	17
Nozzle inlet diameter	r_2	152.0 mm	70.0 mm
Nozzle vane height	b_2	10.2 mm	10.2 mm
Rotor inlet tip diameter	d_4	99.06 mm	99.06 mm
Rotor inlet tip width	b_4	10.2 mm	10.2 mm
Rotor inlet blade angle	$\beta_{blade\ ,4}$	0 deg	0 deg
Rotor blade number	-	11	12
Rotor exducer tip diameter	r_{5t}	79.0 mm	34.0 mm
Rotor exducer hub diameter	r_{5h}	30.0 mm	19.0 mm
Rotor exducer blade thickness	t_5	1.6 mm	1.6 mm
Rotor exit radial clearance	ε	0.4 mm	0.4 mm

Table 5-6: Thermodynamic parameters for the three turbines.

Parameter	Symbol	Turbine A	Turbine B	Turbine C
Inlet Stagnation Pressure [kPa]	P_{01}	141.86 – 506.63	220 - 440	180 - 900
Inlet Stagnation Temperature [K]	T_{01}	400	393.15	423.15 – 437.5
Mass Flow Rate [kg/s]	MFR	0.094 – 0.153	0.019 – 0.07	0.03 – 0.815
Pressure Ratio [-]	PR	1.3 - 5	1 - 4	1.38 - 7
Rotational Speed [RPM]	N	30,000 – 60,000	20,000 – 51,000	15,000 – 20,000

5.7.3 Off-Design Results

5.7.3.1 Parametric Study

Similar to the design point, a parametric study has been performed in the performance prediction analysis prior to validating the model. This is very crucial in order to evaluate the effects of the empirical input parameters that are under the control of the designer. These input parameters are deviation angles, blockage factors, and rotor incidence angle. It is worth mentioning that the operating conditions for the parametric study are the same as the conditions mentioned in turbine A.

Figure 5-15 presents the influence of the stator deviation angle on the MFR and efficiency of radial inflow turbines. The figure clearly shows that the turbine MFR is very sensitive to the stator deviation angle. As the angle increases from 0 to 2, the MFR decreases by 12%. Changing the deviation angle from 0 to -2, the MFR increases by 12%. The relationship between the MFR and the stator deviation angle is related to the definition of the MFR at the stator exit. The deviation angle is defined as the difference between the vane angle (setting angle) and the flow angle. As the flow angle moves towards the negative direction (the deviation moves towards the positive direction), the mass flow significantly decreases, and vice versa. Figure 5-15 also shows that the stator deviation has moderate impact on the turbine efficiency. As the deviation angles moves to the negative direction, the Mach

number increases at stator exit[258], [268]which results in lower turbine efficiency.

The turbine MFR and efficiencywerealso investigated by changing the rotor deviation angle by ±2°. It is obvious that the rotor deviation angle has no impact on the MFR. Its effect on the turbine efficiency is small but not negligible. The efficiency decreases as the deviation angles moves to the positive direction and increases in the negative direction. This is justified by the increase and decrease of the swirl at the rotor exit. As the deviation angle moves to the positive direction, the swirl increases which results in slightly lower efficiencies.

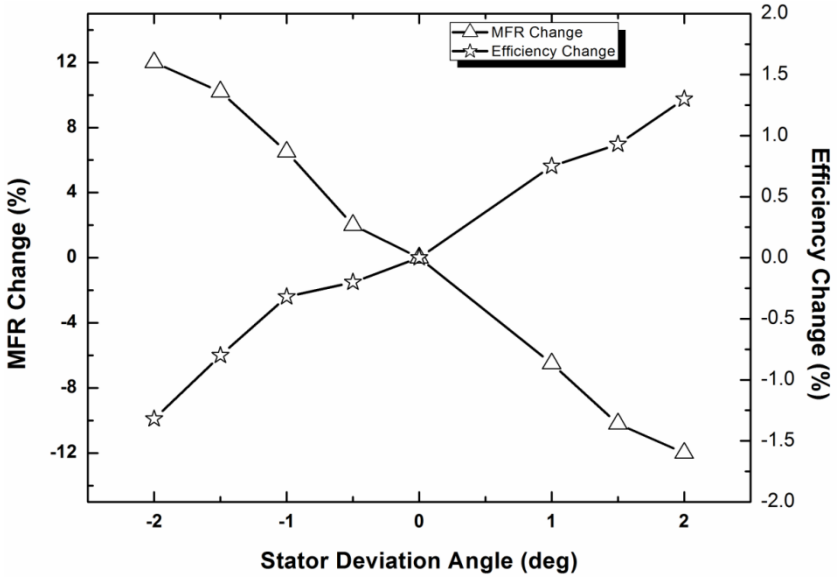

Figure 5-15: Effect of stator deviation angle on turbine η_{ts} and MFR.

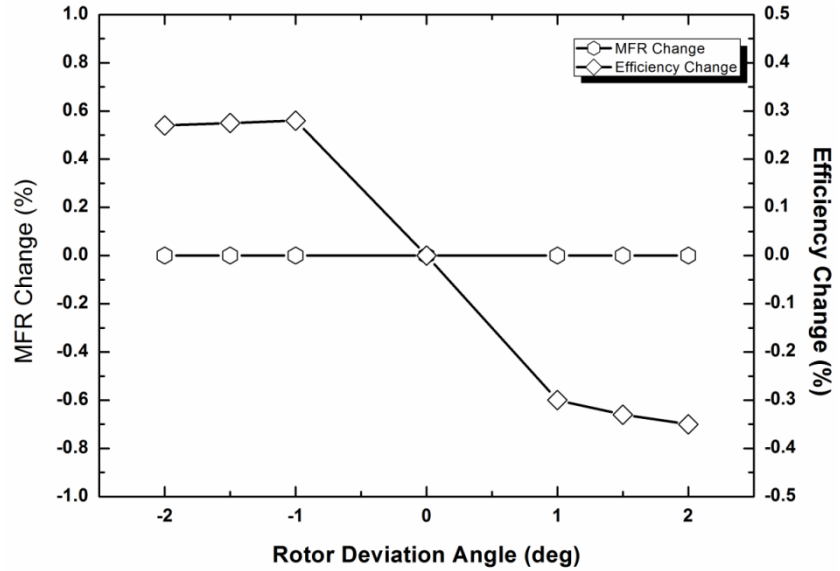

Figure 5-16: Effects of rotor deviation angle on turbine η_{ts} and MFR.

In addition, the blockage factors were evaluated as shown in Figure 5-17and Figure 5-18. Increasing the stator blockage has severe impact on the MFR as the flow area decreases with increasing the blockage factor. As the blockage increases from 0 to 0.2, the MFR decreases by 20%. On the other, the stator blockage has insignificant impact on the turbine performance with a maximum reduction of 0.46% when the blockage increases from 0 to 0.2. This slight effect is related to the change in the incidence angle which results in higher velocity (absolute velocity) at the stator exit.

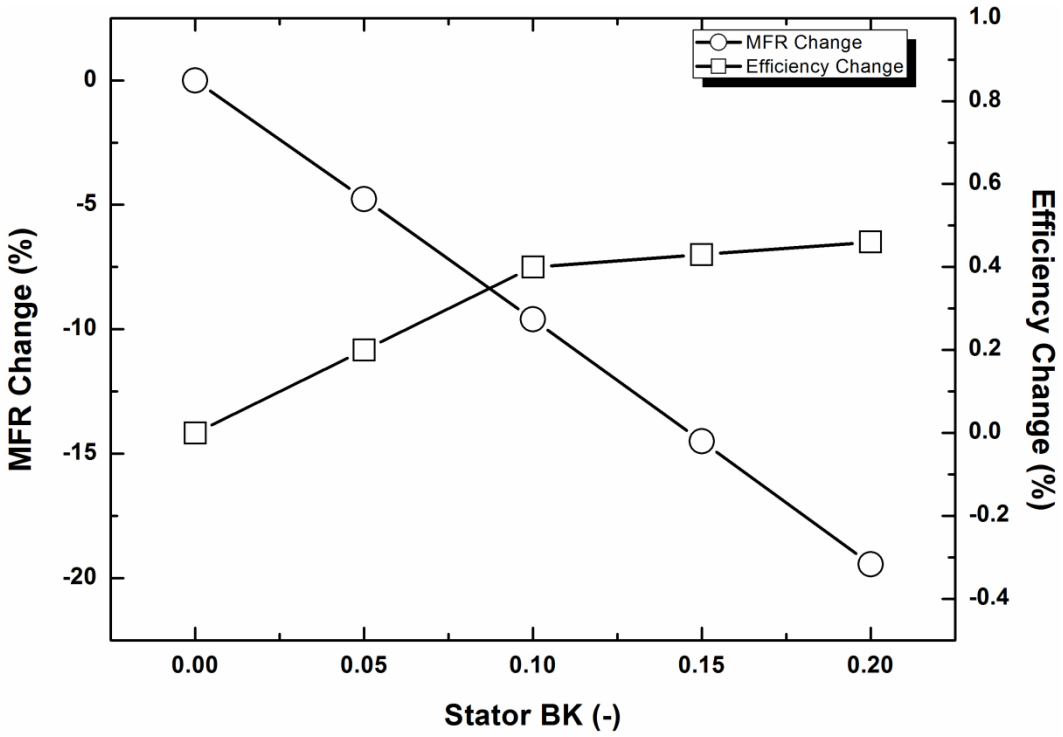

Figure 5-17: Effects of stator blockage factor on turbine η_{ts} and MFR.

The impact of the rotor on the MFR and efficiency is plotted in Figure 5-18. The effect of the blockage on the MFR is directly related to equation(5-13). The efficiency is relatively sensitive to the rotor blockage due to, beside the reduction in MFR, the increased kinetic energy loss at the rotor exit. As the blockage increases from 0 to 0.2, the MFR and efficiency decrease by 1.3% and 6.27%, respectively.

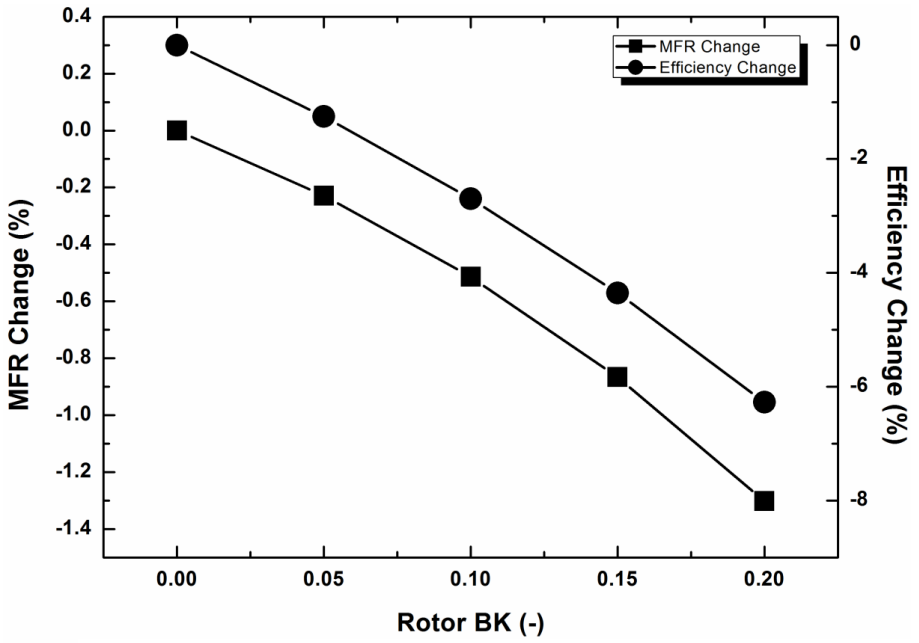

Figure 5-18: Effects of rotor blockage factor on turbine η_{ts} and MFR.

Last but not least, the rotor incidence angle was investigated and the results are depicted in Figure 5-19. According to the measurement ofWoolley and Hatton[269], the flow became more uniform as the incidence angle moved from 0 to negative values until reaching -40. Beyond -40, the flow separation appeared again on the pressure side. Baines [270] agreed with Wooley and Hatton regarding the fact that the best turbine performance is achieved when the incidence angle lies in the range of -20 to -40. He also stated that zero or positive incidence has the effect of reducing the cross-passage pressure gradient which results in flow separation on the suction surface. In addition, Kline et al. [271]stated that positive incidence results in higher exit energy loss, leadingto lower turbine efficiency. The results shown in Figure 5-19 are in agreement with what mentioned above. The best performance is achieved with the incidence angle in the range of -20 to -40. At -50, the efficiency drops dramatically. At low pressure ratios (up to 1.75), the performance of the turbine is similar for different incidence angles. At higher values (PR > 1.75), the incidence angles -40, -20, and 0 respectivelyshow best performance.

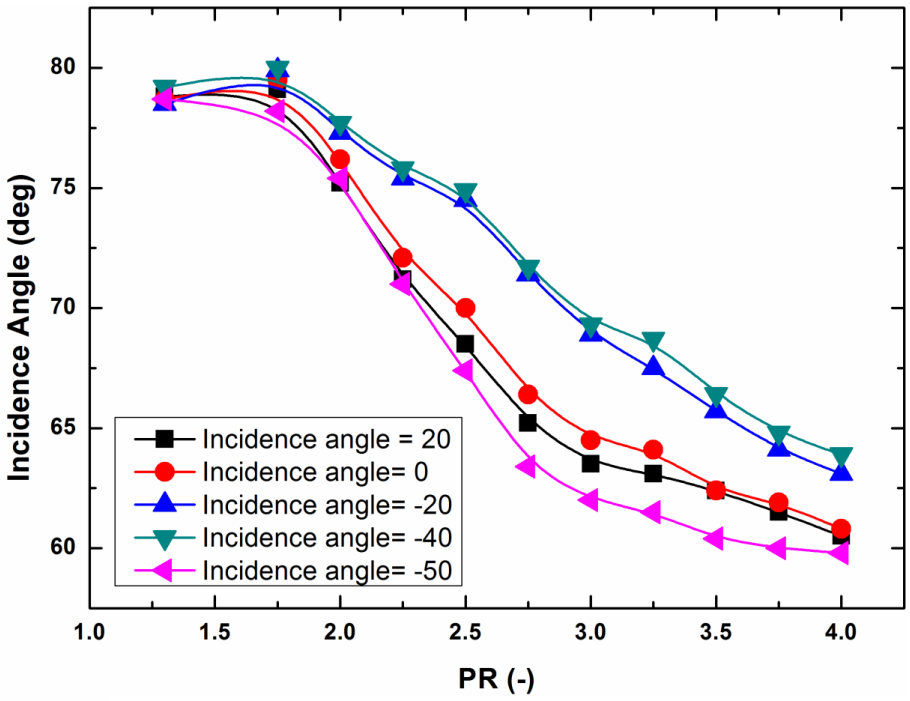

Figure 5-19: Effects of rotor incidenceangle on turbine η_{ts} and MFR.

5.7.3.2 Validation of the MOC using CFD

Prior to the experimental validation, the MOC was validated with the CFD results of Turbine C (detailed in Chapter 6). The results are presented inFigure 5-20 and Figure 5-21. Firstly, it is clear that the turbine performance at off-design speeds (20,000 rpm and 30,000 rpm) is better than the design point speed at very low pressure ratios. This is expected since the turbine has been designed to operate under high pressure ratios. At pressure ratio (PR≥5), the design point speed (40,000 rpm) presents better performance compared to the off-design speeds. At the design point, the peak efficiency reaches 73.4% at PR = 7.

Figure 5-20 and Figure 5-21 also depict the comparison between the CFD steady-state results and MOC at 40,000 rpm. It is obvious that the results are in very good agreement especially at low pressure ratios. As the pressure ratio increases, the efficiency slightly deviates with a maximum deviation of 2.8% at PR = 6.9.

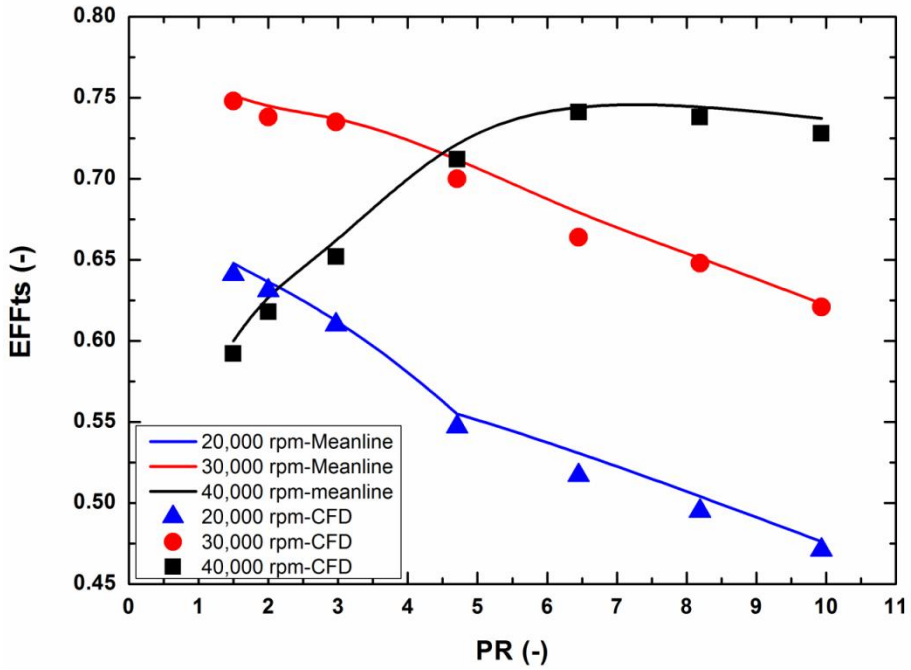

Figure 5-20: η_{ts} comparison betweenMOC and CFD results.

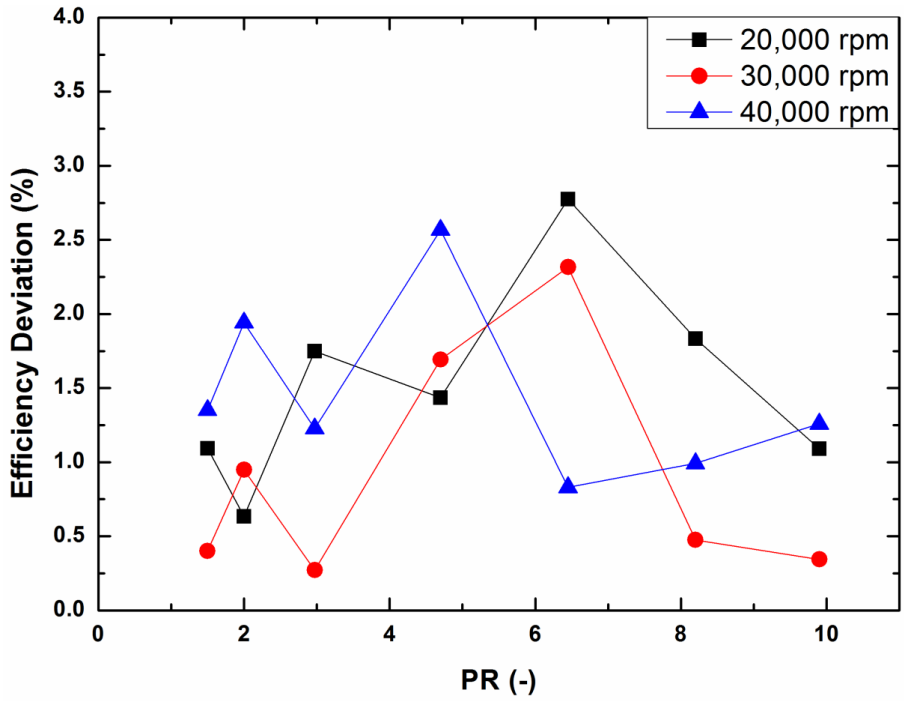

Figure 5-21: Deviation in η_{ts} between MOC and CFD.

As stated, supersonic flow is likely to take place in ORC turbines operating under high pressure ratio. Therefore, the corrected mass flow is applied instead of the real mass flow rate. In this case, the mass flow rate relies only on the corrected mass flow rate and the operating conditions regardless of the turbine speed and enthalpy drop, as shown in equation(5-97). The

corrected mass flow rate is also known as mass flow parameter (MFP). The results are presented in Figure 5-22. As expected, the turbine chokes at $PR \geq 4.8$. The highlighted zone in the figure shows the operating range for the turbine of the current project.

$$MFP = \frac{\dot{m}\cdot\sqrt{T_{01}}}{P_{01}} \qquad 5\text{-}97)$$

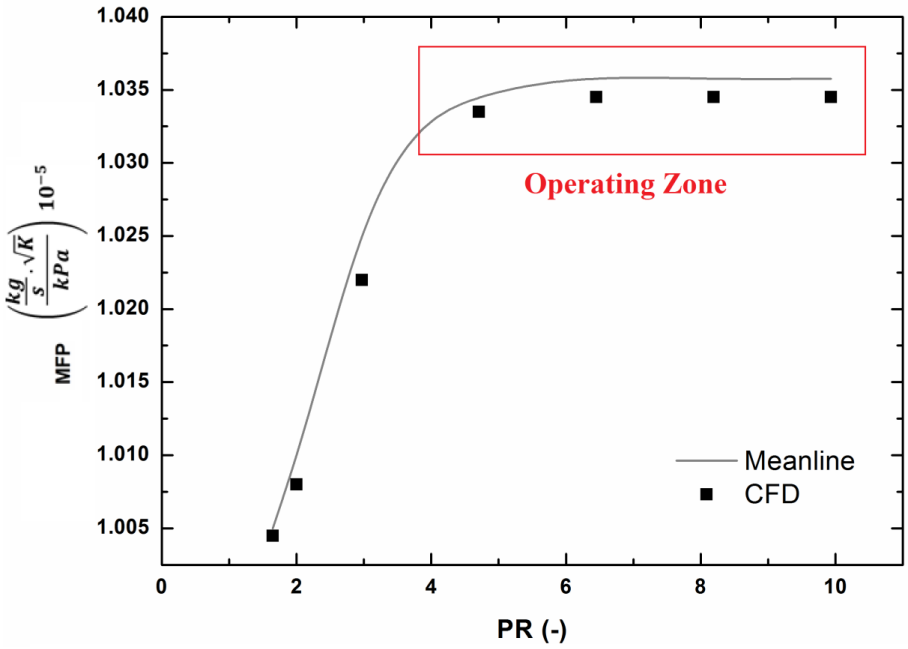

Figure 5-22: MFP operaring range in the MOC.

5.7.3.3 Validation of the MOC using Experimental Work

a) Radial Turbine for Ideal Gases (Turbine A)

Figure 5-23presents the comparison between the predicted and measured flow rates of Turbine A at different speed and pressure ratio conditions. Figure 5-24alsodepicts the deviation between the predicted and measured values. The predicted values using the MOC are in fairly good agreement with the experimental results. A maximum deviation of 6% is noticed in the 40,000 rpm, followed by the 30,000 rpm with a maximum deviation of 5.6%. For the 30,000 rpm and 60,000 rpm speed lines, the errors are below 3% and

3.8%, respectively, for the whole range of operation. These results indicate that the applied stator model is very appropriate for the current methodology. It is worth mentioning that, independently of the turbine speed, the deviation angle for the stator in equation(5-69)is set to -0.45^o. This value was selected after investigating a set of values located in the range of $-2^o\ to\ 2^o$ as shown in Figure 5-15. In addition, the optimum incidence angle is set to-40^o which lies in the range recommended in[231]. Moustapha et al.[231] reported that radial inflow turbines present optimum performance when the incidence angle lies in the range of $-40^o\ to\ -20^o$. Within this range, the incidence angle of -40^oshowed the best consensus between the predicted and measured mass flow rates. Figure 5-23depicts also the extrapolation of the existing turbine map where the pressure ratio range is extended to PR = 5. The results clearly showed that the flow chokes at $PR \geq 4.5$.

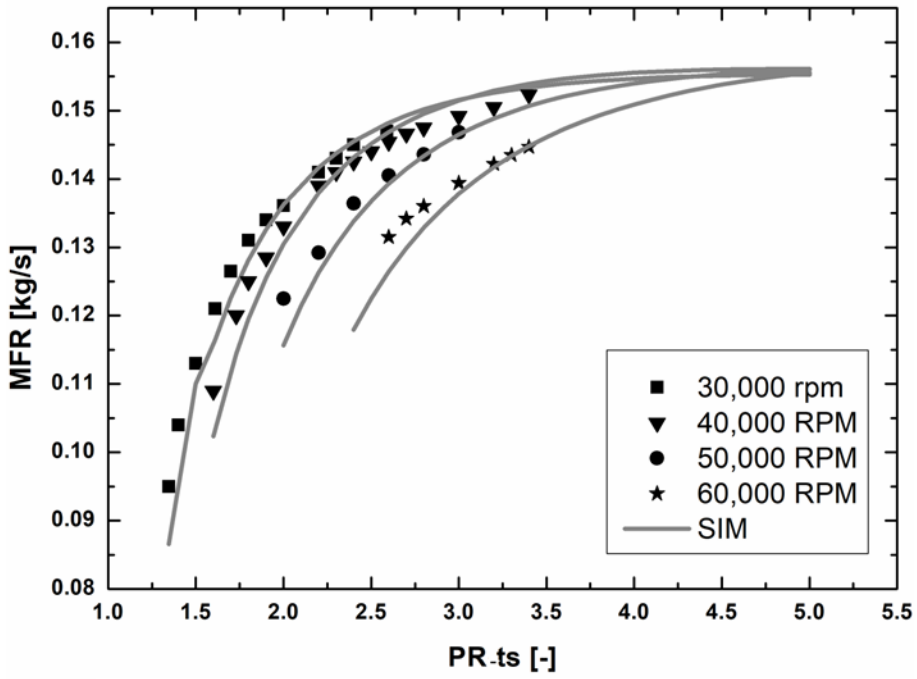

Figure 5-23: Comparison between predicted and measured MFR for Turbine A.

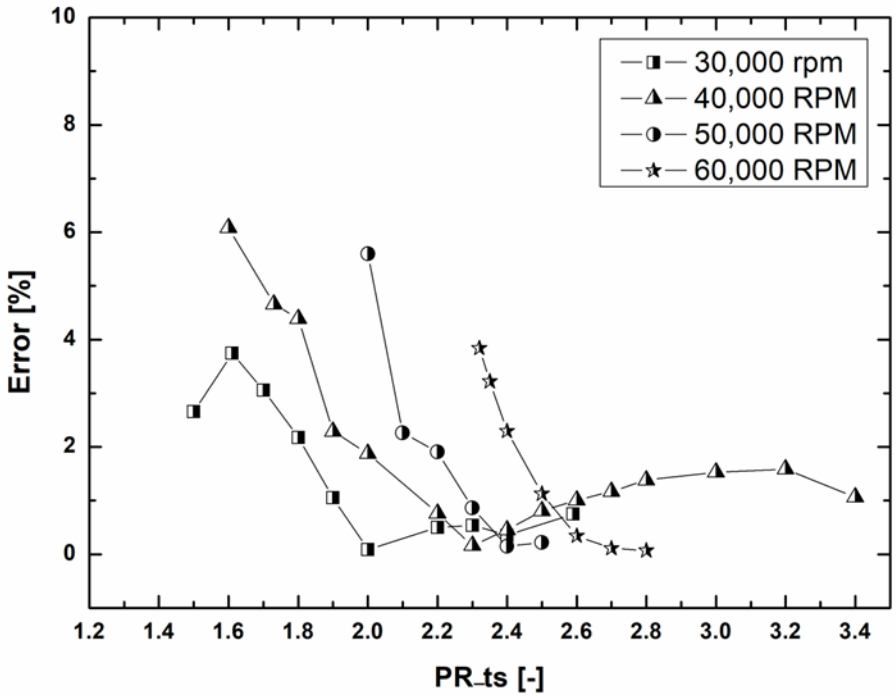

Figure 5-24: Deviation between predicted and measured MFR for Turbine A.

Figure 5-25and Figure 5-26show the comparison between the predicted and measured total to static efficiency, and the deviation between the two sets, respectively. In order to obtain more practical results, the modelling parameters have to be consistent. Therefore, the stator deviation angle and the rotor incidence angle are kept -0.45^o and -40^o , respectively. Figure 5-25shows a good prediction of the turbine total to static efficiency. The 30,000 rpm speed line showed the highest discrepancy with a maximum deviation of 5.67% followed by the 40,000 rpm speed line with a maximum deviation of 5.54%. For the 50,000 rpm and 60,000 rpm speed lines, the deviations don't exceed 3.2% and 1.6%, respectively, for the whole range of operation. Overall, the agreement between the predicted and measured values of total to static efficiency η_{ts} is quite good over the entire range of operation.

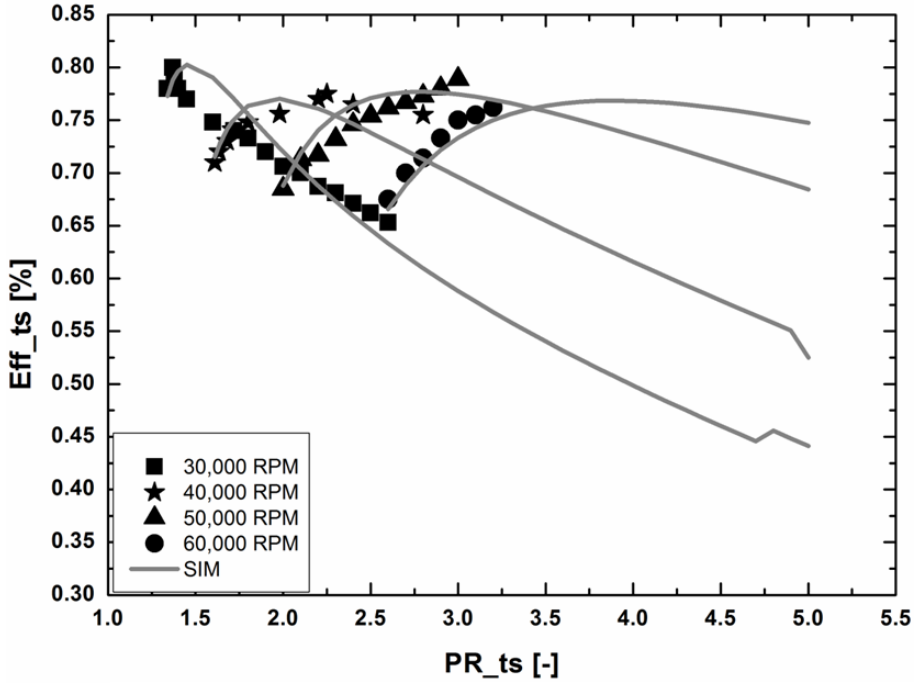

Figure 5-25: Comparison between predicted and measured η_{ts} for Turbine A.

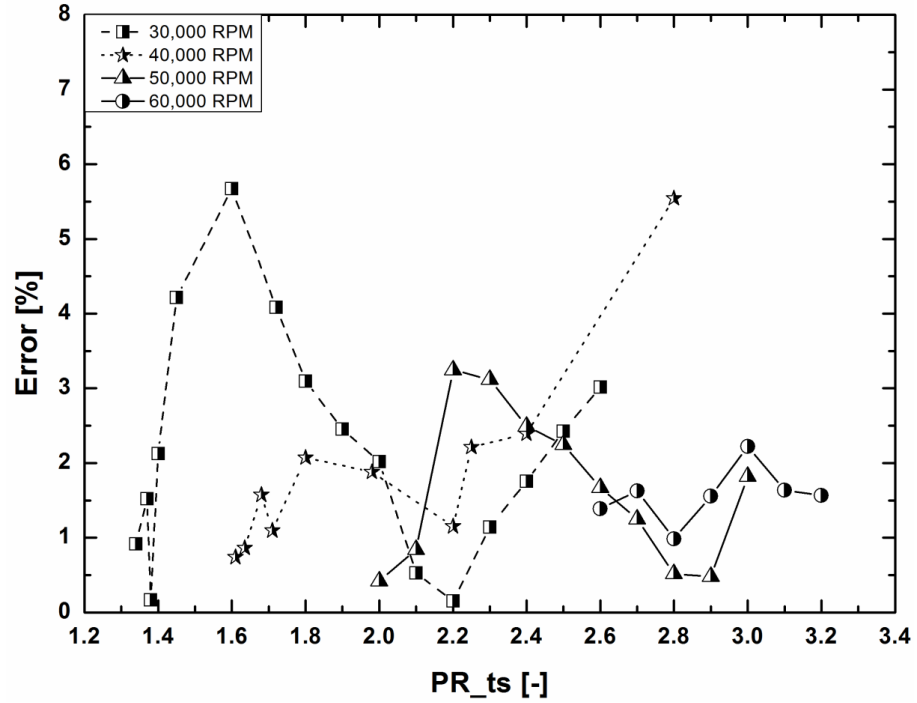

Figure 5-26: Deviation between predicted and measured η_{ts} for Turbine A.

The above results confirmed the accuracy of the proposed off-design methodology (MOC) in building performance maps of radial inflow turbines. The next section evaluates the suitability of the methodology in ORC radial turbines where real fluids are adapted.

b) Radial Turbine for Real Fluids (Turbine B)

The geometrical and input parameters have been imported to the MOC, and the results are shown inFigure 5-27, Figure 5-28andFigure 5-29. Contrary to Turbine A, the deviation angle and the incidence angle for the current turbine are changed to -0.4^{o} and -20^{o} for more accurate prediction. The prediction of the turbine efficiency is satisfactory over the entire range of operation. The maximum deviation of 6.6% is reached at the 51,000 rpm followed by 4.2% at 44,000 rpm.

The turbine power predicted by the MOC is the expansion power. In the work of [267], on the other hand, the power measurements are based on the generator power. However, the generator efficiency is not provided in the paper. Therefore, the generator efficiency is assumed to be 90%, and the results are depicted in Figure 5-28. The predicted power outputs fairly match the measured values over the entire values of rotational speeds with a maximum deviation of 6.2% at 44,000 rpm.

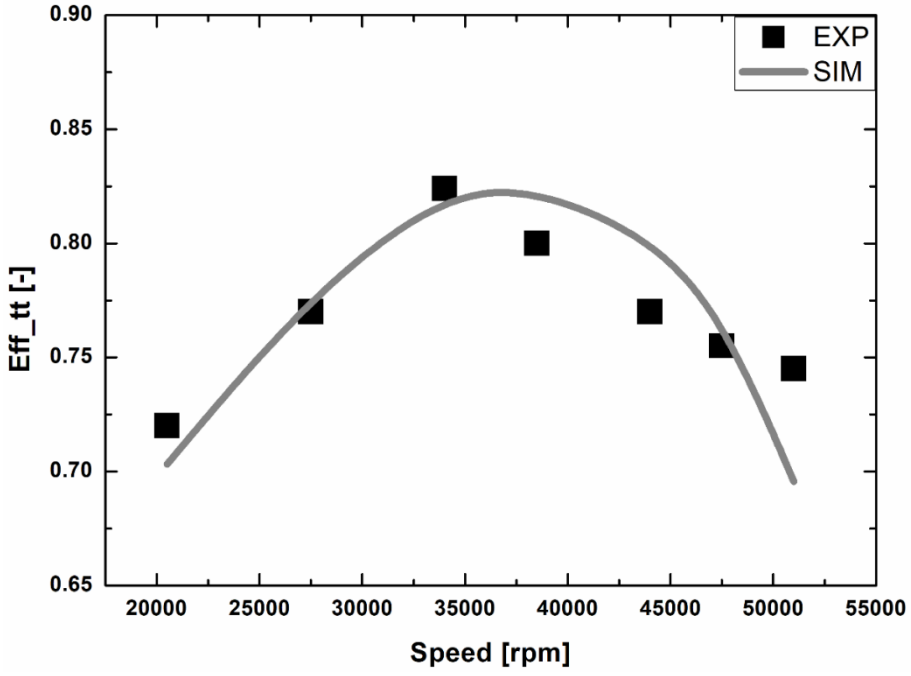

Figure 5-27: Comparison between predicted and measured η_{ts} for Turbine B.

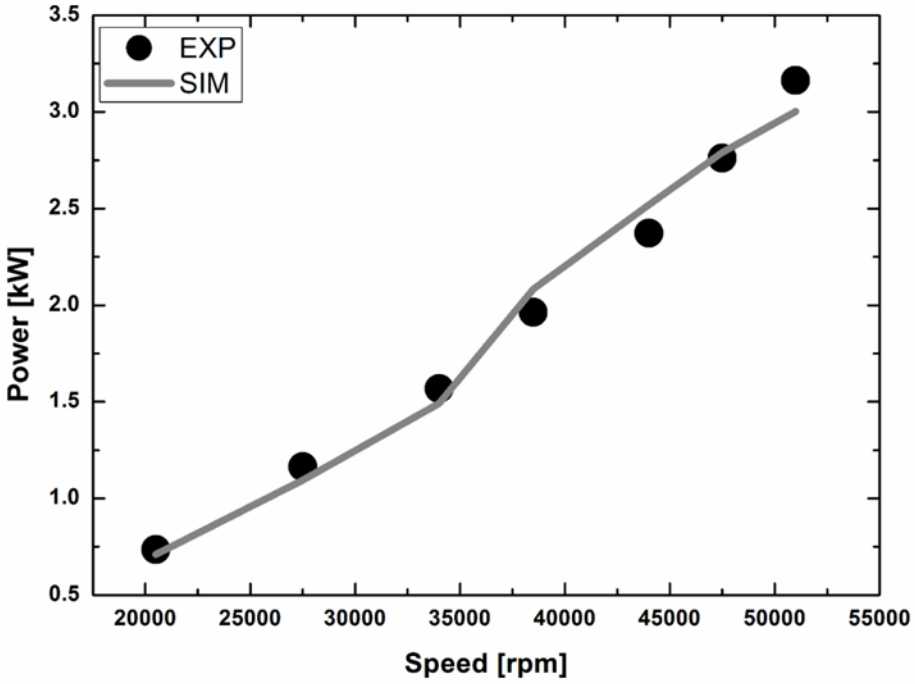

Figure 5-28: Comparison between predicted and measured W_{out} for Turbine B.

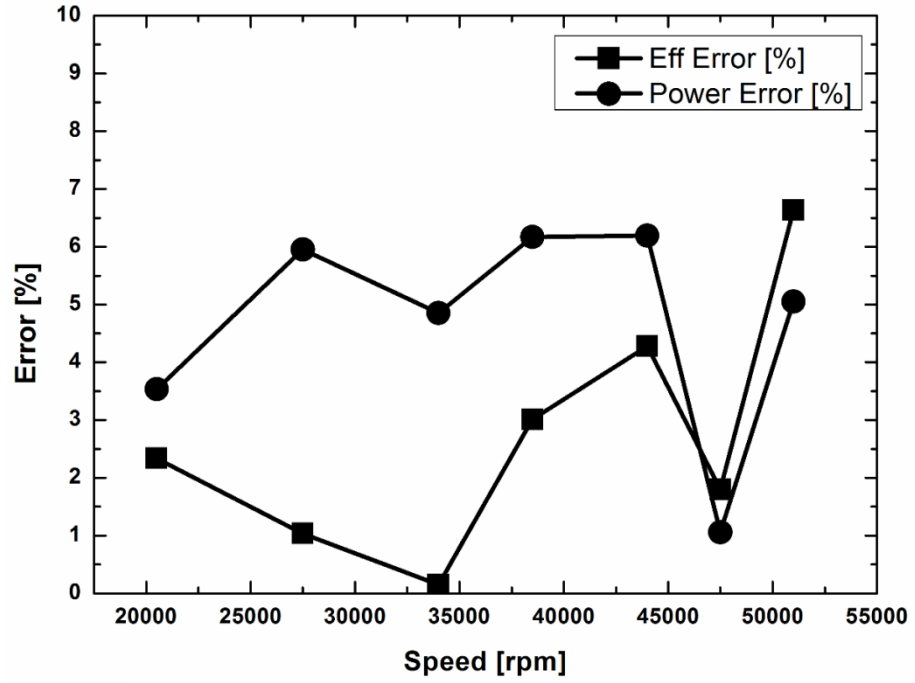

Figure 5-29: Deviation between predicted andmeasured η_{ts} and W_{out} for Turbine B.

Before validating the MOC with current turbine (Turbine C), the map of turbine B is extrapolated as shown in Figure 5-30and Figure 5-31.Therefore, the values of the pressure ratio have extended to 4 instead of 2.7 in the existing turbine [267]. The definition of the efficiency is the total to static efficiency rather than the total to total efficiency that was used in [267].The

peak total to static efficiency of the turbine is 58.44% at 20,000 rpm. However, the efficiency dramatically drops as the pressure ratio increases. At higher pressure ratios ($PR \geq 2$), the 40,000 rpm speed line presents the best performance followed by the 30,000 rpm speed line, while the 50,000 rpm speed line presents the poorest performance along the whole range of pressure ratios.

Figure 5-31depictsthe curves of MFR along the same range of pressure ratios and speeds. Generally, the mass flow rate increases with increasing the pressure ratio, but decreases with increasing the turbine speed. The advantage of extending the operating pressure ratios beyond the experimental ones is clear in the figure. The results show that the turbine is choked at high pressure ratios ($PR \geq 3.25$).

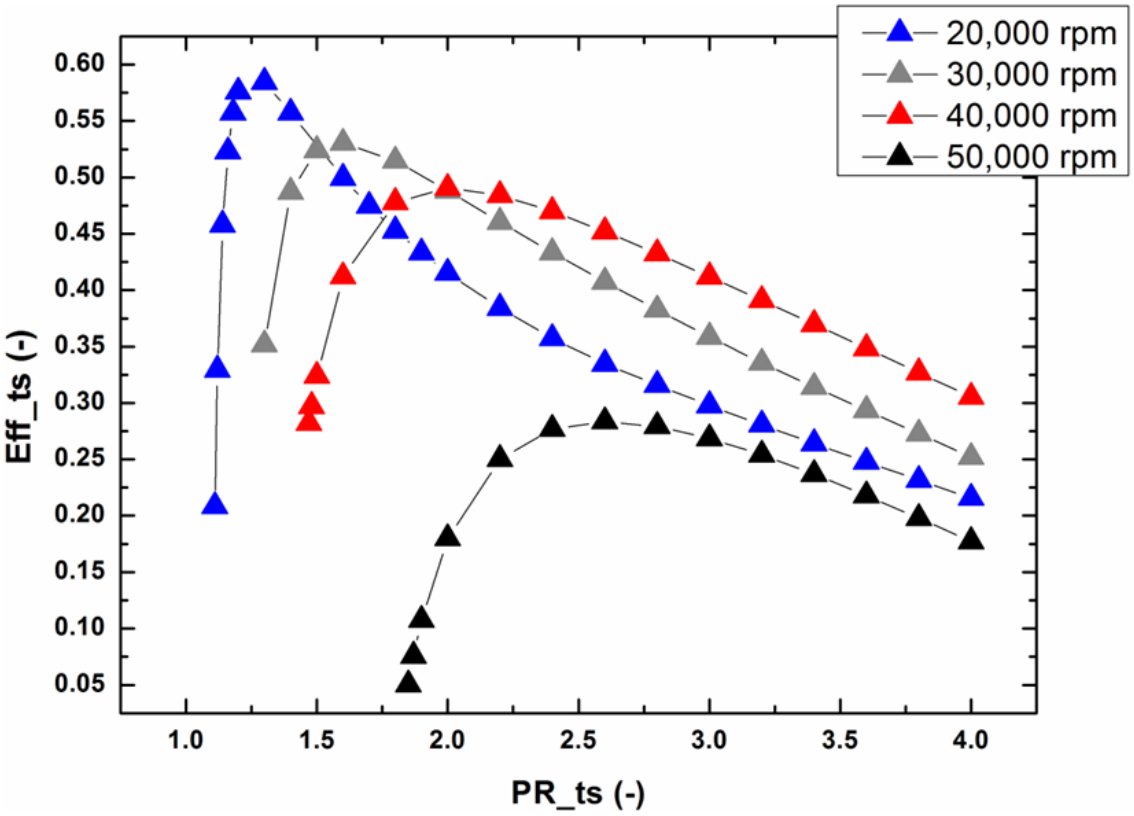

Figure 5-30: Performance of Turbine B under wide range of operating conditions using MOC.

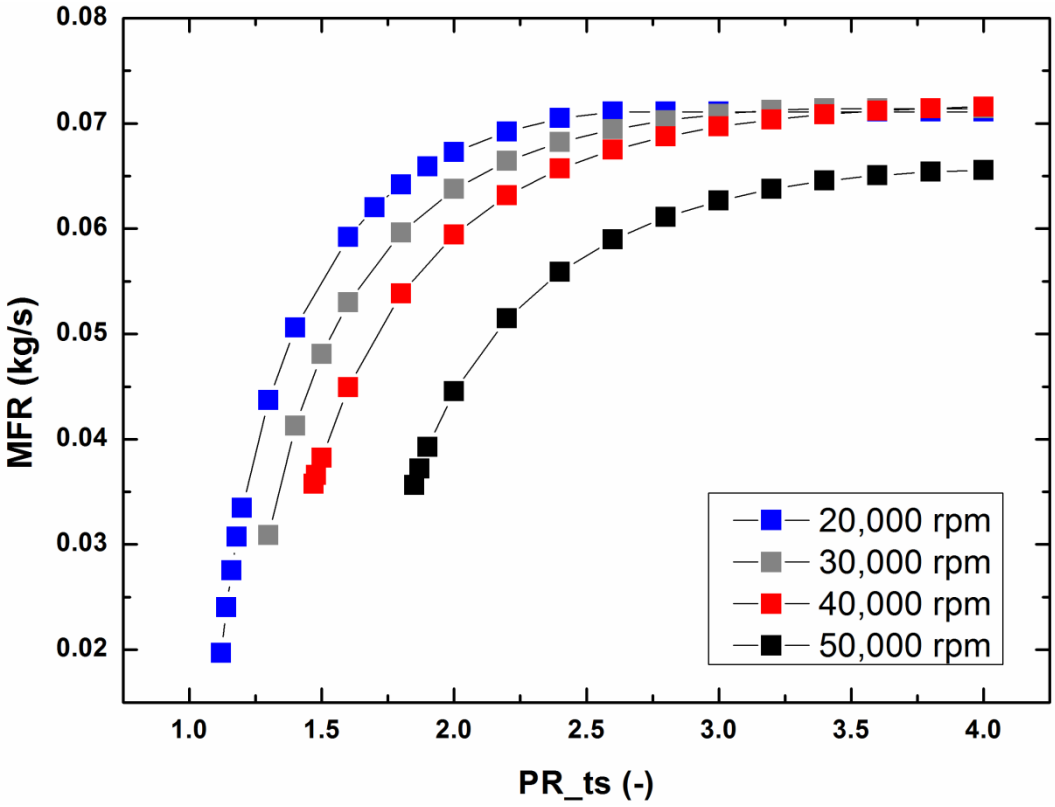

Figure 5-31: MFR of Turbine B under wide range of operating conditions using MOC.

c) *Radial Turbine for Real Fluids (Turbine C)*

The experimental set up and results of Turbine C are detailed in Chapter 7. However, the final results are included in this chapter just for validating the MOC. Since the turbine has been designed from scratch, all the geometrical details are known which make the comparison more accurate. The results are shown in Figure 5-32. The predicted η_{tt} is in good agreement with the measured one. The maximum deviation is 2.8% at $PR = 4.6$ and $PR = 5.9$. For the rest of the range, the deviations are less than 2%. This indicates that the proposed MOC is very accurate when all the required parameters are available.

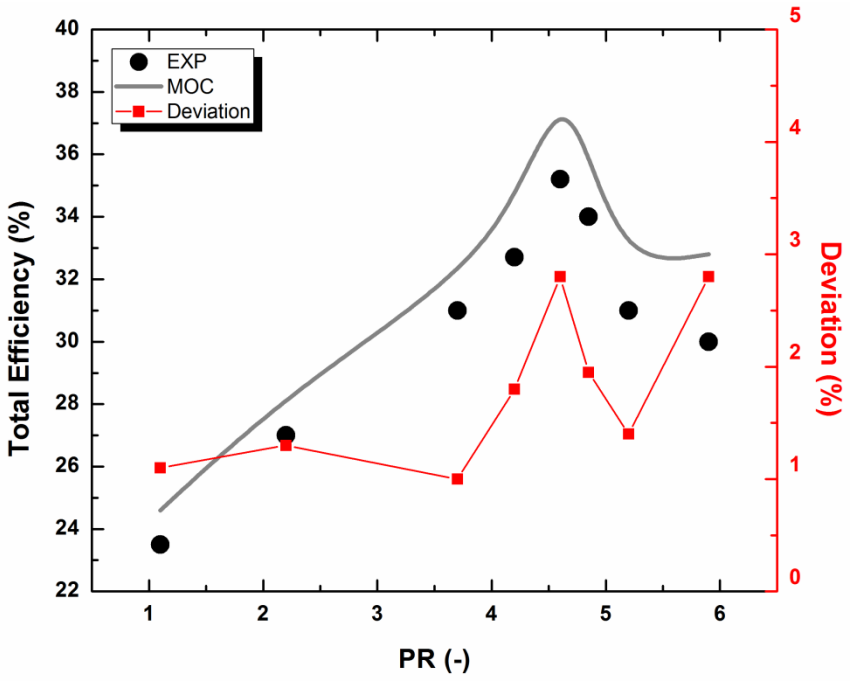

Figure 5-32: Comparison between predicted and measured η_{tt} for Turbine C.

Overall, the developed numerical model (MOC)is capable of building a full turbine map and investigating the variation of mass flow rate and isentropic efficiency (either total-to-total or total-to-static) with pressure ratios and speeds. The MOC proved to be an accurate and fast model that could generate a full turbine map with different pressure ratios and speeds in less than 1 minute for 5x5 matrix (5 points of pressure ratios and 5 points for speeds). By comparison with three different turbines, the MOC can be integrated in both a turbocharger model to predict the map characteristics and in ORC model where real gas EoS is necessary.

5.8 Conclusion

This chapter presented a numerical model for the design, optimisation and performance prediction of ORC radial inflow turbines. Two designs models were built based on two groups of parameters: specific speed, and loading and flow coefficients. The two models were connected to an optimisation algorithm to optimize the user-specified objective function. The two models were also integrated with a DoE technique to evaluate the effect of the design input parameters on the turbine performance and geometry. Last but

least, a novel mean-line off-design code (MOC) was built to build the map characteristics for radial inflow turbines. MOC could be coupled to both a turbocharger model and ORC model.

The turbine was designed and optimized to deliver a power output of 13.6 kW using single stage. The optimized η_{ts} was 74.4% at $PR = 7$. The optimized geometry was then exported to the MOC to build the turbine map. The MOC was validated with CFD results, and experimental works from three turbines. The predicted results were in very good agreement with the results of the tested turbines.

The CFD analysis are presented in the following chapter. Such analyses are very crucial in order to visualise the flow nature within the blades.

Chapter 6 : 3D Model Generations and CFD Analysis

6.1 Introduction

Although mean-line is a useful tool for full optimisation purposes, a 3D analysis is required. Thus, 3D simulations are needed. Mean-line modelling is yet incapable of capturing the flow behaviour, such as flow separation and shock waves. CFD is essential when the 3D nature of flow is used to restrict undesirable featuresbecauseflow in turbo-machines is strongly 3D, viscous and turbulent. CFD, which is a discipline of fluid mechanics, is the use of numerical mathematical and physical techniques to visualise the flows of fluid within a system. When set properly, CFD is a powerful tool to investigate the flow phenomena within the turbine,thereby avoiding the need forprototype manufacturing and reducing time and cost.

CFD is widely used in the application of radial inflow turbines to predict the performance and to study the flow nature within the stage. When organic fluids (non-ideal gases) are adapted, certain complexities, such as supersonic conditions, arise at the stator exit. Therefore, applying CFD techniques in ORC turbines has received a great attention recently. Colonna et al. [272] developed an in-house Euler solver to perform complete CFD simulations for supersonic turbines. They mainly focused on the effects of the different EOS for real gases. The results showed a significant deviation if the ideal gas EOS is applied, while the Span-Wagner or Peng-Robinson-Stryjek-Vera equations were very similar. Harinck et al. [273] performed a complete steady state simulation for their supersonic radial inflow turbine using ANSYS CFX. The property tables were generated using REFPROP. Their results showed that the improved stator model was able to deliver the required tangential velocity components with a Mach number value as high as 2.85. Uusitalo et al.[274]simulated a high supersonic small scale ORC turbine stator where a real gas model was implemented in a CFD solver using both the $k-\varepsilon$ and $k-\omega$ STT turbulence models. The results showed that the Mach number at the stator exit was 2.27 for $k-\varepsilon$ solver and 2.31 for $k-\omega$ STT.More recently, White [13] performed a full CFD analysis using ANSYS CFX as a validation for his mean-line model of the ORC radial turbine. The agreement between the mean-line and CFD was very good with a deviation of 0.3% in the total to static efficiency. He also validated his

model with the CFD by comparing the stagnation and thermodynamic properties at the inlet and exit of the rotor. The results were very accurate with a maximum deviation of 6.3% in the static pressure at rotor inlet. Similarly, Verma et al. [275] validated his 1D model with a complete CFD simulation using ANSYS CFX, and the deviation between the mean-line and CFD simulation in the turbine efficiency was 0.17%. His CFD results showed a choking condition at the design point with Mach number of 1.55. Other studies regarding the application of CFD simulations in ORC radial inflow turbines can be found at [14], [151], [240], [244], [248], [276], [277]. The brief review shows that CFD analysis allows the calculation of the flow field considering the viscous effects which are usually neglected in 1D model. Moreover, CFD can be applied as a reference of validation of mean-line models.

This chapter presents the construction of the 3D model of the turbine stage and complete CFD analyses of the constructed 3D components. In order to speed up the simulation, the investigation of flow within the volute is excluded in this chapter since its losses is insignificant compared to those of the rotor and stator.

6.2 Generation of the 3D Model

This section presents the construction of the 3D model of the full turbine stage, namely, volute, stator and rotor.

6.2.1 Volute Model

The conventional mean-line method that is used to design the volute is explained in Section 5.3.5. The area and radius distributions versus azimuth angle where the volute tongue begins at 0° are shown in Figure 6-1.

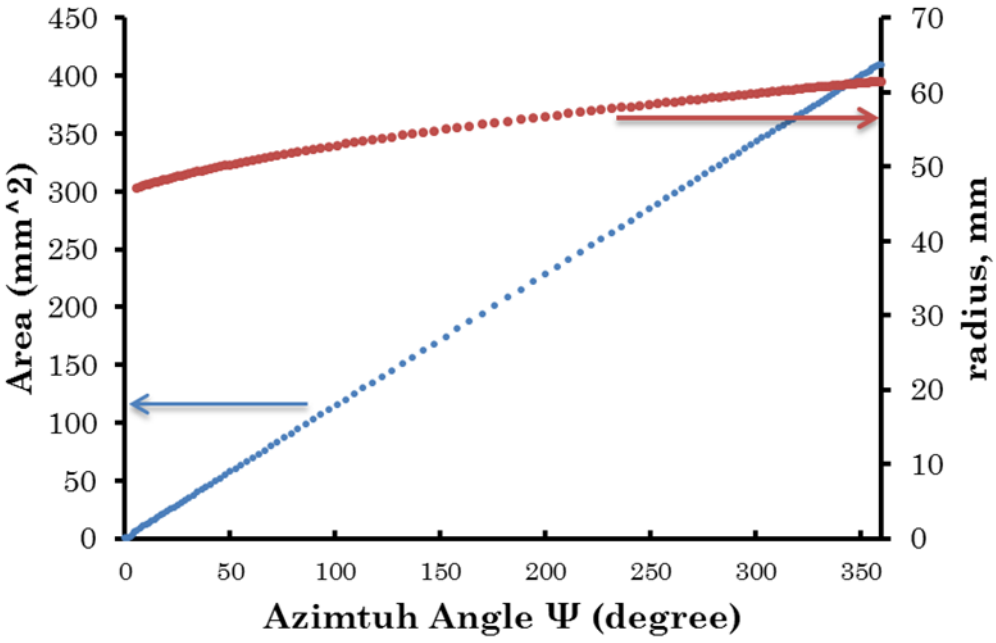

Figure 6-1: Volute area and radius at each azimuth angle.

The cross-sectional area profiles at each azimuth angle are shown in Figure 6-2. SolidWorks was used to generate the volute flow path by lofting the cross-sectional profiles.

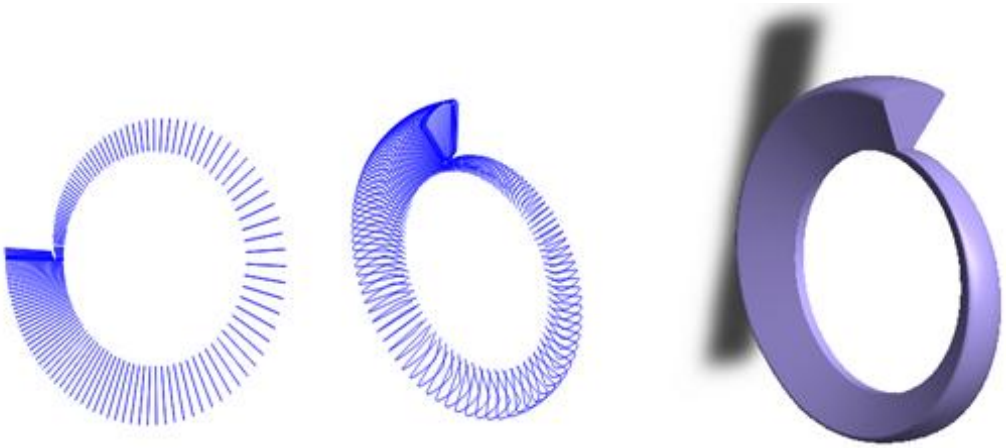

Figure 6-2: 3D model of the volute.

The inlet pipe was designed separately to match the exit pipe of the evaporator. The area of the evaporator pipe is 856 mm^2, and the area at the volute throat is 400 mm^2. Therefore, the area of the pipe was constantly increased from the throat to the pipe inlet (Figure 6-3).

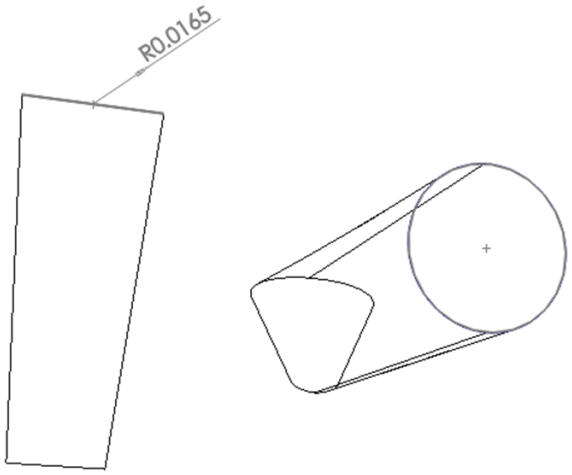

Figure 6-3: Connection pipe between the volute and the evaporator.

6.2.2 Stator 3D Model

The inlet and exit vane angles are 76.35° and 66.75°, respectively. The distribution of thickness is outlined in Appendix A according to the procedure proposed byAungier[234]. The full geometry of the stator vanes was designed using SolidWorks, as shown in Figure 6-4. The single stator vane flow path was then generated using ANSYS DesignModeler and then exported to ANSYS Turbogrid for meshing purposes.

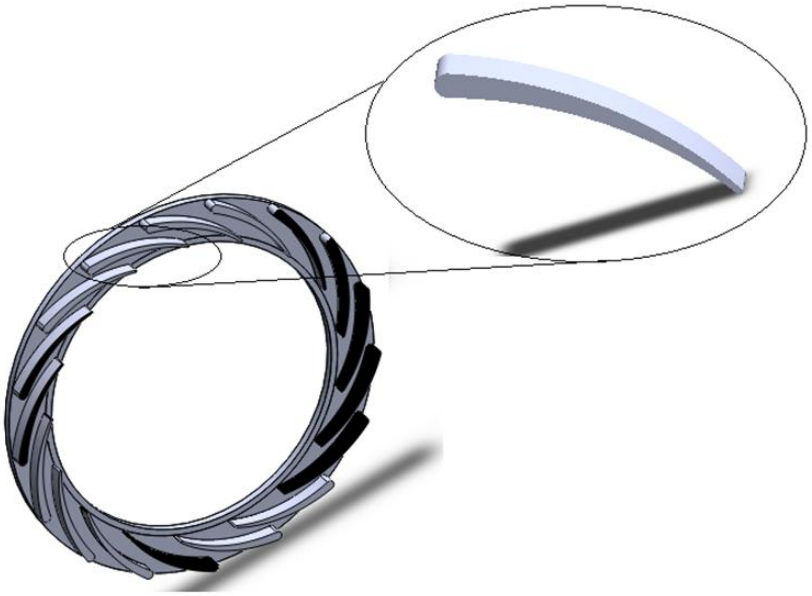

Figure 6-4: 3D model of the stator.

6.2.3 Rotor 3D Model

The following geometrical aspects were constructed to generate the full rotor blade:

- Meridional profiles
- Blade angle distribution
- Thickness distribution

6.2.3.1 Meridional Profiles

The 2D rotor meridional profiles (end-wall contours) are defined by applying the methodology presented in Atkinson[278]. In this study, a quarter ellipse is applied to define the three meridional profiles, namely, hub, mean and tip, as shown inFigure 6-5. a and b denotes the major and minor semi-axes of the ellipse, respectively. The values of these semi-axes can be easily found because the main geometrical parameters were computed using the design methodology explained in Chapter 5. The profiles can be obtained subsequently, as shown in Figure 6-6.

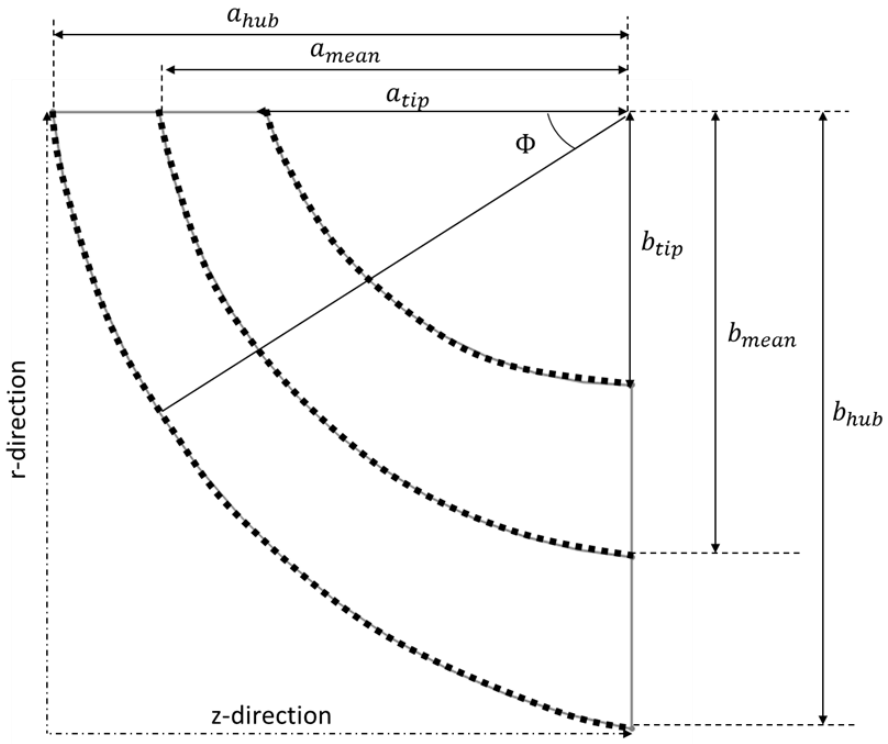

Figure 6-5: 2D meridional profiles of the turbine blade.

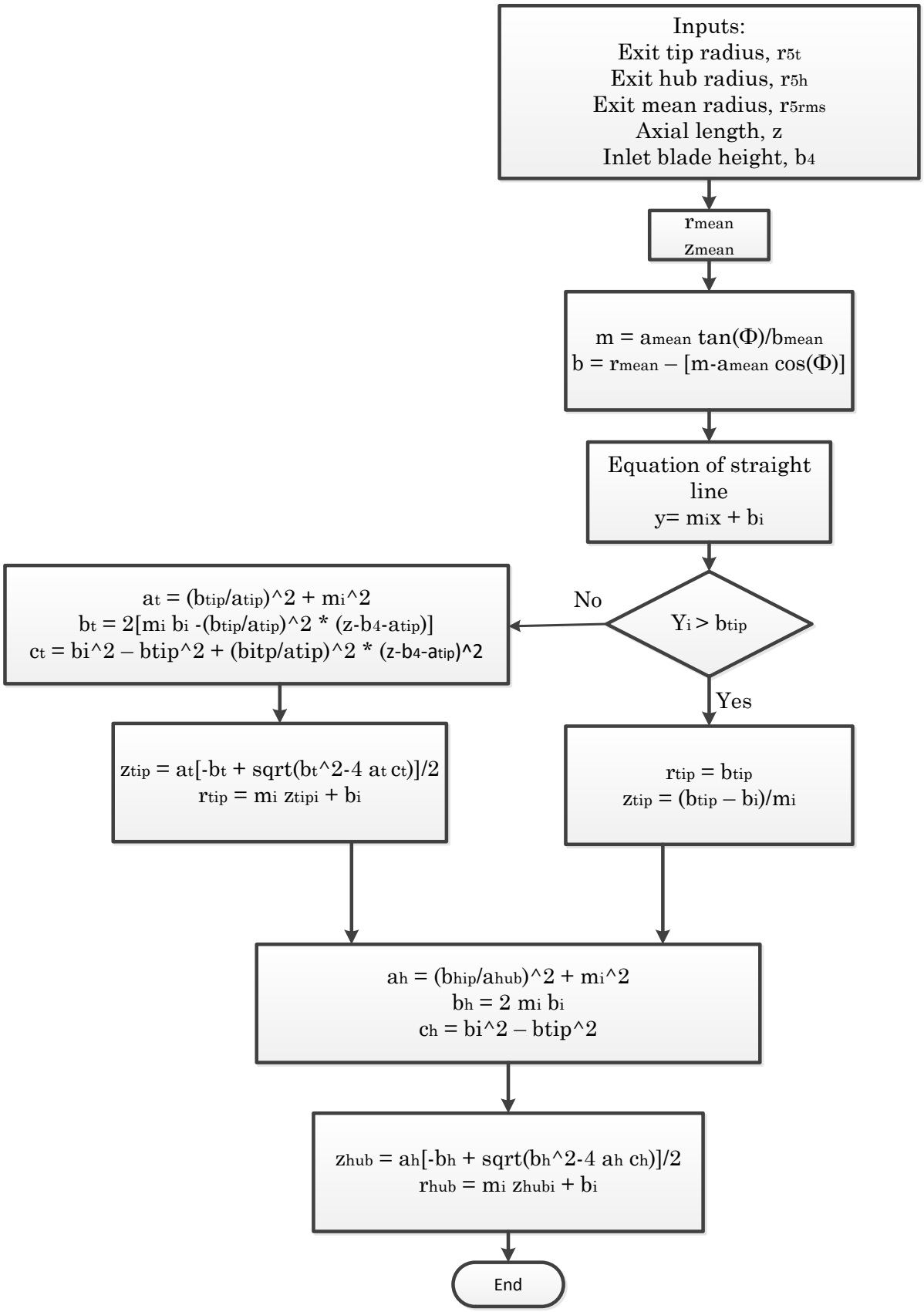

Figure 6-6: Construction of the meridional profiles.

To generate the full paths, each profile is divided into points where the axial length z and the radius r are calculated at each point i. Φ is the angle from 0° to 90°. At the mean profile, the radius and axial length are calculated using the parametric definition of the ellipse, as shown in the following equations.

$$r_{mean} = r_4 - b_{mean}\, sin\Phi_i \tag{6-1}$$

$$z_{mean} = z - a_{mean}\, cos\Phi_i \tag{6-2}$$

Calculating the values of z and r at the hub and tip requires some tedious algebra, as presented in Figure 6-6.

6.2.3.2 Blade Angle Distribution

In conventional radial turbines, in which the blade is radially fibred, equation (6-3) is held true at any axial distance [13]. In this case, blade angles at the tip and hubof rotor exit are straightforward, as shown in equations (6-4) and (6-5), respectively.

$$\frac{\tan\beta}{r} = constant \tag{6-3}$$

$$tan\beta_{5t} = \frac{r_{5t}\, tan\beta_5}{r_5} \tag{6-4}$$

$$tan\beta_{5h} = \frac{r_{5h}\, tan\beta_5}{r_5} \tag{6-5}$$

However, in this work, the blade is not radially fibred; therefore, the aforementioned equations are not applicable. Thus, the methodology explained in [234] is used to generate the angle distribution along the total meridional length of the counter. The blade angle coordinate is determined by the numerical integration of equations (6-6) and (6-7), where m is the meridional distance along the $Z - R$ contour. Equation (6-6)is the blade camber-line along the shroud contour, whereasequation (6-7) is the camber-

line along the hub contour. The coefficients in equations(6-6) and (6-7) are presented in Appendix A. The final blade profile is shown in Figure 6-7.

$$\theta(m) = Am + Bm^2 + Cm^4 \tag{6-6}$$

$$\theta(m) = Dm + Em^2 + Fm^4 \tag{6-7}$$

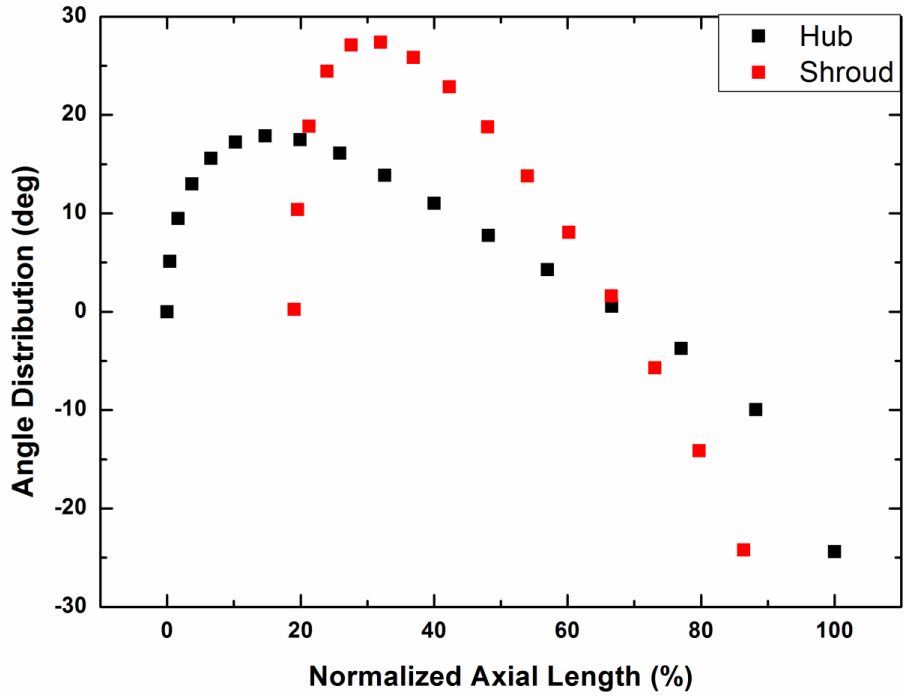

Figure 6-7: Blade angle distribution at hub and shroud of the rotor blade.

6.2.3.3 Thickness Distribution

Thickness is distributed in three regions of the blade, namely, leading edge, meridional profile and trailing edge. Thickness is tapered linearly from shroud to hub because the thicknesses at hub t_{lh} and tip t_{lt} of the leading edge are determined by the mean-line method (Chapter 5), as shown in Figure 6-8. Similarly, the thickness of the trailing edge is tapered linearly from shroud to hub becausethe thicknesses of the tip t_{tt} and hub t_{th} at the trailing edge are known from the mean-line model. The thickness distribution along the blade profile is performed in two regions, hub and shroud. At the hub, the thickness is set equal to the thickness of the blade inlet at the hub, except for the last 35% of the length where thickness is

linearly tapered to the thickness of the exit blade. Similarly, the thickness of the blade at the shroud is set equal to the thickness of the blade inlet at the shroud, except for the last 35% of the length where the thickness is linearly tapered to the thickness of the exit blade.

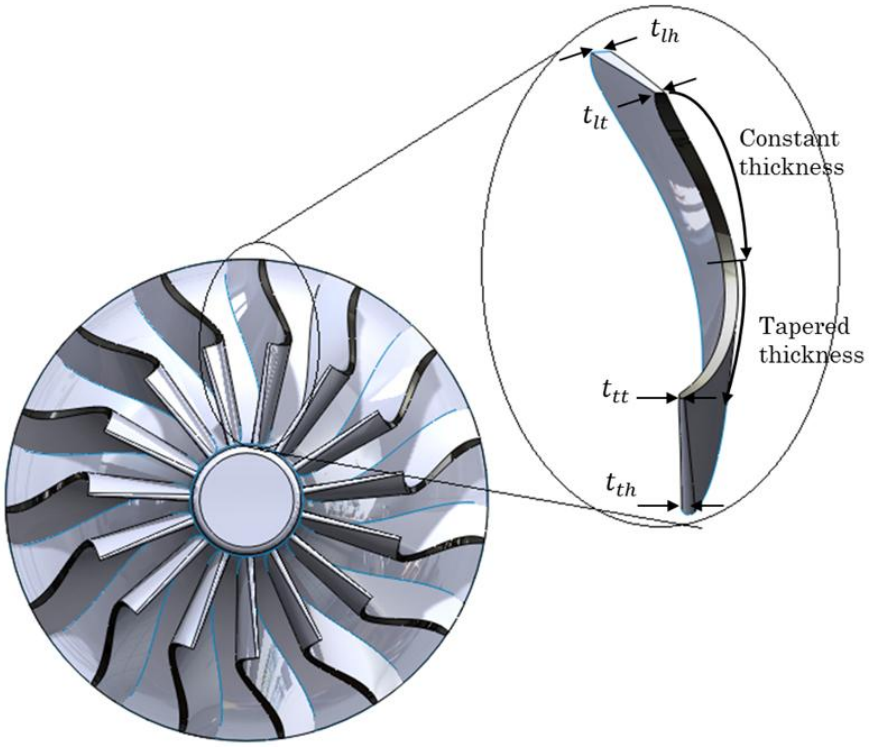

Figure 6-8: 3D model of the turbine rotor.

6.3 Computational Fluid Dynamics

Before sending the turbine out for manufacturing, a complete CFD study of the full turbine stage was accomplished using ANSYS. In this section, the set up of turbulence model, physical domain, boundary conditions and the organic fluid (NOVEC 649) are presented. A grid-independent study isalso performed to ensure that the results are independent of the number of nodes. In addition, the results from the complete CFD analysis are presented in detail for steady state simulations. Figure 6-9 depicts the basic steps for the numerical process of the radial turbine using ANSYS.

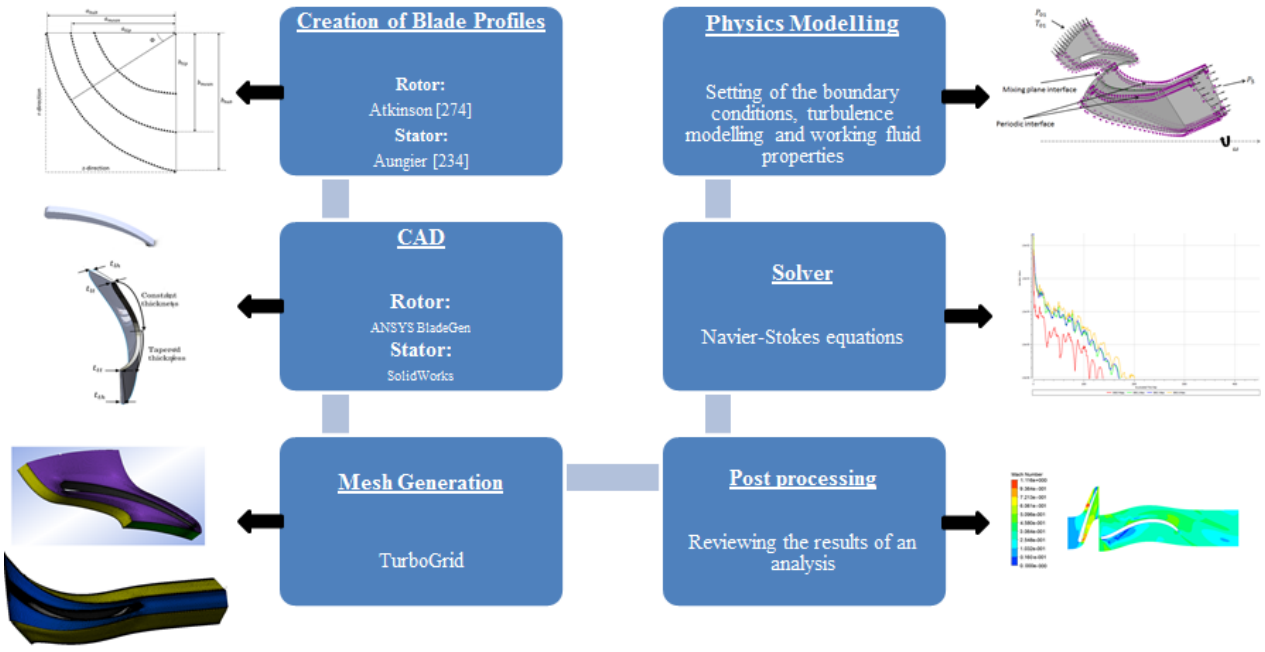

Figure 6-9: Steps for CFD simulation using ANSYS.

6.3.1 Governing Equations

CFD is a powerful tool to solve complex flows in turbomachinery using Navier–Stokes equations that are discretised by a finite volume approach. These equations are applied to solve for velocity, pressure and temperature associated with a moving fluid. Navier–Stokes equations describe the conservation of mass, momentum and energy, as shown in equations (6-8), (6-9)and (6-10), respectively. The Reynolds's average Navier–Stokes (RANS) equations are also used to account for the turbulence in the flow. These equations are solved to obtain the time-average properties of the flow without the need for resolution of the turbulent fluctuations [279].

$$\frac{\partial \rho}{\partial t} + \frac{\partial}{\partial x_j}\left(\rho . u_j\right) = 0 \tag{6-8}$$

$$\frac{\partial}{\partial t}\left(\rho . u_i\right) + \frac{\partial}{\partial x_j}\left(\rho . u_j . u_i\right) = -\frac{\partial p}{\partial x_i} + \frac{\partial \tau_{ij}}{\partial x_j} + \rho f_i \tag{6-9}$$

$$\frac{\partial}{\partial t}\left(\rho . h\right) + \frac{\partial}{\partial x_j}\left(\rho . u_j . h\right) = \frac{\partial P}{\partial t} + u_j \frac{\partial P}{\partial x_j} + \tau_{ij} \frac{\partial u_i}{\partial x_j} - \frac{\partial q_j}{\partial x_j} + W_{ext} + q_H \tag{6-10}$$

ANSYS CFX solver is used for the design and off-design simulations because it is well suited to simulate flows within turbo-machines.

Furthermore, it adopts a multiple frame of reference approach, in which the flow variables are calculated in a separate frame of reference in the rotor domain. Monitoring and using the derived statistical quantities (average, standard deviation and time integral) of any plotted value to examine its convergence to a quasi-steady state solution is now possible[279].

6.3.2 Turbulence Modelling

Selection of a proper turbulence model is crucial to adequately evaluate the formation of eddies and the flow separation. Reynolds number Re is a dimensionless number that describes the ratio between the inertial and viscous forces. Flow can be classified as either laminar or turbulentbased on the value of Re. In turbomachinery, flow is complex, in which adverse pressure gradients and flow separation are likely to occurwith time within substantial regions. Moreover, the assumption of a fully turbulent flow is justified because the turbine is located downstream of several heat exchangers [280]. Therefore, selecting a proper turbulence model to adequately capture the formation of eddies and flow separation is essential.

During the past two decades, two main turbulence models have been developed: $k-\epsilon$ model, which is based on the turbulence dissipation rate ϵ, and $k-\omega$ model, which is based on the specific dissipation rate ω.Fajardo[281] indicated that $k-\omega$ is more accurate than $k-\epsilon$ in computing the near-wall layers. However, $k-\epsilon$ converges faster and is robust with real gas applications [282]. Menter[283] developed a less complex and less computationally expensive model called shear stresstransport (SST) model. The SSTmodel applies the $k-\omega$ model to capture the near-wall regionaccurately and switches to the $k-\epsilon$ model in the free-stream to avoid the sensitivity of $k-\omega$ to the effects of free-stream turbulence. His predicted results using the SST model are in good agreement with the experimental data. Therefore, $k-\omega$ SST is applied in the current analysis for design point and off-design analyses.

6.3.3 Setting of the Working Fluid (NOVEC 649)

In conventional air turbines, air is considered as an ideal, and hence,a constant specific heat ratio is applicable. In ORC turbines, where a real fluid is modelled, the assumption of constant specific heat is not practical. ANSYS CFX has four real gas models, namely, Standard Redlich Kwong (SRK), Aungier Redlich Kwong (ARK), Soave Redlich Kwong (SORK) and Peng Robinson (PR).Redlich and Kwong[284] proposed a temperature-dependence approach that improved the accuracy of van der Waals EoS. Later, Soave [285] andPeng and D. B. Robinson[286] proposed additional modifications to the Redlich–Kwong [284]EoS to predict vapour pressure, liquid density and equilibrium ratios more accurately. Fluid properties, such as critical point, specific volume, acentric factor and molar mass, should be specified in all the aforementioned EoS. Moreover, the coefficients of a zero pressure polynomial are required to determine entropies, enthalpies and internal energies. The detailed definitions of the aforementioned EoS are presented in Appendix B.

Martin [13] investigated the accuracy of the aforementioned EoSs by comparing their results with the more accurate and advanced REFPROP [230]. His results showed that a deviation in the pressure is observed between 0.8% and 1.57%. The results also showed that a more significant deviation in the enthalpy calculations than that found for the pressure calculation is predicted with a maximum value of 4%. Therefore, RGP tables are the suitable solution to avoid such deviations.

As previously mentioned, REFPROP contains EOSs that are more accurate and advanced than the readily available EoSs[13]. Thus, REFPROP [230] was used to construct the fluid property tables for NOVEC 649. Some parameters, such as maximum temperature and pressure, dynamic viscosity and thermal conductivity, have to be specified. According to the modelling guide [287], selecting the Rigid Non-Interacting Sphere and Interacting Sphere Model for dynamic viscosity is highly recommended because it is valid for gases that use user-supplied EoS. The following parameters should be specified in the tables as functions of temperature and pressure:

* Enthalpy, h
* Thermal conductivity, k
* Entropy, s
* Dynamic Viscosity, μ
* Speed of sound, a
* Specific heat capacity at constant pressure, c_p
* Specific heat capacity at constant volume, c_v
* Specific volume, v

The look-up tables are discretised in 500 × 500 arrays with pressure (50–1200kPa) and temperature (400–500K) as independent variables.

6.3.4 Grid Generation

This task is challenging because the quality of the mesh depends on the type, size, placement and density of the grid. Once these parameters are set, the quality of the mesh can be evaluated by checking the maximum and minimum face angles, element volume ratio, edge length ratio and number of connectivity.

The solid parts were imported to the ANSYS TurboGrid to generate the appropriate meshes, as shown in Figure 6-10 and Figure 6-11. In this study, an automatic topology (ATM Optimised) was selected so the ANSYS TurboGrid couldselect the suitable topology for the blade passage. If the mesh quality at a certain region, such as the rotor leading edge, is poor, then the control points can be adjusted by the user to solve the problem. Figure 6-12 presents the sensitivity analysis of the element number of the passage to the turbine isentropic efficiency and the static exit temperature at rotor exit.

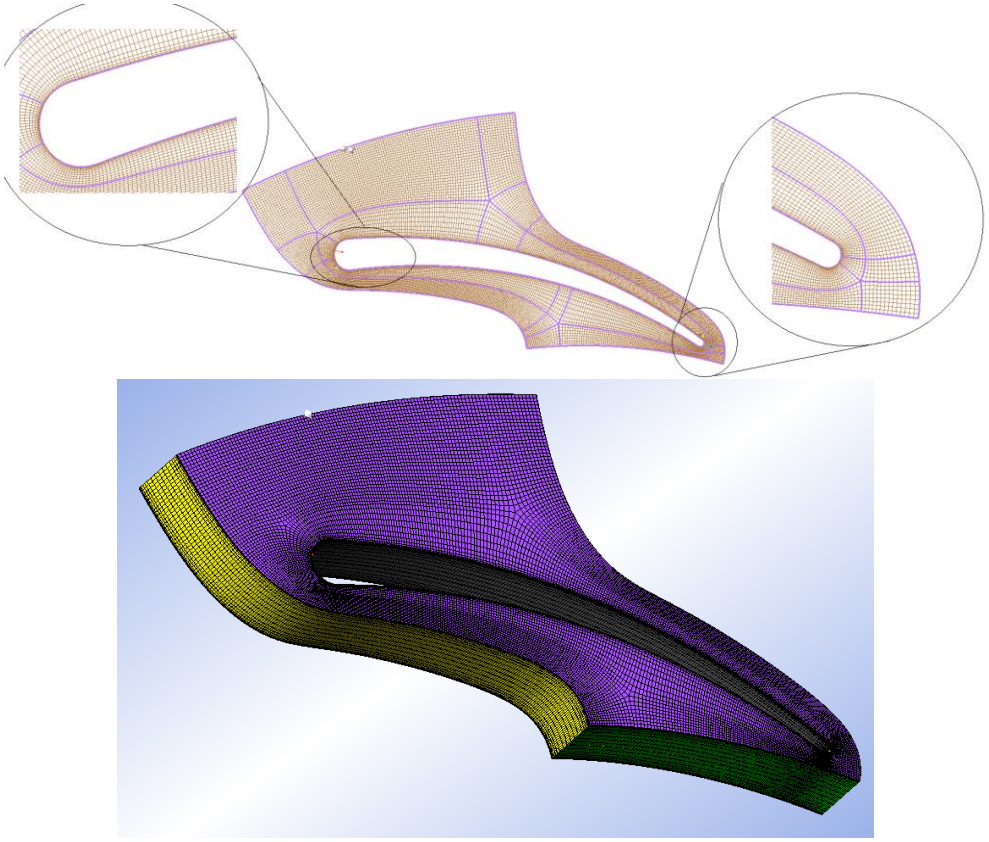

Figure 6-10: Stator mesh of 5.6 x 105 nodes using ANSYS (top) hub region and (bottom) 3D mesh.

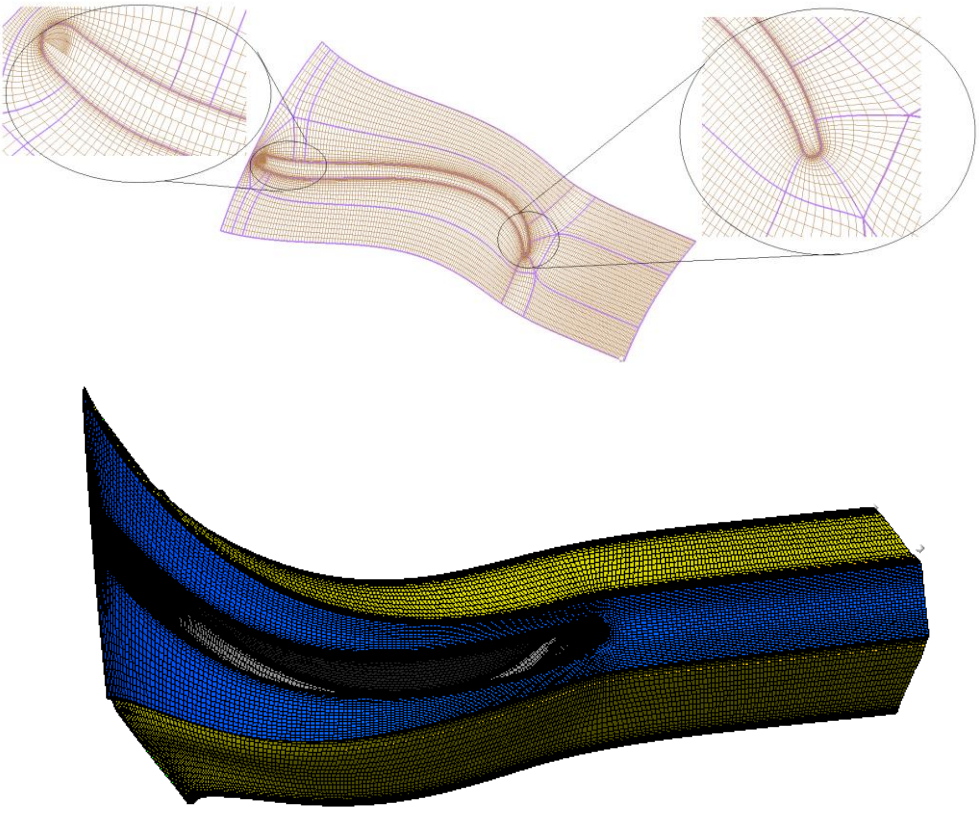

Figure 6-11: Rotor mesh of 5.9 x 10^5 nodes using ANSYS (top) tip region and (bottom) 3D mesh.

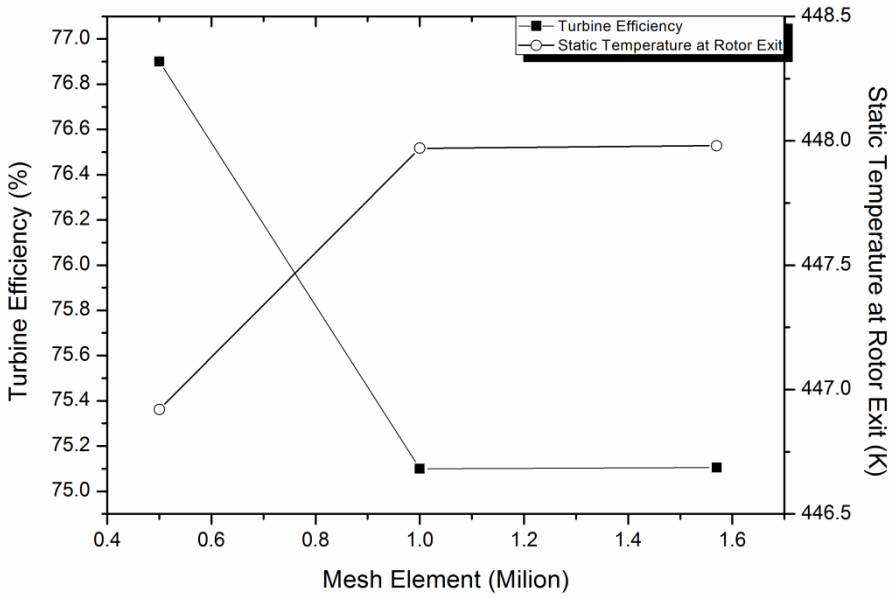

Figure 6-12: Mesh independence study using ANSYS TurboGrid.

6.3.5 Physical Domain and Boundary Conditions

Boundary conditions are required at the borders of the control volume to solve the mathematical system. Two models of boundary conditions can be applied in ANSYS CFX. The first model applies total pressure and temperature at the turbine inlet and static pressure at the exit, whereas the second model is defined with the combination of mass flow rate at the inlet and static pressure at the outlet. In this study, the first model was applied because it provides the best numerical stability and convergence rates [288]. To include the effect of heat transfer, the total energy model was included in the simulation because it depicts the transport of enthalpy and considers the flow kinetic energy [279]. All solid surfaces were modelled as smooth walls using a no-slip boundary condition.The simulation was run for the following boundary conditions (design point):

- Turbine inlet stagnation temperature, $T_{01} = 471.5\ K$.
- Turbine inlet stagnation pressure, $P_{01} = 900\ kPa$.
- Turbine exit static pressure, $P_5 = 130\ kPa$.
- Turbine shaft speed, $N = 40{,}000\ rpm$

To reduce computational time, a single flow passage for the rotor and stator was simulated and rotational periodicity was applied by setting an appropriate pitch ratio at the interface between the stator and the rotor.

Different meshing was required because the different components of the turbine are considered in the simulation. Therefore, the position of the grid nodes in one domain may not match those in the other domains. General grid interface is applied to avoid such non-matching interface. Domain interfaces are required because a change in reference frame between stationary (stator) and rotating (rotor) domains occurs. ANSYS CFX has two main interfaces, namely, mixing plane and frozen rotor. The main difference between the two interfaces is that the mixing plane applies the average qualities on the interface for upstream and downstream components;therefore, it was applied in the current study.Figure 6-13 shows the modelled components with the corresponding fluid domains.

Using the above boundary conditions, the solution from the CFD solver was monitored during the numerical iterations as shown inFigure 6-14. Convergence is considered achieved because the Root-Mean-Square (RMS) is less than $1.0\,e10^{-6}$ for mass and momentum. Figure 6-14also presents the mass flow behaviour during the numerical simulation, and the figure clearly shows that the mass continuity equation is achieved, therefore; solution is accomplished.

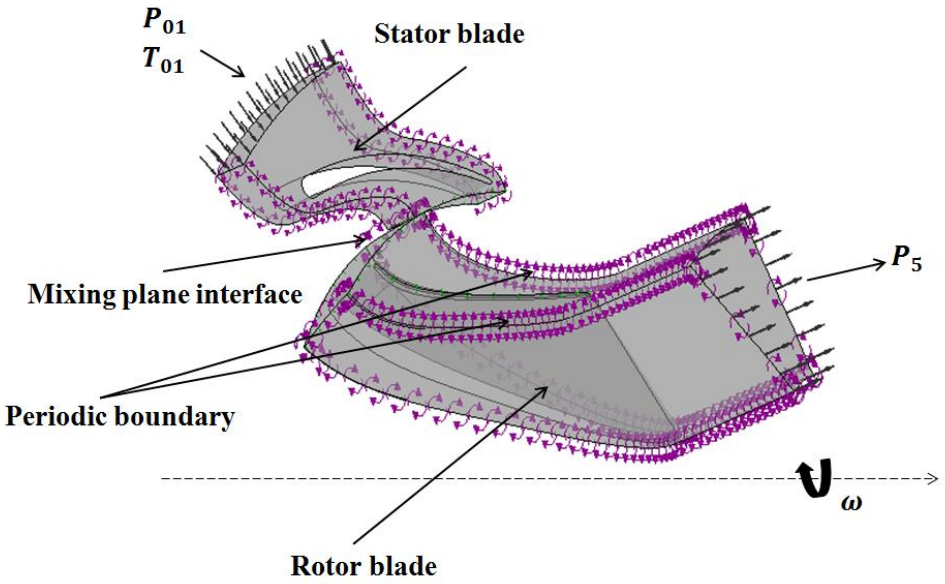

Figure 6-13: Computational fluid domains for stator and rotor.

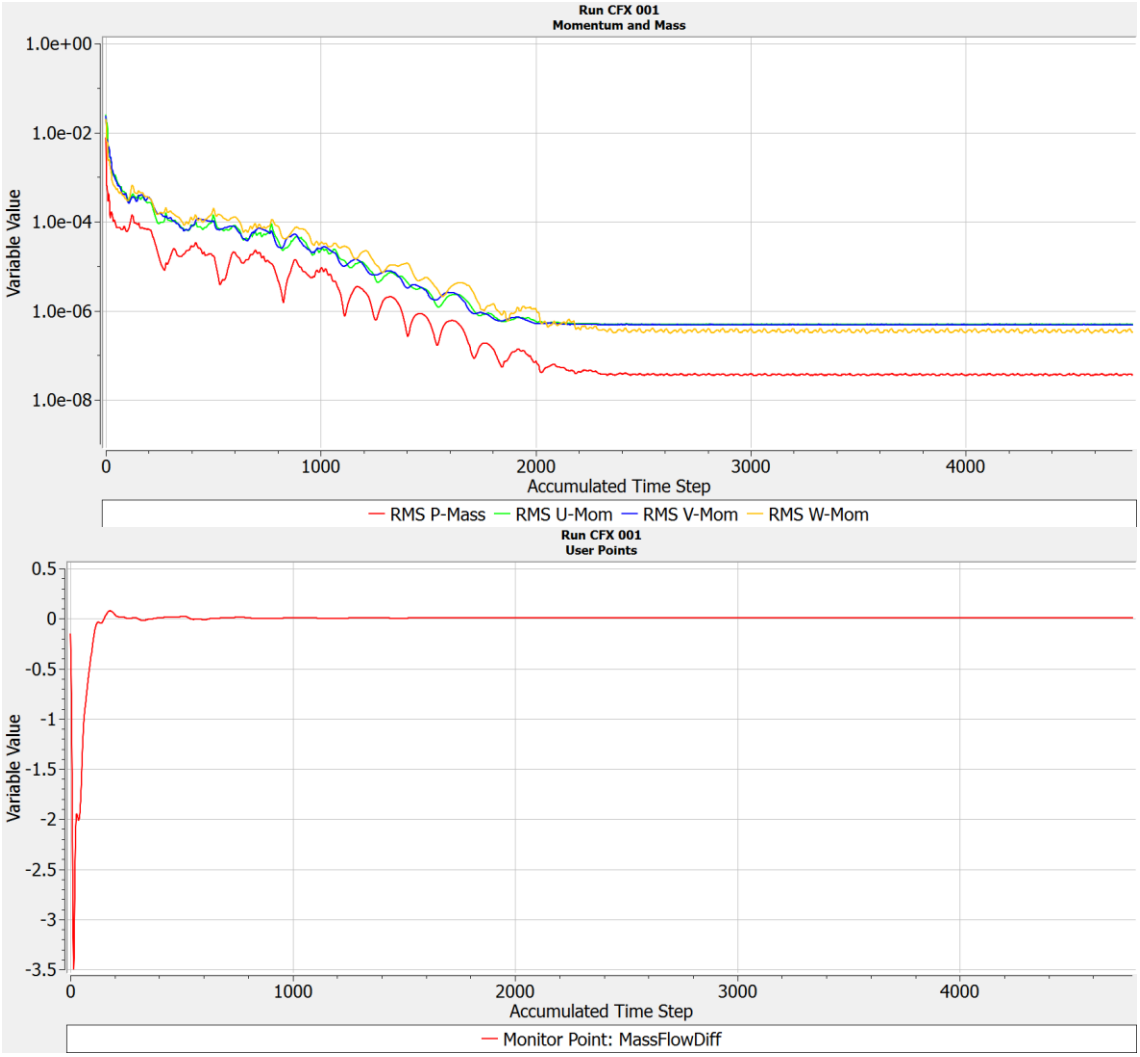

Figure 6-14: Residual plots for momentum and mass (top), and mass flow difference bwteen turbine inlet and exit (bottom).

6.3.6 CFD Results

6.3.6.1 Results at Design point

The results in this section are based on the boundary conditions presented in the previous section (6.3.5). Figure 6-15depicts the contours of the total pressure and temperature through the turbine stage at a span of 50%. From the inlet of the stator to the exit of the rotor, the pressure decreases from 900 kPa to 130 kPa, whilethe temperature decreases from 471 K to 448 K. The pressure drop through the turbine stage satisfies the expansion requirement of the current project.

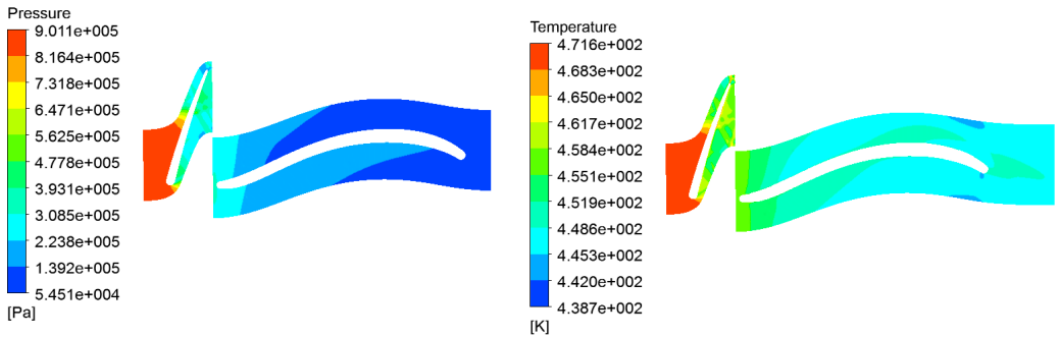

Figure 6-15: Pressure and temperature distributions at design point (N=40,000 rpm, PR=6.9).

However, the high pressure ratio results in high Mach number values at the stator exit, resulting in higher friction losses and, therefore, lower efficiency, as shown in Figure 6-16. However, these high values of Mach number are expected (and are close to the estimated values in the mean-line model) owingto the sudden expansion of flow at this area. Mach number is also influenced by the operating mass flow rate of the working fluid and the throat opening of the stator vanes. The pressure drop across the stator vanes is used to accelerate the organic fluid as it moves towards the circumferential direction. However, the pressure loss across the stator vane is significantly high and results in shock waves. Through the rotor blades, the values of Mach number are below unity.

Figure 6-17shows the blade loading. As the enclosed area by the pressure and suction surfaces increases, the turbine produces higher power output (net torque). At the three profiles, blade loadingis uniform in the pressure and suction surfaces. The lower pressure values in the suction surface correspond to the location of the throat, where area is the lowest and speed is the highest.

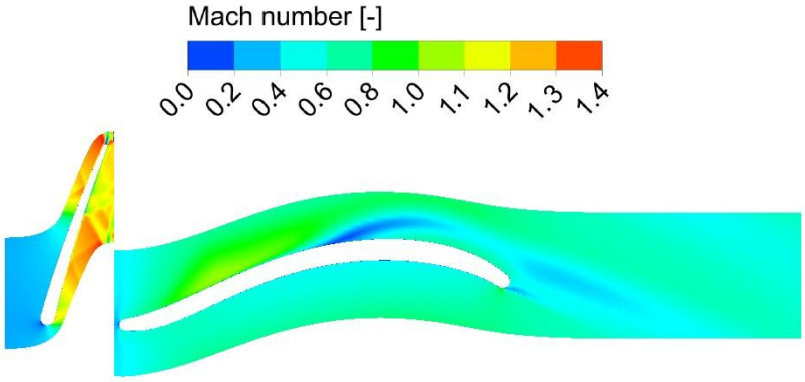

Figure 6-16: Mach number distribution at design point (N=40,000 rpm, PR=6.9).

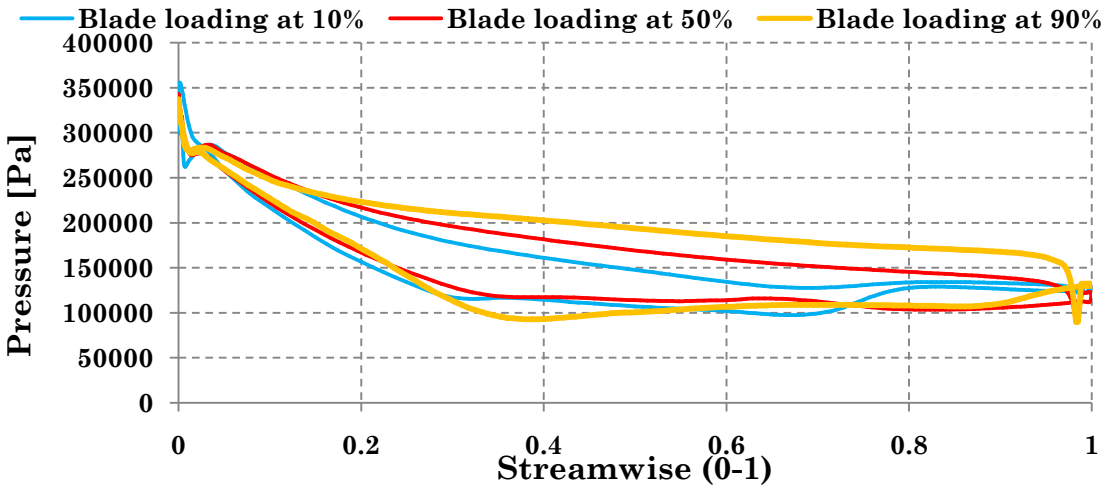

Figure 6-17: Bladeloading through the rotor blades.

Figure 6-18 portrays the flow streamlines through the turbine stage. The fluid flows smoothly, and the velocity is homogenously distributed along the blade without any flow reversals at a span of 90%. The flow is smooth at the leading edge at a span of 50%, signifying that the incidence angle at the rotor leading edge is optimum. However, flow recirculation is observed downstream of the rotor blades at the suction side, resulting in a moderate level of diffusion at this area. Such flow recirculation occurs due to the difference between the actual and idealised flows in the blade passage. The fluid velocities in the end-wall boundary layers are lower than thoseof the mainstream, thereby causing the fluid to turn sharply and resulting in flow vortices.

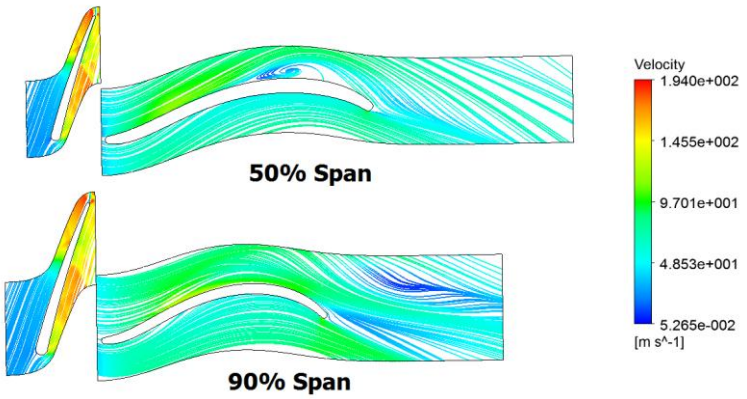

Figure 6-18: Velocity streamline at 50% span (top) and 90% span (bottom), at design point (N=40,000 rpm, PR=6.9).

Figure 6-19 depicts the flow nature near the hub and shroud. Flow in the hub and tip is uniform at the rotor leading edge. This finding confirms that the incidence angle of the non-radial blade is optimum. A flow recirculation near the hub is observed near the middle of the suction side. However, this flow recirculation disappears in the downstream of the blade where it is mixed out with the mainstream. The fluids near the rotor tip move through the gap (tip clearance gap) from the pressure surface to the suction surface, resulting in strong leakage flow that behaves similar to a jet flow in the same region. The flow in this region has a different magnitude and direction compared with the main flow. Figure 6-19shows that the direction of the flow near the tip changes from streamwise to spanwise.

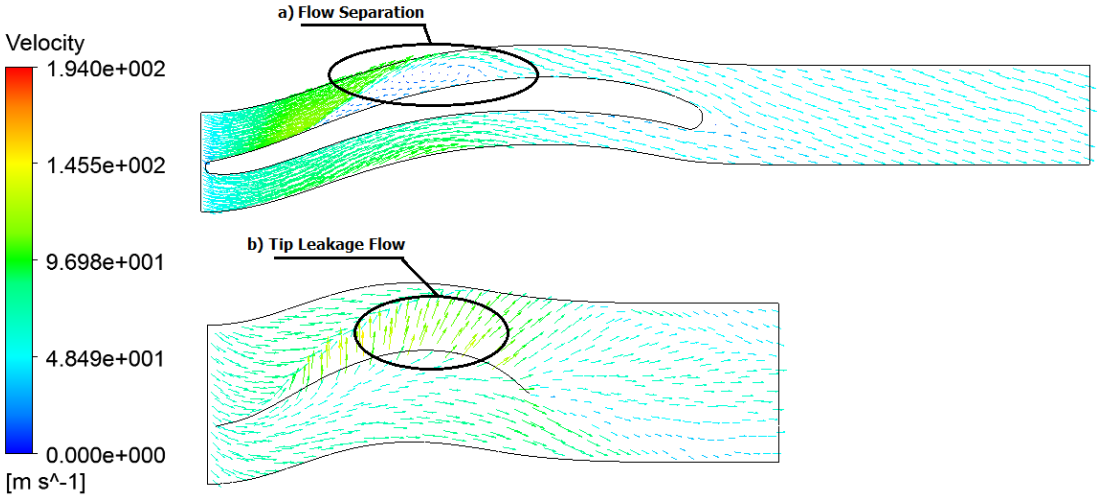

Figure 6-19: Velocity vectors (a) near hub and (b) near shroud, at design point (N=40,000 rpm, PR=6.9).

Last but not least, the key results from the mean-line model were compared against the CFD results as shown in Table 6-1. It is clearly shown that the majority of the parameters are in good agreement. This indicates that the proposed methodology can fairly predict the turbine performance and flow featuresfor ORC turbines.

Table 6-1: Comparison between the proposed methodolgy and CFD results.

Parameter	Symbol (Unit)	1D Method	CFD
	Rotor Inlet		
Total pressure	$P_{04}\ (kPa)$	743.20	740.25
Total temperature	$T_{04}\ (K)$	470.41	470.35
Static pressure	$P_4\ (kPa)$	317.61	307.74
Static temperature	$T_4(K)$	460	457.71
Absolute velocity	$C_4\ (^m/_s)$	148.40	139.8
	Rotor Exit		
Total pressure	$P_{05}\ (kPa)$	166.43	165.25
Total temperature	$T_{05}\ (K)$	452.10	451
Static pressure	$P_5\ (kPa)$	130	130
Static temperature	$T_5(K)$	449.70	447.98
Absolute velocity	$C_5\ (^m/_s)$	66.20	71
	Performance Summary		
Pressure ratio	$PR\ (-)$	6.9	6.9
Mass flow rate	$\dot{m}\left(^{kg}/_s\right)$	0.80	0.807
Isentropic efficiency	$\eta_{ts}\ (\%)$	74.40	73.85
Rotational speed	$N\ (rpm)$	40,000	40,000

6.3.6.2 Results at Off-Design Points

The aerodynamic behaviour of the turbine is crucially influenced by the Mach number of the flow. In turbines, the Mach number depends on the rotational speed, the pressure ratio through the stage, and the speed of sound of the working fluid. The results in the previous sub-section indicated that the flow choked at the interspace (gap between stator and rotor). This means that the turbine operates at fixed mass flow rate, regardless of the pressure ratio. This, in turn, results in shock waves and performance deteriorationof the turbine. However, higher values of specific power are achieved at choked flow. Therefore, the turbine was designed to operate at choked conditions based on the simulation of the thermodynamic cycle. In the current CFD simulation, pressure ratio and the turbine speed are under the control of the designer. Therefore, they were changed and the simulation was re-run as shown in the next paragraphs.

At high pressure ratio, the mass flow parameter is nearly in the same level as shown in Figure 5-22. In this case, the mass flow rate becomes intensive to the pressure ratio i.e. flow is choked. Therefore, it was very essential to run the simulation at different operating conditions. Since the choking began at PR = 4 as shown in Figure 5-22,the simulation results at PR = 3 were presented. This was performed by reducing the inlet stagnation pressure from 900 kPa to 400 kPa at the stator inlet.

Figure 6-20 presents the Mach number distribution through the turbine stage. The figure clearly shows that there is no choking at the interspace between the stator exit and rotor inlet, and the Mach number at this region is ≤ 0.93 .However, the turbine geometry was built based on the cycle conditions presented in section 6.3.5. Running the turbine at off-design points, such as PR=3, results in a non-optimum turbine performance which results in deficient flow as shown in Figure 6-21. At 50% of the rotor blade, a flow recirculation is formed at the rotor leading edge in the pressure side because of the non-optimum incidence angle, before mixing out with the main stream. At 90% span, a flow separation is noticeable at about 43% of the axial length of the rotor passage starting from the rotor leading edge. Compared to the flow conditions in Figure 6-18, the velocity streamlines at off-design conditions are deficient, although no choking was noticed. At these conditions ($N = 40{,}000\ rpm\ and\ PR = 3$) , the turbine power and isentropic efficiency were2.65 kW and 65.1%, respectively, compared to 13.56 kW and 73.85% at the design point.

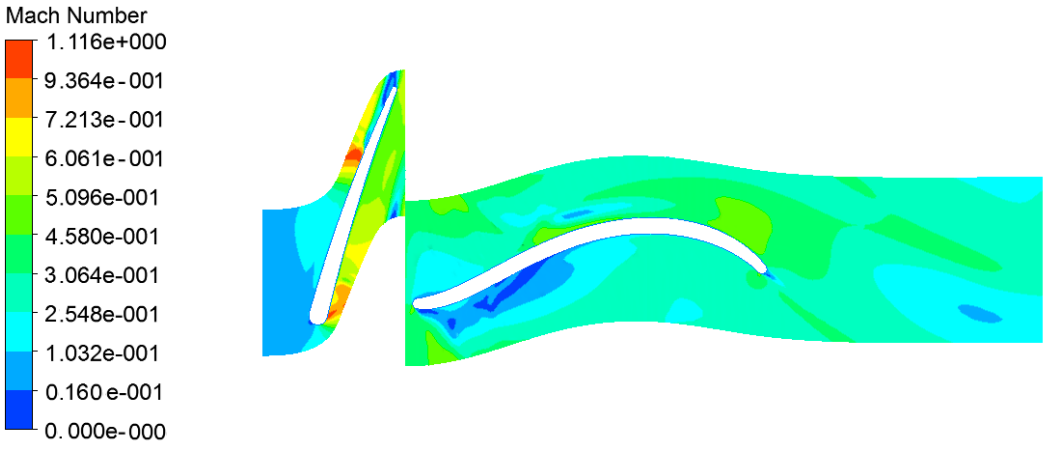

Figure 6-20: Mach number distribution at off-design conditions (N=40,000 rpm, PR=3).

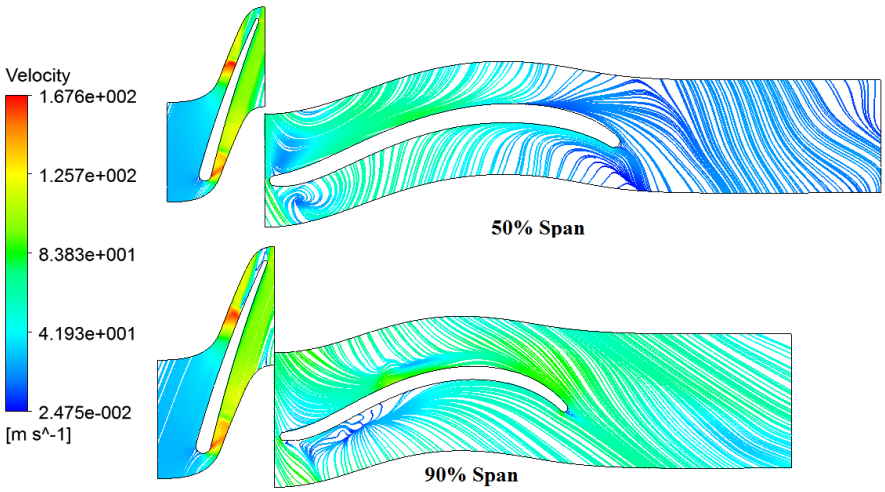

Figure 6-21: Velocity streamlines at off-design conditions (N=40,000 rpm, PR=3).

The simulation was then re-run again at two different pressure ratios $PR = 3\ and\ PR = 7$) with 30,000 rpm (instead of 40,000 rpm at the design point).Figure 6-22and Figure 6-23 show the Mach number distribution and flow streamline at $PR = 3$ and 30,000 rpm. It is known thatturbine size is inversely proportional to the turbine speed. Therefore, the turbine size with 30,000 rpm is considered overestimated which makes the flow doesn't follow the blade passage properly as shown inFigure 6-23.Mach number in this case is higher than that in Figure 6-20, although they have the same pressure ratio. However, this is clarified by the higher absolute velocities as shownFigure 6-23.

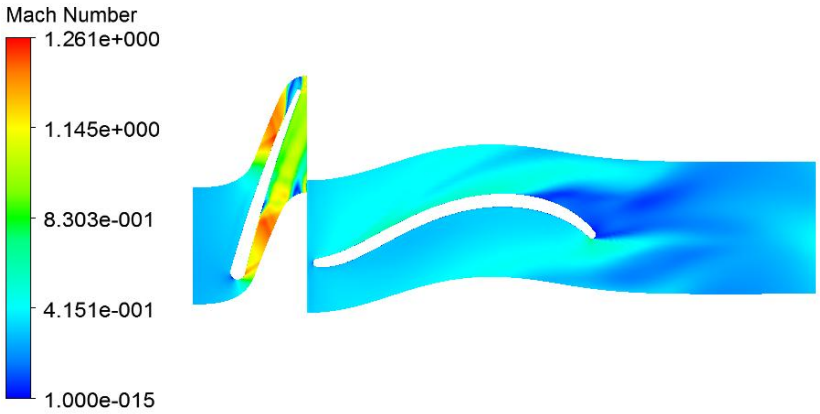

Figure 6-22: Mach number distribution at off-design conditions (N=30,000 rpm, PR=3).

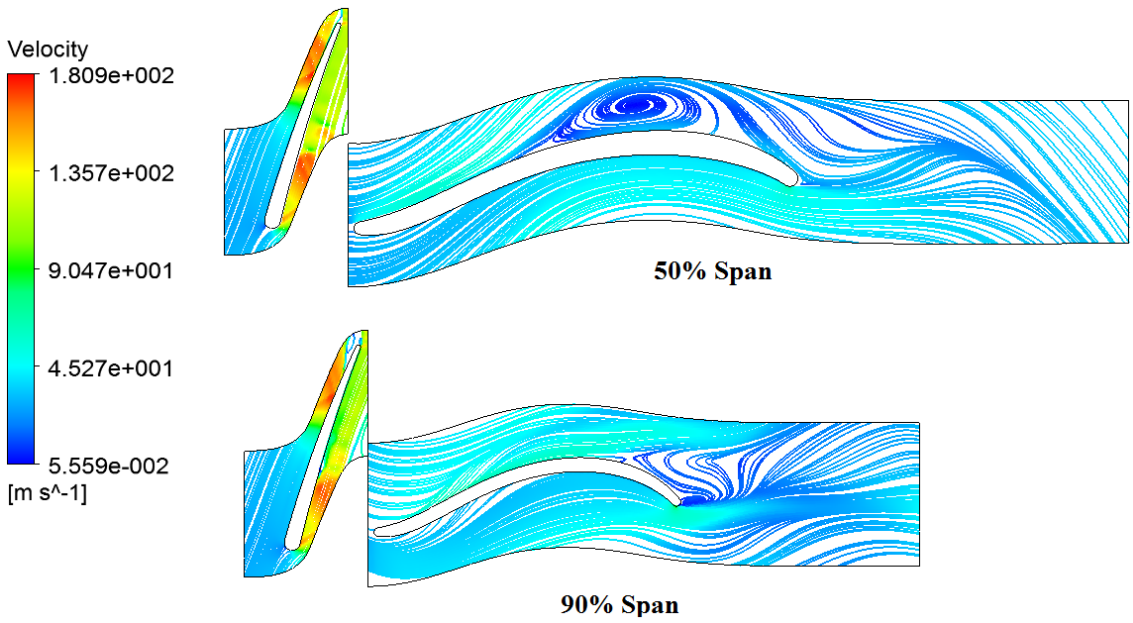

Figure 6-23: Velocity streamlines at off-design conditions (N=30,000 rpm, PR=3).

Figure 6-24 and Figure 6-25 presents the results at $PR = 7$ and 30,000 rpm. Compared to the 40,000 rpm, Mach numbers are higher due to the higher velocities as shown in Figure 6-25. In addition, the flow is more uniform in the 40,000 rpm case while strong vorticity is created in the 30,000 rpm. The turbine efficiency and power output were 66% and 12.10 kW, respectively, at$PR = 7$ and 30,000 rpm

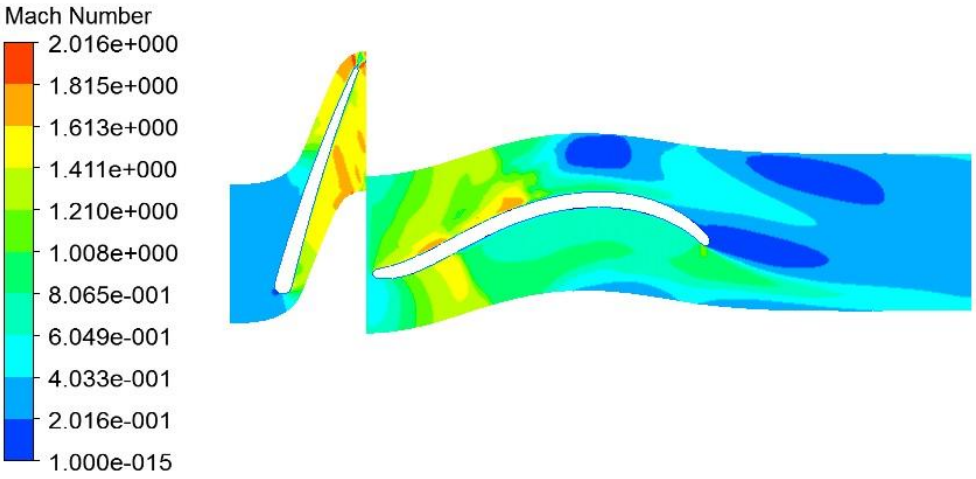

Figure 6-24: Mach number distribution at off-design conditions (N=30,000 rpm, PR=7).

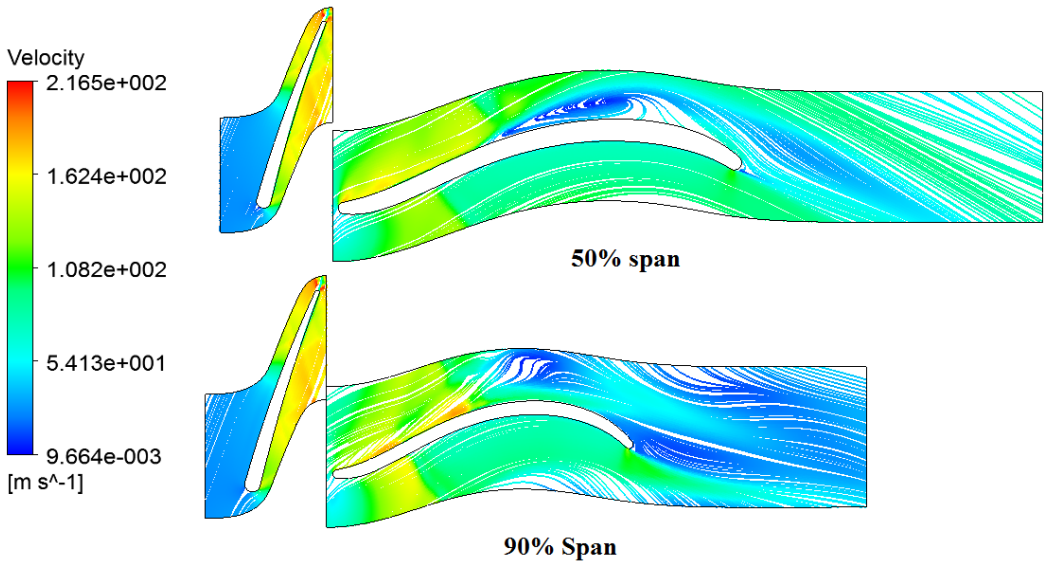

Figure 6-25: Velocity streamlines at off-design conditions (N=30,000 rpm, PR=7).

Last but not least, a parametric study was performed using ANSYS CFX in order to evaluate the turbine efficiency at different pressure ratios and rotational speeds. The results are presented in Figure 6-26. It is clearly shown that the turbine operates more efficiently at off-design speeds ($20{,}000\ rpm\ and\ 30{,}000\ rpm$) than the design point ($40{,}000\ rpm$) at low pressure ratios. However, this is expected since the turbine was designed to operate under high pressure ratios, which clarifies the high turbine efficiencies at high pressure ratios.

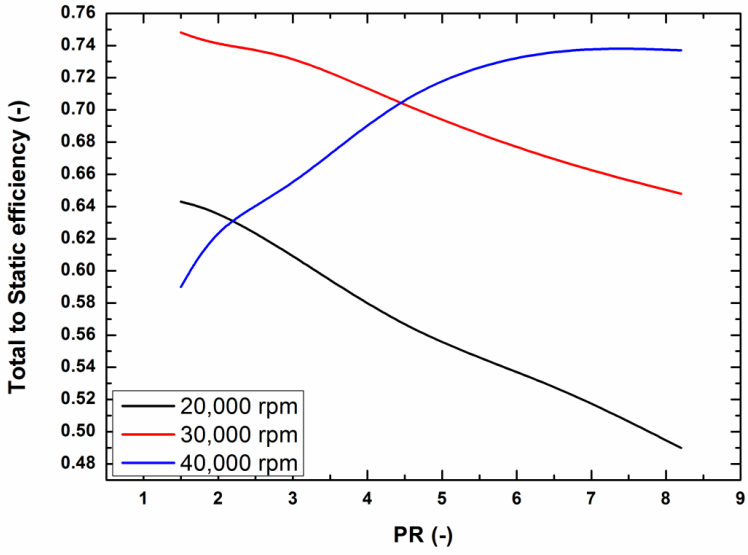

Figure 6-26: Parametric study using ANSYS for the proposed turbine.

6.3.6.3 Discussion of the CFD Results

Design Point

The aim of the CFD simulation at the design point is to validate the mean-line model, and to study the flow field within the turbine stage. Therefore, the computational results for the rotor of the turbine were compared with mean-line analysis as presented inTable 6-1. ANSYS provides a summary of the mass or area averaged solution variables (**mass averaged variables**: total pressure and temperature and static temperature. **Area averaged variables**: static pressure and velocities), and derived quantities (such as total to static efficiency) computed at the inlet and exit of each component of the turbine. These values, which are shown inTable 6-1, were selected as comparison variables between the 1D and 3D simulations.

As shown in Table 6-1, maximum deviations of 6.15% and 6.7% were noticed in rotor inlet absolute velocity and exit velocities, respectively, between the CFD and the mean-line model. This is justified by the assumption of the isentropic flow through the stator as shown in equation(5-39). As a result, at fixed mass flow rate (design point), the meridional velocity increased to conserve the mass as shown in equation (5-13). This increase in the meridional velocity results in higher absolute velocity. This is not the case in the CFD analysis where the stagnation pressure drop in the stator was taken into account; therefore, the flow is not isentropic as shown in Figure 6-15. Therefore, a significant difference was noticed between the CFD and 1D analyses. Similar analysis was performed by White [13]. He compared the total and static conditions, mass flow rate, velocities and efficiencies of the mean-line model with his CFD results. A very good agreement was achieved between the 1D and CFD results. The deviation between the total to static efficiency in White's results was 0.15%, while it was 0.75% in the current results. Compared to 6.15% deviation of the velocity in the current results, the deviation in Martin's case was 7.5%. His higher deviation was due to the assumption of constant stagnation pressure between the stator exit and rotor inlet (P03 = P04). This also justifies the higher deviation in the estimation of the static pressure at rotor inlet which was 6.3%, compared to 3.2% in the current simulation.

As stated, supersonic condition are always expected in ORC turbines due the high pressure ratio through the turbine stage which results in high loading on the turbine blades and high Mach number as shown in Figure 6-16. The maximum Mach number at the design point was 1.4 at the stator exit. A similar study by Zhang et al. [289] was performed using ANSYS CFX. However, they focused on the differences between several turbulence models available in ANSYS CFX. At the design point, Mach number at the stator exit was 1.23 in their simulation. [290] simulated their radial inflow turbine with pressure ratio of 7.95 using ANSYS CFX. The stator model applied in their study was similar to the one discussed in Chapter 5. Their results showed a Mach number of 1.4 at the stator exit.

In addition, the flow recirculation is always expected in ORC turbines due to the high loading on the turbine blades, as depicted in Figure 6-18. The high loading results in a flow separation in the suction side of the blade in the 50% span which makes the blade unable to accelerate the flow relative velocity to high levels. However, the incidence angle was optimised in the mean-line model which resulted in a uniform flow at the rotor inlet as shown in 6-18. Similar studies such as [248][291][14]were performed using ANSYS CFX. Their results showed a flow separation on the blade suction surface due to the aforementioned reasons.

Off-Design Conditions

For the off-design simulations, the pressure ratio was varied from 1.5 to 8.2 while the speed was changed from 50% to 100% of the design speed (40,000 rpm), as presented in Figure 6-26. It is clearly shown that the highest turbine efficiency was achieved at the equivalent design point which indicates the effectiveness of the mean-line model. At the same pressure ratio, the efficiency of the turbine continually decreases with the other turbine speeds (20,000 rpm and 30,000 rpm) as shown in Figure 6-26. This is expected since the turbine geometry (especially the blade throat) was designed to achieve the required expansion at 40,000 rpm; therefore, bad flow conditions (such as strong vortices) were detected with other the speed, as depicted in Figure 6-23 and Figure 6-25. However, at lower rotational

speeds, the turbine showed better performance at low pressure ratios which is quite common in radial turbines, as reposted by Han et al. [148]. Last but not least, at 30,000 rpm, higher Mach number was predicted at the stator exit, compared to that of the 40,000 rpm at, at the same pressure ratio. This is expected due to the higher absolute velocities, a shown Figure 6-18and Figure 6-25.

6.4 Conclusion

This chapter presented the CFD analyses of the optimized turbine using ANSYS CFX.The results showed that the optimised turbine presented power output of 13.56 kW and 73.85. At off-design conditions, the turbine presented lower efficiencies compared to the design point. In addition, the results of the 1D mean-line methodology were in close proximity with CFD results, indicating the fairly accuracy of the proposed methodology for ORC turbines.

The next chapter presents the test rig built at Brunel University London. The chapter presents also the results of the experimental work related to the ORC system with focusing on the radial inflow turbine.

Chapter 7 : Organic Rankine Cycle System Experimental Study

7.1 Introduction

The application of ORCs as WHR systems in ICEs is still under an early stage of development. Therefore, examining such applications experimentally with real engines is of great importance in the field.

Several recent studies have investigated ORC technology and show promise in solar systems [292]–[296], biomass [297]–[302] and geothermal applications [156], [216], [303], [304]. In recent years, studies that concentrate on ICE applications have increased.Guillaume et al.[192] used the exhaust gases of a truck diesel engine as the heat source for their ORC system. They used a radial-inflow turbine as the expansion machine and two working fluids, namely, R245fa and R1233zd. However, the turbine used was developed mainly using components modified from truck turbocharger designs. In addition, the heat wasted by the truck through the exhaust gases was simulated using an electric oil boiler coupled to the ORC loop. The maximum electric power and turbine efficiency were 2.8 kW (using R245fa) and 32% (using R1233zd), respectively. Yang et al.[305] presented a thermo-economic model of a dual-loop ORC system using the performance map of a six-cylinder CNG engine. The thermal efficiency of the dual-loop ORC system is in the range of 8.97%–10.19% over the entire operating range. Furukawaet al. [306] conducted an experimental test on the ORC used to recover the heat of the engine coolant usinghydro-fluoro-ether as the working fluid. The fuel consumption decreased by 7.5%. Other similarlypromising experimental works on ORC systems in ICEs in the academic sector are found in [307]–[310]. In the industry sector, a recent study was published through cooperation among AVL, FPT and Iveco [311]. The exhaust gas of a four-stroke diesel engine was used as the heat source of the ORC system, and tests were conducted on public roads. An axial piston expander was selected as the expansion machine. The results showed that fuel consumption could be reduced by 2.5%–3.4%. Honda [312], [313] installed an ORC system on a hybrid vehicle that runs at constant speed, and the thermal efficiency increased by 13.2% compared to the base vehicle.

The brief literature survey in the previous paragraph indicates that these investigations were either performed using simulated engine data (academic

sector) or expander types other than radial turbine (industry sector). AlthoughGuillaume et al.[192] used a radial-inflow turbine in their study, the turbine was developed using the components of truck turbochargers. Electric oil boiler was applied as the heat source as well. The coupling of a custom-designed radial turbine (and generator) on-engine to explore ORC WHR system performance is an area in which little available literature exists. To allow a realistic appreciation of the ORC system's contribution to heavy-duty diesel engine, a coupling of ORC system with real engine is essential.

Therefore, a test rig that contains an ORC thermal oil loop was built around anHDD engine and tested inthis chapter. From the engine point of view, part-load performance is seldom investigated in depth. Thus, this study focused on this topic. For this study, the engine was operated at 40% of its maximum power to target a representative, mean operating condition. The exhaust gas of a heavy duty diesel engine was applied as the heat source for the thermal oil loop. Subsequently, the oil exchanged heat with the ORC unit.

7.2 ORC Thermodynamic Definitions Used in the Experiment

This section presents the experimental set-up tested and the principal theoretical expressions used in the definition of theperformance of ORC system and expander. Figure 7-1 presents the schematic of the ORC test rig. The working principal of the cycle is discussed in Section 3.3. The turbine is directly coupled to a high-speed, synchronous electric generator to convert the turbine mechanical power to electricity. In the test bench, a load bank is installed for the dissipationof electric power.

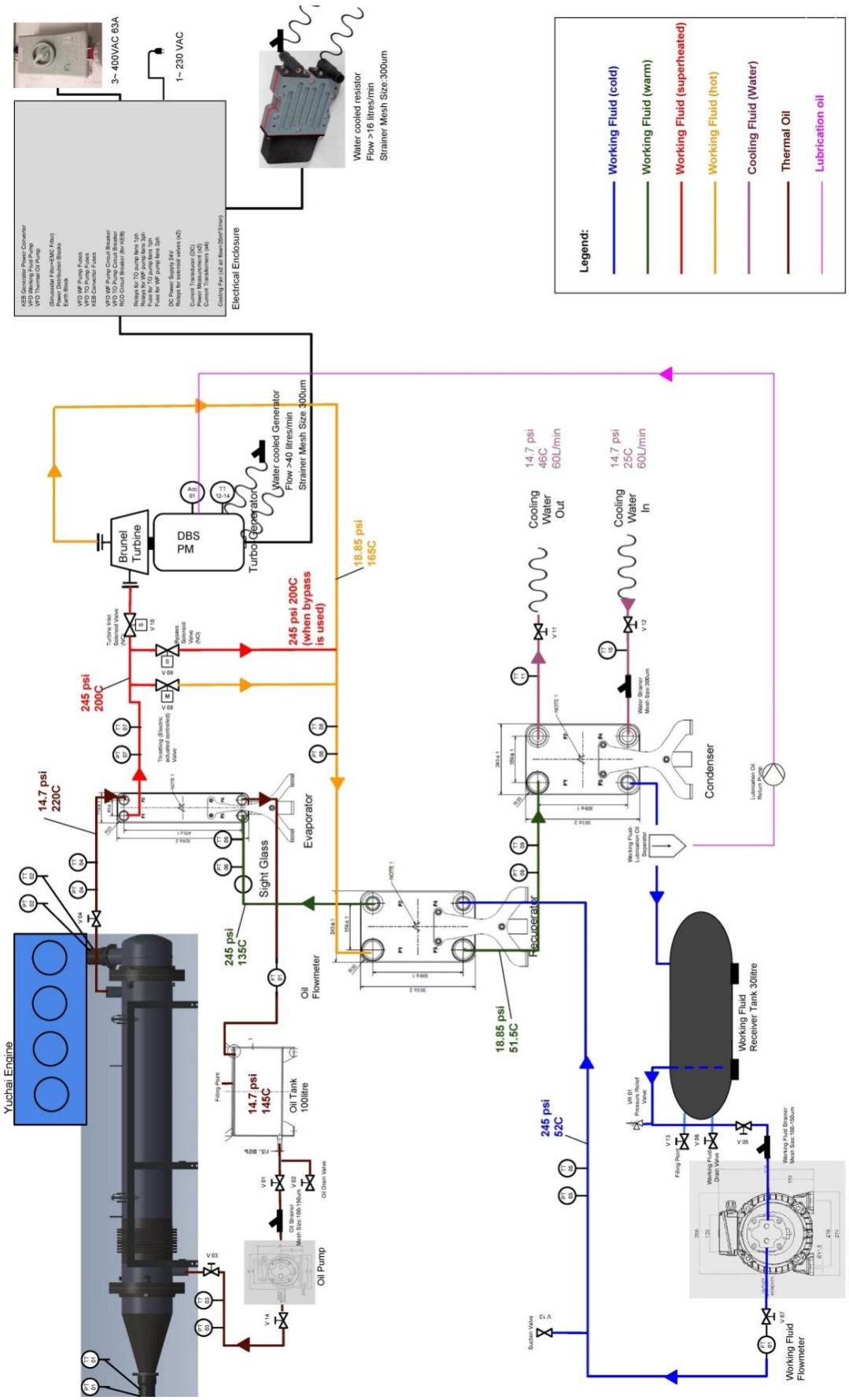

Figure 7-1: Schematic of the Test Bench.

The principal thermodynamic equations of each component are discussed in Section 3.3. The performance of the ORC system is measured using the definition of the thermal efficiency η_{ORC}, as shown in equation(7-1). Thermal efficiency is defined as the ratio between the cycle work net and the heat extraction in the evaporator. W_{net} is the cycle power, and it is the difference between the electrical power generated by the generator and the power consumed by the pumps (working fluid pump and thermal oil pump), equation(7-2).

$$\eta_{ORC} = \frac{W_{net}}{Q_{evap}} \tag{7-1}$$

$$W_{net} = P_e - (W_{pump,wf} + W_{pump,to}) \tag{7-2}$$

The turbine performance is measured using bulk properties for the total-to-total isentropic efficiency definition, as shown inequation(7-3). Another indicator of turbineperformance is the turbine expansion power, which is defined using Euler's equation which represents the second term of the right hand side of equation (7-4). A well-known expression in turbo-machinery book is the combination of Euler's equation and the velocity triangle. This combination is the last term of equation (7-4).

$$\eta_{tt} = \frac{h_{07} - h_{08}}{h_{07} - h_{05s}} \tag{7-3}$$

$$W_{out} = \dot{m}\Delta h_{act} = \dot{m}(U_a C_{\theta a} - U_b C_{\theta b}) = 0.5\,[(U_a^2 - U_b^2) - (W_a^2 - W_b^2) + (C_a^2 - C_b^2)] \tag{7-4}$$

7.3 Experimental Apparatus

The test rig consists of two main components, namely, HDD engine (Figure 7-2) and the ORC skid (Figure 7-3).

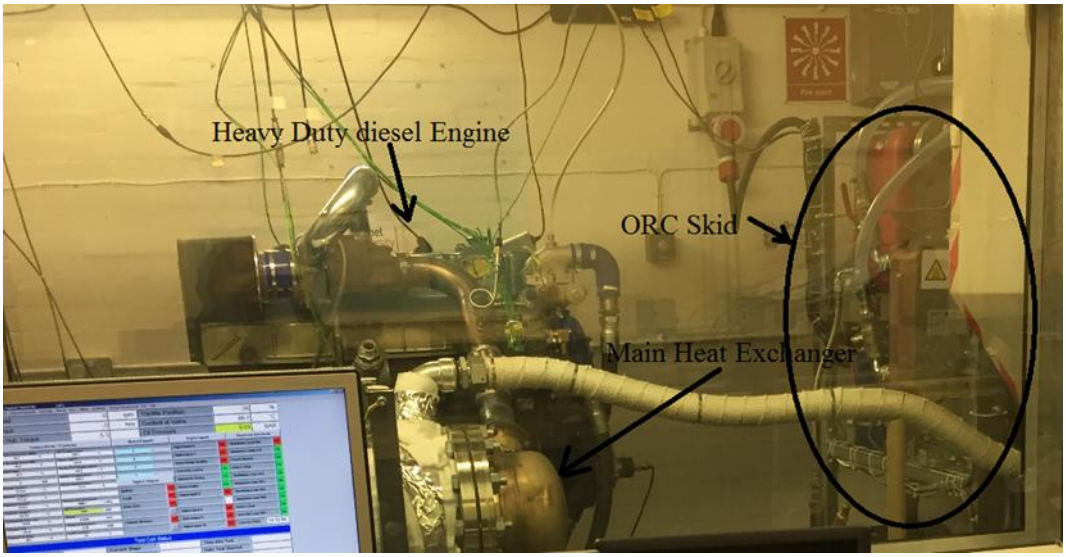

Figure 7-2: Description of the test components.

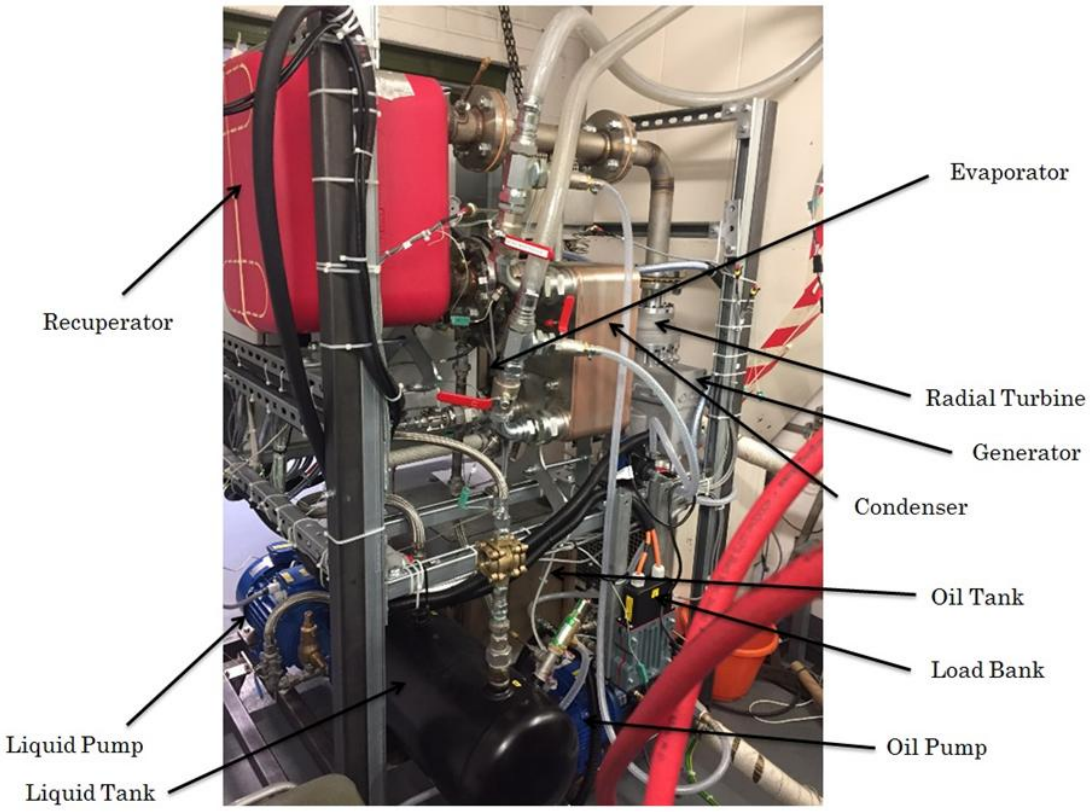

Figure 7-3: Description of the ORC components.

7.3.1 Description of the Heavy-duty Diesel Engine

The characteristics of the HDD engine are presented in Table 3-2. Figure 7-4 presents the exhaust gas heat map of the engine and the selected operating point for the ORC design analysis and current test. It is observed that the maximum exhaust energy is wasted at maximum power conditions,

which was also considered as the design point of this ORC unit, in order to maximize the ORC system power output.However, the engine was not able to run at full load because of the technical issues of the dynamometer. The maximum power output presented in this study is nearly 40% (the red dot in Figure 7-4)of the maximum engine power (the black dot in Figure 7-4). In fact, this could be more practical. In transient automotive applications, the ORC system rarely operates at the design conditions. The presented tested off-design conditions of the ORC system are at 40% (81 kW) of the maximum engine power. This operating point represents an average steady state operation between high and low engine load and speed of the non-road transient cycle (NRTC) test protocol. NRTC is a legislative driving cycle developed by US EPA in collaboration with EU and is utilized worldwide for type approval of non-road engines. The normalized engine speed and torque profile are also presented inFigure 7-4.

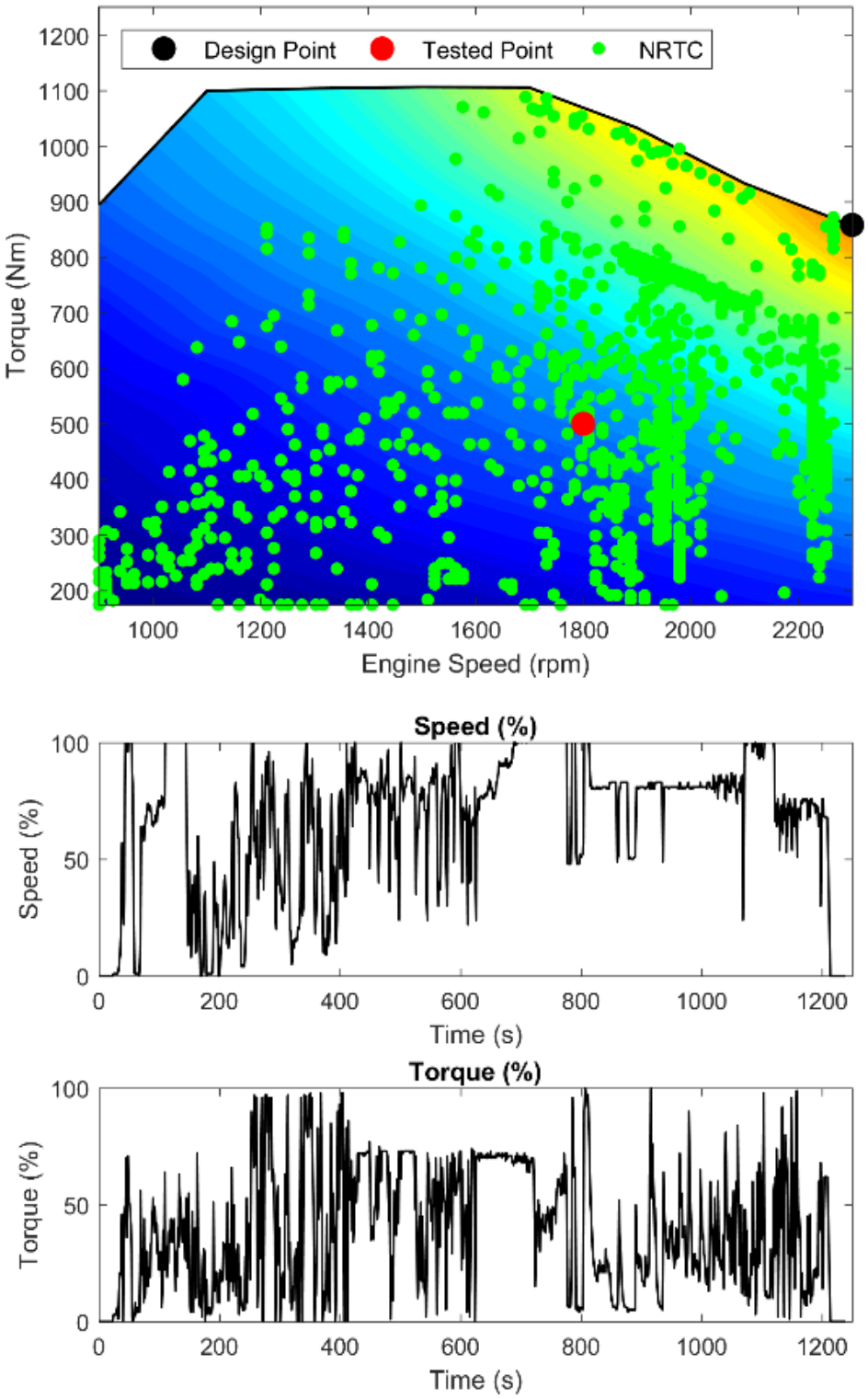

Figure 7-4: : (top) Exhaust heat diesel engine map, (bottom) The Non-road Transient Cycle (NRTC) protocol.

7.3.1.1 Gas–Oil Heat Exchanger (Main heat exchanger)

In the gas–oil heat exchanger, heat transfer occurs between the exhaust of the engine and the thermal oil, as shown in Figure 7-5. This exchanger is a single-flow heat STHE manufactured by Entropea Labs.

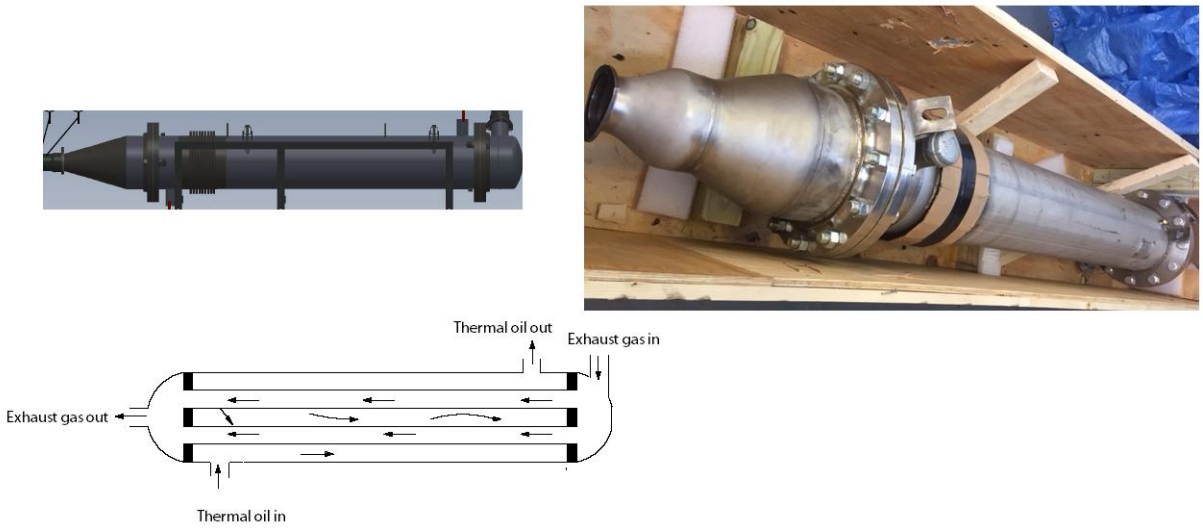

Figure 7-5: Thermal oil–exhaust gas heat exchanger (main heat exchanger).

7.3.1.2 Evaporator, Condenser and Recuperator

The evaporator, condenser and recuperator units are all counter-current flow, brazed plate heat exchangers. The counter-current configuration in the condenser is beneficial to insure that saturated liquid leaves the condenser. Therefore, the working fluid pump can operate more efficiently. The brazing is made of copper, and connections inside the heat exchangers are made of stainless steel to withstand the operating conditions of the cycle. Brazed plate heat exchangers consist of a pack of plates that are pressed together to eliminate the use of gaskets. The heat exchangers are manufactured by SWEP Limited. The maximum temperature and test pressure of the heat changers are 225 °C and 46 bar for the evaporator, 225 °C and 40 bar for the condenser and 225 °C and 72 bar for the recuperator. The condenser is cooled by a water loop controlled by a throttling valve. Figure 7-6 presents

the three components and the schematic of the counter-current configuration.

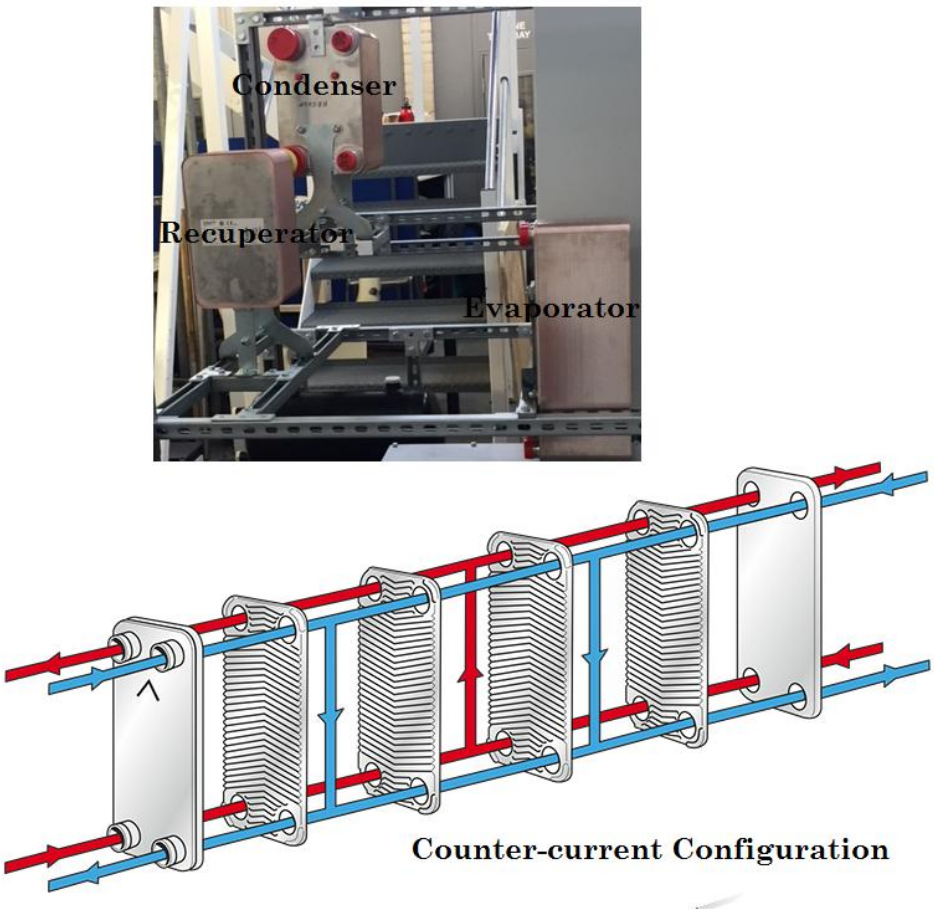

Figure 7-6: Heat exchangers (top) and flow configuration(bottom).

7.3.1.3 Pumps

Two pumps are available in the test rig: one for the oil loop and the other for the working fluid loop. Both pumps are of the positive displacement type (gear pumps) and are manufactured by GVR POMPE SRL. The pumps are connected to an electrical motor with the same maximum speed. The characteristics of both pumps are listed in Table 7-1. The two pumps are presented in Figure 7-3.

Table 7-1: Pump Specifications

Pump	Speed (rpm)	Flow Rate (lt/min)	Power (kW)
Oil pump	1400	40	1.1
Working fluid pump	1400	60	5.5

7.3.1.4 Turbo-generator

The designed radial turbine presented in the previous chapters was manufactured by TURBOCAM(Figure 7-7). The rotor and the stator are made of Titanium 6Al-4V bar stock, whilethe volute is made of aluminium alloy.

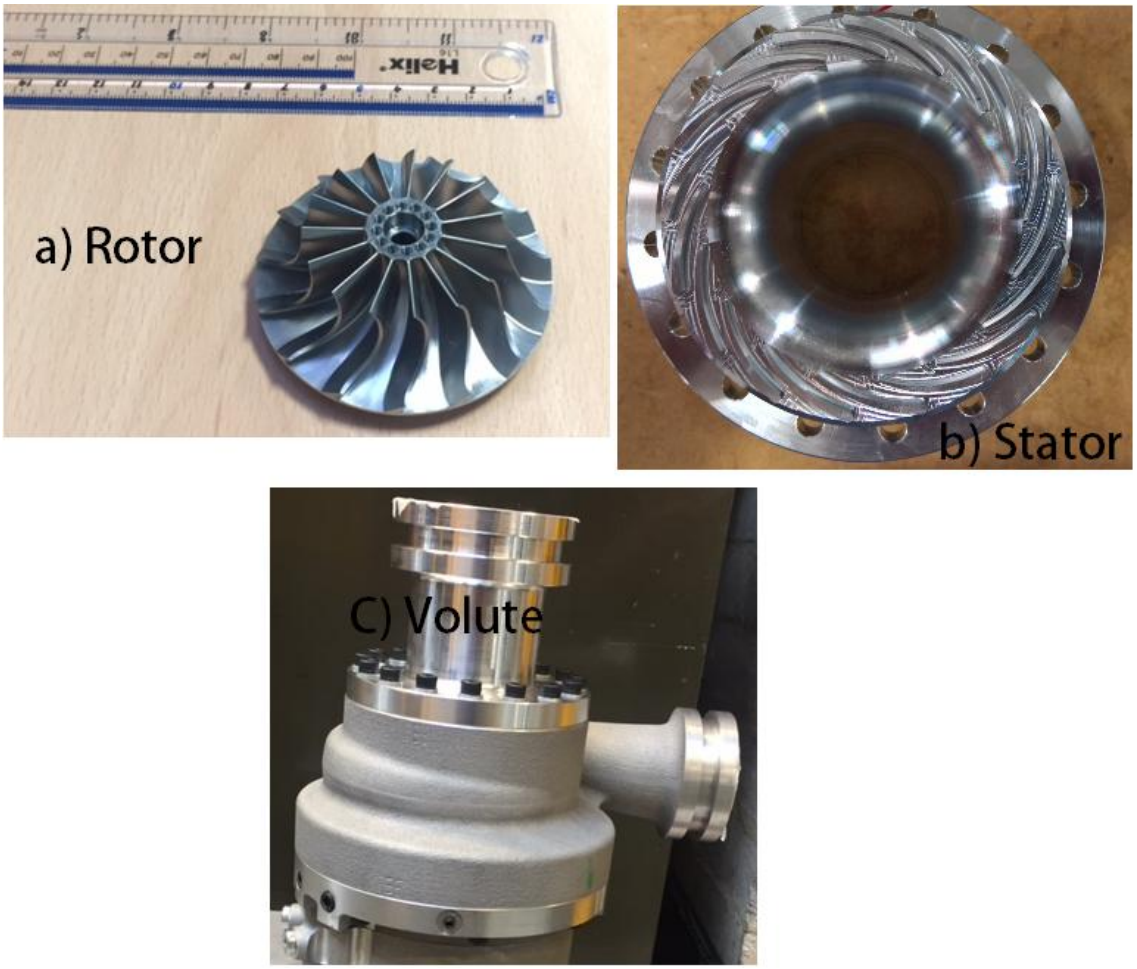

Figure 7-7: Components of the radial-inflow turbine.

The generator is a high-speed permanent magnet three-phase AC developed by DBS. The generator component has rated conditions of uninterrupted 20kWe output at 40,000 rpm with an over-spin design safety ofnot less than 45,000 rpm. Furthermore, the generator has a fully integrated lubrication system direct driven from the main generator shaft;hence, an external power supply is not required. However, oil leakage is expected; therefore, the specified oil should be compatible with the

working fluid (NOVEC 649). To this regard, an oil separator is implemented after the condenser. The generator includes a water jacket for the rotor/stator to enable the electrical power components to safeguard the equipment for the operating conditions. The generator's manufacturer provided the warning, alarm and tripping limits, as shown in Table 7-2. Figure 7-8 presents the turbo-generator unit. To prevent fluid leakage, air blown seals were applied for the turbo-generator unit.

Table 7-2: Operating Limits of the Generator.

Sensor	Warning	Alarm	Trip
Drive end bearing temperature	110 ℃	120 ℃	125 ℃
Non-drive end bearing temperature	110 ℃	120 ℃	125 ℃
Stator temperature	110 ℃	120 ℃	135 ℃
Oil tank temperature	40 ℃	50 ℃	55 ℃
Rotational speed	40,000 rpm	43,000 rpm	45,000 rpm
Vibration level	4 mm/s	6.5 mm/s	7.5 mm/s

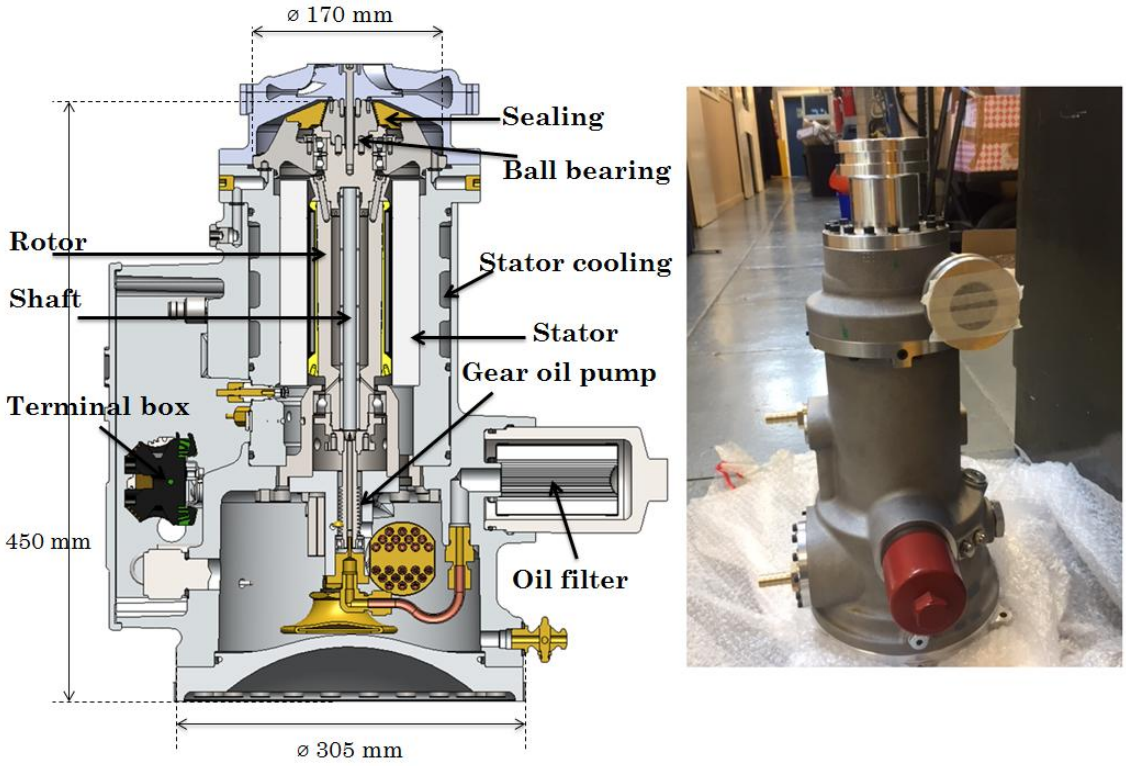

Figure 7-8: Turbo-generator unit.

7.3.1.5 Instrumentation

The test facility is instrumented with measuring devices at the inlet and exit of the components to measure total pressure, total temperature and/or mass flow rate to evaluate the efficiency of ORC, power and efficiency of the turbine and the generated electrical power at different operating conditions. All the thermocouples are of K type (nickel chromium/nickel aluminium). These thermocouples are highly flexible, and their sheath can be formed or bent to suit the required applications. They are also usually robust and relatively inexpensive. The pressure transducers use piezo-resistive sensing technology with application-specific integrated circuit signal conditioning in brass housing and Metri-Pack 150 or cable harness electrical connections. The mass flow rates of thermal oil and working fluid are measured using flowmetres. The turbine is directly coupled to the generator and the speed can be controlled by the user. The operating range and accuracy of the measuring devices are described in Table 7-3. The thermocouple, transducer and flow metre are presented in Figure 7-9.

Table 7-3: Operating Range and Accuracy of the Measuring Devices.

Measurement	Range	Accuracy
Total temperature	−40 °C – 1100 °C	n/a
Total pressure	1 – 50 bar	± 0.25 full scale
Working fluid flow rate	1 – 8 GPM	± 3% of reading

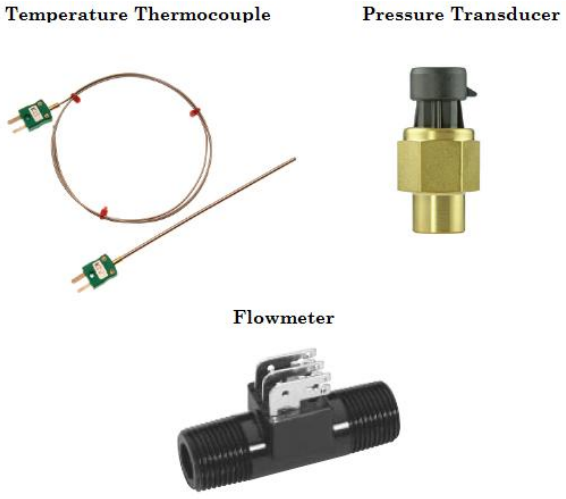

Figure 7-9: Instrumentations applied in the test rig.

7.4 Results and Discussion

Steady-state testing was performed at 40% of the maximum engine power owingto the limitations of the dynamometer. This pointcorresponds to 1790 rpm, 450 N.m and 81 kW as represented in Figure 7-4 (red dot).

7.4.1 Overview of the Results

The recording of test data was initiated once the thermal equilibrium (steady state) was achieved. Therefore, the time (x-axis) shown in latter figures in this section is the time after recording and not the time from the beginning of the test.

The temperature of the exhaust gas is the main external factor that affects cycle performance. Figure 7-10 and Figure 7-11 present the effect of the exhaust gas temperature on the temperature and pressure of both the oil through the evaporator and the working fluid through the turbine at constant working fluid mass flow rate (0.33 Kg/s). Figure 7-10shows that the oil temperature increases at a constant rate with the exhaust gas temperature. Consequently, the temperature of the working fluid at the turbine inlet increases proportionately. Furthermore, the temperature at the turbine exit increases proportionately with the temperature of the exhaust gas. The temperature drop between the inlet and exit of the turbine is a result of the expansion process within the turbine. The maximum difference in the temperature of the oil between the inlet and exit of the evaporator is 14.4°C, whereas it is 12.3°C forthe organic fluid between turbine inlet and exit at the maximum exhaust gas temperature. Figure 7-11 presents the effect of the exhaust gas temperature on the pressure of oil and working fluid. As can be seen in the figure, the increase of the oil pressure at the inlet and exit of the main heat exchanger is negligible,indicating a steady-state condition. The pressure of the turbine inlet increases by 0.4 bar with the temperature of exhaust gas. However, the turbine exit pressure is almost constant during the process because the exit pressure is not directly related to the evaporator exit. As previously mentioned, these resultsamples are taken at a constant working fluid mass

flow rate. Figure 7-12 shows that the turbine inlet pressure increases with the working fluid mass flow rate. As the mass flow rate increases from 0.05 Kg/s to 0.83 Kg/s, the turbine inlet pressure increases from 1.45 bar to 8.3 bar.

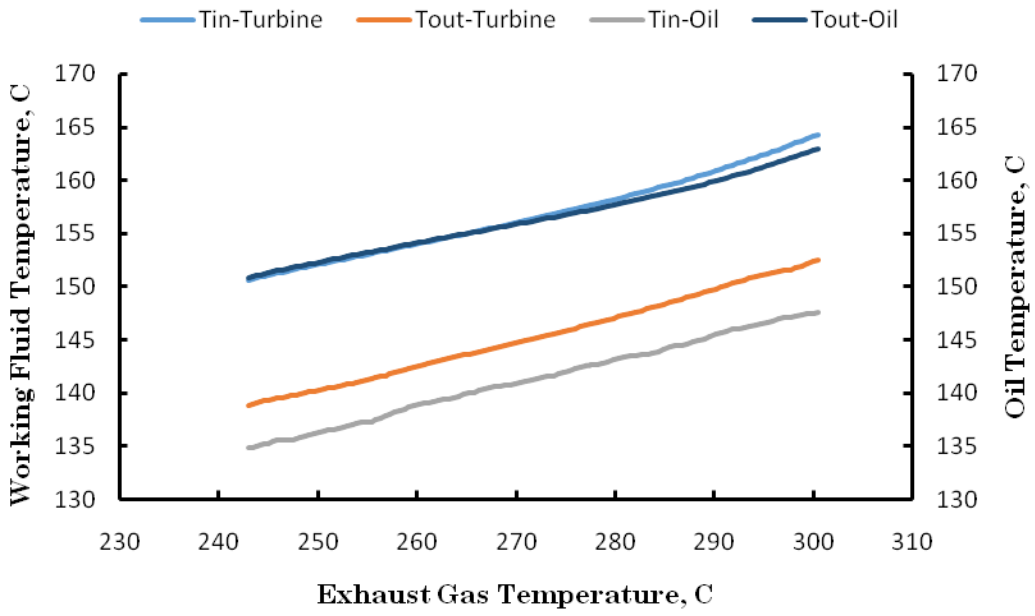

Figure 7-10: Effect of heat source temperature on working fluid and oil temperature.

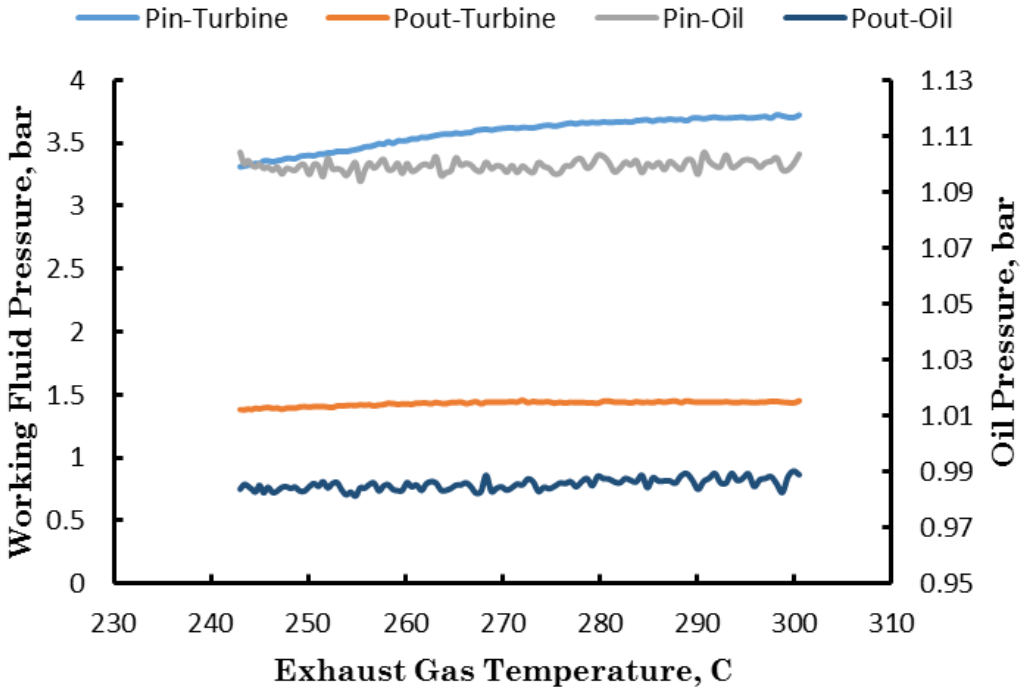

Figure 7-11: Effect of heat source temperature on working fluid and oil pressures.

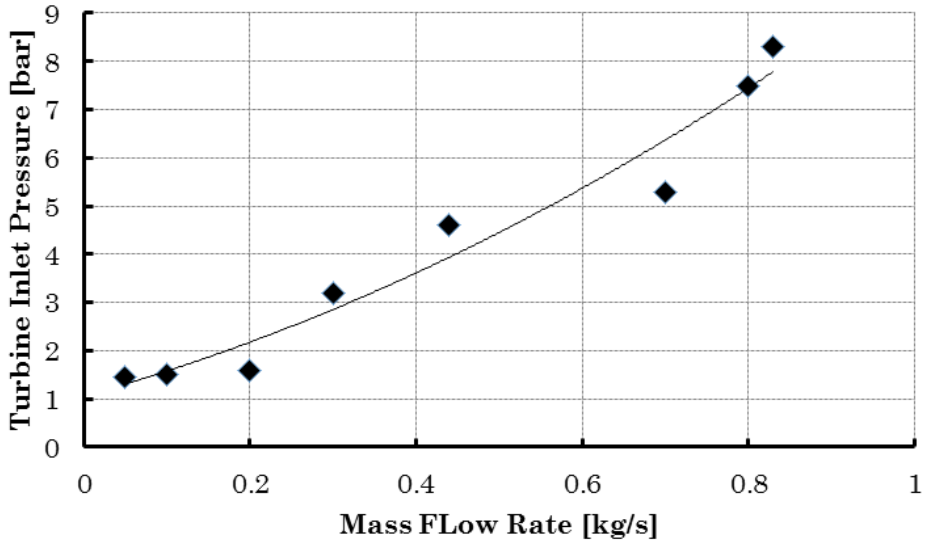

Figure 7-12: Effect of working fluid mass flow rate on turbine inlet pressure.

As previously stated, the test was run at 81 kW of engine power (40% of the maximum engine power). Therefore, the heating of the thermal oil could not be sustained,that is, the power of the oil will diminish with time. Thus, the power generation in the electric generator lasts for approximately 30 minutes, with a maximum power of 6.3 kW before falling sharply in the last five minutes. Figure 7-13 presents the variation of the electrical and oil power with time.

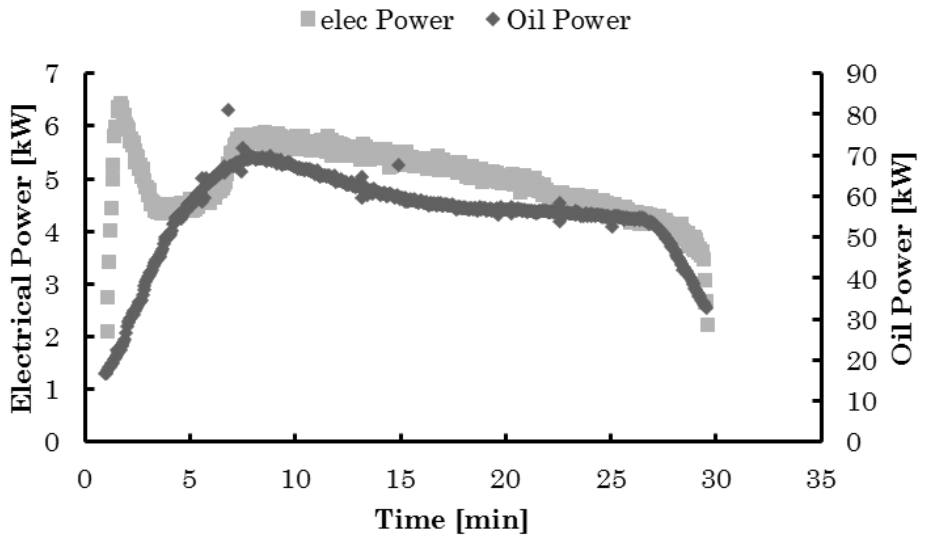

Figure 7-13: Relationship between oil power and electrical power.

The equations presented in Section 3.3were applied to calculate the performance for the three heat exchangers involved (gas-oil heat exchanger, evaporator and condenser) at different heat source temperatures. The points in which two-phase flow occurs are excluded in the analysis due to the difficulty of measuring the thermodynamic properties (i.e. enthalpies) involved at those stations. Figure 7-14 shows that the maximum deviation in the main heat exchanger (gas–oil heat exchanger) is 1.9% at 239°C. The same analysis was performed on the evaporator and condenser, in which the maximum errors were 3.7% and 4.1%, respectively. The aforementioned errors are relatively low and could be explained as due to the inaccuracies in the temperature measurements and the heat loss in the connecting pipes,which are not insulated.

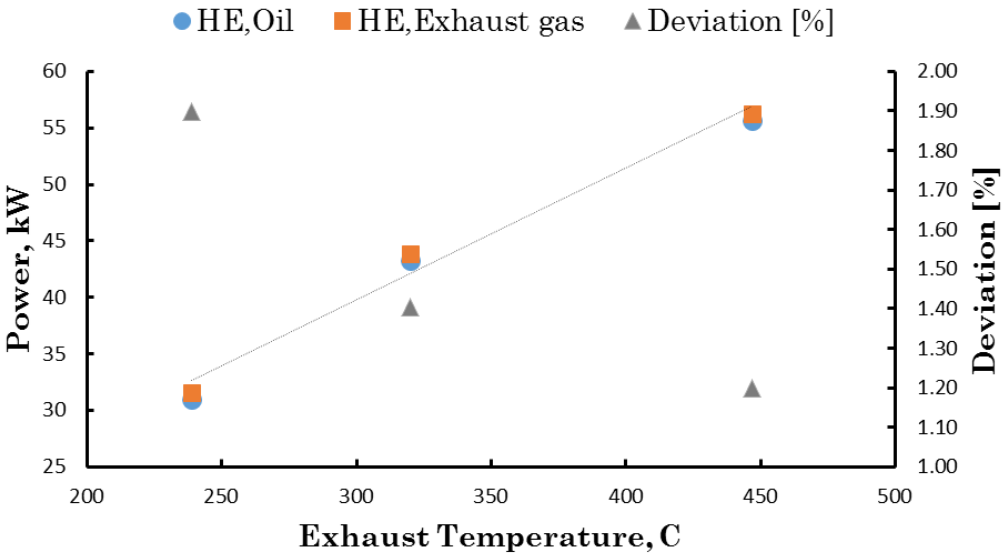

Figure 7-14: Energy balance through the main heat exchanger.

The thermal efficiency of the cycle is investigated with time, as depicted in Figure 7-15. The cycle efficiency is far below the design point value (9.3%) because the cycle was operated well within off-design conditions. For instance, the turbo-generator operated at 20,000 rpm, which is far below its rated rotational speed (40,000 rpm). The cycle efficiencyis in the range of 1.4%–4.3%. The efficiency reaches its peak after approximately 12 minutes

of testing and then decreases to 2.8% due to the reduction of the electrical power in the generator, as shown inFigure 7-13.

The main purpose of the ORC as a WHR system is to improve the engine performance or, conversely, the reduction of fuel consumption. The results show that the BSFC is decreased by an average value of 3% after the implementation of the ORC at these conditions (40% of the maximum engine power).

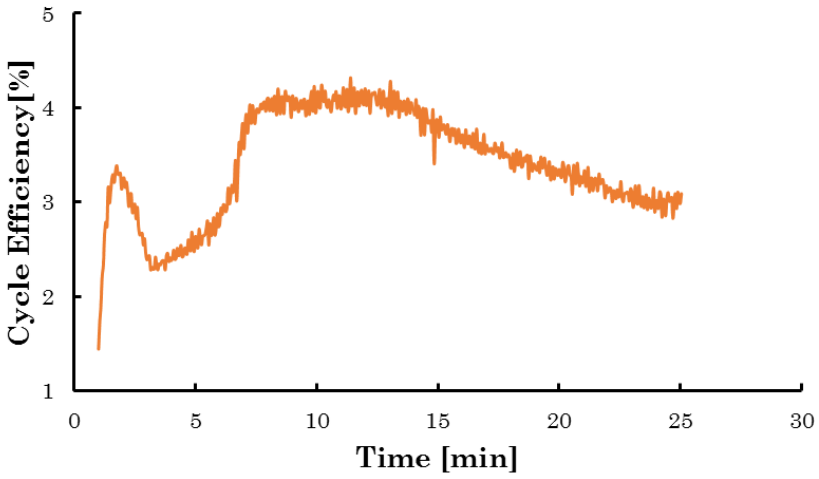

Figure 7-15: Cycle efficiency evolution with time.

7.4.2 Turbo-Generator Characteristics

This section presents the results of the turbo-generator at the tested engine point.

7.4.2.1 Electrical Power

The electrical power generated by the generator is investigated at different conditions. Figure 7-16shows the relationship between the generated power and the turbo-generator speed. The electrical power increases linearly with speed. As speed increases from 5000 rpm to 7000 rpm, the increase in power is insignificant. The power then increases gradually from 8000 rpm to 20,000 rpm, with a maximum power of 6.3 kW at 20,000 rpm.

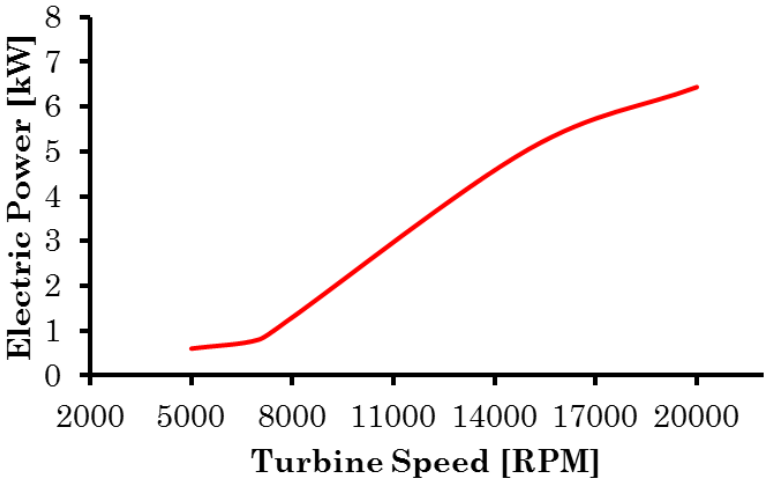

Figure 7-16: Power generation with speed.

In addition, the generated power is investigated at different turbine pressure ratios, as shown in Figure 7-17. The generated power linearly increases with the expansion ratio between turbine inlet and exit. The expansion is increased by controlling the mass flow rate using the working fluid gear pump. The turbine inlet pressure increases asthe mass flow rate increases, as shown in Figure 7-12. The results in Figure 7-17 are demonstrated at a constant turbo-expander speed (20,000 rpm). The maximum obtained electrical power is 6.3 kW at 5.9 pressure ratio. For the 15,000 rpm speed, the maximum electrical power achieved is 5.1 kW at 3.8 pressure ratio.

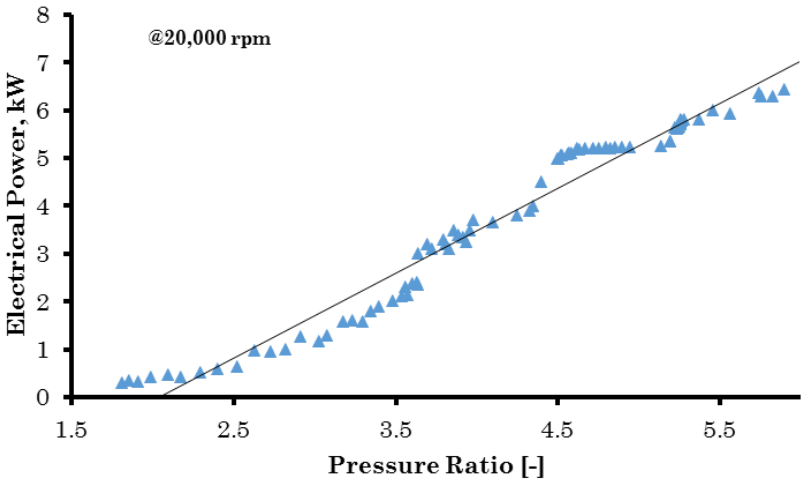

Figure 7-17: Power generation with turbine pressure ratio at 20,000 rpm.

7.4.2.2 Turbine Performance

The turbine performance is investigated at different speed and mass flow rate conditions and at constant heat source temperature.

For the evaluation of the efficiency of the turbo-expander, the isentropic total-to-total efficiency definition is applied, as shown in equation (7-1). The heat source temperature is maintained constant, whereas the mass flow is increased to control the pressure ratio through the expander for each speed line. The turbine is directly coupled to the generator. Therefore, the turbo-generator speed can be controlled by the user. Two speed lines are selected, namely, 15,000 and 20,000 rpm. Each single value of the pressure ratio is taken as the average value for approximately 3 minutes of testing. Figure 7-18 shows that both speed lines have the same trend,that is, the efficiency increases until its peak is reached, and then decreases as the pressure ratio increases. This decrease is expected in radial turbines due to the choked flow at high pressure ratios as can been seen inFigure 5-22. At PR $\geq$ 4.2, the flow becomes supersonic at the nozzle exit which results in choking condition for any further increase in the pressure ratio. In case of choking, total losses especially the incidence and frictional losses increase. The choking condition results also in raising the flow velocity in the rotor much more than that in the nozzle. The latter phenomenon results in shock waves in the radial gap between the stator exit and rotor inlet. The aforementioned problems arising from the flow choking result in lower turbine efficiency as the pressure ratio exceeds the choked value. With 20,000 rpm speed, the efficiency increases with the pressure ratio until its peak of 35.2% is reached at a pressure ratio of 4.6 before it decreases to 30% at 5.9 pressure ratio. At 15,000 rpm, the isentropic efficiency varies from 10%, reaching its peak of 27.3% at 3.5 pressure ratio to 14% at a pressure ratio of 5.5. The cumulated measurement uncertainty is nearly constant for each speed line. For the 20,000 rpm, the uncertainty measurement is 1.5%, while it is approximately3% for the 15,000 rpm.

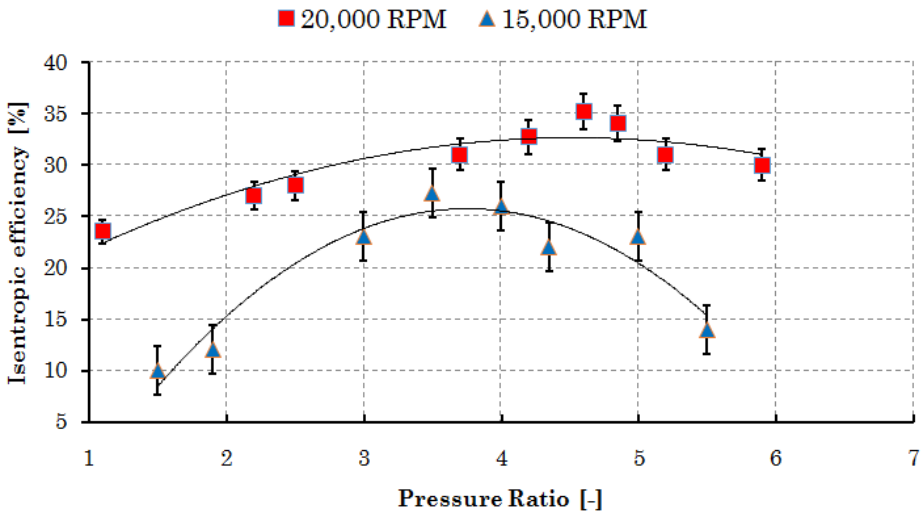

Figure 7-18: Turbine isentropic efficiency at two speeds.

The turbine power is investigated at different mass flow rates and speeds. Euler equation, as shown inequation (7-4), contains two terms. The first term is the product of the mass flow rate and the enthalpy drop, and the second term is the product of the torque and turbine speed. The results are presented in Figure 7-19 and Figure 7-20, respectively. The power of the turbine increases linearly with the mass flow. Increasing the mass flow rate, by adjusting the gear pump, results in a high pressure ratio through the turbine stage. As the pressure ratio increases, the enthalpy drop increases, leading to higher turbine power output. Figure 7-19 shows that the maximum obtained power is 10.2 kW at 0.85 Kg/s mass flow rate. Unlike mass flow rate, turbine power increases non-linearly along with the turbine speed with a maximum value of 10.2 kW at 20,000 rpm, as depicted in Figure 7-20. The non-linear increasing of turbine power is justified by the term$(U_4^2 - U_5^2)$ which represents the last term of equation(7-4).

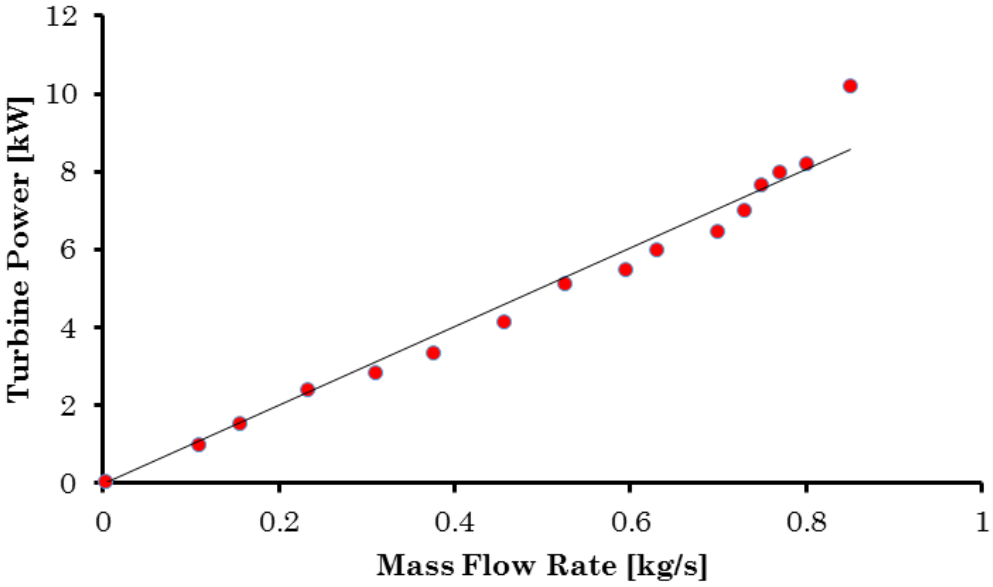

Figure 7-19: Variation of power with working fluid mass flow rates.

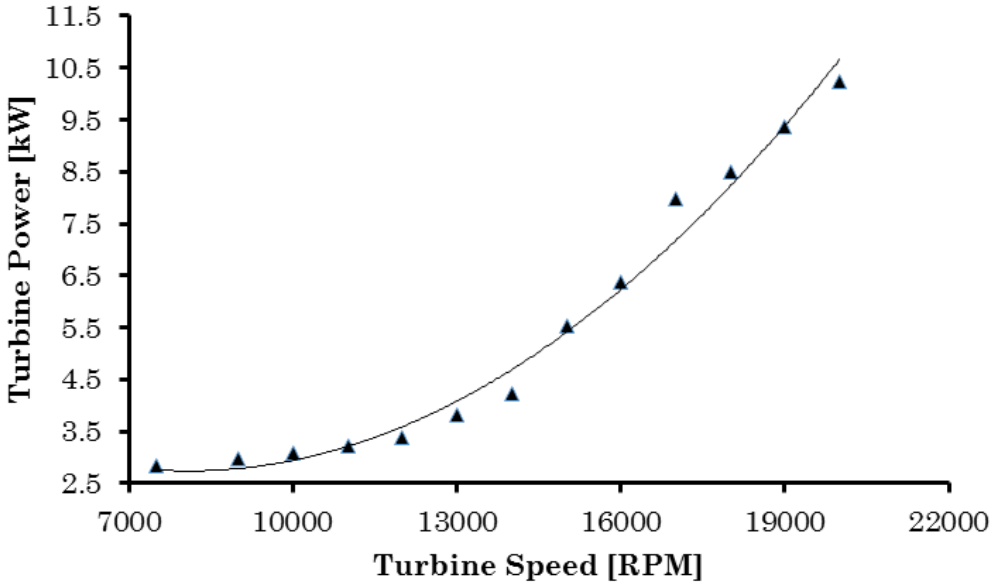

Figure 7-20: Variation of power with turbine speed.

Last but not least, the simulation results were compared with the experimental ones at off-design conditions as shown in Table 7-4. Table 7-4 indicates that the results are in fairly good agreement with a maximum deviation of 2.87% in the turbine efficiency and 3.07% in the mass flow rate.

Table 7-4: Comparsion between simulation and experimental results.

Speed	20,000 rpm											
Parameter	Simulation						Experiment					
PR	1.1	3.7	4.2	4.6	5.2	5.9	1.1	3.7	4.2	4.6	5.2	5.9
$\dot{m}$	0.153	0.365	0.42	0.482	0.591	0.67	0.15	0.36	0.41	0.47	0.58	0.65
η_{tt}	23.8	31	32.7	35.2	31	30	23	30	30.7	32.4	29.2	27.2

7.5 Conclusion

Following the development of the mean-line methodology, it was required to manufacture the developed turbine and test it using the test rig. The ORC system, including the turbine, was built at Brunel University London, and instrumented in order to measure the cycle and turbine efficiencies under off-design conditions. The test rig was coupled to a real engine in order to obtain more practical results. The main heat exchanger was connected to the exhaust gas port to harvest the wasted heat, and the results were obtained at steady state conditions. Unfortunately, the engine was not able to work at full load conditions due to the limitations of the dynamometer.

The results showed that an electrical power output of 6.3 kW was obtained at 20,000 rpm and 40% engine power. The maximum ORC thermal efficiency and turbine η_{tt} were 4.3% and 35.2%, respectively.

Chapter 8 : Conclusions and Future Work

8.1 Introduction

Although the electric vehicle is a new concept in the world of cars, some concerns, such as limited range, lack of power, long refuelling time and higher cost (vehicles and battery packs), are still surrounding its use on the road. In addition, electric vehicles indirectly cause pollution because of the toxic fumes generated by the toxic elements in the batteries. Therefore, improving the current technology (i.e. ICEs) by means of WHR technologies is important because the transport sector has not yet altered its near-total dependence on petroleum fuels. One of the promising and reliable WHR technologies is ORC, which can recover wasted heat in low to medium applications, such ICEs. In this regard, expansion machine is the key component among the other ORC components because it is the interface where power conversion occurs. Therefore, its performance has a significant impact on the overall efficiency of the cycle.

8.2 Conclusions

The main aim of this work was to develop a performance prediction methodology using mean-line analysis for ORC radial-inflow turbines. To achieve this aim, a comprehensive literature review of the current expansion machines in ORC-ICE applications was undertaken. The outcome of the literature review necessitated the development of the proposed design methodology due to the unstable and uncontrollable conditions of the heat source. The key findings and contributions of the current research are summarised as follows:

- The effect of ORC as WHR technologies in ICEs was investigated by constructing two models. The first model intensively investigated the effects of radial turbine characteristics on the ORC system and the ICE. Results showed that the performance of ORC varied substantially by altering the operating conditions at the turbine inlet or by replacing the working fluid. The results of the first model also proved that the assumption of the constant expander's efficiency,

which is widely used in ORC studies, was not applicable due to the significant effects of the operating conditions on the cycle performance. By changing the MFR from 0.05 Kg/s to 0.3 Kg/s, the performance of ORC improved by 1.65%. ORC performance also substantially varied by changing the working fluids,in which R1233zde presented a cycle efficiency of 11.09% compared to that of R123with 6.77%. The second model investigated the influence of the specifically designed ORC system, in which an intermediate oil loop was implemented on the performance and fuel consumption ofthe available off-highway HDD engine. The results showed that the increase in surface area of the heat exchanger leads to higher heat recovered at the expense of higher exhaust backpressure and WHR system weight as ΔT between the fluids approached zero. Consequently, the increase in weight of the heat exchanger was illustrated as the main parameter that limits the ORC system design in vehicular applications. Results also showed that the optimum heat exchanger length was a trade-off among exhaust backpressure, required net ORC power and weight increase.

- A methodology for design, optimisation and performance prediction of the ORC radial-inflow turbine was developed using mean-line analysis. This methodology encompassed a DOE technique to evaluate the effect of one or more design input parameters on the turbine performance (power and efficiency), overall size and Mach number at the rotor leading edge. The results of the design point were validated using a well-known code foundin the literature [238]. These results were in good agreement with the real case, witha maximum deviation of 5.38% in the radius of the rotor tip. The optimisation algorithm was then applied to design an efficient radial turbine for the current application. Furthermore, the leading edge was manually adjusted, where the angle increased from 0^o to 54^owhich resulted in higher turbine power and efficiency according to the Euler equation. The optimised turbine presented a total to static efficiency η_{ts} and

power output W_{out} of 74.4% and 13.6 kW, respectively. The code also presented a turbine with a compact size ($r_1 = 50.7\,mm$), which could be beneficial in vehicular applications. The novel MOC was validated with experimental works from three turbines and presented good prediction. The maximum deviation was 6.6% with the turbine that had missing geometrical parameters. For the turbine designed and tested in the current thesis, the maximum deviation was 2.8%.

- The optimised turbine was further evaluated by performing an intensive CFD analysis using ANSYS CFX. The CFD results were useful for the designed turbine for two reasons. Firstly, they were used to validate the proposed methodology. Secondly, they were used to investigate the complex flow nature within the turbine.

- Lastly, a test rig that contained an ORC thermal oil loop was built around anHDD engine and was tested at partial load conditions due to the technical limit of the dynamometer. The current literature lacks such realistic tests in ICEs. Therefore, the results of the test were beneficial to the field. The test results were also crucial for validating the proposed design methodology in the current work. The results showed that the maximum thermal efficiency of the ORC was approximately 4.3%. Simultaneously, the maximum generated power was 6.3 kW at 20,000 rpm and a pressure ratio of 5.9. The isentropic efficiency reached its peak of 35.2% at 20,000 rpm and 27% at 15,000 rpm. The test was run at an operating point away from the optimum due to the technical issue of the dynamometer.

8.3 Recommendations for Future Work

In addition to other key contributions, this thesis covered two of the most frequently mentioned aspects forfuture work in recent studies [13], [14], [240]; specifically, the development of an performance prediction methodology and an experimental test rig. However, the following aspects require further research:

- Examining the benefits of scalloped radial turbines is beneficial because scalloping can assist in the reduction of weight, inertia and centrifugal stresses. Although scalloped turbines have been investigated in turbocharger applications, the open literature still lacks such technology in ORC applications.
- Although VGT has been theoretically investigated in this thesis, it is important to investigate such technology using real tests because the theoretical results showed the potential for better cycle and engine performance compared to the FGT.
- The development of a dual-stage transonic turbine is important because shock waves and supersonic losses are expected phenomena in high pressure ratios. However, this approach is subject to cost and available space for the component.
- Fast genetic algorithms, such as the algorithm presented by [314], are suggested because the optimisation technique in this study (fmincon) is relatively slow (takes up to 10 minutes in some cases). This optimisation technique is fast because only the global optima is located regardless the number of existing local optima.
- Alongside the developed off-design model for the turbine, suitable off-design models for the heat exchangers (evaporator, condenser and recuperator) should also be developed to present a complete ORC system.
- The evaluation of available heat sources in the engine, such as EGR, CAC and engine coolant, is important to understand the potential of these sources compared to that applied in this study (exhaust gases).
- The feasibility of the ORC as a WHR system in mobile engines rather than stationary ones should be examined to consider the vehicle weight because the added weight is a performance deterioration factor caused by the effort required by the engine to propel the vehicle.
- The performance of the ORC system, including the turbine, under different speed/load conditions must be examined.

Bibliography

[1] J. Greenwald, “Oil Sands up Close,” 2012. [Online]. Available: https://www.c2es.org/energy/source/oil. [Accessed: 01-Jan-2017].

[2] Department for Transport, “Fuel Consumption,” 2013. [Online]. Available: https://www.gov.uk/government/statistical-data-sets/env01-fuel-consumption. [Accessed: 01-Jan-2017].

[3] Department for Business Energy and Industrial Strategy, “Annual January prices of road fuels and petroleum products,” 2013. [Online]. Available: https://www.gov.uk/government/statistical-data-sets/oil-and-petroleum-products-annual-statistics. [Accessed: 01-Jan-2017].

[4] A. Hernandez, A. Desideri, C. Ionescu, and S. Quoilin, “Towards the optimal operation of an Organic Rankine Cycle unit by means of model predictive control,” in *3rd International Seminar on ORC Power Systems, Brussels, Belgium*, 2015, pp. 1–10.

[5] J. B. Heywood, *Internal combustion engine fundamentals*. McGraw-Hill Education, 1988.

[6] Freight Transport Association, “The logistics report,” pwc UK, 2014.

[7] B. Sharpe, N. Lutsey, O. Delgado, and R. Muncrief, “United States Efficiency and Greenhouse Gas Emission Regulations for Model Year 2018-2027 Heavy-Duty Vehicles, Engines, and Trailers,” International Council on Clean Transportation, 2016.

[8] R. Stobart and R. Weerasinghe, “Heat Recovery and Bottoming Cycles for SI and CI engines - A Perspective,” *SAE Techinical Pap. 2006-01-0662*, vol. 2006, no. 724, 2006.

[9] D. T. Hountalas, G. C. Mavropoulos, C. Katsanos, and W. Knecht, “Improvement of bottoming cycle efficiency and heat rejection for HD truck applications by utilization of EGR and CAC heat,” *Energy Convers. Manag.*, vol. 53, no. 1, pp. 19–32, 2012.

[10] M. He, X. Zhang, K. Zeng, and K. Gao, “A combined thermodynamic cycle used for waste heat recovery of internal combustion engine,” *Energy*, vol. 36, no. 12, pp. 6821–6829, 2011.

[11] J. Vazquez, M. a Sanz-Bobi, R. Palacios, and A. Arenas, “State of the art of thermoelectric generators based on heat recovered from the exhaust gases of automobiles,” *7th Eur. Work. Thermoelectr.*, vol. 17, 2002.

[12] Erian Baskharone, *Principles of Turbomachinery in Air-Breathing Engines*. Cambridge University Press, 2006.

[13] M. White, “The design and analysis of radial inflow turbines implemented within low temperature organic Rankine cycles,” PhD thesis. City University London, 2015.

[14] C. S. Wong, “Design Process of Low Temperature Organic Rankine Cycle (LT-ORC),” Ph.D Thesis, University of Canterbury, 2015.

[15] IPCC, “Climate Change 2014: Mitigation of Climate Change. Contribution of Working Group III to the Fifth Assessment Report of the Intergovernmental Panel on Climate Change,” Intergovernmental Panel on Climate Change, Cambridge, United Kingdom and New York, NY, USA, 2014.

[16] ICCT, “European Vehicle Market Statistics,” The International Council on Clean Transportation, 2016.

[17] T. V Johnson, “Review of Vehicular Emissions Trends,” *SAE Int. J. Engines. 8(3)1152-1167, 2015, doi 10.4271/2015-01-0993.*, 2015.

[18] T. V Johnson, “Diesel Emissions in Review,” *SAE Int. J. Engines*, vol. 4, no. 1, pp. 143–157, Apr. 2011.

[19] W. Torrey and D. Murray, “An Analysis of the Operational Costs of Trucking: A 2014 Update,” American Transportation Research Institute, Atlanta, GA, 2014.

[20] I. Arsie, A. Cricchio, V. Marano, C. Pianese, M. De Cesare, and W. Nesci, “Modeling Analysis of Waste Heat Recovery via Thermo Electric Generators for Fuel Economy Improvement and CO2 Reduction in Small Diesel Engines,” *SAE Int. J. Passeng. Cars - Electron. Electr. Syst.*, vol. 7, no. 1, pp. 246–255, Apr. 2014.

[21] C. Sprouse and C. Depcik, “Review of organic Rankine cycles for internal combustion engine exhaust waste heat recovery,” *Appl. Therm. Eng.*, vol. 51, no. 1–2, pp. 711–722, 2013.

[22] H. Tian, G. Shu, H. Wei, X. Liang, and L. Liu, “Fluids and parameters optimization for the organic Rankine cycles (ORCs) used in exhaust heat recovery of Internal Combustion Engine (ICE),” *Energy*, vol. 47, no. 1, pp. 125–136, 2012.

[23] T. Wang, Y. Zhang, Z. Peng, and G. Shu, “A review of researches on thermal exhaust heat recovery with Rankine cycle,” *Renew. Sustain. Energy Rev.*, vol. 15, no. 6, pp. 2862–2871, 2011.

[24] A. F. Agudelo, R. García-Contreras, J. R. Agudelo, and O. Armas, “Potential for exhaust gas energy recovery in a diesel passenger car under European driving cycle,” *Appl. Energy*, vol. 174, no. Supplement C, pp. 201–212, 2016.

[25] S. Kim, S. Park, S. Kim, and S.-H. Rhi, “A Thermoelectric Generator Using Engine Coolant for Light-Duty Internal Combustion Engine-Powered Vehicles,” *J. Electron. Mater.*, vol. 40, no. 5, p. 812, Mar. 2011.

[26] J. Fu, J. Liu, R. Feng, Y. Yang, L. Wang, and Y. Wang, “Energy and exergy analysis on gasoline engine based on mapping characteristics experiment,” *Appl. Energy*, vol. 102, no. Supplement C, pp. 622–630, 2013.

[27] BCS, “Waste Heat Recovery: Technology and Opportunities in U.S. Industry,” U.S. Department of Energy: Industrial Technologies Program, 2008.

[28] V. Dolz, R. Novella, A. García, and J. Sánchez, “HD Diesel engine equipped with a bottoming Rankine cycle as a waste heat recovery system. Part 1: Study and analysis of the waste heat energy,” *Appl. Therm. Eng.*, vol. 36, no. Supplement C, pp. 269–278, 2012.

[29] S.L.Nadaf and P.B.Gangavati, “A review on Waste Heat Recovery and Utilization from Diesel Engines,” *Int. J. Adv. Eng. Technol.*, vol. vol. E-ISS, 2014.

[30] M. Talbi and B. Agnew, “Energy recovery from diesel engine exhaust gases for performance enhancement and air conditioning,” *Appl. Therm. Eng.*, vol. 22, no. 6, pp. 693–702, 2002.

[31] H. Teng and G. Regner, “Improving Fuel Economy for HD Diesel Engines with WHR Rankine Cycle Driven by EGR Cooler Heat Rejection,” in *SAE 2009 Commercial Vehicle Engineering Congress & Exhibition*, 2009.

[32] H. Teng, G. Regner, and C. Cowland, “Waste Heat Recovery of Heavy-Duty Diesel Engines by Organic Rankine Cycle Part I: Hybrid Energy System of Diesel and Rankine Engines,” in *SAE World Congress & Exhibition*, 2007.

[33] N. Espinosa, L. Tilman, V. Lemort, S. Quoilin, and B. Lombard, “Rankine Cycle for Waste Heat Recovery on Commercial Trucks: Approach, Constraints and Modelling,” in *Diesel International Conference and Exhibition*, 2010.

[34] A. Boretti, “Recovery of exhaust and coolant heat with R245fa organic Rankine cycles in a hybrid passenger car with a naturally aspirated gasoline engine,” *Appl. Therm. Eng.*, vol. 36, no. Supplement C, pp. 73–77, 2012.

[35] T. Wang, Y. Zhang, J. Zhang, G. Shu, and Z. Peng, “Analysis of recoverable exhaust energy from a light-duty gasoline engine,” *Appl. Therm. Eng.*, vol. 53, no. 2, pp. 414–419, 2013.

[36] R. Cipollone, G. Bianchi, A. Gualtieri, D. Di Battista, M. Mauriello, and and F. Fatigati, “Development of an Organic Rankine Cycle system for exhaust energy recovery in internal combustion engines,” *J. Phys. Conf. Ser.*, vol. 655 (2015), 2015.

[37] K. Yang *et al.*, “Performance Analysis of the Vehicle Diesel Engine-ORC Combined System Based on a Screw Expander,” *Energies*, vol. 7, no. 5, pp. 3400–3419, 2014.

[38] C. O. Katsanos, D. T. Hountalas, and E. G. Pariotis, “Thermodynamic analysis of a Rankine cycle applied on a diesel truck engine using steam and organic medium,” *Energy Convers. Manag.*, vol. 60, no. Supplement C, pp. 68–76, 2012.

[39] E. H. Wang, H. G. Zhang, Y. Zhao, B. Y. Fan, Y. T. Wu, and Q. H. Mu, “Performance analysis of a novel system combining a dual loop organic Rankine cycle (ORC) with a gasoline engine,” *Energy*, vol. 43, no. 1, pp. 385–395, 2012.

[40] J. Galindo *et al.*, “Experimental and thermodynamic analysis of a bottoming Organic Rankine Cycle (ORC) of gasoline engine using swash-plate expander,” *Energy Convers. Manag.*, vol. 103, no. Supplement C, pp. 519–532, 2015.

[41] A. S. Panesar, “Waste Heat Recovery Using Fluid Bottoming Cycles for Heavy Duty Diesel Engines,” Ph.D Thesis, University of Brighton, 2015.

[42] L. Pan and H. Wang, “Improved analysis of Organic Rankine Cycle based on radial flow turbine,” *Appl. Therm. Eng.*, vol. 61, no. 2, pp. 606–615, 2013.

[43] O. Badr, P. W. O’Callaghan, and S. D. Probert, “Performances of Rankine-cycle engines as functions of their expanders’ efficiencies,” *Appl. Energy*, vol. 18, no. 1, pp. 15–27, 1984.

[44] J. Song, C. Gu, and X. Li, “Performance estimation of Tesla turbine applied in small scale Organic Rankine Cycle (ORC) system,” *Appl. Therm. Eng.*, vol. 110, no. Supplement C, pp. 318–326, 2017.

[45] G. Qiu, H. Liu, and S. Riffat, “Expanders for micro-CHP systems with organic Rankine cycle,” *Appl. Therm. Eng.*, vol. 31, no. 16, pp. 3301–3307, 2011.

[46] Z. Xinxin, Z. Ke, B. A. I. Sujuan, Z. Ying, and M. HE, “Exhaust Recovery of Vehicle Gasoline Engine Based on Organic Rankine Cycle,” in *SAE 2011 World Congress & Exhibition*, 2011.

[47] J. Bao and L. Zhao, “A review of working fluid and expander selections for organic Rankine cycle,” *Renew. Sustain. Energy Rev.*, vol. 24, pp. 325–342, 2013.

[48] R. Saidur, M. Rezaei, W. K. Muzammil, M. H. Hassan, S. Paria, and M. Hasanuzzaman, “Technologies to recover exhaust heat from internal combustion engines,” *Renew. Sustain. Energy Rev.*, vol. 16, no. 8, pp. 5649–5659, 2012.

[49] M. Karvonen, R. Kapoor, A. Uusitalo, and V. Ojanen, “Technology competition in the internal combustion engine waste heat recovery: a patent landscape analysis,” *J. Clean. Prod.*, vol. 112, no. Part 5, pp. 3735–3743, 2016.

[50] W. M. S. R. Weerasinghe, R. K. Stobart, and S. M. Hounsham, “Thermal efficiency improvement in high output diesel engines a comparison of a Rankine cycle with turbo-compounding,” *Appl. Therm. Eng.*, vol. 30, no. 14–15, pp. 2253–2256, 2010.

[51] J. Galindo, C. Guardiola, V. Dolz, and P. Kleut, “Further analysis of a compression-expansion machine for a Brayton Waste Heat Recovery cycle on an IC engine,” *Appl. Therm. Eng.*, vol. 128, no. Supplement C, pp. 345–356, 2018.

[52] S. Quoilin, V. Lemort, and J. Lebrun, “Experimental study and modeling of an Organic Rankine Cycle using scroll expander,” *Appl. Energy*, vol. 87, no. 4, pp. 1260–1268, 2010.

[53] A. Schuster, S. Karellas, E. Kakaras, and H. Spliethoff, “Energetic and economic investigation of Organic Rankine Cycle applications,” *Appl. Therm. Eng.*, vol. 29, no. 8, pp. 1809–1817, 2009.

[54] H. Tian, G. Shu, H. Wei, X. Liang, and L. Liu, “Fluids and parameters optimization for the organic Rankine cycles (ORCs) used in exhaust heat recovery of Internal Combustion Engine (ICE),” *Energy*, vol. 47, no. 1, pp. 125–136, 2012.

[55] Yunus A. Cengel and M. A. Boles, *Thermodynamics: An Engineering Approach, Section: 10.5*, 5th

ed. McGraw-Hill Education, 2006.

[56] J. Brandsar, “Offshore Rankine Cycles,” Master thesis, Norwegian University of Science and Technology, 2012.

[57] W. J. Still, “International Combustion Engine,” England Patnet 1230617, 1917.

[58] A. Legros, L. Guillaume, V. Lemort, M. Diny, I. Bell, and S. Quoilin, “Investigation on a scroll expander for waste heat recovery on internal combustion engines,” *Int. Conf. compressors their Syst.*, vol. 1, p. 10, 2013.

[59] D.A. Reay, *Heat Recovery Systems: A Directory of Equipment and Techniques*. E. & F. N.Spon, 1979.

[60] E. Patel, P. Doyle, “Compounding the Truck Diesel Engine with an Organic Rankine-Cycle System,” *SAE Tech. Pap. 760343*, 1976.

[61] M. Erba and A. Biyikoglu, “Design of Low Temperature Organic Rankine Cycle and Turbine,” *4th Int. Conf. Power Eng. Energy Electr. Drives*, no. May, pp. 1065 – 1070, 2013.

[62] T. Endo *et al.*, “Study on Maximizing Exergy in Automotive Engines,” *SAE Tech. Pap. Ser.*, 2007.

[63] K. Damon and D. Koeberlein, “Technology and System Level Demonstration of Highly Efficient and Clean, Diesel Powered Class 8 Trucks,” DoE SuperTruck Program, 2013.

[64] S. Quoilin, “Experimental study and modeling of a low temperature Rankine cycle for small scale cogeneration,” Electro-Mechanical Engineer Thesis, University OF Liege, 2007.

[65] J. Ringler, M. Seifert, V. Guyotot, and W. Hübner, “Rankine cycle for waste heat recovery of IC engines,” *SAE Int. J. Engines*, vol. 2, no. 1, pp. 67–76, 2009.

[66] A. Karvountzis-Kontakiotis *et al.*, “Effect of an ORC Waste Heat Recovery System on Diesel Engine Fuel Economy for Off-Highway Vehicles.” SAE International , 2017.

[67] M. Imran, M. Usman, B.-S. Park, and D.-H. Lee, “Volumetric expanders for low grade heat and waste heat recovery applications,” *Renew. Sustain. Energy Rev.*, vol. 57, no. Supplement C, pp. 1090–1109, 2016.

[68] Y. Oh, J. Park, J. Lee, M. Do Eom, and S. Park, “Modeling effects of vehicle specifications on fuel economy based on engine fuel consumption map and vehicle dynamics,” *Transp. Res. Part D Transp. Environ.*, vol. 32, no. Supplement C, pp. 287–302, 2014.

[69] D. Di Battista, M. Mauriello, and R. Cipollone, “Waste heat recovery of an ORC-based power unit in a turbocharged diesel engine propelling a light duty vehicle,” *Appl. Energy*, vol. 152, pp. 109–120, 2015.

[70] T. A. Horst, W. Tegethoff, P. Eilts, and J. Koehler, “Prediction of dynamic Rankine Cycle waste heat recovery performance and fuel saving potential in passenger car applications considering

interactions with vehicles' energy management," *Energy Convers. Manag.*, vol. 78, no. Supplement C, pp. 438–451, 2014.

[71] A. Boretti, "Stoichiometric H2ICE with water injection and exhaust and coolant heat recovery through organic Rankine cycles," *Int. J. Hydrogen Energy*, vol. 36, no. 19, pp. 12591–12600, 2011.

[72] A. a. Boretti, "Energy Recovery in Passenger Cars," *J. Energy Resour. Technol.*, vol. 134, no. 2, p. 022203, 2012.

[73] J. P. Roy, M. K. Mishra, and A. Misra, "Performance analysis of an Organic Rankine Cycle with superheating under different heat source temperature conditions," *Appl. Energy*, vol. 88, no. 9, pp. 2995–3004, 2011.

[74] M. J. Lee, D. L. Tien, and C. T. Shao, "Thermophysical capability of ozone-safe working fluids for an organic rankine cycle system," *Heat Recover. Syst. {CHP}*, vol. 13, no. 5, pp. 409–418, 1993.

[75] K. Rahbar, S. Mahmoud, R. K. Al-Dadah, and N. Moazami, "Modelling and optimization of organic Rankine cycle based on a small-scale radial inflow turbine," *Energy Convers. Manag.*, vol. 91, pp. 186–198, 2015.

[76] T. C. Hung, T. Y. Shai, and S. K. Wang, "A review of organic rankine cycles (ORCs) for the recovery of low-grade waste heat," *Energy*, vol. 22, no. 7, pp. 661–667, 1997.

[77] S. Quoilin, "Sustainable Energy Conversion Through the Use of Organic Rankine Cycles for Waste Heat Recovery and Solar Applications .," Ph.D Thesis, University of Liege, 2011.

[78] a Borsukiewiczgozdur and W. Nowak, "Comparative analysis of natural and synthetic refrigerants in application to low temperature Clausius–Rankine cycle," *Energy*, vol. 32, no. 4, pp. 344–352, 2007.

[79] B. Dong, G. Xu, T. Li, X. Luo, and Y. Quan, "Parametric analysis of organic Rankine cycle based on a radial turbine for low-grade waste heat recovery," *Appl. Therm. Eng.*, vol. 126, no. Supplement C, pp. 470–479, 2017.

[80] J. Nouman, "Comparative studies and analyses of working fluids for Organic Rankine Cycles - ORC," Master Thesis, KTH Royal Institute of Technology, 2012.

[81] B. T. Liu, K. H. Chien, and C. C. Wang, "Effect of working fluids on organic Rankine cycle for waste heat recovery," *Energy*, vol. 29, no. 8, pp. 1207–1217, 2004.

[82] L. Zhang *et al.*, "Nominal condensing capacity and performance evaluation of evaporative condenser," *Appl. Therm. Eng.*, vol. 107, no. Supplement C, pp. 79–85, 2016.

[83] H. Chen, D. Y. Goswami, and E. K. Stefanakos, "A review of thermodynamic cycles and working fluids for the conversion of low-grade heat," *Renew. Sustain. Energy Rev.*, vol. 14, no. 9, pp. 3059–3067, 2010.

[84] T. C. Hung, S. K. Wang, C. H. Kuo, B. S. Pei, and K. F. Tsai, “A study of organic working fluids on system efficiency of an ORC using low-grade energy sources,” *Energy*, vol. 35, no. 3, pp. 1403–1411, 2010.

[85] T.-C. Hung, “Waste heat recovery of organic Rankine cycle using dry fluids,” *Energy Convers. Manag.*, vol. 42, no. 5, pp. 539–553, 2001.

[86] B. Saleh, G. Koglbauer, M. Wendland, and J. Fischer, “Working fluids for low-temperature organic Rankine cycles,” *Energy*, vol. 32, no. 7, pp. 1210–1221, 2007.

[87] E. H. Wang, H. G. Zhang, B. Y. Fan, M. G. Ouyang, Y. Zhao, and Q. H. Mu, “Study of working fluid selection of organic Rankine cycle (ORC) for engine waste heat recovery,” *Energy*, vol. 36, no. 5, pp. 3406–3418, 2011.

[88] G. Shu, X. Li, H. Tian, X. Liang, H. Wei, and X. Wang, “Alkanes as working fluids for high-temperature exhaust heat recovery of diesel engine using organic Rankine cycle,” *Appl. Energy*, vol. 119, pp. 204–217, 2014.

[89] A. Javanshir, N. Sarunac, and Z. Razzaghpanah, “Thermodynamic analysis of a regenerative organic Rankine cycle using dry fluids,” *Appl. Therm. Eng.*, vol. 123, no. Supplement C, pp. 852–864, 2017.

[90] X. Dai, L. Shi, Q. An, and W. Qian, “Thermal stability of some hydrofluorocarbons as supercritical ORCs working fluids,” *Appl. Therm. Eng.*, vol. 128, no. Supplement C, pp. 1095–1101, 2018.

[91] C. M. Invernizzi, P. Iora, G. Manzolini, and S. Lasala, “Thermal stability of n-pentane, cyclo-pentane and toluene as working fluids in organic Rankine engines,” *Appl. Therm. Eng.*, vol. 121, no. Supplement C, pp. 172–179, 2017.

[92] E. Saloux, M. Sorin, H. Nesreddine, and A. Teyssedou, “Reconstruction procedure of the thermodynamic cycle of organic Rankine cycles (ORC) and selection of the most appropriate working fluid,” *Appl. Therm. Eng.*, vol. 129, pp. 628–635, 2018.

[93] S. He, H. Chang, X. Zhang, S. Shu, and C. Duan, “Working fluid selection for an Organic Rankine Cycle utilizing high and low temperature energy of an LNG engine,” *Appl. Therm. Eng.*, vol. 90, no. Supplement C, pp. 579–589, 2015.

[94] S. Seyedkavoosi, S. Javan, and K. Kota, “Exergy-based optimization of an organic Rankine cycle (ORC) for waste heat recovery from an internal combustion engine (ICE),” *Appl. Therm. Eng.*, vol. 126, no. Supplement C, pp. 447–457, 2017.

[95] D. Wei, X. Lu, Z. Lu, and J. Gu, “Performance analysis and optimization of organic Rankine cycle (ORC) for waste heat recovery,” *Energy Convers. Manag.*, vol. 48, no. 4, pp. 1113–1119, 2007.

[96] D. Hountalas and G. Mavropoulos, “Potential for Improving HD Diesel Truck Engine Fuel Consumption Using Exhaust Heat Recovery Techniques,” *New Trends Technol. Devices, Comput. Commun. Ind. Syst.*, vol. 2, pp. 313–340, 2010.

[97] L. Arnaud, G. Ludovic, D. Mouad, Z. Hamid, and L. Vincent, “Comparison and Impact of Waste

Heat Recovery Technologies on Passenger Car Fuel Consumption in a Normalized Driving Cycle," *Energies*, vol. 7, no. 8, pp. 5273–5290, 2014.

[98] Q. Hussain and D. Birgham, "Organic Rankine cycle for light duty passenger vehicles," in *Directions in Engine-Efficiency and Emissions Research (DEER) Conference, Detroit, Michigan*, 2011.

[99] A. M. I. bin Mamat and W. A. N. bin Wan Mohamed, "Thermal Analysis of Heat Recovery Unit to Recover Exhaust Energy for Using in Organic Rankine Cycle," *Appl. Mech. Mater.*, vol. 393, pp. 781–786, 2013.

[100] Apostolos Pesiridis, *Automotive Exhaust Emissions and Energy Recovery*. NOVA, 2014.

[101] J. Larjola, "Electricity from industrial waste heat using high-speed organic Rankine cycle (ORC)," *Int. J. Prod. Econ.*, vol. 41, no. 1–3, pp. 227–235, 1995.

[102] D. T. Crane and G. S. Jackson, "Optimization of cross flow heat exchangers for thermoelectric waste heat recovery," *Energy Convers. Manag.*, vol. 45, no. 9–10, pp. 1565–1582, 2004.

[103] C.-T. Hsu, G.-Y. Huang, H.-S. Chu, B. Yu, and D.-J. Yao, "Experiments and simulations on low-temperature waste heat harvesting system by thermoelectric power generators," *Appl. Energy*, vol. 88, no. 4, pp. 1291–1297, 2011.

[104] M. Hatami, D. D. Ganji, and M. Gorji-Bandpy, "A review of different heat exchangers designs for increasing the diesel exhaust waste heat recovery," *Renew. Sustain. Energy Rev.*, vol. 37, pp. 168–181, 2014.

[105] X. Zhang and K. T. Chau, "An automotive thermoelectric–photovoltaic hybrid energy system using maximum power point tracking," *Energy Convers. Manag.*, vol. 52, no. 1, pp. 641–647, 2011.

[106] C. Yu and K. T. Chau, "Thermoelectric automotive waste heat energy recovery using maximum power point tracking," *Energy Convers. Manag.*, vol. 50, no. 6, pp. 1506–1512, 2009.

[107] A. B. Ma. Mohd, "Design and Development of a High Performance LPT for Electric Turbocompounding Energy Recovery Unit in a Heavily Downsized Engine," Ph.D Thesis, Imperial College London, 2012.

[108] W. Liu, Q. Jie, H. S. Kim, and Z. Ren, "Current progress and future challenges in thermoelectric power generation: From materials to devices," *Acta Mater.*, vol. 87, no. 155, pp. 357–376, 2015.

[109] X. Liang, X. Wang, G. Shu, H. Wei, H. Tian1, and X. Wang2, "A review and selection of engine waste heat recovery technologies using analytic hierarchy process and grey relational analysis," *Int. J. energy Res.*, vol. Int. J. En, 2014.

[110] R. Capata and G. Hernandez, "Proposal Design Procedure and Preliminary Simulation of Turbo Expander for Small Size (2?10 kW) Organic Rankine Cycle (ORC)," *ASME Int. Mech. Eng. Congr. Expo. Proc.*, vol. 6, 2014.

[111] H. Teng, J. Klaver, T. Park, G. L. Hunter, and B. van der Velde, “A Rankine Cycle System for Recovering Waste Heat from HD Diesel Engines - WHR System Development,” *SAE Int.*, vol. 1, pp. 1–11, 2011.

[112] P. Garg, G. M. Karthik, P. Kumar, and P. Kumar, “Development of a generic tool to design scroll expanders for {ORC} applications,” *Appl. Therm. Eng.*, vol. 109, Part , pp. 878–888, 2016.

[113] I. Papes, J. Degroote, and J. Vierendeels, “Development of a thermodynamic low order model for a twin screw expander with emphasis on pulsations in the inlet pipe,” *Appl. Therm. Eng.*, vol. 103, no. Supplement C, pp. 909–919, 2016.

[114] L. Zhao, M. Li, Y. Ma, Z. Liu, and Z. Zhang, “Simulation analysis of a two-rolling piston expander replacing a throttling valve in a refrigeration and heat pump system,” *Appl. Therm. Eng.*, vol. 66, no. 1, pp. 383–394, 2014.

[115] B. Yang, X. Peng, Z. He, B. Guo, and Z. Xing, “Experimental investigation on the internal working process of a CO2 rotary vane expander,” *Appl. Therm. Eng.*, vol. 29, no. 11, pp. 2289–2296, 2009.

[116] A. Reid, “Low Temperature Power Generation Using HFE-7000 in a Rankine Cycle,” Master Thesis, San Diego State University, 2012.

[117] S. Quoilin, M. Van Den Broek, S. Declaye, P. Dewallef, and V. Lemort, “Techno-economic survey of Organic Rankine Cycle (ORC) systems,” *Renew. Sustain. Energy Rev.*, vol. 22, pp. 168–186, 2013.

[118] L. Zhao, M. Li, and Z. Liu, “Simulation analysis of a two rolling piston expander replacing throttling valve in conventional refrigerant heat pump system,” in *International Compressor Engineering Conference, Purdue University USA*, 2012.

[119] M. Badami and M. Mura, “Preliminary design and controlling strategies of a small-scale wood waste Rankine Cycle (RC) with a reciprocating steam engine (SE),” *Energy*, vol. 34, no. 9, pp. 1315–1324, 2009.

[120] N. Paltrinieri, “A Mean-Line Model to Predict the Deaign Performance of Radial Inflow Turbines in Organic Rankine Cycles,” Master Thesis, University of Padua, 2014.

[121] O. Badr, S. Naik, P. W. O’Callaghan, and S. D. Probert, “Expansion machine for a low power-output steam Rankine-cycle engine,” *Appl. Energy*, vol. 39, no. 2, pp. 93–116, 1991.

[122] O. Badr, S. Naik, P. W. O’Callaghan, and S. D. Probert, “Rotary Wankel engines as expansion devices in steam Rankine-cycle engines,” *Appl. Energy*, vol. 39, no. 1, pp. 59–76, 1991.

[123] M. Antonelli, A. Baccioli, M. Francesconi, U. Desideri, and L. Martorano, “Operating maps of a rotary engine used as an expander for micro-generation with various working fluids,” *Appl. Energy*, vol. 113, pp. 742–750, 2014.

[124] O. Badr, P. W. O’Callaghan, M. Hussein, and S. D. Probert, “Multi-vane expanders as prime movers for low-grade energy organic Rankine-cycle engines,” *Appl. Energy*, vol. 16, pp. 129–146,

1984.

[125] G. Lofstrand, “A mechanical model of an axial piston machine,” Licentiate Thesis, KTH Industrial Engineering and Management, 2009.

[126] G. Wenzhi, Z. Junmeng, L. Guanghua, B. Qiang, and F. Liming, “Performance evaluation and experiment system for waste heat recovery of diesel engine,” *Energy*, vol. 55, pp. 226–235, 2013.

[127] H. Oomori and S. Ogino, “Waste heat recovery of passenger car using a combination of Rankine bottoming cycle and evaporative engine cooling system,” *SAE Tech. Pap.*, no. 412, 1993.

[128] M. Kane, “Small hybrid solar power system,” *Energy*, vol. 28, no. 14, pp. 1427–1443, 2003.

[129] M. Kane, D. Favrat, G. B, and O. Andres, “Scroll expander organic Rankine cycle (ORC) efficiency boost of biogas engines,” in *ECOS, Padova, Italy*, 2007, pp. 1–8.

[130] J. A. Mathias, J. R. Johnston, J. Cao, D. K. Priedeman, and R. N. Christensen, “Experimental Testing of Gerotor and Scroll Expanders Used in, and Energetic and Exergetic Modeling of, an Organic Rankine Cycle,” *J. Energy Resour. Technol.*, vol. 131, no. 1, p. 012201, 2009.

[131] S. Clemente, D. Micheli, M. Reini, and R. Taccani, “Energy efficiency analysis of Organic Rankine Cycles with scroll expanders for cogenerative applications,” *Appl. Energy*, vol. 97, pp. 792–801, 2012.

[132] G. Yu, G. Shu, H. Tian, H. Wei, and L. Liu, “Simulation and thermodynamic analysis of a bottoming Organic Rankine Cycle (ORC) of diesel engine (DE),” *Energy*, vol. 51, pp. 281–290, 2013.

[133] Y. Kim, D. Shin, and C. Kim, “Optimization of Design Pressure Ratio of Positive Displacement Expander for Vehicle Engine Waste Heat Recovery,” *Energies*, pp. 6105–6117, 2014.

[134] P. Petr, C. Schröder, J. Kohler, and M. Graber, “Optimal Control of Waste Heat Recovery Systems Applying Nonlinear Model Predictive Control (NMPC),” in *3rd Seminar on ORC Systems, Brussels, Belgium*, 2015.

[135] H. Leibowitz, I. K. Smith, and N. Stosic, “Cost Effective Small Scale ORC Systems for Power Recovery From Low Grade Heat Sources,” in *ASME International Mechanical Engineering Congress and Exposition*, 2006, vol. 2006, pp. 521–527.

[136] Y. Wu, B. Lei, W. Wang, and Y. Zhang, “Experimental Study on Organic Rankine Cycle System with Single-Screw Expander for Waste Heat Recovery from Diesel,” in *3rd International Seminar on ORC Power Systems, Brussels, Belgium*, 2015, pp. 1–10.

[137] E. Poulin, R. Demler, I. Krepchin, and D. Walker, “Steam bottoming cycle for an adiabatic diesel engine,” DOE/NASA-0030-1; NASA-CR-168255 ON: DE85001318, United States, 1984.

[138] I. Kubo, “Technical and Economic Study of Stirling and Rankine Cycle Bottoming Systems for

Heavy Truck Diesel Engines," DOE/NASA/0361-1, NASA-CR-180833, CTR-0723-87001, Washington, DC USA, 1987.

[139] D. Seher, T. Lengenfelder, J. Gerhardt, N. Eisenmenger, M. Hackner, and I. Krinn, "Waste Heat Recovery for Commercial Vehicles with a Rankine Process," in *21 st Aachen Colloquium Automobile and Engine Technology, Aachen, Germany*, 2012.

[140] R. Daccord, A. Darmedru, and J. Melis, "Oil-Free Axial Piston Expander for Waste Heat Recovery," in *SAE 2014 World Congress & Exhibition*, 2014.

[141] M. C. Chiong, S. Rajoo, and A. Romagnoli, "Nozzle Steam Piston Expander for Engine Exhaust Energy Recovery," *11th Int. Conf. Automot. Eng.*, pp. 2–6, 2015.

[142] J. Galindo, V. Dolz1, L. Royo, R. Haller, and J. Melis, "Study of a Volumetric Expander Suitable for Waste Heat Recovery from an Automotive IC Engine Using n ORC with Ethanol," in *3rd International Seminar on ORC Power Systems, Brussels, Belgium*, 2015, pp. 1–17.

[143] M. B, M. Tahir, N. Yamada, and T. Hoshino, "Efficiency of Compact Organic Rankine Cycle System with Rotary-Vane-Type Expander for Low-Temperature Waste Heat Recovery," *Int. J. Environ. Sci. Eng.*, no. 2(1):11–6., 2010.

[144] F. Ayachi, E. B. Ksayer, P. Neveu, and A. Zoughaib, "Experimental investigation and modeling of a hermetic scroll expander," *Appl. Energy*, vol. 181, no. Supplement C, pp. 256–267, 2016.

[145] S. Declaye, S. Quoilin, L. Guillaume, and V. Lemort, "Experimental study on an open-drive scroll expander integrated into an ORC (Organic Rankine Cycle) system with R245fa as working fluid," *Energy*, vol. 55, no. Supplement C, pp. 173–183, 2013.

[146] J.-F. Oudkerk, S. Quoilin, S. Declaye, L. Guillaume, E. Winandy, and V. Lemort, "Evaluation of the Energy Performance of an Organic Rankine Cycle-Based Micro Combined Heat and Power System Involving a Hermetic Scroll Expander," *J. Eng. Gas Turbines Power*, vol. 135, no. 4, pp. 42306–42310, Mar. 2013.

[147] H. Wang, R. B. Peterson, and T. Herron, "Experimental performance of a compliant scroll expander for an organic Rankine cycle," *Proc. Inst. Mech. Eng. Part A J. Power Energy*, vol. 223, no. 7, pp. 863–872, Jun. 2009.

[148] S. Han, J. Seo, and B.-S. Choi, "Development of a 200 kW ORC radial turbine for waste heat recovery," *J. Mech. Sci. Technol.*, vol. 28, no. 12, pp. 5231–5241, Dec. 2014.

[149] Y. Zheng, D. Hu, Y. Cao, and Y. Dai, "Preliminary design and off-design performance analysis of an Organic Rankine Cycle radial-inflow turbine based on mathematic method and CFD method," *Appl. Therm. Eng.*, vol. 112, no. Supplement C, pp. 25–37, 2017.

[150] K. G. Nithesh and D. Chatterjee, "Numerical prediction of the performance of radial inflow turbine designed for ocean thermal energy conversion system," *Appl. Energy*, vol. 167, no. Supplement C, pp. 1–16, 2016.

[151] A. Al Jubori, A. Daabo, R. K. Al-Dadah, S. Mahmoud, and A. B. Ennil, "Development of micro-scale

axial and radial turbines for low-temperature heat source driven organic Rankine cycle," *Energy Convers. Manag.*, vol. 130, no. Supplement C, pp. 141–155, 2016.

[152] T. Yamamoto, T. Furuhata, N. Arai, and K. Mori, "Design and testing of the Organic Rankine Cycle," *Energy*, vol. 26, no. 3, pp. 239–251, 2001.

[153] H. Russel, A. Rowlands, C. Ventura, and I. Jahn, "Design and Testing Process for a 7kW Radial Inflow Refrigerant Turbine at the University of Queensland," in *ASME Turbo Expo 2016: Turbomachinery Technical Conference and Exposition*, 2016, no. 49866, p. V008T23A036.

[154] I. Papes, J. Degroote, and J. Vierendeels, "New insights in twin screw expander performance for small scale ORC systems from 3D CFD analysis," *Appl. Therm. Eng.*, vol. 91, no. Supplement C, pp. 535–546, 2015.

[155] Y. Zhang, "Experimental Study on the Performance of Single Screw Expander with 195 mm Diameter Screw," in *2nd International Seminar on ORC Power Systems, Rotterdam, The Netherlands*, 2013.

[156] H. Tang, H. Wu, X. Wang, and Z. Xing, "Performance study of a twin-screw expander used in a geothermal organic Rankine cycle power generator," *Energy*, vol. 90, no. Part 1, pp. 631–642, 2015.

[157] W. Wang, Y. Wu, C. Ma, L. Liu, and J. Yu, "Preliminary experimental study of single screw expander prototype," *Appl. Therm. Eng.*, vol. 31, no. 17, pp. 3684–3688, 2011.

[158] D. Ziviani *et al.*, "Characterizing the performance of a single-screw expander in a small-scale organic Rankine cycle for waste heat recovery," *Appl. Energy*, vol. 181, no. Supplement C, pp. 155–170, 2016.

[159] J. Oudkerk, R. Dickes, O. Dumont, and V. and Lemort, "Experimental performance of a piston expander in a smallscale organic Rankine cycle," in *9th International Conference on Compressors and their Systems, London*, 2015.

[160] N. Zheng, L. Zhao, X. D. Wang, and Y. T. Tan, "Experimental verification of a rolling-piston expander that applied for low-temperature Organic Rankine Cycle," *Appl. Energy*, vol. 112, no. Supplement C, pp. 1265–1274, 2013.

[161] V. Lemorta, L. Guillaumea, A. Legrosa, S. Declayea, and S. Quoilina, "A Comparison of Piston, Screw and Scroll Expanders for Small- Scale Rankine Cycle Systems," in *3rd International Confernce on Microgeneration and Related Technologies, Napoli,* 2013.

[162] Y. Han, R. Li, Z. Liu, J. Tian, X. Wang, and J. Kang, "Feasibility analysis and performance characteristics investigation of spatial recuperative expander based on organic Rankine cycle for waste heat recovery," *Energy Convers. Manag.*, vol. 121, no. Supplement C, pp. 335–348, 2016.

[163] V. Vodicka, L. Guillaume, J. Mascuch, and V. and Lemort, "Testing and Modelling A Vne Expander Used in an ORC Working With HexamethyldisIloxane (MM)," in *3rd International Seminar on ORC Power Systems, Brussels, Belgium*, 2015.

[164] P. Kolasiński, “The Influence of the Heat Source Temperature on the Multivane Expander Output Power in an Organic Rankine Cycle (ORC) System,” *Energies*, vol. 8, no. 5, pp. 3351–3369, 2015.

[165] X. Jia, B. Zhang, L. Pu, B. Guo, and X. Peng, “Improved rotary vane expander for trans-critical CO2 cycle by introducing high-pressure gas into the vane slots,” *Int. J. Refrig.*, vol. 34, no. 3, pp. 732–741, 2011.

[166] A. La Seta, A. Meroni, J. G. Andreasen, L. Pierobon, G. Persico, and F. Haglind, “Combined Turbine and Cycle Optimization for Organic Rankine Cycle Power Systems—Part B: Application on a Case Study,” *Energies*, vol. 9, no. 6, 2016.

[167] Shadreck M. Situmbeko Freddie L. Inambao, “Small Scale Axial Turbine Preliminary Design and Modelling,” *Int. J. Eng. Res. Technol.*, vol. Vol. 5, no. 07, 2016.

[168] A. Lazzaretto and G. Manente, “A New Criterion to Optimize ORC Design Performance using Efficiency Correlations for Axial and Radial Turbines,” *Int. J. Thermodyn.*, vol. Vol. 17 (N, pp. pp. 173–181, 2014.

[169] Y.-Q. Zhang *et al.*, “Development and experimental study on organic Rankine cycle system with single-screw expander for waste heat recovery from exhaust of diesel engine,” *Energy*, vol. 77, no. Supplement C, pp. 499–508, 2014.

[170] A. M. Mahmoud, S. A. Sherif, and W. E. Lear, “Frictional and Internal Leakage Losses in Rotary-Vane Two-Phase Refrigerating Expanders,” *J. Energy Resour. Technol.*, vol. 132, no. 2, pp. 21007–21010, Jun. 2010.

[171] G. Latz, S. Andersson, and K. Munch, “Selecting an Expansion Machine for Vehicle Waste-Heat Recovery Systems Based on the Rankine Cycle,” *SAE Int.*, vol. 1, pp. 1–15, 2013.

[172] Gorla S.R. Rama and Aijaz A. Khan, *Turbomachinery: Design and Theory*. Marcel Dekker, INC., 2005.

[173] K. M. Khalil, S. Mahmoud, R. K. Al-Dadah, and A. B. Ennil, “Investigate a hybrid open-Rankine cycle small-scale axial nitrogen expander by a camber line control point parameterization optimization technique,” *Appl. Therm. Eng.*, vol. 127, no. Supplement C, pp. 823–836, 2017.

[174] B. Dong, G. Xu, X. Luo, L. Zhuang, and Y. Quan, “Analysis of the supercritical organic Rankine cycle and the radial turbine design for high temperature applications,” *Appl. Therm. Eng.*, vol. 123, no. Supplement C, pp. 1523–1530, 2017.

[175] D. J. Patterson and R. W. Kruiswyk, “An Engine System Approach to Exhaust Waste Heat Recovery,” in *Diesel Engine-Efficiency and Emissions Research (DEER), Detroit, Michigan*, 2007.

[176] H. Saravanamuttoo, G. Rogers, H. Cohen, and P. Straznicky, *Gas Turbine Theory*, 6th ed. Pearson Education Limited, 2009.

[177] TMI Staff & Contributers, “Axial and radial turbines,” Turbomachinery International, Dec-2012.

[178] F. Alshammari, A. Karvountzis-Kontakiotis, and A. Pesiridis, “Radial turbine expander design for organic rankine cycle, waste heat recovery in high efficiency, off-highway vehicles,” in *3rd Biennial International Conference on Powertrain Modelling and Control (PMC 2016), Loughborough, UK*, 2016.

[179] E. Sauret and A. S. Rowlands, “Candidate radial-inflow turbines and high-density working fluids for geothermal power systems,” *Energy*, vol. 36, no. 7, pp. 4460–4467, 2011.

[180] E. Doyle, L. DiNanno, and S. Kramer, “Installation of a Diesel-Organic Rankine Compound Engine in a Class 8 Truck for a Single-Vehicle Test,” *SAE Tech. Pap. 790646*, 1979.

[181] G. Hnat, J. S. Patten, L. M. Bartone, and J. C. Cutting, “Industrial Heat Recovery With Organic Rankine Cycles,” in *4th Industrial Energy Technology Conference*, 1982, pp. 524–532.

[182] H. Kunte and J. Seume, “Partial Admission Impulse Turbine for Automotive ORC Application,” *SAE Tech. Pap.*, vol. 6, 2013.

[183] D. Serrano *et al.*, “Improving Train Energy Efficiency by Organic Rankine Cycle (ORC) for Recovering Waste Heat from Exhaust Gas,” in *3rd International Seminar on ORC Power Systems, Brussels, Belgium*, 2015.

[184] R. Cipollone, D. Di Battista, and F. Bettoja, “Performances of an ORC power unit for Waste Heat Recovery on Heavy Duty Engine,” *Energy Procedia*, vol. 129, no. Supplement C, pp. 770–777, 2017.

[185] T. E. Briggs, R. Wagner, D. Edwards, S. Curran, and E. Nafziger, “A Waste Heat Recovery System for Light Duty Diesel Engines,” *SAE Tech. Pap.*, 2010.

[186] F. J. Cogswell, D. W. Gerlach, T. C. Wagner, and J. Mulugeta, “Design of an Organic Rankine Cycle for Waste Heat Recovery From a Portable Diesel Generator,” *ASME Int. Mech. Eng. Congr. Expo.*, vol. 4, no. 54907, pp. 707–716, 2011.

[187] T. Park, H. Teng, G. L. Hunter, B. van der V. A, and J. Klaver, “A Rankine Cycle System for Recovering Waste Heat from HD Diesel Engines - Experimental Results,” *SAE Int.*, vol. 1, 2011.

[188] W. Lang, P. Colonna, and R. Almbauer, “Assessment of Waste Heat Recovery From a Heavy-Duty Truck Engine by Means of an ORC Turbogenerator,” *J. Eng. Gas Turbines Power*, vol. 135, no. 4, p. 042313, 2013.

[189] T. Furukawa, M. Nakamura, K. Machida, and K. Shimokawa, “A Study of the Rankine Cycle Generating System for Heavy Duty HV Trucks,” in *SAE 2014 World Congress & Exhibition*, 2014.

[190] A.W. Costall, A. Gonzalez Hernandez, P. J. Newton, and R. F. Martinez-Botas, “Design methodology for radial turbo expanders in mobile organic Rankine cycle applications,” *Appl. Energy*, pp. 1–15, 2015.

[191] O. Rudenko, L. Moroz, M. Burlaka, and C. Joly, “Design of Waste Heat Recovery Systems Based on Supercritical ORC for Powerful Gas and Diesel Engines,” in *3rd International Seminar on ORC Power Systems, October,Brussels, Belgium*, 2015, pp. 1–10.

[192] L. Guillaume, A. Legros, A. Desideri, and V. Lemort, “Performance of a Radial-Inflow Turbine Integrated in an ORC System and Designed for a WHR on Truck Application: An Experimental Comparison between R245fa and R1233zd,” *Appl. Energy*, vol. 186, pp. 408–422, 2017.

[193] P. Leduc, P. Smague, A. Leroux, and G. Henry, “Low temperature heat recovery in engine coolant for stationary and road transport applications,” *Energy Procedia*, vol. 129, no. Supplement C, pp. 834–842, 2017.

[194] F. Alshammari, A. Karvountzis-Kontakiotis, A. Pesiridis, and T. Minton, “Radial Expander Design for an Engine Organic Rankine Cycle Waste Heat Recovery System,” *Energy Procedia*, vol. 129, pp. 285–292, Sep. 2017.

[195] Andreas P. Weib, “Volumetric Expander versus Turbine – Which Is the Better Choice for Small ORC Plants,” in *3rd International Seminar on ORC Power Systems, Brussels, Belgium*, 2015, pp. 1–10.

[196] O. Balje, *Turbomachines: A Guide to Design Selection and Theory*. Wiley, 1981.

[197] S. L. Dixon and C. Hall, *Fluid Mechanics and Thermodynamics of Turbomachinery*. Butterworth-Heinemann: Burlington, 2010.

[198] O. Badr, S. D. Probert, and P. W. O’Callaghan, “Selecting a working fluid for a Rankine-cycle engine,” *Appl. Energy*, vol. 21, no. 1, pp. 1–42, 1985.

[199] N. Watson and M. S. Janota, *Turbocharging the internal combustion engine*, 1st ed. MacMilan, 1982.

[200] L. Pierobon, T.-V. Nguyen, U. Larsen, F. Haglind, and B. Elmegaard, “Multi-objective optimization of organic Rankine cycles for waste heat recovery: Application in an offshore platform,” *Energy*, vol. 58, no. Supplement C, pp. 538–549, 2013.

[201] S. Lecompte, H. Huisseune, M. van den Broek, S. De Schampheleire, and M. De Paepe, “Part load based thermo-economic optimization of the Organic Rankine Cycle (ORC) applied to a combined heat and power (CHP) system,” *Appl. Energy*, vol. 111, no. Supplement C, pp. 871–881, 2013.

[202] S. Quoilin, S. Declaye, B. F. Tchanche, and V. Lemort, “Thermo-economic optimization of waste heat recovery Organic Rankine Cycles,” *Appl. Therm. Eng.*, vol. 31, no. 14, pp. 2885–2893, 2011.

[203] G. Yu, G. Shu, H. Tian, H. Wei, and X. Liang, “Multi-approach evaluations of a cascade-Organic Rankine Cycle (C-ORC) system driven by diesel engine waste heat: Part B-techno-economic evaluations,” *Energy Convers. Manag.*, vol. 108, no. Supplement C, pp. 596–608, 2016.

[204] P. Garg, M. S. Orosz, and P. Kumar, “Thermo-economic evaluation of {ORCs} for various working fluids,” *Appl. Therm. Eng.*, vol. 109, Part , pp. 841–853, 2016.

[205] D. Meyer, C. Wong, E. Engel, and S. Krumdieck, “Design and Build of a1 Kilowatt Organic Rankine Cycle Power Generatio,” in *35th New Zealand Geothermal Workshop, Rotorua, New*

*Zealand,*2013.

[206] C. G. Gutiérrez-Arriaga, F. Abdelhady, H. S. Bamufleh, M. Serna-González, M. M. El-Halwagi, and J. M. Ponce-Ortega, "Industrial waste heat recovery and cogeneration involving organic Rankine cycles," *Clean Technol. Environ. Policy*, vol. 17, no. 3, pp. 767–779, Mar. 2015.

[207] R. Turton, R. Bailie, W. Whiting, and J. Shaeiwitz, *Synthesis and Design of Chemical Processes*, 3rd ed. Pearson Education, Inc, 2009.

[208] S. Lemmens, "Cost Engineering Techniques and Their Applicability for Cost Estimation of Organic Rankine Cycle Systems," *Energies*, vol. 9, no. 7, 2016.

[209] D. Walraven, B. Laenen, and W. D'haeseleer, "Economic system optimization of air-cooled organic Rankine cycles powered by low-temperature geothermal heat sources," *Energy*, vol. 80, no. Supplement C, pp. 104–113, 2015.

[210] X. Liu, M. Wei, L. Yang, and X. Wang, "Thermo-economic analysis and optimization selection of ORC system configurations for low temperature binary-cycle geothermal plant," *Appl. Therm. Eng.*, vol. 125, no. Supplement C, pp. 153–164, 2017.

[211] S. Li and Y. Dai, "Thermo-economic comparison of Kalina and CO2 transcritical power cycle for low temperature geothermal sources in China," *Appl. Therm. Eng.*, vol. 70, no. 1, pp. 139–152, 2014.

[212] A. Toffolo, A. Lazzaretto, G. Manente, and M. Paci, "A multi-criteria approach for the optimal selection of working fluid and design parameters in Organic Rankine Cycle systems," *Appl. Energy*, vol. 121, no. Supplement C, pp. 219–232, 2014.

[213] Z. Shengjun, W. Huaixin, and G. Tao, "Performance comparison and parametric optimization of subcritical Organic Rankine Cycle (ORC) and transcritical power cycle system for low-temperature geothermal power generation," *Appl. Energy*, vol. 88, no. 8, pp. 2740–2754, 2011.

[214] G. Pei, J. Li, Y. Li, D. Wang, and J. Ji, "Construction and dynamic test of a small-scale organic rankine cycle," *Energy*, vol. 36, no. 5, pp. 3215–3223, 2011.

[215] H.-C. Jung, L. Taylor, and S. Krumdieck, "An experimental and modelling study of a 1 kW organic Rankine cycle unit with mixture working fluid," *Energy*, vol. 81, no. Supplement C, pp. 601–614, 2015.

[216] M. Li *et al.*, "Construction and preliminary test of a low-temperature regenerative Organic Rankine Cycle (ORC) using R123," *Renew. Energy*, vol. 57, no. Supplement C, pp. 216–222, 2013.

[217] G. Zywica, T. Kaczmarczyk, and E. Ihnatowicz, "Expanders for dispersed power generation: maintenance and diagnostics problems," *Trans. Inst. FLUID-FLOW Mach.*, vol. ISSN 0079-, 2016.

[218] G. Zywica, T. Z. Kaczmarczyk, and E. Ihnatowicz, "A review of expanders for power generation in small-scale organic Rankine cycle systems: Performance and operational aspects," *Proc. Inst. Mech. Eng. Part A J. Power Energy*, vol. 230, no. 7, pp. 669–684, Jul. 2016.

[219] P. Kolasinski, P. Błasiak, and J. Rak, “Experimental and Numerical Analyses on the Rotary Vane Expander Operating Conditions in a Micro Organic Rankine Cycle System,” *Energies*, vol. 9, no. 8, 2016.

[220] M. C. Brands, J. R. Werner, J. L. Hoehne, and S. Kramer, “Vechicle Testing of Cummins Turbocompound Diesel Engine,” in *SAE Technical Paper*, 1981.

[221] D. T. Hountalas, C. Katsanos, and V. T. Lamaris, “Recovering energy from the diesel engine exhaust using mechanical and electrical turbocompounding,” *SAE Technical Paper*, no. 724. pp. 776–790, 2007.

[222] C. O. Katsanos, D. T. Hountalas, and E. G. Pariotis, “Thermodynamic analysis of a Rankine cycle applied on a diesel truck engine using steam and organic medium,” *Energy Convers. Manag.*, vol. 60, pp. 68–76, 2012.

[223] D. Walraven, B. Laenen, and W. D’haeseleer, “Comparison of shell-and-tube with plate heat exchangers for the use in low-temperature organic Rankine cycles,” *Energy Convers. Manag.*, vol. 87, no. Supplement C, pp. 227–237, 2014.

[224] R. Mastrullo, A. W. Mauro, R. Revellin, and L. Viscito, “Modeling and optimization of a shell and louvered fin mini-tubes heat exchanger in an ORC powered by an internal combustion engine,” *Energy Convers. Manag.*, vol. 101, no. Supplement C, pp. 697–712, 2015.

[225] G.-Q. Shu, G. Yu, H. tian, H. Wei, and X. Liang, “Simulations of a Bottoming Organic Rankine Cycle (ORC) Driven by Waste Heat in a Diesel Engine (DE),” in *SAE 2013 World Congress & Exhibition*, 2013.

[226] P. Bastani, J. B. Heywood, and C. Hope, “A Forward-Looking Stochastic Fleet Assessment Model for Analyzing the Impact of Uncertainties on Light-Duty Vehicles Fuel Use and Emissions,” *SAE Int. J. Engines*, vol. 5, pp. 452–468, 2012.

[227] L. W. Cheah, A. P. Bandivadekar, K. M. Bodek, E. P. Kasseris, and J. B. Heywood, “The Trade-off between Automobile Acceleration Performance, Weight, and Fuel Consumption,” *SAE Int. J. Fuels Lubr.*, vol. 1, pp. 771–777, 2008.

[228] L. Wang, K. Kelly, K. Walkowicz, and A. Duran, “Quantitative Effects of Vehicle Parameters on Fuel Consumption for Heavy-Duty Vehicle,” in *SAE Technical Paper*, 2015.

[229] M. Usman, M. Imran, Y. Yang, and B.-S. Park, “Impact of organic Rankine cycle system installation on light duty vehicle considering both positive and negative aspects,” *Energy Convers. Manag.*, vol. 112, no. Supplement C, pp. 382–394, 2016.

[230] E. Lemmon, M. Huber, and M. McLinden, “NIST Standard Reference Database 23: Reference Fluid Thermodynamic and Transport Properties-REFPROP, Version 9.0, National Institute of Standards and Technology, Standard Reference Data Program, Gaithersburg, Maryland, USA.” 2010.

[231] H. Moustapha, M. F. Zelesky, N. C. Baines, and D. Japikse, *Axial and Radial Turbines*, 1st ed. White River Junction: Concepts NREC, 2003.

[232] H. Chen, M. Abidat, N. C. Baines, and M. R. Firth, “The Effects of Blade Loading in Radial and Mixed Flow Turbines,” no. 78934. p. V001T01A049, 1992.

[233] A. Whitfield and N. C. Baines, *Design of Radial Turbomachines*. Longman Scientific and Technical, Harlow, England, 1990.

[234] R. H. Aungier, *Turbine aerodynamics: Axial-flow and radial-inflow turbine design and analysis*, 1st ed. New York, 2006.

[235] C. Rodgers, “Small High Pressure Ratio Radial Turbine Technology,” *VKI Lect. Ser.*, 1987.

[236] The MathWorks, “MATLAB and Statistics Toolbox Release 2014b.” 2014.

[237] H. E. Rohlik, “Analytical Determination of Radial Inflow Turbine Design Geometry for Maximum Efficiency,” *NASA TN D-4384*, 1968.

[238] A. Glassman, “Computer Program for Design Analysis of Radial-Inflow Turbines,” NASA, Washington, D. C., USA., 1976.

[239] C. Rodgers and R. Geiser, “Performance of a High-Efficiency Radial/Axial Turbine,” *J. Turbomach.*, vol. 109, no. 2, pp. 151–154, Apr. 1987.

[240] Carlos Ventura, “Aerodynamic Design and Performance Estimation of Radial Inflow Turbines for Renewable Power Generation Applications,” Ph.D Thesis, The University of Queensland, 2012.

[241] A. W. H. Jamieson, *“The radial turbine”, Gas turbine principles and practice*, Roxbee-Cox. 1955.

[242] J. F. Suhrmann, D. Peitsch, M. Gugau, T. Heuer, and U. Tomm, “Validation and Development of Loss Models for Small Size Radial Turbines,” no. 44021. pp. 1937–1949, 2010.

[243] I. Watanabe, I. Ariga, and T. Mashimo, “Effect of Dimensional Parameters of Impellers on Performance Characteristics of a Radial-Inflow Turbine,” *J. Eng. Power*, vol. 93, no. 1, pp. 81–102, Jan. 1971.

[244] S. Li, E. M. Krivitzky, and X. Qiu, “Meanline Modeling of a Radial-Inflow Turbine Nozzle With Supersonic Expansion,” no. 49729. p. V02DT42A036, 2016.

[245] J. C. Emery, J. Herrig, J. R. Erwin, and A. R. Felix, “Systematic two-dimensional cascade tests of NACA 65-series compressor blades at low speeds,” Technical report, NACA, Cranfiled, UK, 1957.

[246] O. Balje, “Contribution to the Problem of Designing Radial Turbomachines,” *Trans ASME 741451*, 1952.

[247] W. D. Marscher, “Structural Analysis: Stresses due to Centrifugal, Pressure and Thermal Loads,” *Radial Turbines, von Kármán Inst. Fluid Dyn.*, 1992.

[248] K. Rahbar, S. Mahmoud, and R. K. Al-Dadah, “Mean-line modeling and CFD analysis of a

miniature radial turbine for distributed power generation systems," *Int. J. Low-Carbon Technol.*, pp. 1–12, 2014.

[249] R. Capata and G. Hernandez, "Preliminary Design and Simulation of a Turbo Expander for Small Rated Power Organic Rankine Cycle (ORC)," *Energies*, vol. 7, no. 11, pp. 7067–7093, 2014.

[250] A. Pesiridis, B. Vassil, M. Padzillah, and R. Martinez-Botas, "A Comparison of flow control devices for variable geometry turbocharger application," *International Journal of Automotive Engineering and Technologies*, vol. 3. Murat CİNİVİZ, pp. 1–21, 2013.

[251] W. Jansen and E. B. Qvale, "A Rapid Method for Predicting the Off-Design Performance of Radial-Inflow Turbines," *ASME -PUBLICATIONS-*, no. 80067, p. V001T01A002, 1967.

[252] A. Dadone and M. Pandolfi, "A method for evaluating the off-design performance of a radial inflow turbine and comparison with experiments," *Int. J. Mech. Sci.*, vol. 11, no. 3, pp. 241–252, 1969.

[253] C. A. Wasserbauer and A. J. Glassman, "Fortran Program for Predicting Off-Design Performance of Radial-Inflow Turbines," National Aeronautics and Space Administration, Washington, D.C, 1975.

[254] P. L. Meitner and A. J. Glassman, "Off-design performance loss model for radial turbines with pivoting, variable-area stators," NASA Technical Paper, Cleveland, OH, USA, 1980.

[255] S. K. Ghosh, "Experimental and Computational Studies on Cryogenic Turboexpander," PhD thesis. National Institute of Technology, 2008.

[256] N. C. Baines, "A Meanline Prediction Method for Radial Turbine Efficiency," in 6th International Conference on Turbocharging and Air Management Systems," *Concepts ETI, Inc*, 1998.

[257] N. C. Baines, "Radial Turbines, an integrated design approach," in *6th European conference on Turbomachinery- Fluid Dynamics and Thermodynamics.*, 2005.

[258] R. S. Benson, "An Analysis of the Losses in a Radial Gas Turbine," *Proc. Inst. Mech. Eng. Conf. Proc.*, vol. 180, no. 10, pp. 41–53, Jun. 1965.

[259] G. F. Hiett and I. H. Johnston, "Experiments Concerning the Aerodynamic Performance of Inward Flow Radial Turbines," *Proc. Inst. Mech. Eng. Conf. Proc.*, vol. 178, no. 9, pp. 28–42, Jun. 1963.

[260] R. S. Benson, W. G. Cartwright, and S. K. Das, "An Investigation of the Losses in the Rotor of a Radial Flow Gas Turbine at Zero Incidence under Conditions of Steady Flow," *Proc. Inst. Mech. Eng. Conf. Proc.*, vol. 182, no. 8, pp. 221–231, Sep. 1967.

[261] S. W. Churchill, "Empirical Expressions for the Shear Stressing Turbulent Flow in Commercial Pipe," *AIChE J.*, vol. 19, no. 2, pp. 375–376, 1973.

[262] S. . Churchill, "Friction-factor Equation Spans all Fluid Flow Regimes," *Chem. Eng. (New York) 84 (24), pp. 91–92*, 1977.

[263] R. S. Benson, “A review of methods for assessing loss coefficients in radial gas turbines,” *Int. J. Mech. Sci.*, vol. 12, no. 10, pp. 905–932, 1970.

[264] P. He, Z. Sun, B. Guo, H. Chen, and C. Tan, “Aerothermal Investigation of Backface Clearance Flow in Deeply Scalloped Radial Turbines,” *J. Turbomach.*, vol. 135, no. 2, pp. 21002–21012, Oct. 2012.

[265] J. W. Daily and R. E. Nece, “Chamber Dimension Effects on Induced Flow and Frictional Resistance of Enclosed Rotating Disks,” *J. Basic Eng.*, vol. 82, no. 1, pp. 217–230, Mar. 1960.

[266] S. W. T. Spence, W. J. Doran, and D. W. Artt, “Experimental performance evaluation of a 99.0 mm radial inflow nozzled turbine at larger stator-rotor throat area ratios,” *Proc. Inst. Mech. Eng. Part A J. Power Energy*, vol. 213, no. 3, pp. 205–218, May 1999.

[267] L. Shao, J. Zhu, X. Meng, X. Wei, and X. Ma, “Experimental study of an organic Rankine cycle system with radial inflow turbine and R123,” *Appl. Therm. Eng.*, vol. 124, no. Supplement C, pp. 940–947, 2017.

[268] K. R. Pullen, N. C. Baines, and S. H. Hill, “The Design and Evaluation of a High Pressure Ratio Radial Turbine,” *ASME Publ.*, no. 78934, p. V001T01A050, 1992.

[269] H. Woolley and P. Hatton, “viscous flow in radial turbomachine blade passages,” in *Inst Mech Engrs conference proceedings*, 1973.

[270] N. C. Baines, “Flow Development in Radial Turbine Rotors,” in *nternational Gas Turbine and Aeroengine Congress and Exhibition, Birmingham, UK*, 1996, no. 78729, p. V001T01A021.

[271] J.F. Kline, T.P. Moffitt, and R.G Stabe, “Incidence Loss for Fan Turbine Rotor Blade in Two-Dimensional Cascade,” NASA, Cleveland, OH, United States, 1983.

[272] P. Colonna, S. Rebay, J. Harinck, and A. Guardone, “Real-gas effects in ORC turbine flow simulations: Influence of thermodynamic models on flow fields and performance parameters,” in *European Conference on Computational Fluid Dynamics*, 2006.

[273] J. Harinck, D. Pasquale, R. Pecnik, J. van Buijtenen, and P. Colonna, “Performance improvement of a radial organic Rankine cycle turbine by means of automated computational fluid dynamic design,” *Proc. Inst. Mech. Eng. Part A J. Power Energy*, vol. 227, no. 6, pp. 637–645, Aug. 2013.

[274] A. Uusitalo, T. Turunen-Saaresti, A. Guardone, and A. Grönman, “Design and Flow Analysis of a Supersonic Small Scale ORC Turbine Stator With High Molecular Complexity Working Fluid,” no. 45660. p. V03BT26A004, 2014.

[275] R. Verma, A. A. Sam, and P. Ghosh, “CFD Analysis of Turbo Expander for Cryogenic Refrigeration and Liquefaction Cycles,” *Phys. Procedia*, vol. 67, pp. 373–378, 2015.

[276] A. M. Daabo, A. Al Jubori, S. Mahmoud, and R. K. Al-Dadah, “Parametric study of efficient small-scale axial and radial turbines for solar powered Brayton cycle application,” *Energy Convers.*

Manag., vol. 128, no. Supplement C, pp. 343–360, 2016.

[277] D. Fiaschi, G. Innocenti, G. Manfrida, and F. Maraschiello, “Design of micro radial turboexpanders for ORC power cycles: From 0D to 3D,” *Appl. Therm. Eng.*, vol. 99, pp. 402–410, 2016.

[278] M. j. Atkinson, “The Design of Efficient Radial Turbines for Low Power Applications,” P.hD. Thesis, University of Sussex, 1998.

[279] ANSYS Inc, “ANSYS CFX-Solver Theory Guide, Release 15.0,” 2015.

[280] A. Marasn and S. Moreau, “Analysis of the Flow Structure in aRadial Turbine,” in *11th European Conference on Turbomachinery Fluid dynamics & Thermodynamics*, 2015.

[281] D. P. Fajardo, “\Methodology for the Numerical Characterization of a Radial Turbine under Steady and Pulsating Flow,” P.hD. Thesis, Universitat Politecnica De Valencia, 2012.

[282] E. Sauret and Y. Gu, “Three-dimensional off-design numerical analysis of an organic Rankine cycle radial-inflow turbine,” *Appl. Energy*, vol. 135, no. Supplement C, pp. 202–211, 2014.

[283] F. R. Menter, “Two-equation eddy-viscosity turbulence models for engineering applications,” *AIAA J.*, vol. 32, no. 8, pp. 1598–1605, Aug. 1994.

[284] O. Redlich and J. Kwong, “On the Thermodynamics of Solutions. V. An Equation of State. Fugacities of Gaseous Solutions.,” *Chem. Rev.*, vol. 44, no. 1, pp. 233–244, 1949.

[285] G. Soave, “Equilibrium constants from a modified Redlich-Kwong equation of state,” *Chem. Eng. Sci.*, vol. 27, no. 6, pp. 1197–1203, 1972.

[286] D.-Y. Peng and D. B. Robinson, “A New Two-Constant Equation of State,” *Ind. Eng. Chem. Fundam.*, vol. 15, no. 1, pp. 59–64, 1976.

[287] ANSYS Inc, “ANSYS CFX-Solver Modeling Guide, Release 14.5,” 2012.

[288] A. T. Simpson, S. W. Spence, and J. K. Watterson, “A Comparison of the Flow Structures and Losses Within Vaned and Vaneless Stators for Radial Turbines,” *J. Turbomach.*, vol. 131, no. 3, pp. 31010–31015, Apr. 2009.

[289] L. Zhang, W. Zhuge, Y. Zhang, and T. Chen, “Similarity Theory Based Radial Turbine Performance and Loss Mechanism Comparison between R245fa and Air for Heavy-Duty Diesel Engine Organic Rankine Cycles,” *Entropy*, vol. 19 (1): 25, 2017.

[290] Y. Li and X. Ren, “Investigation of the organic Rankine cycle (ORC) system and the radial-inflow turbine design,” *Appl. Therm. Eng.*, vol. 96, pp. 547–554, Mar. 2016.

[291] M. Arifin, *Performance Of A Radial Turbine For Small Organic Rankine Cycle Power Generation System*. 2014.

[292] K. Qiu and E. Thorsteinson, “An organic Rankine cycle system for solar thermal power applications,” in *International Conference on Renewable Energy Research and Application (ICRERA), Milwaukee, USA*, 2014.

[293] T. Chambers, J. Raush, and B. Russo, “Installation and Operation of Parabolic Trough Organic Rankine Cycle Solar Thermal Power Plant in South Louisiana,” *Energy Procedia*, vol. 49, no. Supplement C, pp. 1107–1116, 2014.

[294] S. Quoilin, M. Orosz, H. Hemond, and V. Lemort, “Performance and design optimization of a low-cost solar organic Rankine cycle for remote power generation,” *Sol. Energy*, vol. 85, no. 5, pp. 955–966, 2011.

[295] X. D. Wang, L. Zhao, J. L. Wang, W. Z. Zhang, X. Z. Zhao, and W. Wu, “Performance evaluation of a low-temperature solar Rankine cycle system utilizing R245fa,” *Sol. Energy*, vol. 84, no. 3, pp. 353–364, 2010.

[296] M. Petrollese, D. Cocco, and G. Cau, “Small-scale CSP plant coupled with an ORC system for providing dispatchable power: the Ottana Solar Facility,” *Energy Procedia*, vol. 129, no. Supplement C, pp. 708–715, 2017.

[297] P. Kolasiński, P. Błasiak, and J. Rak, “Experimental investigation on multi-vane expander operating conditions in domestic CHP ORC system,” *Energy Procedia*, vol. 129, no. Supplement C, pp. 323–330, 2017.

[298] A. Landelle, N. Tauveron, P. Haberschill, R. Revellin, and S. Colasson, “Organic Rankine cycle design and performance comparison based on experimental database,” *Appl. Energy*, vol. 204, pp. 1172–1187, 2017.

[299] H. Liu, G. Qiu, Y. Shao, F. Daminabo, and S. B. Riffat, “Preliminary experimental investigations of a biomass-fired micro-scale CHP with organic Rankine cycle†,” *Int. J. Low-Carbon Technol.*, vol. 5, no. 2, pp. 81–87, 2010.

[300] G. Qiu, Y. Shao, J. Li, H. Liu, and S. B. Riffat, “Experimental investigation of a biomass-fired ORC-based micro-CHP for domestic applications,” *Fuel*, vol. 96, no. Supplement C, pp. 374–382, 2012.

[301] M. A. Ancona *et al.*, “A Micro-ORC Energy System: Preliminary Performance and Test Bench Development,” *Energy Procedia*, vol. 101, no. Supplement C, pp. 814–821, 2016.

[302] G. Żywica, T. Z. Kaczmarczyk, E. Ihnatowicz, and T. Turzyński, “Experimental investigation of the domestic CHP ORC system in transient operating conditions,” *Energy Procedia*, vol. 129, no. Supplement C, pp. 637–643, 2017.

[303] C. J. Bliem and G. L. Mines, “Initial Results for Supercritical Cycle Experiments Using Pure and Mixed-Hydrocarbon Working Fluids,” in *Transactions - Geothermal Resources Council*, 1984, vol. 8, pp. 27–32.

[304] P. Klonowicz, A. Borsukiewicz-Gozdur, P. Hanausek, W. Kryłłowicz, and D. Brüggemann, “Design and performance measurements of an organic vapour turbine,” *Appl. Therm. Eng.*, vol. 63, no. 1, pp. 297–303, 2014.

[305] F. Yang, H. Cho, H. Zhang, and J. Zhang, “Thermoeconomic Multi-Objective Optimization of a Dual Loop Organic Rankine Cycle (ORC) for CNG Engine Waste Heat Recovery,” *Appl. Energy*, vol. 205, no. Supplement C, pp. 1100–1118, 2017.

[306] T. Furukawa, M. Nakamura, K. Machida, and K. Shimokawa, “A Study of the Rankine Cycle Generating System for Heavy Duty HV Trucks,” *SAE Tech. Pap.*, 2014.

[307] E. Wang, Z. Yu, H. Zhang, and F. Yang, “A regenerative supercritical-subcritical dual-loop organic Rankine cycle system for energy recovery from the waste heat of internal combustion engines,” *Appl. Energy*, vol. 190, no. Supplement C, pp. 574–590, 2017.

[308] V. Lemort, S. Quoilin, C. Cuevas, and J. Lebrun, “Testing and modeling a scroll expander integrated into an Organic Rankine Cycle,” *Appl. Therm. Eng.*, vol. 29, no. 14, pp. 3094–3102, 2009.

[309] H. G. Zhang, E. H. Wang, and B. Y. Fan, “A performance analysis of a novel system of a dual loop bottoming organic Rankine cycle (ORC) with a light-duty diesel engine,” *Appl. Energy*, vol. 102, no. Supplement C, pp. 1504–1513, 2013.

[310] C. Sellers, “Field operation of a 125kW ORC with ship engine jacket water,” *Energy Procedia*, vol. 129, no. Supplement C, pp. 495–502, 2017.

[311] M. Glensvig *et al.*, “Testing of a Long Haul Demonstrator Vehicle with a Waste Heat Recovery System on Public Road,” in *SAE 2016 Commercial Vehicle Engineering Congress*, 2016.

[312] T. Endo *et al.*, “Study on Maximizing Exergy in Automotive Engines,” in *SAE World Congress & Exhibition, Detroit, Michigan*, 2007.

[313] B. Ibaraki S., Endo T., Kojima Y., Takahashi T. and K. S. T., “Research of a Rankine Cycle On-board heat waste heat recovery system,” *J. Soc. Automot. Eng. Japan*, 2006.

[314] D. R. Jones, C. D. Perttunen, and B. E. Stuckman, “Lipschitzian optimization without the Lipschitz constant,” *J. Optim. Theory Appl.*, vol. 79, no. 1, pp. 157–181, Oct. 1993.

Appendices

Appendix A: Stator and Rotor 3D Model

Stator

The thickness distribution is performed on a parabolic-arc camber-line as outlined in[234]. The governing equation for a parabolic-arc camber-line is shown in equation (A-1). The coordinate (x, y) are shown inFigure A-0-1.

$$x^2 + \frac{c-2a}{b}xy + \frac{(c-2a)^2}{4b^2}y^2 - cx - \frac{c^2-4ac}{4b} = 0 \quad \text{(A-1)}$$

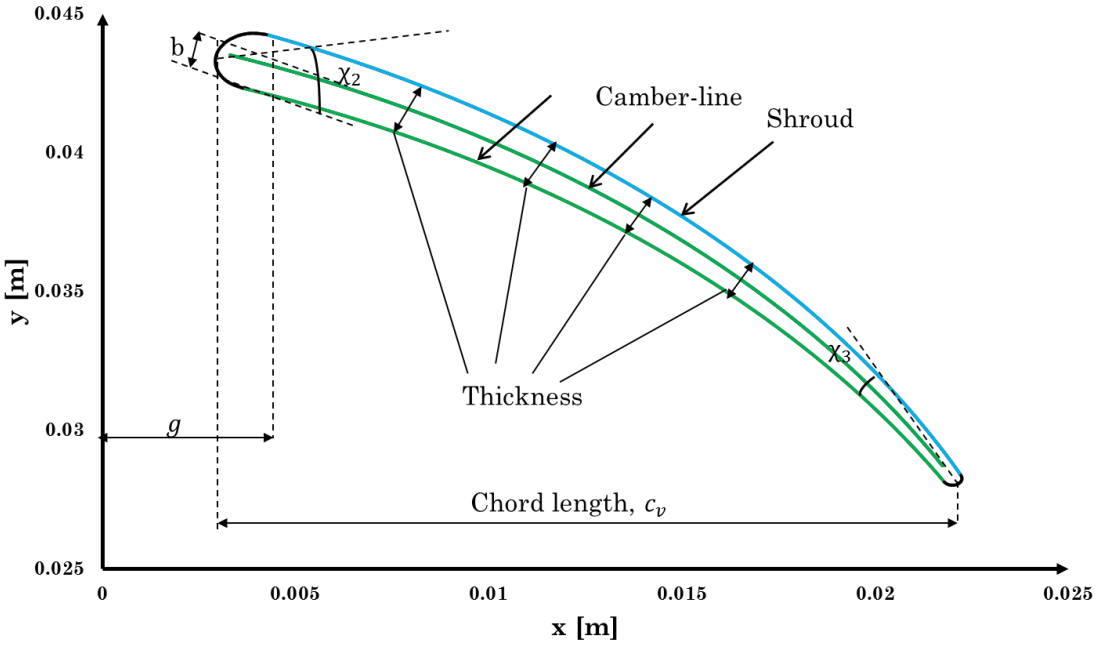

Figure A-0-1: Creation of stator 3D model.

The stator geometrical parameters can then be obtained based on the value of x. The required parameters are chord lengthc_v, maximum camber$b$ and its location g. The leading χ_2 and trailing$\chi_3$edge blade angles can be obtained using equations (A-2)and (A-3). The angle of the blade comber-line is then the sum of the two blade angles.

$$tan\chi_2 = \frac{4b}{(4g - c_v)} \quad \text{(A-2)}$$

$$tan\chi_3 = \frac{4b}{(3c_v - 4a)} \quad \text{(A-3)}$$

Aungier [234]proposed an equation to calculate the blade thickness at any location along the camber-line as shown in equations (A-4) to (A-8).

$$t = t_{ref} + [t_{max} - t_{ref}]\xi^e \quad \text{(A-4)}$$

$$t_{ref} = t_2 + [t_3 - t_2](\frac{x}{d}) \quad \text{(A-5)}$$

$$\xi = \frac{x}{d} \quad for\ x \le d \quad \text{(A-6)}$$

$$\xi = \frac{c - x}{c - d} \quad for\ x > d \quad \text{(A-7)}$$

$$e = [0.95\left(1 - \frac{x}{c}\right)(1 - \xi) + 0.05]\sqrt{\frac{0.4d}{c}} \quad \text{(A-8)}$$

t_{max} and d are the maximum blade thickness and its location, respectively. The leading t_2 and trailing $t_3$edge blade thicknesses can be specified by the designer

Rotor

The camber-line in the hub and shroud contours are shown in equations (A-9)and (A-10), respectively.

$$\theta(m) = Am + Bm^2 + Cm^4 \quad \text{(A-9)}$$

$$\theta(m) = Dm + Em^2 + Fm^4 \quad \text{(A-10)}$$

Where:

$$A = \frac{cot\beta_{5t}}{r_{5t}}$$

$$B = \frac{1}{m_4^2}\left[\frac{cot\beta_4}{r_4} - \frac{cot\beta_{5t}}{r_{5t}}\right]$$

$$C = -\frac{B}{2m_4}$$

$$D = \frac{cot\beta_{5h}}{r_{5h}}$$

$$E = \frac{3\theta_4}{m_4^2} - \frac{1}{m_4}\left[2\frac{cot\beta_{5h}}{r_{5h}} + \frac{cot\beta_4}{r_r}\right]$$

$$F = -\frac{2\theta_4}{m_4^3} + \frac{1}{m_4^2}\left[\frac{cot\beta_{5h}}{r_{5h}} + \frac{cot\beta_4}{r_r}\right]$$

Appendix B: Cubic Equations of State

The Standard Redlich Kwong (SRK) Model

$$p = \frac{RT}{v-b+c} - \frac{a(T)}{v(v+b)} \quad \text{(B1)}$$

$$a = a_0 \left(\frac{T}{T_c}\right)^{-n} \quad \text{(B2)}$$

$$a_0 = \frac{0.42747\ R^2 T_c^2}{P_c} \quad \text{(B3)}$$

$$b = \frac{0.08664\ RT_c}{P_c} \quad \text{(B4)}$$

v is the specific volume and n is 0.5. The parameter c is set to zero in the SRK.

The Aungier Redlich Kwong Model (ARK) Model

The The Aungier Redlich Kwong Model (ARK) is similar to SRK except c and n, and they are defined as in the equations below.

$$c = \frac{RT_c}{P_c + \frac{a_0}{v_c(v_c+b)}} + b - v_c \quad \text{(B5)}$$

$$n = 0.4986 + 1.1735\omega + 0.4754\omega^2 \quad \text{(B6)}$$

The Soave Redlich Kwong Model (SORK) Model

The Soave Redlich Kwong Model is similar to SRK except $a(T)$ and n which are defined as following:

$$a(T) = a_0 \left(1 + n\left(1 - \sqrt{\frac{T}{T_c}}\right)\right)^2 \quad \text{(B7)}$$

$$n = 0.480 + 1.574\omega - 0.176\omega^2 \quad \text{(B8)}$$

Peng Robinson (PR) Model

$$p = \frac{RT}{v-b} - \frac{a(T)}{v^2+2bv-b^2} \quad \text{(B9)}$$

$$b = 0.0778\frac{RT_c}{P_c} \quad \text{(B10)}$$

$$a(T) = a_0\left(1 + n\left(1 - \sqrt{\frac{T}{T_c}}\right)\right)^2 \tag{B11}$$

$$a_0 = \frac{0.45724\ R^2 T_c^2}{P_c} \tag{B12}$$

$$n = 0.37464 + 1.5422\omega - 0.26993\omega^2 \tag{B13}$$

Appendix C: 3D Models

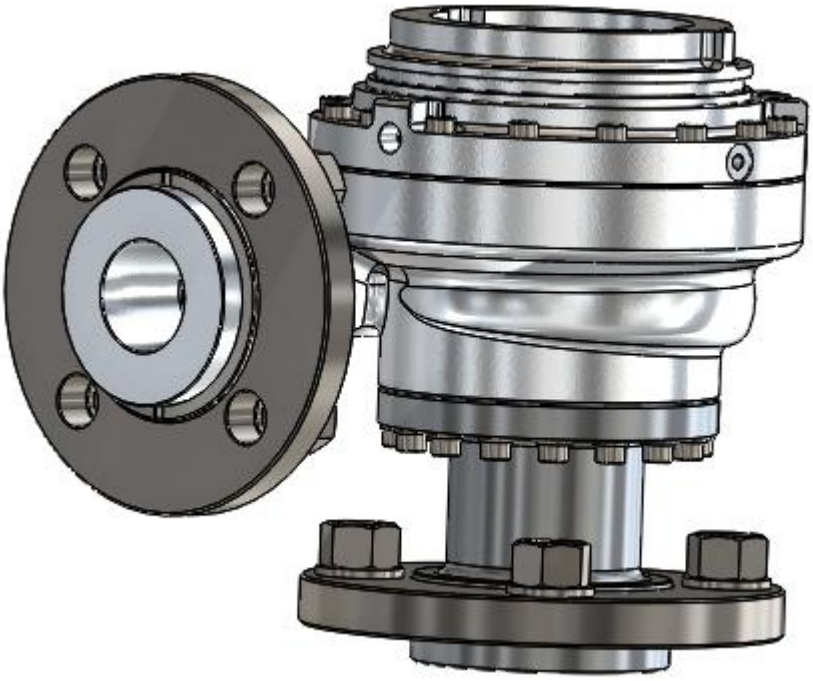

Figure C-1: Volute assembly

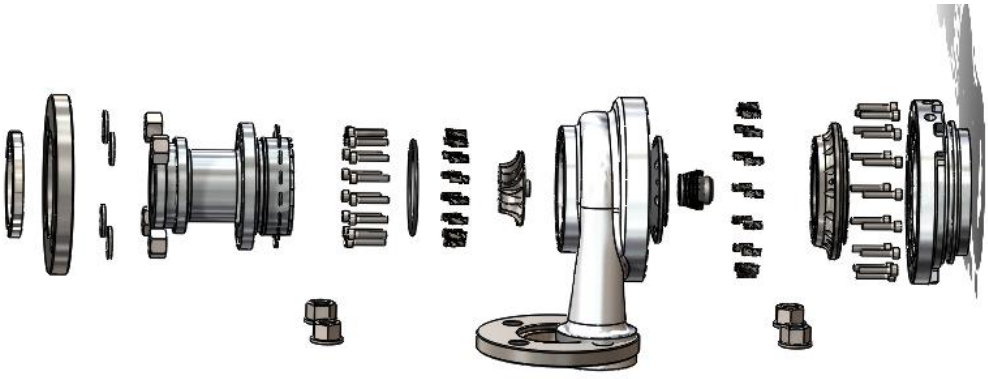

Figure C-2: Exploded view of the turbine set

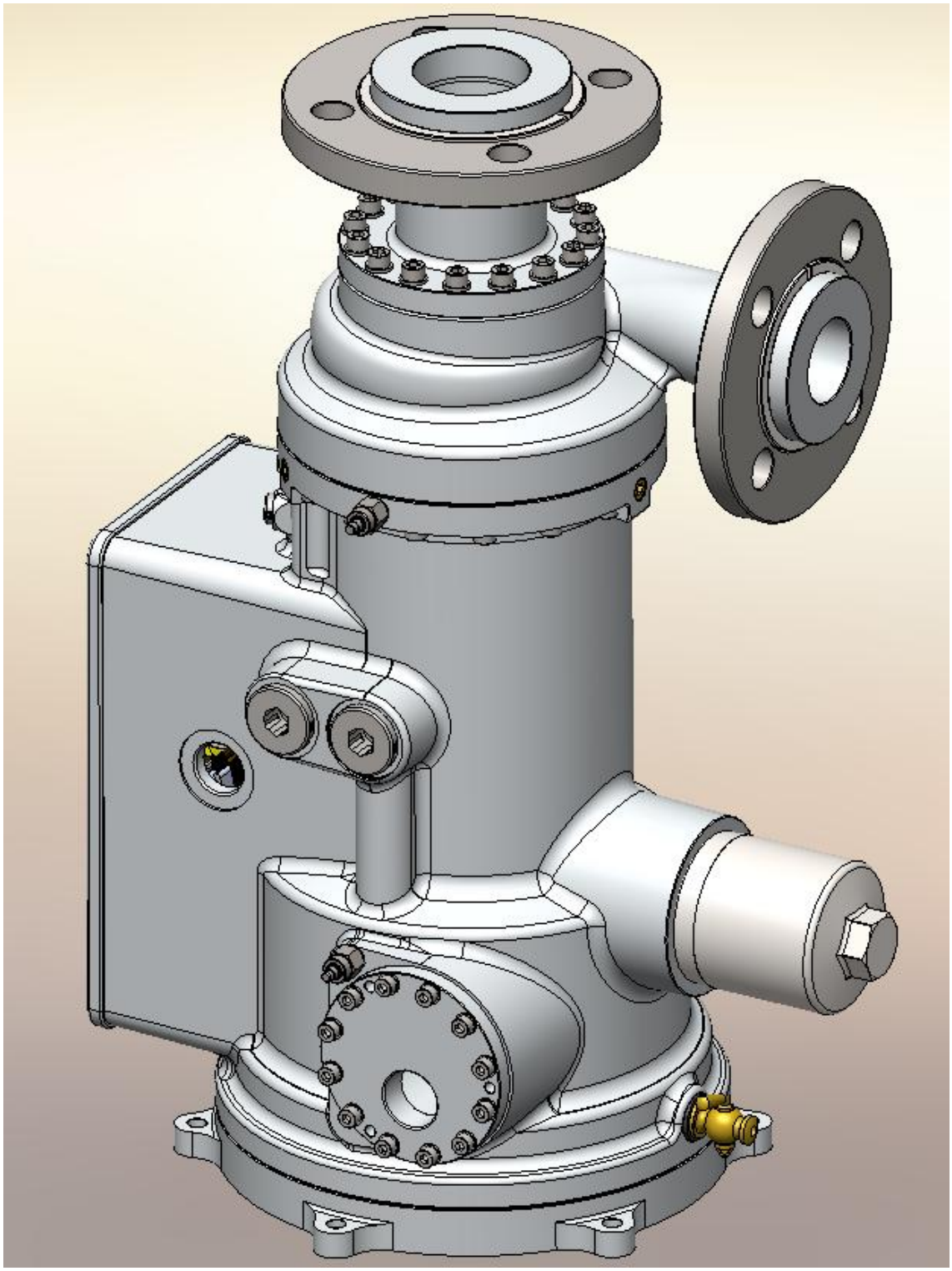

Figure C-3: Turbo-generator unit

Appendix D: Manufacturing

Figure D-1: Manufactured volute

Figure D-2: Manufactured nozzle

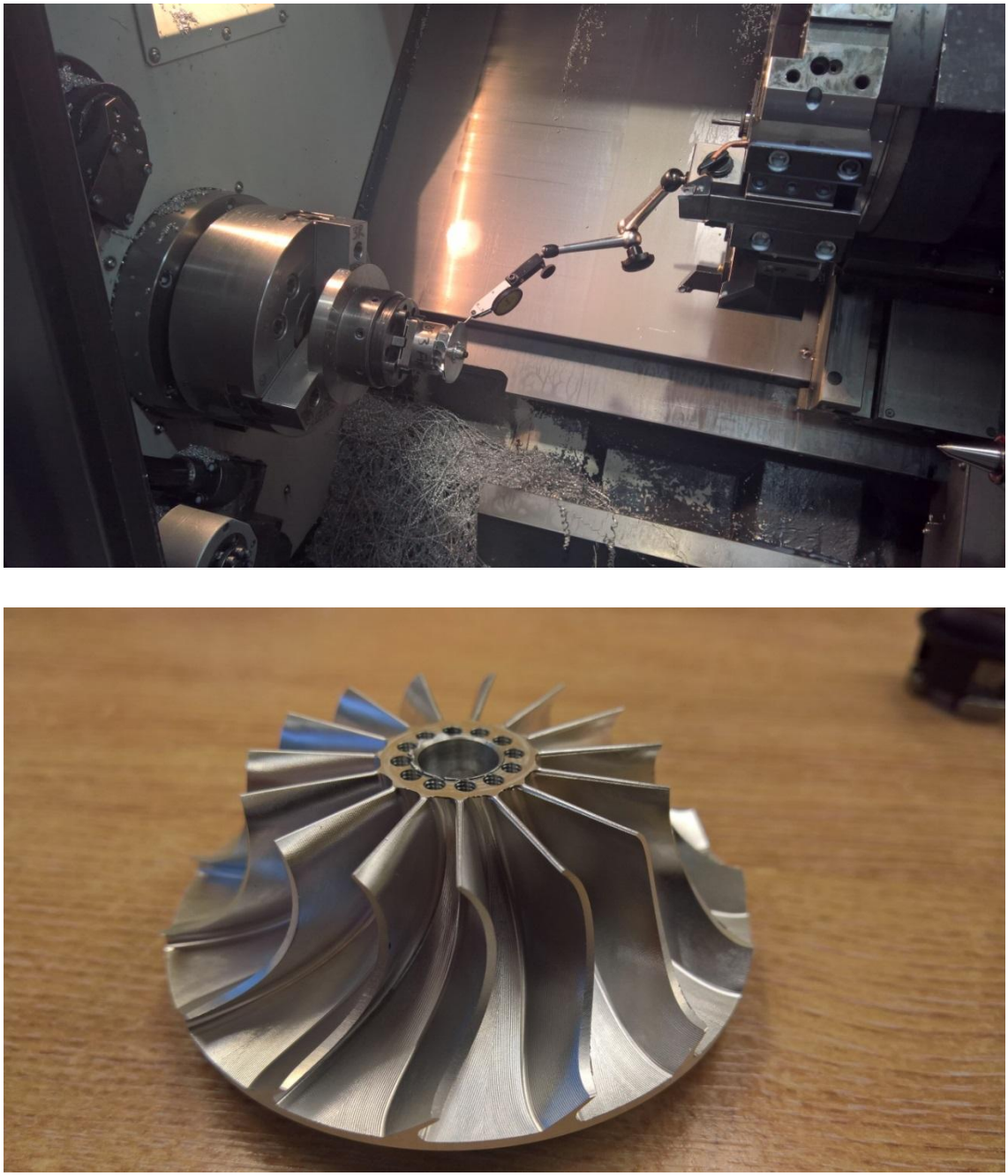

Figure D-3: Manufacturing of the rotor part (Aluminium)

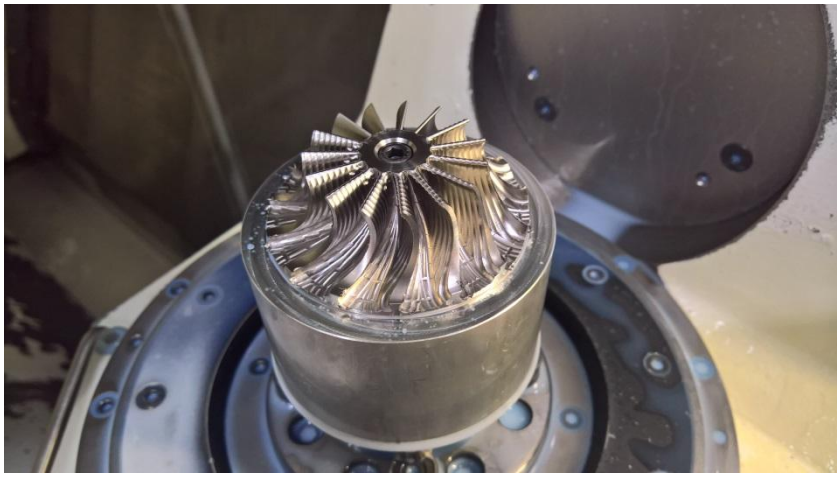

Figure D-4: Pre-finish milling of the Titanium-made rotor

Figure D-5: Inspection of the Titanium-made rotor

Figure D-6: Finished Titanium-made rotor